# Molecular Gas and Star Formation in the Central Regions of Virgo Spiral Galaxies

Thesis by

Blaise Canzian

In Partial Fulfillment of the Requirements

for the Degree of

Doctor of Philosophy

California Institute of Technology

Pasadena, California

1990

Submitted May 25, 1990


4321
4501
4254
4569
4654
4535
4303
4536

Can't keep my eyes

From the circling skies;

Tongue-tied and twisted,

Just an earth-bound misfit,

I.

"Learning to Fly"

David Gilmour and Nick Mason

# Acknowledgements

Thank you, Mom and Dad, for providing a wonderful environment to grow up in, so much stimulation and indulgence, and much support for and toleration of all my interests over the years. The completion of this project is, more than anything, a tribute to you. Thank you, too, Dr. Drake, for your encouragement and support. I am grateful that you gave me so many opportunities to see what doing astronomy is all about. Thank you, Dr. Lee and Dr. Wilkins, for showing me how enjoyable physics is through your zesty teaching and your devotion in and out of the classroom. Thank you, especially, Dr. Lynds, for being such a patient, tolerant, and generous guide on my introduction to astronomical work. Thank you also for introducing me to the greater world of which astronomy is but a small part: some of the people, some of the places, and some of the customs and ideas amongst which we all must somehow fit. Thank you, Dr. Six and Dr. Davis, for providing further stimulation of my astronomical interests. You helped to provide a marvelous environment in which I learned much about the celestial spheres but, even more, much about the larger sphere of life. And thank you, Dr. Kulkarni, Dr. Mould, and Dr. Scoville, for much sage advice, personal consideration, support, and counsel on the way toward completing this project and embarking on my career. I thank you, Terri, for all of your unfailing support and for kindly giving so much of yourself to help me in so many ways.

# Abstract

The central regions of eight normal spiral galaxies in the Virgo Cluster spanning a wide range of morphological types have been observed in CO ($J = 1 \rightarrow 0$) emission using the Owens Valley mm-wave interferometer. Broadband optical and H$\alpha$ CCD photometry was obtained using the Palomar 60-inch telescope.

The $H_2$ masses in the central five kiloparsecs of the spirals are large, typically several $10^8$ solar masses, far exceeding the atomic hydrogen masses. $H_2$ densities in the cloud complexes are comparable to those of Galactic center complexes such as Sgr B2. Molecular gas comprises a substantial fraction of the dynamical mass of the central regions. The gas mass fraction, typically 5–15% at 2.5 kiloparsec radius, increases to 15–30% at the center. Molecular gas in the interferometer maps is concentrated in structures with scale lengths of only 400–750 parsecs. Such massive gas disks are, nonetheless, dynamically stable. The $H_2$ masses may be overestimated in some spirals because of cloud heating. The main source of heating is probably dissipation of turbulence, which is probably greater at the centers of spirals based on CO line widths.

Current central star formation rates are about a few solar masses per year. The star formation rate in the central regions of most of the spirals has been relatively constant over a Hubble time, although some galaxies are currently undergoing star formation bursts. Several mechanisms are suggested that could supply enough gas

to maintain current star formation rates. The current rate of star formation is well correlated with the mean square molecular gas surface density computed from interferometer maps. Such a correlation is expected if cloud-cloud collisions or another stimulation mechanism acting between clouds is the principle means to produce high-mass stars where the concentration of clouds is greatest. The $B$ luminosity is better correlated with the total gas mass surface density, which supports a stochastic or independent mode of forming intermediate-mass stars in the general cloud population.

# Table of Contents

# List of Tables

# List of Figures

# Chapter 1
# Introduction

## 1.1. Overview of the Issues

Amidst the complexity of stars and swirling gas in a spiral galaxy, the inevitable focal point is the nucleus. The nuclear region is a source of or sink for very energetic or relentless phenomena. Starburst and Seyfert nuclei, for instance, release prodigious amounts of energy but must depend on an equally ample supply of fuel. Infalling gas which has been robbed from the disk is generally believed to provide the fuel necessary to power nuclear phenomena. Dynamical processes operating in the disk may provide the means by which the gas can be delivered to the nucleus. Answers to questions about the amount of gas available, the amount demanded by the nuclear energetics, the connection between dynamics and morphology, and the timescale and efficiency of processes to transport gas will provide a clearer understanding of the nuclear regions of spiral galaxies.

Despite the knowledge of the widespread presence of molecular gas in spiral galaxies, surprisingly little detailed information is known about its distribution. Individual molecular clouds have been observed in only two external spiral galaxies, M31 and M33 (Vogel, Boulanger, and Ball 1987; Wilson *et al.* 1988), and detailed maps of CO emission from spiral disks are only now being made, such as one of M51 by Rand and Kulkarni (1990). Major axis scans using a single dish (Kenney 1987) indicate

that the CO emission from many disk galaxies follows an exponential law with scale length 1–2 kpc and radial extent 5–10 kpc. Morris and Rickard (1982) noted that many spirals had strong, central CO peaks superposed on the usual disk emission. Based on single-dish maps, Sofue (1988) has asserted that the typical late-type spiral houses a very small ($< 1$ kpc) nuclear molecular disk. This inner molecular disk is characterized by large density and high velocity dispersion and is distinct from the more extended disk outside it.

Just how much gas is at the centers of spirals? In contemplating the maintenance of spiral structure in a gas disk, Toomre (1981) conjectured that the dynamical evolution of spirals has caused gas to migrate inward. By redistributing its mass, a disk may create an inner Lindblad resonance, the presence of which may be necessary to regulate swing amplification of spiral structure. Analysis of the distribution of gas mass and the shape of the inner rotation curves of spirals could verify the existence of the conjectured central gas concentrations and, perhaps, locate the positions and influence of Lindblad resonances. The mechanism responsible for the inward transport of gas is not clear, but it could involve either cloud collisions aided by differential rotation or else dynamical friction. Knowing the amount of gas present and its rate of conversion into stars could place constraints that identify the physical process responsible for gas transport. Gas may be a dynamically significant constituent of the inner disks of spirals. The presence of very large amounts of gas could alter the results of numerical simulations of spiral structure (Sanders and Huntley 1976; Huntley 1980; Mulder 1986), which have either ignored the self-gravity of the gas or have assumed that its mass fraction is small.

The properties of molecular hydrogen clouds deduced from extensive molecular transition observations in the disk of our Galaxy may not carry over to molecular clouds near spiral nuclei. After all, the nuclear environment has a much larger mass

density and higher radiation field energy density than the disk, making it plausible that molecular clouds will have different characteristics in the two regions. How different might nuclear molecular clouds be? The central region of our Galaxy has the largest and most CO-luminous molecular cloud complexes in the Galaxy. The ambient radiation field, considering both ultraviolet ionizing photons and cosmic rays, could possibly raise cloud mean temperatures. Kutner and Leung (1985) have predicted from numerical modeling that increased CO emissivity results from increased cloud temperature. Since detection of molecular clouds relies on the presence of CO, metallicity variations could influence cloud properties, too. Maloney and Black (1988) have theorized that very low-metal molecular clouds are quite under-luminous in CO emission. In contrast to this result is the observation that molecular clouds between a 2 kpc and 10 kpc radius in our Galaxy have very similar CO emissivities (based on gamma ray observations, Bloemen *et al.* 1986) despite the changing metallicity over that region. At issue is the justifiability of using observed properties of Galactic molecular clouds to induce properties of extragalactic molecular clouds based on integrated observations of a cloud ensemble. The use of CO emission to deduce molecular gas mass in our Galaxy has extensive observational justification (Young 1990). Even so, application of this method to the nuclear regions of spirals should be done with caution. Estimation of the central molecular gas mass of a spiral should be accompanied by an analysis of the effects of the nuclear environment on the clouds. Only with extraordinary evidence can extraordinary claims, such as the large central gas concentrations conjectured in literature cited above, be reliably supported.

The relationship between gas density and the rate of star formation first proposed by Schmidt (1959) has been investigated and elaborated upon to the present day (Kennicutt 1989). Although stars must form only where there is gas, the relationship between the star formation rate and extensive properties of the gas is understood

at a rudimentary level at best. Do stars form strictly in proportion to increasing gas density, or is the relationship nonlinear? In particular, if there is a large central concentration of gas in the typical spiral, then why are nuclear starbursts not more widespread among spirals? Other physical influences may bear on the star formation rate, such as the frequency of molecular cloud collisions. Comparison of rotation curve shapes with star formation efficiencies should illuminate this issue. Finally, what has been the star formation history of the central regions of spirals? If gas is transported to the center, has its mass flux fueled a constant star formation rate over time, or has the rate steadily declined?

## 1.2. Overview of the Observations

In this thesis, eight spiral galaxies in the Virgo Cluster have been analyzed in detail using both optical and millimeter wavelength observations. The galaxies were chosen to be bright CO emitters spanning a range of morphological types and having neither interacting companions nor obvious barred structure. Their location in the Virgo Cluster helps to lessen distance-dependent effects so that comparisons between galaxies are reliable. The nuclear CO observations are most important, since they show the molecular gas distribution and motions. It was expected that the amount and distribution of molecular gas would play the part of tea leaves in a cup and indicate the greater fortunes of stars and gas in the disk of the galaxy. It is plausible that a connection exists between the nucleus and disk, since the dynamical effects that lead to spiral arms rely on resonance phenomena with effects near the nucleus.

NGC 4254 and NGC 4321 have well-defined spiral arms and disks which are very actively forming high-mass stars. NGC 4321 has a classical two-armed spiral shape, while the spiral arms of NGC 4254 are more chaotic and more numerous. NGC 4535 and NGC 4536 have much narrower spiral arms than NGC 4254 and NGC 4321 and are not forming high-mass stars in their disks as actively. Their spiral structure is

much more open, with greater arm-interarm contrast in optical continuum light. The outer disk of NGC 4535 is surprisingly active in producing high-mass stars. NGC 4303 resembles NGC 4535 and NGC 4536 in the open, two-armed appearance of its inner disk, which is weakly barred. Its outer disk resembles NGC 4254 in its more chaotic appearance and in the rampant high-mass star formation occurring there. NGC 4654 is a very late-type spiral with a small bar at its center and spiral arms which are not well delineated at all. NGC 4501 is a very large, early-type spiral with short, feathery spiral arm segments. Relatively little high-mass star formation is evident in its disk. NGC 4569 is a very early-type spiral; it has two thick, ill-defined spiral arms accompanied by extensive dust lanes. Its nucleus is bright and very blue, but there is no evidence of much high-mass star formation anywhere else in this galaxy.

The CO observations have a typical spatial resolution of 400 pc across a field of view 5 kpc wide centered on the nucleus. Spectra have a velocity resolution of $13\,\mathrm{km\,sec^{-1}}$ across a filterbank $416\,\mathrm{km\,sec^{-1}}$ wide, and enable construction of detailed velocity fields. Optical CCD images of the galaxies have rather better spatial resolution than the CO data, about 150 pc. Exposures in $B$, $V$, $r$, and $i$ bands enclose the entire optical disks of the galaxies. H$\alpha$ emission images were formed using a continuum subtraction process with on- and off-line exposures.

## 1.3. Scientific Goals

In this thesis, the detailed distribution of molecular gas at the centers of spiral galaxies is explored using interferometric maps of CO emission. The radial behavior of the emission is measured and, in particular, the hypothesis of a central molecular disk of high density is investigated. Also of interest are the correspondences to be found between molecular gas morphology and optical features, such as dust lanes, spiral arms, and star formation sites. Dynamical processes have a large role in shaping the features that are noted.

The dynamical mass within a given region may be estimated using the galactic rotation curve. High-resolution rotational information from CO velocity fields is combined with optical and H I rotation curve data. Of special interest is the fraction of the central mass which is in gaseous form. The gas mass estimates are tempered by consideration of the effects of the nuclear environment on molecular clouds. Particular emphasis is placed on the change in CO emissivity with cloud temperature. The effect of the gas mass on the dynamics and stability of the galactic disk is also addressed.

Of interest is the form of the star formation law relating the star formation rate to the gas density. Previous investigations of the relationship between star formation and gas density have used the mean density averaged over large areas. Such an approach ignores the potential difference between star formation in isolated clouds and star formation in clouds that are part of dense molecular cloud complexes. The high-resolution data in this thesis allow investigation of the local star formation laws and inquiry into the possibility of environmental influences on the star formation rate. H$\alpha$ fluxes provide estimates of the current star formation rate. The total mass distribution governs differential rotation effects and the timescales of cloud orbits and cloud collisions; it, too, influences the star formation rate. The relationship between the star formation rate and the shape of the rotation curve is investigated. By combining information from rotation curves, H$\alpha$ and $B$-band flux data, and $B-V$ color data, rough pictures of the star formation histories of Virgo spirals are drawn.

There is presentation of a considerable amount of data in the first chapters of this thesis. A substantial amount of ink is devoted to descriptions of techniques and procedures, morphological descriptions, and accumulation of data in forms useful for answering questions posed in §1.1. The heart of the thesis is in Chapter 7 and Chapter 8, which address questions about the amount of molecular gas at the centers of Virgo spirals and its physical and dynamical state, the star formation histories of the

central regions of Virgo spirals, and physical mechanisms controlling the rate of star formation and gas collection in the central regions of Virgo spirals. Conclusions are summarized in Chapter 9. The reader with a scientific interest in these astronomical matters in particular is advised to refer to the latter chapters. Readers interested in techniques and details of data analysis are provided with ample pedagogical material in the initial chapters and in the extensive appendices.

## References

Bloemen, J. B. G. M., Strong, A. W., Blitz, L., Cohen, R. S., Dame, T. M., Grabelsky, D. A., Hermsen, W., Lebrun, F., Mayer-Hasselwander, H. A., and Thaddeus, P. 1986, *Astron. Ap.*, **154**, 25.

Huntley, J. M. 1980, *Ap. J.*, **238**, 524.

Kennicutt, R. C., Jr. 1989, *Ap. J.*, **344**, 685.

Kenney, J. D. 1987, Ph.D. Thesis, University of Massachusetts.

Kutner, M. L., and Leung, C. M. 1985, *Ap. J.*, **291**, 188.

Maloney, P., and Black, J. H. 1988, *Ap. J.*, **325**, 389.

Morris, M., and Rickard, L. J. 1982, *Ann. Rev. Astron. Ap.*, **20**, 517.

Mulder, W. A. 1986, *Astron. Ap.*, **156**, 354.

Rand, R. J., and Kulkarni, S. R. 1990, *Ap. J. (Letters)*, **349**, L43.

Sanders, R. H., and Huntley, J. M. 1976, *Ap. J.*, **209**, 53.

Schmidt, M. 1959, *Ap. J.*, **129**, 243.

Sofue, Y. 1988, in *Molecular Clouds in the Milky Way and External Galaxies,* ed. R. L. Dickman, R. L. Snell, and J. S. Young (Berlin: Springer-Verlag), p. 375.

Toomre, A. 1981, in *The Structure and Evolution of Normal Galaxies,* ed. S. M. Fall and D. Lynden-Bell (Cambridge: Cambridge University Press), p. 111.

Vogel, S. N., Boulanger, F., and Ball, R. 1987, *Ap. J. (Letters)*, **321**, L145.

Wilson, C. D., Scoville, N., Freedman, W. L., Madore, B. F., and Sanders, D. B. 1988, *Ap. J.*, **333**, 611.

Young, J. S. 1990, in *The ISM in Galaxies,* ed. H. Thronson and M. Shull, in press.

# Chapter 2
# The Virgo Galaxy Sample

## 2.1. Overview and Global Properties

Being nearby and bright, Virgo Cluster spirals have been investigated by photometric, spectroscopic, and radio interferometric means. The Virgo spirals that are the subject of this study were selected primarily on the basis of their brightness in CO emission. Of secondary concern was the assembly of a wide range of morphological types. (All morphological types are from de Vaucouleurs *et al.* 1976.) It was also required that normal spirals without strong bars or close, interacting companions be selected. A precise definition of the "normal" spiral is elusive and perhaps mythical. The observational overviews presented below will indicate that each of the spirals is an interesting individual and that "nearly normal" is a better description of the group in general.

The central regions of a total of eight spiral galaxies in the Virgo Cluster were observed in CO emission using the Owens Valley mm-wave interferometer. Seven of the galaxies were also observed in Johnson $B$ and $V$ (Johnson *et al.* 1966) and Thuan-Gunn $r$ and $i$ bands (Thuan and Gunn 1976) and in H$\alpha$ emission using the Palomar 60-inch telescope. CCD photometry encompassing the full optical disks was obtained. Of primary concern in selecting the galaxies was CO brightness: interferometer images with reasonable signal-to-noise were required to investigate gas

morphology. Additionally, galaxies spanning a wide range of morphological types were desired so that systematic variations by type could be investigated. Nearly normal spirals were chosen, not spirals in interacting pairs or with strong bars, so that the link between star formation and normal spiral structure could be investigated. Finally, membership in the Virgo Cluster minimizes distance-dependent effects and so facilitates direct comparison of the galaxies. The galaxies observed and their morphological types are listed in Table 2–1. The list is representative of bright spirals of various types, but is not intended to be a complete sample in any sense.

TABLE 2–1. GLOBAL PROPERTIES

| NGC | Type | (1) $V_{\rm LSR}$ km sec$^{-1}$ | (2) $M_{\rm H\,I}$ $10^9$ M$_\odot$ | (3) $M_{\rm H_2}$ $10^9$ M$_\odot$ | (4) $M_{\rm dyn}$ $10^9$ M$_\odot$ | (5) $L_B$ $10^9$ $L_{B\odot}$ | (6) $L_{\rm FIR}$ $10^9$ $L_\odot$ |
|---|---|---|---|---|---|---|---|
| 4254 | Sc | 2408 | 4.2 | 8.7 | 102 | 32 | 20 |
| 4303 | Sbc | 1566 | 5.8 | 6.6 | 70 | 39 | 18 |
| 4321 | Sbc | 1575 | 2.2 | 9.7 | 187 | 43 | 15 |
| 4501 | Sb | 2274 | 1.8 | 6.5 | 279 | 43 | 11 |
| 4535 | Sc | 1966 | 5.0 | 4.6 | 173 | 27 | 6.6 |
| 4536 | Sbc | 1793 | 4.0 | 2.2 | 251 | 24 | 12 |
| 4569 | Sab | −224 | 0.7 | 4.4 | 195 | 45 | 5.1 |
| 4654 | Scd | 1088 | 3.3 | 2.1 | 74 | 19 | 7.0 |

The recession velocities of the galaxies in column (1) are from fits to the velocity fields seen in H I interferometric observations (Guhathakurta *et al.* 1988). The atomic hydrogen masses in column (2) are computed from total H I fluxes reported by Giovanelli and Haynes (1983). The standard conversion formula

$$M_{\rm H\,I} = (2.36 \times 10^5)\, D^2_{\rm Mpc}\, S_{\rm Jy\,km\,sec^{-1}}({\rm H\,I})\ {\rm M}_\odot \qquad (2-1)$$

is used. The distance to the Virgo Cluster is assumed to be 15.7 Mpc (Pierce and

Tully 1988) throughout this thesis. Molecular hydrogen masses in column (3) use total CO fluxes from Kenney (1987) and the conversion formula

$$M_{\mathrm{H_2}} = (1.18 \times 10^4)\, D^2_{\mathrm{Mpc}}\, S_{\mathrm{Jy\,km\,sec^{-1}(CO)}}\ \mathrm{M_\odot}, \qquad (2-2)$$

which is derived from an assumed ratio of molecular hydrogen column density to integrated CO intensity $N_{\mathrm{H_2}}/I_{\mathrm{CO}} = 3 \times 10^{20}\,\mathrm{cm^{-2}\,(K\,km\,sec^{-1})^{-1}}$. No correction for helium is included. The dynamical masses in column (4) are computed assuming a spherically symmetric mass distribution using the formula

$$M_{\mathrm{dyn}}(R) = (6.76 \times 10^4)\, D_{\mathrm{Mpc}}\, R_{\mathrm{arcmin}}\, V^2_{\mathrm{km\,sec^{-1}}}\ \mathrm{M_\odot}. \qquad (2-3)$$

The radius $R$ at which equation (2-3) was evaluated was chosen to be the radius at which the galaxy surface brightness falls to 25 $B$ mag arcsec$^{-2}$ (de Vaucouleurs *et al.* 1976). Rotation speeds at such large radii are well into the flat, asymptotic region of the rotation curves of these galaxies. H I rotation curves from Guhathakurta *et al.* (1988) supplied most of the velocity data. For a full discussion of the rotation curves of these galaxies, see Chapter 6. $B$-band luminosities in column (5) are computed using

$$L_B = (1.543 \times 10^{12})\, D^2_{\mathrm{Mpc}}\, 10^{-0.4\, B^0_T}\ \mathrm{L_{B\odot}}, \qquad (2-4)$$

where $B^0_T$ is the total $B$ magnitude corrected for inclination and extinction (de Vaucouleurs *et al.* 1976). One solar $B$-band luminosity is $\mathrm{L_{B\odot}} = 5.48 \times 10^{32}\,\mathrm{erg\,sec^{-1}}$ (Allen 1973), and the radiancy at 0.00 $B$ magnitude is $7.06 \times 10^{-13}\,\mathrm{W\,cm^{-2}}$ (Johnson 1965). The far infrared luminosity in column (6) is computed using

$$L_{\mathrm{FIR}} = (3.13 \times 10^{19})\, D^2_{\mathrm{Mpc}}\, 10^{\mathrm{FIR}}\ \mathrm{L_\odot}, \qquad (2-5)$$

where FIR $= 1.26[F(60) + F(100)]$ is the quantity listed by Helou *et al.* (1988) that estimates the total infrared flux in a rectangular bandpass centered at 82.5 $\mu$m with

a width of 80 $\mu$m, and the bolometric solar luminosity is $L_\odot = 3.8 \times 10^{33} \mathrm{erg\,sec^{-1}}$ (Allen 1973).

Using the results of galaxy surveys and studies of galaxies in the Virgo Cluster in particular, global orientation parameters have been adopted for the eight program galaxies. The position angle is that of the receding side of the galaxy, measured east from north. The inclination of the galaxy to the line of sight is defined so that a face-on galaxy has zero inclination and an edge-on galaxy has an inclination of 90°. Measured values for the orientation parameters have been culled from many sources. Published values are reproduced in Table 2–2; the values have been adapted to conform to a uniform convention, and any ambiguities have been resolved. A 3° correction has been added to inclinations computed from axial ratios according to an empirical recipe of Aaronson *et al.* (1987) based on the Holmberg formula

$$i = 3^\circ + \arccos\sqrt{[(b/a)^2 - (0.2)^2]/[1 - (0.2)^2]} \qquad (2-6)$$

Tully (1988), where the axial ratio is $b/a$. The "HEA" column contains information from Helou *et al.* (1981; 1984), which is based in part on Nilson (1973) and de Vaucouleurs *et al.* (1976). The "BST" columns contain information from Binggeli *et al.* (1984; 1985), and de Vaucouleurs and Pence (1979). Data in the "FT" column are from Fisher and Tully (1981), and in the "T" column are from Tully (1988). Information in the "GGKB" column is from Guhathakurta *et al.* (1988). The information in the "P60" column is based on outer isophote fitting of $V$-band CCD images taken with the Palomar 60-inch telescope.

## 2.2. General Morphological Descriptions

All of the galaxies studied here are bright and large. Several are distinguished by the strength of their spiral structure, and two galaxies have particularly strong spiral arms with large amounts of star formation throughout their disks. NGC 4254

TABLE 2–2. ORIENTATION PARAMETERS

| NGC | HEA | BST | FT | T | GGKB | P60 | Adopted |
|---|---|---|---|---|---|---|---|
| **POSITION ANGLE** | | | | | | | |
| 4254 | 45[a*] | | | | 62 | 63.7 | 63 |
| 4303 | −45[ac] | | | | −42 | 0.1[d*] | −44 |
| 4321 | −150[f*] | | | | 153 | 121.0[d*] | 153 |
| 4501 | 140 | | | | 142 | 140.6 | 141 |
| 4535 | 180 | | | | 177 | −170.9 | −178 |
| 4536 | −51[g] | | | | | −57.0[d] | −54 |
| 4569 | 23 | | | | 24 | 21.6 | 23 |
| 4654 | 118 | | | | 121 | | 120 |
| **INCLINATION** | | | | | | | |
| 4254 | 31 | 28 | 31 | | 33 | 30[b*] | 37.2 | 32 |
| 4303 | 28 | 39 | 28 | | 17 | 27[b*] | 20.3[e*] | 28 |
| 4321 | 31 | 31 | 31 | | 37 | 27[b*] | 28.4[d*] | 33 |
| 4501 | 61 | 62 | 61 | 59 | 65 | 56 | 72.5[d*] | 61 |
| 4535 | 46 | 31 | 46 | 29 | 50 | 40 | 52.2 | 42 |
| 4536 | | 68 | 67 | | 69 | | 81.1[e*] | 68 |
| 4569 | 66 | 65 | 66 | | 64 | 56 | 76.4* | 63 |
| 4654 | 55 | 63 | 55 | 50 | 59 | 49 | | 55 |

[a] Determined kinematically from at least two off-axis HI measurements.
[b] Optical value is quoted, though paper deals with radio measurements.
[c] The PA was not correctly deduced. A 180 degree error was made.
[d] May not be reliable, as stable value was not reached in outer isophotes.
[e] Though value is stable, may not be reliable due to ([d]).
[f] Marked in Nilson (1973) with warning about small inclination.
[g] Taken directly from Nilson (1973).
* Excluded from average when computing adopted value.

and NGC 4321 have spiral arms that are well delineated by H II regions and that dominate their optical disks. As Table 2–1 shows, these two galaxies have gas disks which are among the most massive of the sample listed; molecular hydrogen dominates the gas mass in both spirals. The relatively large blue luminosity of NGC 4321 is a further indication of the amount of star formation in this galaxy. The large far

infrared luminosity of NGC 4254 indicates that there are copious amounts of dust in this galaxy that convert the stellar radiation to infrared. The larger amount of dust in NGC 4254 is evident in the appearance of its spiral arms, which are rather thick and cloudy, as is typical for an Sc galaxy. The contrast between NGC 4254 and NGC 4321 shows that spiral structure can be well defined, and star formation prodigious, even if the spiral structure is not well organized. NGC 4321 has two well-defined, symmetrical spiral arms. They are narrower than those of NGC 4254, as befits its earlier morphological type. There are three large spiral arms in NGC 4254, and one is particularly long and dominates its side of the disk.

Two other galaxies, NGC 4535 and NGC 4536, are similar in their global properties and in the appearance of their spiral structure as well. Although their spiral arms are prominent and well defined, they are rather narrow and are not marked by as much high mass star formation as the arms in NGC 4254 and NGC 4321 described above. Both NGC 4535 and NGC 4536 have rather large, bright nuclei from which two spiral arms emerge. The arcs traced out by the arms are particularly smooth and symmetrical. There is little high mass star formation in their interarm regions, and high mass star formation is curiously more evident in the outer parts of their disks, particularly in NGC 4535. The similarity between these two galaxies extends to their global properties, as well. Interestingly, there is more atomic hydrogen than molecular hydrogen, by mass, in their disks. This fact may be important in explaining the open appearance of the spiral arms in these galaxies. Although it is the more massive galaxy of the two, NGC 4536 has somewhat less gas than NGC 4535, which is consistent with its earlier morphological type. The blue luminosities of these galaxies are very similar and are comparatively small. This is consistent with the lack of many large H II regions along their arms.

The appearance of NGC 4303 differs from the spirals described so far. The spiral

structure in NGC 4303 is fragmentary but bright, with many H II regions marking the arm segments in the outer half of the disk. The inner disk is dominated by a smooth, oval distortion from the ends of which spiral arms emerge. There is little high mass star formation within the radius of the oval except in the very center of the galaxy, where there is a bright nucleus. The spiral arms are composed of short, straight segments which contain many large H II regions. Arm spurs are common. The large amount of star formation in this galaxy, at least in the outer half of its disk, is supported by the relatively large gas mass of the disk. The far infrared and blue luminosities of this galaxy are both relatively high. In fact, relative to its mass, the far infrared luminosity of NGC 4303 is as high as that of NGC 4254.

NGC 4654 is relatively small compared to the other galaxies. The bar is bright and blue, but is small and does not appear to dominate the appearance of the disk as does the oval in NGC 4303. NGC 4654 is a very late-type galaxy, and its spiral structure is not particularly well defined. Interestingly, the disk of NGC 4654 contains more atomic hydrogen by mass than molecular hydrogen. However, the gas mass fraction of its disk is comparable to that of the other galaxies listed. NGC 4654 is very luminous in the far infrared for its size, a fact which is consistent with its late morphological type and the accompanying large amount of dust in its disk. The large luminosities of NGC 4303 and NGC 4654 in the far infrared may be connected with the presence of the central bar or oval.

Two spirals show very weak spiral structure: NGC 4501 and NGC 4569. These galaxies are the earliest morphological types of the spirals studied here. NGC 4501 has a smooth disk with many very short, feathery spiral arms and not much arm-interarm contrast. The disk of NGC 4569 is exceptionally smooth and the spiral arms are fat. High mass star formation is confined to the inner half-disk of both galaxies. NGC 4569 is notably deficient in atomic hydrogen. As is consistent with their early

types, the total gas masses for both galaxies are small relative to their large total masses. The far infrared luminosities of these galaxies are small relative to their large sizes, which is probably the result of a relative lack of dust. NGC 4569 has a blue luminosity which is curiously large, given its lack of high mass star formation. Its nucleus is exceptionally bright, blue, and stellar in appearance.

## References

Aaronson, M., Mould, J. M., and Huchra, J., 1980, *Ap. J.*, **237**, 655.

Allen, C. W. 1973, *Astrophysical Quantities* (London: Pergamon Press).

Binggeli, B., Sandage, A., and Tammann, G. A., 1985, *A. J.*, **90**, 1681.

Binggeli, B., Sandage, A., and Tarenghi, M., 1984, *A. J.*, **89**, 64.

de Vaucouleurs, G., and Pence, W. D., 1979, *Ap. J. Supp.*, **40**, 425.

de Vaucouleurs, G., de Vaucouleurs, A., and Corwin, H. G., Jr. 1976, *Second Reference Catalogue of Bright Galaxies* (Austin: University of Texas Press).

Fisher, J. R., and Tully, R. B., 1981, *Ap. J. Supp.*, **47**, 139.

Giovanelli, R., and Haynes, M. P. 1983, *Astron. Ap.*, **88**, 881.

Guhathakurta, P., van Gorkom, J. H., Kotanyi, C. G., and Balkowski, C. 1988, *A. J.*, **96**, 851.

Helou, G., Giovanardi, C., Salpeter, E. E., and Krumm, N., 1981, *Ap. J. Supp.*, **46**, 267.

Helou, G., Hoffman, G. L., and Salpeter, E. E., 1984, *Ap. J. Supp.*, **55**, 433.

Helou, G., Khan, I. R., Malek, L., and Boehmer, L. 1988, *Ap. J. Suppl.*, **68**, 151.

Johnson, H. L. 1965, *Comm. Lunar Planet. Lab.*, **3**, 73.

Johnson, H. L., Mitchell, R. I., Irarte, B., and Wisniewski, W. Z. 1966, *Comm. Lunar Planet. Lab.*, **4**, 99.

Kenney, J. D. 1987, Ph.D. thesis, University of Massachusetts.

Nilson, P., 1973, *Uppsala General Catalog of Galaxies* (Uppsala: Uppsala Offset Center AB).

Pierce, M. and Tully, R. B. 1988, *Ap. J.*, **330**, 579.

Thuan, T. X., and Gunn, J. E. 1976, *P.A.S.P.*, **88**, 543.

Tully, R. B., 1988, *Nearby Galaxies Catalog* (Cambridge: Cambridge University Press).

# Chapter 3
# Observation and Analysis Techniques

## 3.1. CO Observations

### 3.1.1. Overview

CO ($J = 1 \rightarrow 0$) observations using the Owens Valley mm-wave interferometer began in 1986 October and continued into 1989 February. A typical data set for one galaxy consisted of at least one transit in four different configurations of the interferometer antennas. Each 10.4 m antenna was equipped with a liquid helium-cooled SIS receiver (Woody, Miller, and Wengler 1985). Velocity coverage of 416 km s$^{-1}$ was provided by a 32-channel filterbank with 5 MHz resolution, or 13 km s$^{-1}$ at 115.3 GHz. At the assumed distance of the Virgo Cluster, 15.7 Mpc (Pierce and Tully 1988; Burstein and Raychaudhury 1989), the 65″ primary beam covers the inner 5 kpc diameter of the survey spirals. Interferometer baselines extended to as much as 100 m east-west and 60 m north-south, yielding spatial resolutions ranging from 4.″0 × 6.″6 to 6.″4 × 8.″2 or about 400 pc × 560 pc. Amplitude calibration of the data involved a self-consistent combination of fluxes from planets (Mars and Uranus) and quasars (3C84, 3C273, and 3C345). The quasar 3C273 was employed for phase calibration. The *uv* data was processed in AIPS using the cleaning routine MX. Individual channel maps containing emission were summed to create a map of integrated emission for each galaxy. The gas velocity field was constructed from spectra by computing the flux-weighted average velocity at each pixel position.

### 3.1.2. Data Collection and Calibration

The dates of the CO observations and the configurations are shown in Table 3–1.

Some of the configurations had only two working antennas, or are short tracks; apparent duplications of effort are actually multiple attempts to gain full data. Table 3–2 lists the FWHM sizes and position angles of the synthesized beams resulting from the *uv* coverages.

TABLE 3–1. VIRGO SPIRAL GALAXY CO OBSERVATIONS

| Object | Date | Configuration | Object | Date | Configuration |
|---|---|---|---|---|---|
| NGC 4254 | 17oct86 | 30w 50w 65w | NGC 4535 | 08dec87 | 00 40n 60n |
| | 23oct86 | 30w 50w 65w | | 29dec87 | 65w 50w 20w |
| | 01nov86 | 50e 00 30w | | 23jan88 | 30w 10n 30e |
| | 11nov86 | 50e 40n 50w | | 01feb88 | 30w 30n 30e |
| | 16nov86 | 50e 40n 50w | | 05feb88 | 30w 30n 30e |
| | 19nov86 | 00 60n 40n | | | |
| | 02jun87 | 00 40n 60n | | | |
| | 03jun87 | 00 40n 60n | | | |
| NGC 4303 | 02mar87 | 30e 50n 30w | NGC 4536 | 09mar87 | 30e 50n 30w |
| | 08mar87 | 30e 50n 30w | | 17mar87 | 30e 50n 30w |
| | 23mar87 | 30e 30n 30w | | 24mar87 | 30e 30n 30w |
| | 03may87 | 20w 50w 65w | | 25mar87 | 30w 10n 30e |
| | 06apr88 | 10w 30w 65w | | 02may87 | 20w 50w 65w |
| | 29may87 | 10w 30w 65w | | 20may87 | 10w 30w 65w |
| NGC 4321 | 18oct86 | 30w 50w 65w | NGC 4569 | 19oct86 | 30w 50w 65w |
| | 24oct86 | 30w 50w 65w | | 25oct86 | 30w 50w 65w |
| | 02nov86 | 50e 00 30w | | 04nov86 | 50e 00 30w |
| | 03nov86 | 50e 00 30w | | 13nov86 | 50e 40n 50w |
| | 05nov86 | 50e 00 30w | | 21nov86 | 00 60n 40n |
| | 12nov86 | 50e 40n 50w | | | |
| | 20nov86 | 00 60n 40n | | | |
| NGC 4501 | 20oct86 | 30w 50w 65w | NGC 4654 | 01nov88 | 10w 65w 30w |
| | 26oct86 | 30w 50w 65w | | 24nov88 | 30e 30w 10n |
| | 06nov86 | 50e 00 30w | | 22jan89 | 60n 00 40n |
| | 07nov86 | 50e 00 30w | | 01feb89 | 30n 30w 30e |
| | 14nov86 | 50e 40n 50w | | 02feb89 | 30n 30w 30e |
| | 08apr88 | 00 40n 60n | | | |
| | 11apr88 | 00 40n 60n | | | |

The signal-to-noise ratios reported in Table 3–2 are ratios of the peak flux density

TABLE 3–2. IMAGE QUALITY

| Object NGC | Beam arcseconds | PA degrees | S/N |
|---|---|---|---|
| 4254 | 7.2×4.0 | −1.8 | 4.8 |
| 4303 | 7.0×6.2 | 71.3 | 6.3 |
| 4321 | 6.9×4.4 | −3.5 | 8.4 |
| 4501 | 6.6×4.0 | 1.6 | 5.1 |
| 4535 | 8.2×6.4 | −1.6 | 9.0 |
| 4536 | 7.9×6.4 | 3.8 | 7.1 |
| 4569 | 7.8×3.6 | −1.8 | 5.7 |
| 4654 | 7.6×6.2 | −0.5 | 16.6 |

among all the individual 5 MHz channel maps with the rms noise in a flux-free channel. Although the first objects observed are among the brightest galaxies in CO emission in the Virgo Cluster, the signal-to-noise ratios are nonetheless rather low. This is due to the sensitivity of the OVRO system at the time. The comparatively high S/N of NGC 4654, the most recently observed galaxy, is a tribute to the gains in sensitivity achieved with recent modifications to the system.

Bad data was detected and thrown out on the basis of several discriminators. Some data editing was done by examining records of individual antenna system temperatures made during the observations. Significant fluctuations in system temperature could be due to, but are not limited to, bad weather or poor tuning. Such data was removed, especially if a list of scan-averaged amplitudes and phases for bright quasars or planets showed uncharacteristic variation over the same period. Shadowing occurs when a projected baseline drops below the diameter of a dish, 10.4 m. The shadowed antenna often detects the LO of another antenna in one of its beam sidelobes. This results in a signal with corrupted phase and discrepant amplitude. When an antenna was shadowed, data from the two baselines involving that shadowed

antenna were discarded. Once the *uv* data were moved into AIPS, further editing was done as described below.

Phase changes due to the changing equivalent path length of the signal through the atmosphere have a timescale of about 30 minutes. Residual phase errors caused by a baseline position error also change on this timescale (because of the changing projection of the baseline). These errors may be removed, for the most part, by occasionally measuring the phase of plane waves from a nearby, bright point source. The quasar 3C273, one of the brightest objects in the millimeter sky, is positioned near the Virgo Cluster and is within 10° of all Virgo spirals studied here. Baseline errors are held to less than 0.1 wavelength, so phase calibrators within about 30° on the sky are acceptable. The brightness and proximity of 3C273 made it an ideal phase calibrator. Closure phase was enforced when calibrating phase. Phase errors in the calibrated data are $< 30°$.

Phases of all channels in the 64-channel filterbank were referred to the phase of the 300 MHz-wide continuum channel. The amplifiers and cables which make up the IF chain have frequency-dependent gains whose effect on the measured amplitude and phase is linear to first approximation. As a result of these frequency-dependent effects, it is common to see a phase ramp spanning a few tens of degrees across the 5 MHz filterbank. A linear trend in amplitude and phase across the filterbank was removed using observations of a bright quasar.

Amplitude calibration was accomplished using a self-consistent combination of planet and quasar fluxes. A simple model of the planets based on a mean brightness temperature and distance from the sun was used to estimate the planet fluxes. Mars (207 K) and Uranus (120 K) served as the basis of the amplitude calibration scale. A correction was made for the resolution of the circular planetary disk. In general, Mars was the more reliable calibrator because of its brightness; Uranus was often

too low in the sky, because of its southern declination, to be of much use. Flux measurements of as many of the bright quasars 3C84, 3C273, 3C345, 3C274, and 3C454.3 as possible were made during each track. In this manner, over a period of a few days, a self-consistent, reliable flux scale was established. The adopted or measured fluxes at 115 GHz of planets and quasars during the observing epochs relevant to Virgo spiral galaxy observations are reported in Table 3–3. Fluxes for the planets are representative values for the listed period of time. Errors in quasar fluxes are as much the result of calibration inaccuracy as they are due to real fluctuations in emission from the quasars during the indicated period of time. Uncertainty in the amplitude calibration is $\leq 15\%$.

TABLE 3–3. FLUX* CALIBRATION SCALE

| Epoch | Uranus | Mars | 3C84 | 3C273 | 3C345 |
|---|---|---|---|---|---|
| late 1986 | $\sim 11.2$ | ... | 31.8 | $18 \pm 2$ | $8 \pm 1$ |
| spring 1987 | $\sim 12.6$ | $\sim 25.1$ | $23 \pm 7$ | $18 \pm 3$ | $7 \pm 1$ |
| winter 1987 | ... | $\sim 26.5$ | ... | $15.7 \pm 0.1$ | $4.2 \pm 0.2$ |
| early 1988 | ... | $\sim 37.8$ | $20 \pm 3$ | $18 \pm 1$ | $4 \pm 1$ |
| spring 1988 | $\sim 12.2$ | $\sim 76.1$ | $17 \pm 1$ | $32 \pm 3$ | $3.7 \pm 0.1$ |
| winter 1988 | $\sim 11.1$ | $\sim 495$ | $13.7 \pm 0.8$ | 19.6 | $2.5 \pm 0.9$ |
| early 1989 | $\sim 10.8$ | $\sim 140$ | $15.0 \pm 0.9$ | 18.3 | $2.9 \pm 0.6$ |

*All fluxes are in Jy.

Images were made from the *uv* data using AIPS. The data was weighted uniformly; that is, all *uv* points carried equal weight. Since almost all of the data for each spiral galaxy was taken within a few months, no weighting by system temperature was used.

Further data editing was accomplished with AIPS task UVPLT. A graph of ampli-

tude versus *uv* distance should show a rather flat or falling distribution of amplitudes with increasing *uv* distance. A discrepant baseline shows up as a column of high points poking far above the general distribution. A malfunctioning filterbank channel will show a flurry of high points at many distances. The AIPS task CLIP can be used to remove all data within a range of *uv* distance, and can also be used to remove all data above a certain amplitude. Very gentle clipping was done on Virgo spiral data by removing only the very highest, obviously discrepant points. In some cases, channel 9 was found to contain corrupted data due to a malfunctioning circuit board, and the clipping then affected that channel almost exclusively.

### 3.1.3. Making CO Maps

The task UVSRT was used to sort the *uv* data in preparation for making maps with MX. The task MX is a CLEAN-type deconvolution algorithm, and it was used exclusively to make images. MX has quite a few parameters which may be varied to control the cleaning. The maps are 256 × 256, and each pixel is 1″.5. These choices make smoother maps because of the large number of pixels within a beam area (see Table 3–2). The large map size also eliminates problems of aliasing. The primary beamsize, 65″ or 43 pixels, is well within the cleaned area of 100 × 100 pixels. Parameters were chosen which made the cleaning as slow and gentle as possible in order to maximize the recovery of faint, extended emission. A minor-cycle gain of 0.1 and a "speed-up factor" of −0.3 were used (see the AIPS description of MX). This is because the small *uv* coverages of the three-antenna array make beams with substantial sidelobe levels, about 20% for the data used here. Fast, brutal cleaning with beams having large sidelobes will fail to recover fainter, extended emission. The inner 51 pixels of the synthesized beam were used in the deconvolution, a choice which also aids in recovery of faint structures. Uniform weighting was employed with no taper and no zero-spacing flux was supplied. The *uv* data were Fourier

transformed directly (meaning that no gridding and interpolation was done) because of the relatively small number of *uv* data points (typically 3000–4000). This method is more accurate than gridding, which is necessary for large data sets because of computer time constraints.

Cleaning an image is an open-ended process. Once the clean algorithm has located all of the emission in a map, it should be stopped. Further cleaning will only serve to "push the noise around" the image, causing an artificially smooth and uniform appearance within the cleaned area. A deterministic method has been devised and used in the cleaning of all the Virgo spiral galaxy data. Its use leads to a reasonable noise level in the maps. This method is described below.

A "dirty" map is made of each channel. This is just the direct Fourier transform of the *uv* data with no subsequent cleaning. Channels which obviously contain no emission are noted. The rms noise within the primary beam area in those flux-free channels is then measured; the depth of subsequent clean iterations will be measured in units of this noise level. A very wide clean box is specified, typically 1.5 times the size of the primary beam (65 pixels across). MX will search for clean components only within this box. The use of a clean box is useful to the clean algorithm because it provides information about where the emission is located. The more information about source structure that is supplied to a deconvolution algorithm, the better-constrained (or, for practical purposes, "unique") the final map will be.

The amount of cleaning is controlled by the AIPS adverb FLUX; cleaning stops when all residuals are less than FLUX. A deeply cleaned image (FLUX= $1\sigma$, where $\sigma$ is the rms noise in a flux-free channel) appears smooth, while an insufficiently cleaned image is blotchy and sharp-edged. The eye is often a good judge of what is a reasonably cleaned image. However, a quantitative means by which to gauge a reasonable amount of cleaning is necessary for uniformity among the maps presented

here together. Measurements of noise, signal amplitude, and cleaned flux for data from NGC 4654 are shown in Table 3–4. $1\sigma$ in Table 3–4 equals 0.04 Jy beam$^{-1}$. It is interesting that the peak emission *decreases* with deeper cleaning, although the total emission, as expected, increases with deeper cleaning (more emission is found). The decrease in peak emission with deeper cleaning is due to the smoothing which occurs: MX is given more clean components with which to approximate the exact height of the peak. Sharp features are treated as noise and their emission is spread over the image by convolution with the synthesized beam. The increasing smoothness of the image with deeper cleaning is evident in the decreasing rms noise level and the increasing signal-to-noise ratio, S/N, defined as peak flux density divided by rms noise.

TABLE 3–4. TEST-CLEANING NGC 4654

| Emission in Channel 14 | | | | |
|---|---|---|---|---|
| FLUX | $1\sigma$ | $1.5\sigma$ | $2\sigma$ | $3\sigma$ |
| Peak (Jy beam$^{-1}$) | 0.508 | 0.509 | 0.512 | 0.518 |
| Total (Jy) | 0.827 | 0.800 | 0.756 | 0.766 |
| S/N | 18.3 | 16.3 | 14.9 | 13.6 |
| # of components | 276 | 152 | 91 | 34 |

| Noise in Channel 2 | | | | |
|---|---|---|---|---|
| FLUX | $1\sigma$ | $1.5\sigma$ | $2\sigma$ | $3\sigma$ |
| Mean ($10^{-4}$ Jy beam$^{-1}$) | 3.1 | 3.9 | 2.2 | $-1.9$ |
| rms Noise (Jy beam$^{-1}$) | 0.0277 | 0.0312 | 0.0342 | 0.0380 |

Cleaning should be stopped after the total cleaned flux has leveled off. The graph of total cleaned flux versus clean component number for NGC 4654 channel 14 is shown in Figure 3–1. Note the quick rise when most of the strongest emission is first found, the gradual rise when low-level emission is located, and the leveling-off as noise is shuffled around. Graphs for other channels and other galaxies are similar,

although most level off by 100 iterations since the S/N is generally lower for the other galaxies. In this case, the cleaning was terminated at iteration #168, when the total cleaned flux had peaked, but any iteration number between about 80 and 170 would have been a reasonable place to stop.

Given an iteration number to stop at, interpolation from values such as in Table 3–4 indicates the appropriate clean depth (value for FLUX). An estimate of the S/N for the indicated FLUX is made, and PHAT = $N^2/2S^2$ is calculated (as recommended in AIPS). All channels are now cleaned with the chosen FLUX and PHAT. The use of PHAT helps to eliminate the striping of noise in images, an artifact which is common in CLEAN-type algorithms. A clean box should be chosen which is the smallest box encompassing all of the emission in all of the channels. The procedure of cleaning, measuring S/N, choosing the clean depth, and updating the clean box may be iterated until there is no further increase in map fidelity. (Note that the procedure always begins with the dirty map, and does not operate on a previously cleaned map). MX should cycle through two or three major iterations on channels with flux. Excessive looping through major iterations indicates that the map is being cleaned too deeply. A single major iteration means that there has been no cleaning on the residuals, and that a deeper clean should be made.

Maps of the integrated emission and the velocity field were made using AIPS task MOMNT. Only those channels with emission should be included in order that the contrast between emission and blank sky is maximized. ICUT sets a lower limit on the accepted flux. The integrated emission, or so-called "moment-0" map, is computed using the formula

$$I(x,y) = \sum_{S_\nu \geq \text{ ICUT}} S_\nu(x,y)\,\Delta v, \qquad (3-1)$$

where $S_\nu(x,y)$ is the flux density at pixel position $(x,y)$ and $\Delta v$ is the width of one velocity channel. The velocity field or "moment-1" map is the emission-weighted

average velocity:

$$V(x,y) = \frac{1}{I(x,y)} \sum_{S_\nu \geq \mathrm{ICUT}} v S_\nu(x,y)\, \Delta v. \qquad (3-2)$$

When making an integrated emission ("moment-0") map for the purpose of presentation, the parameter ICUT was set to $\approx 1.5\sigma$–$2\sigma$, where $\sigma$ is the rms noise in a flux-free channel. This choice makes images with great contrast between the background noise and the emission region while still including most of the significant flux. Only positive contributions to the total emission are included. When making a velocity field ("moment-1") map, ICUT $\approx 2.5\sigma$–$3\sigma$. The higher cutoff produces more reliable velocity fields because there is less contamination of the average by high noise spikes.

### 3.1.4. Method of Determining Total Flux

The operation of MOMNT is a lot like harvesting corn by picking all plants (corn or weeds – that is, object and noise pixels) taller than a prescribed height. Since corn plants grow high, choosing a moderately high picking height will ensure that only corn plants (only pixels with emission) are picked. The pile of plants may then be weighed to estimate the total amount of corn (the total flux) picked from each sector of the garden. Note that near the edges of the garden, where the fertilizer does not fall so freely and where the sun is not so good, the corn will be stunted, so some corn will be missed if the picking height is too high. The weeds are tallest near the garden edges, so some weeds may be taller than corn there, too. Creeping of grass into the garden may blur the garden's edge.

The analogy illustrates the conundrum of the radio astronomer wishing to find the total integrated emission from an object. Too high a threshold will miss much of the emission, while too low a threshold will include too much noise. The solution, inspired by techniques of optical astronomy, is to perform synthetic aperture photometry and to compute a curve of growth to estimate the total integrated emission. A low flux

acceptance threshold (ICUT) should be used to compute the "moment-0" map so that all emission from the object is included. The radial surface brightness profile may be computed using the AIPS task IRING. The background value or "sky" in the radial profile map is set by the frequency of occurrence and height of noise spikes in the individual channel maps that rise above the threshold.

In support of the curve of growth method for determining the total integrated emission from an object, the information in Table 3–5 is offered. It contains CO data for eight spiral galaxies with the total integrated emission calculated in two ways from moment-0 maps with varying thresholds. Values produced by by the curve of growth method advocated here are on lines labeled "Photo." Orientation parameters needed to produce the radial profiles are from Table 2–2. The other method, labeled "Masked," involves summing the pixel values within the polygon describing the object boundary. The MOMNT thresholds are given in units of the rms noise $\sigma$ in a flux-free channel map, which serves as an estimate of the noise in any channel map. Note that the curve of growth method gives consistent values for the total integrated emission until the threshold becomes too high, at which point some emission is lost. The "Masked" method of summing pixels within the object boundary gives values that vary substantially with the MOMNT threshold.

### 3.1.5. CO Emission and $H_2$ Mass

To compute the mass of molecular hydrogen corresponding to observed integrated CO emission from another galaxy, two fundamental assumptions must be made. The first assumption is that the molecular gas component of the external galaxy is similar in its physical properties to that in our Galaxy. The second assumption is that the adopted relationship between the CO emission from molecular clouds in our Galaxy and the masses of those clouds is a valid one. By linking the two assumptions, molecular gas masses in other galaxies may be estimated from observations of CO

TABLE 3–5.

COMPARISON OF APERTURE PHOTOMETRY WITH MASKED SUMMATION

| Object | | $\sigma$ in map[a] | Threshold[b] $1\sigma$ | $1.5\sigma$ | $2\sigma$ | $2.5\sigma$ | $3\sigma$ | $I^c_{CO}$ Adopted |
|---|---|---|---|---|---|---|---|---|
| | Sky[d] | | 16.35 | 10.26 | 10.24 | | 10.20 | |
| NGC 4254 | Photo[c] | 0.13 | 35.6 | 33.7 | 33.7 | | 34.2 | 35.6 |
| | Masked[c] | | 296.5 | 192.3 | 106.7 | | 27.7 | |
| | Sky | | 10.91 | 5.42 | 2.57 | 1.04 | 0.30 | |
| NGC 4303 | Photo[c] | 0.12 | 152.9 | 147.2 | 119.9 | 86.5 | 64.8 | 152.9 |
| | Masked | | 251.8 | 169.3 | 104.1 | 86.5 | 62.5 | |
| | Sky | | 14.87 | 7.76 | 2.80 | 0.95 | | |
| NGC 4321 | Photo | 0.15 | 226.4 | 204.5 | 198.4 | 139.1 | | 226.4 |
| | Masked | | 460.2 | 281.6 | 223.8 | 133.7 | | |
| | Sky | | 10.24 | 5.04 | 2.04 | | 0.18 | |
| NGC 4501 | Photo | 0.12 | 40.5 | 32.2 | 23.1 | | 6.3 | 40.5 |
| | Masked | | 79.3 | 49.0 | 25.0 | | 6.3 | |
| | Sky | | 7.50 | 3.92 | 1.51 | | 0.28 | |
| NGC 4535 | Photo | 0.083 | 90.3 | 88.9 | 82.9 | | 57.1 | 90.3 |
| | Masked | | 118.4 | 101.8 | 82.8 | | 55.7 | |
| | Sky | | 19.90 | 12.63 | 5.61 | | 0.71 | |
| NGC 4536 | Photo | 0.15 | 229.3 | 221.2 | 219.9 | | 149.7 | 229.3 |
| | Masked | | 445.6 | 338.6 | 231.1 | | 144.5 | |
| | Sky | | 11.90 | 6.21 | 2.47 | | 0.34 | |
| NGC 4569 | Photo | 0.14 | 162.4 | 127.4 | 91.8 | | 28.8 | 162.4 |
| | Masked | | 351.7 | 150.9 | 87.9 | | 22.7 | |
| | Sky | | 3.78 | 2.43 | 1.48 | | 0.43 | |
| NGC 4654 | Photo | 0.03 | 86.5 | 87.8 | 87.0 | | 83.5 | 87.1 |
| | Masked | | 141.9 | 109.1 | 87.0 | | 86.4 | |

[a] Noise in one 5 MHz channel map. Units are Jy beam$^{-1}$.

[b] Smallest flux density included in the "moment-0" sum, in units of the noise $\sigma$ (column 3) in an individual 5 MHz channel map.

[c] Total integrated CO emission, in units of Jy km sec$^{-1}$.

[d] Mean value of noise in the "moment-0" map, in units of Jy km sec$^{-1}$ beam$^{-1}$.

emission alone, based on known properties of the molecular gas in our Galaxy. The first assumption is the more questionable of the two, but is not without observational

support, as described below. The second assumption is based on a considerable amount of observation, but is nonetheless somewhat controversial.

CO emission and molecular gas mass are related by the empirical relation

$$N_{H_2} = \xi \, I_{CO}, \qquad (3-3)$$

where $N_{H_2}$ is the column density of molecular hydrogen, $I_{CO} = \int T_A \, dv$ is the antenna temperature of the $J = 1 \rightarrow 0$ rotational line integrated over the line profile, and $\xi$ is a constant of proportionality. Despite its superficial resemblance to one, this is not a curve of growth relationship, since CO emission from molecular clouds is almost always optically thick. Instead, it is based on an observed, but not entirely explained, relationship between cloud size and CO line width (see Solomon and Sanders 1985, for example). Several independent methods have been used to estimate the value of the proportionality constant, $\xi$. Frerking, Langer, and Wilson (1982) used the correlation between CO emission and visual extinction $A_V$ in nearby clouds. Comparing masses computed from the virial theorem with masses computed from LTE analysis of $^{13}CO$ and CO observations was the technique used by Sanders, Solomon, and Scoville (1984). The distribution of gamma rays may be related to the column density of nucleons, to which the contribution of molecular hydrogen may be estimated (Bloemen *et al.* 1986). All three methods generally lead to values in the range of $\xi = 2\text{–}4 \times 10^{20} \, \mathrm{cm^{-2}} \, (\mathrm{K \, km \, sec^{-1}})^{-1}$ for molecular clouds in the Galactic disk. Most of the controversy swirls around explaining the discrepancy of a factor of two. In this thesis, a diplomatic value of

$$\xi = 3 \times 10^{20} \, \mathrm{cm^{-2}} \, (\mathrm{K \, km \, sec^{-1}})^{-1} \qquad (3-4)$$

is adopted. The agreement of virial mass estimates with independently determined masses seems to indicate that the value in relation (3–4) may be used with some confidence (Scoville and Good 1989).

Measurements of the CO emission from another galaxy may be interpreted as arising from the spatially averaged sum of emission from independent clouds (Dickman, Snell, and Schloerb 1986). Knowledge about molecular clouds in our Galaxy may then be used to deduce a molecular gas mass from the observed emission. The reliability of this approach hinges on the similarity of the extragalactic molecular cloud ensemble to that of our Galaxy. Models of molecular cloud ensembles (Maloney and Black 1988; Kutner and Leung 1985) indicate a scaling relation

$$N_{\mathrm{H}_2}/I_{\mathrm{CO}} \propto T_k^{-\beta}\,\overline{n}^{1/2}, \qquad (3-5)$$

where $T_k$ is the average kinetic temperature of the clouds and $\overline{n}$ is their mean density. The exponent $\beta$ is in the range of $1 \leq \beta \lesssim 1.3$ and depends on $T_k$, with $\beta \rightarrow 1$ as $T_k \rightarrow 30\,\mathrm{K}$. Therefore, galaxies with systematically warmer or more tenuous molecular clouds will have masses which are overestimated if relation (3–4) is used. As demonstrated by the models of Maloney and Black (1988), the dependence of molecular cloud CO emission on metallicity is probably real. The main cause of declining $I_{\mathrm{CO}}$ with declining metallicity is a decrease in the size of the CO $J = 1 \rightarrow 0$ emitting region within an otherwise normal cloud of molecular hydrogen. The metallicities in the centers of the Virgo spiral galaxies studied here are probably not sufficiently different from the mean metallicity in the Galactic disk to affect $I_{\mathrm{CO}}$ seriously.

There is also observational evidence that the nuclear environments of disk galaxies are similar enough to that of our Galaxy so that equations (3–3) and (3–4) can be used with some confidence. Using multilevel, multiple isotope observations of the spiral IC342, Genzel *et al.* (1990) deduced a conversion factor $\xi = 3\text{–}4 \times 10^{20}\,\mathrm{cm}^{-2}\,(\mathrm{K\,km\,sec}^{-1})^{-1}$ for the central region. The noted variations of metallicity and the generally changing interstellar environment between 2 kpc and 10 kpc in our Galaxy produce no noticeable effect on molecular cloud emissivities (Bloemen *et al.*

1986). Observations of M33 (Wilson and Scoville 1990), which resolve individual molecular clouds, allow computation of virial masses for those clouds; the derived conversion factor $\xi$ is similar to that for our Galaxy.

On the balance of the arguments and evidence outlined above, the application of the Galactic $I_{CO}$-molecular gas mass relation (equations 3–3 and 3–4) to other disk galaxies has significant justification. There is even observational verification in isolated cases. These successes are mitigated by the moderating influence of temperature and density predicted by models (see equation 3–5). Such a caveat is particularly applicable to the CO observations presented in this thesis, which are exclusively of the central regions of spirals. It is to be expected that star formation in such a dense environment as a galactic center could measurably alter molecular cloud properties and thereby alter the proportionality constant of relation (3–4). The approach to be taken in this thesis is to use equations (3–3) and (3–4) until an unphysical situation is indicated, then to resolve the problem using independent information and analysis.

## 3.2. Optical Observations

### 3.2.1. Overview

Optical observations at the Palomar 60-inch telescope were completed in four nights in 1988 March. An 800×800 pixel$^2$, sensitized TI CCD cooled by liquid nitrogen was used with re-imaging optics and the pixels were rebinned 4:1. The image scale was $1''.3$/pixel, yielding a frame $8'.7$ on a side. These images had enough blank sky areas at the edges for photometry. Landolt standards (Landolt 1983) were observed to calibrate the $B$, $V$, $r$, and $i$ photometry. Three narrow (80Å) filters near H$\alpha$ were used to obtain images in emission and nearby continuum. CCD photometry of G-dwarf stars similar to the sun were used to calibrate the H$\alpha$ photometry. Spectrophotometer scans of the filter responses were used to scale and subtract the continuum from the H$\alpha$ emission images. All images were bias-subtracted and then flattened using

illuminated dome exposures. Frame defects such as cosmic ray hits were cleaned by hand. Absolute sky coordinates were found by measuring positions of astrometric standard stars and stars within the field of view on plates from the Palomar 48-inch Schmidt telescope. All frames were registered with CO images through shifting and interpolation to fractional pixels.

### 3.2.2. Broadband Optical Calibration

Initial processing of the optical frames was routine. The frames were flattened using the FIGARO DFLAT macro at the 60-inch dome. Average dome flat frames were used for flattening. Dome flats from the beginning of the night were used to flatten the first half of the night's frames, and dome flats from the end of the night were used for the second half of the night. A scaled, hour-long dark frame was subtracted from the data frames. Cleaning the frames of cosmic ray hits, bad columns, and hot and dead pixels was done frame-by-frame using interpolation across pixels. Sky was measured in three boxes in each frame and the mean value was subtracted from the frame. Registration was accomplished using the centroids of about ten star images in each frame. All images were registered relative to the H$\alpha$ flux-containing frame.

The photometric standard stars were selected from a list made by Landolt (1983) using Johnson *UBVRI* photometry. Many of the same standards were observed each night through Johnson $B$ and $V$ (Johnson *et al.* 1966) and Thuan-Gunn $r$ and $i$ filters (Thuan and Gunn 1976). At least six stars were observed each night: three at the beginning of the night and three at its end. Groups of three stars were chosen so that one was red, one yellow, and one blue. In this manner, a broad color range was explored so that calibration would be more accurate. Three exposures were made of each star on a single frame by moving the telescope between exposures.

Frames of photometric standard stars were flattened and cleaned as described above. Because of the brightness of some of the photometric standards, many of the

frames were defocussed so the CCD would not saturate. It happened that some of the standard stars had faint companions which probably escaped notice in Landolt's survey. These faint companions were included in the photometric measurements without choice and, depending on whether they were also included in Landolt's aperture, may have contributed to scatter in the photometry. Table 3–6 is a list of all the photometric standards used, their spectral classifications (Landolt 1973), and brief notes on their relative utility as photometric standards.

TABLE 3–6. PHOTOMETRIC STANDARDS

| Name[a] | Other Names | Sp[b] | Notes |
|---|---|---|---|
| SA98-193 | | G8 | Poor |
| SA99-6 | | G7: | Very good |
| SA99-438 | HD 64854, BD + 0°2129 | B7 | Good; faint companion |
| HD 72055 | BD – 6°2620 | B8 | Good; faint companion |
| SA100-241 | BD – 0°2081 | A0 | Triple, one faint |
| SA100-280 | | F5 | Okay; fairly crowded field |
| SA101-333 | HD 86135, BD + 0°2588 | K3 III : | Okay; double |
| SA101-282 | BD + 0°2589 | F2 | Good |
| BD + 1°2447 | | M2.5 V | Good, very faint companion |
| G162-66 | | | Very good |
| SA107-970 | | K3 | Very good |
| SA107-1006 | | G3 | Good; faint companion; sl. crowded |
| SA108-551 | BD – 0°3152 | A0 | Very good |

[a] SA = "Selected Area," from Landolt (1983).
HD = "Henry-Draper Catalogue."
BD = "Bonner Durchmasterung."
G = "Giclas *et al.*" in *Lowell Obs. Bulletin* proper motion list.

[b] From Landolt (1973; 1983).

Landolt (1983) gives substantial evidence that his $UBV$ photometry is on the original Johnson *et al.* (1966) system. However, the Landolt $RI$ photometry is based on the Cousins (1976) system. Observations in this work relative to images through $B$ and $V$ filters are calibrated with the Johnson system; images through $r$ and $i$ filters are on the Thuan-Gunn system. Admittedly, this choice results in the loss of some degree of homogeneity. However, the observations being what they are, this choice remains faithful to the actual measurements made. Besides, the substantial historical extragalactic $B-V$ work can be compared with the results of this work, as can the more recent extragalactic $r$ and $i$ work. The choice to use the Thuan-Gunn $ri$ system unfortunately necessitated deriving color transformation equations from the Johnson to the Thuan-Gunn system (see Appendix A). Transformation equations from the Cousins to the Johnson system already exist in the literature (Taylor 1986).

Final flux calibration to physical units was accomplished using the absolute flux calibration worked out by Johnson (1965) for the Johnson $UBV$ system. Johnson's calibration is based on measurements of the Sun and other G-dwarf stars. Using Johnson's calibration for $R$ and $I$ and the color transformation equations worked out in Appendix A, an absolute flux calibration for $r$ and $i$ bands was calculated. Table 3–7 lists the absolute flux density at 0.00 mag in relevant filter bands, and the effective widths of the filters.

For example, consider in detail the procedure for computing the absolute flux calibration in $r$ band. The energy distribution of the Sun, expressed in magnitudes, is

| | $V$ | $B-V$ | $V-R$ | $V-I$ |
|---|---|---|---|---|
| Sun | −26.74 | +0.64 | +0.52 | +0.78 |

(Johnson 1965). So $R_\odot = -27.26$ and $I_\odot = -27.52$. Using the Johnson to Thuan-

TABLE 3–7.
ABSOLUTE FLUX CALIBRATION

| Band | $\lambda_{\rm eff}^a$ $\mu$m | $\Delta\lambda_{\rm eff}^b$ $\mu$m | $F_\lambda$ at 0.00 mag W cm$^{-2}$ $\mu$m$^{-1}$ |
|---|---|---|---|
| $B$ | 0.442 | 0.098 | $7.20\times10^{-12}$ |
| $V$ | 0.540 | 0.089 | $3.92\times10^{-12}$ |
| $R$ | 0.680 | 0.220 | $1.76\times10^{-12}$ |
| $I$ | 0.825 | 0.240 | $8.3\ \times10^{-13}$ |
| $r$ | 0.650 | 0.090 | $2.34\times10^{-12}$ |
| $i$ | 0.820 | 0.130 | $1.7\ \times10^{-12}$ |

[a] Sandage and Smith (1963) and Wade, Hoessel, and Elias (1979).

[b] Allen (1973), Thuan and Gunn (1976), and Wade, Hoessel, and Elias (1979).

Gunn color transformation equations, find $r_\odot = -26.95$ and $i_\odot = -26.76$, or

$$(r-R)_\odot = +0.31, \qquad (i-I)_\odot = +0.76. \tag{3-6}$$

Then the absolute flux calibration for $r$ band is

$$\left(10^{0.4(0.31)}\right)\left(1.76\times10^{-12}\,\mathrm{W\,cm^{-2}\,\mu m^{-1}}\right) = 2.34\times10^{-12}\,\mathrm{W\,cm^{-2}\,\mu m^{-1}} \tag{3-7}$$

at 0.00 $r$ magnitude. The procedure for $i$ band follows similarly.

Conversion from surface brightness in magnitudes per square arcsecond to ergs per square centimeter per second per square arcsecond is accomplished by using the equation

$$\frac{F_\lambda(0.00\,\mathrm{mag})}{s^2}\cdot 10^{-0.4(\mu-2.5\log s^2)}, \tag{3-8}$$

where $s$ is the angular size of a pixel (say, arcsec$^2$) and $\mu$ is the surface brightness in magnitudes per unit area (arcsec$^2$) on the sky.

### 3.2.3. Hα Images

Hα imaging of Virgo spirals was done using narrowband interference filters with re-imaging optics and a CCD detector at the Palomar 60-inch telescope. Three filters

were used in the imaging; their transmission profiles are shown in Figure 3–2. Hα emission from a given galaxy was typically maximal in the center filter, and imagery using the other filters provided an estimate of the continuum at nearby larger and smaller wavelengths. Appendix B provides a detailed account of the calibration procedure for the Hα emission images. Initial processing of the frames, such as flattening, was done at the 60-inch dome as described in §3.2.2.

It was necessary to register the data frames in order to add and subtract scaled images made with the three different filters. Roughly ten bright stars were selected on each frame and were used to register the frames. The measured offsets for the astrometric stars were fairly stable in right ascension but much more unstable in declination. There was evidence of a systematic wandering of the positional offsets over the frame, which could be due to primary-mode flexing of the CCD chip or else rotation of the chip. The timescale for such flexures is at least as fast as the exposure times of the frames, on the order of five to twenty minutes.

Correction for atmospheric extinction was made by multiplication of each data frame by $10^{0.4K_{\mathrm{H}\alpha}\sec Z}$, where $K_{\mathrm{H}\alpha} = 0.08$ is the $K$-correction at Palomar for Hα and $\sec Z$ is very nearly the airmass for small zenith angles $Z$. Multiplication by this factor referred the fluxes to *outside* the atmosphere. Sky was estimated from the average of the mean sky in three boxes in each frame, then subtracted from each frame before further processing. Data frames in each filter band were divided by numerical scaling factors corresponding to equivalent widths of those filters. See Appendix B for details. The scaled frames were then added or subtracted, again according to the procedure detailed in Appendix B, to remove the continuum emission. Absolute flux calibration is detailed in Appendix B. In Table 3–8, the integrated Hα radiancies for the program Virgo spiral galaxies are listed.

The total Hα radiancies in Table 3–8 were measured from the Hα frames by

TABLE 3–8. TOTAL Hα RADIANCIES OF VIRGO SPIRALS

| Object | $f_{H\alpha}$ | $-\log f_{H\alpha}$ | $-\log f_{H\alpha}$ |
|---|---|---|---|
| NGC | $10^{-12}$ erg cm$^{-2}$ sec$^{-1}$ | | (Kennicutt and Kent) |
| 4254 | 26.21 | 10.58 | 10.91 |
| 4303 | 23.75 | 10.62 | 10.85 |
| 4321 | 14.05 | 10.85 | 11.05 |
| 4501 | 6.193 | 11.21 | 11.50 |
| 4535 | 8.612 | 11.06 | 11.43 |
| 4536 | 7.075 | 11.15 | 11.48 |
| 4569 | 2.416 | 11.62 | 11.62 |

constructing curves of growth from surface photometry. Values of these radiancies are uncorrected for internal extinction and [N II] contamination; they are shown with their logarithms for comparison with similar data from Kennicutt and Kent (1983). The radiancies in this study are generally greater than those found by Kennicutt and Kent (1983). The reason for the discrepancy (amounting to an extra 84% on average) is probably the increased sensitivity of the photometry to lower surface brightness emission. The narrow filter subtraction techniques in the Kennicutt and Kent (1983) survey were similar to the ones employed here.

Several corrections could be made to the recorded Hα fluxes to estimate the true Hα flux of the galaxy. There is Galactic extinction, extinction within the target galaxy, and contamination by [N II] emission. Each of these three factors will be discussed below. However, the size of each adjustment is the same as or less than the error in deducing star formation rates from Hα fluxes (Chapter 8), which is the reason that the measurements were made. Moreover, the corrections for internal extinction are nearly offset by the corrections for [N II] emission. For these reasons, corrections

to the measured H$\alpha$ fluxes are superfluous for understanding current star formation rates at the centers of Virgo spiral galaxies.

Galactic extinction at H$\alpha$ is approximated by the formula

$$A_{6563} = 0.08^{\rm mag}(\text{cosec } b_{\rm II} - 1) \qquad (3-9)$$

(Kennicutt and Kent 1983), if $|b_{\rm II}| < 50°$. Since the Virgo Cluster lies at high galactic latitude, extinction is negligible.

Extinction within the target galaxy amounts to $1.1 \pm 0.5$ magnitudes at H$\alpha$ (Kennicutt 1983), or a factor of roughly 2.75. This figure is based on radio continuum measurements, and the stated uncertainty in the extinction is probably due to variations in the dust content from galaxy to galaxy. Anyway, the measurements are dominated by radio continuum emission from the disks of spiral galaxies, in which the effects of dust are much more important than in the nuclei. CCD photometry discussed in Chapter 4 shows that dust is rather rare in the nuclear regions of the Virgo spiral galaxies studied here; in the galaxies in which dust is apparent near the nucleus, the H$\alpha$ emission is not apparently affected.

Finally, contamination by [N II] emission in the passband is unavoidable. Using the spectrophotometry for a sample of spirals of diverse morphological types (Kennicutt and Kent 1983), a mean ratio of H$\alpha$ to [N II] emission may be found. For type Sa through Scd, the relevant ratio is

$$\left\langle \frac{\text{H}\alpha}{\text{H}\alpha + [\text{N II}]} \right\rangle = 0.58 \pm 0.16 \qquad (3-10)$$

for 32 galaxies.

### 3.2.4. Lyman Continuum Production Rate

An estimation of the number of high-mass stars can be made from the H$\alpha$ flux by coupling H$\alpha$ emission to Lyman continuum emission. Most of the H$\alpha$ flux from a

star-forming galaxy comes from H II regions surrounding O and B stars. Within these H II regions, there is ionization equilibrium. Of all the Lyman continuum photons produced, only a fraction of them induce the observed H$\alpha$ transitions (with corresponding energy loss). The relative numbers of H$\alpha$ and Lyman continuum photons are

$$\frac{L_{\mathrm{H}\alpha}/h\nu_{\mathrm{H}\alpha}}{\int_{\nu_0}^{\infty}(L_\nu/h\nu)\,d\nu} \approx \frac{\alpha_{\mathrm{H}\alpha}^{\mathrm{eff}}}{\alpha_B}, \qquad (3-11)$$

where $L_\nu$ is the luminosity at frequency $\nu$ and $\nu_0$ is the frequency corresponding to the ionization energy of a hydrogen atom. The constant $\alpha_B = 2.60 \times 10^{-13}\,\mathrm{cm^3\,sec^{-1}}$ (Osterbrock 1974) is the total recombination coefficient to all levels except the ground state. The effective transition rate $\alpha_{\mathrm{H}\alpha}^{\mathrm{eff}} = 7.83 \times 10^{-14}\,\mathrm{cm^3\,sec^{-1}}$ is calculated from values in Osterbrock (1974). The relative number of H$\alpha$ and Lyman continuum photons is

$$\frac{N_{\mathrm{H}\alpha}}{N_{\mathrm{Ly\,c}}} \approx 0.301, \qquad (3-12)$$

which means that roughly one-third of the Lyman continuum photons lead to an H$\alpha$ photon.

Given the H$\alpha$ flux at earth, the total number of Lyman continuum photons implied is

$$N_{\mathrm{Ly\,c}} = \frac{f_{\mathrm{H}\alpha} \cdot 4\pi D^2}{h\nu'_{\mathrm{H}\alpha}} \frac{1}{0.301}, \qquad (3-13)$$

where $f_{\mathrm{H}\alpha}$ is the H$\alpha$ flux, $D$ is the distance to the source, and $\nu'_{\mathrm{H}\alpha}$ is the redshifted frequency of an H$\alpha$ photon from the source. For nearby sources, this is

$$N_{\mathrm{Ly\,c}} = (1.313 \times 10^{62})\; D_{\mathrm{Mpc}}^2\; f_{\mathrm{H}\alpha}(\mathrm{erg\,cm^{-2}\,sec^{-1}}), \qquad (3-14)$$

where $N_{\mathrm{Ly\,c}}$ is the total number of ionizing photons per second.

### 3.2.5. The Number of OB Stars

The total number of high mass stars may be estimated from the Lyman continuum flux by assuming a form for the initial mass function and using an expression for the

ionizing photon flux from stars of a given mass. Let the number distribution of stars in a mass range be

$$dN = \xi(m)\, dm, \tag{3-15}$$

so the Salpeter initial mass function is $\xi(m) = m^{-2.35}$ and the "extended" Miller-Scalo initial mass function is

$$\xi(m) = \begin{cases} m^{-1.4}, & 0.1\,\mathrm{M}_\odot \leq m \leq 1\,\mathrm{M}_\odot; \\ m^{-2.5}, & 1\,\mathrm{M}_\odot < m \leq 100\,\mathrm{M}_\odot. \end{cases} \tag{3-16}$$

Let $\chi(m_{\rm lo}, m_{\rm up})$ be the normalization of the initial mass distribution function,

$$\chi(m_{\rm lo}, m_{\rm up}) = \int_{m_{\rm lo}}^{m_{\rm up}} \xi(m)\, dm, \tag{3-17}$$

where $m_{\rm lo}$ and $m_{\rm up}$ are the lower and upper cutoffs of the IMF.

The total rate of Lyman continuum photon emission from all stars in the mass range $(m_{\rm lo}, m_{\rm up})$ is

$$\frac{N_*}{\chi(m_{\rm lo}, m_{\rm up})} \int_{m_{\rm lo}}^{m_{\rm up}} n_c(m)\xi(m)\, dm, \tag{3-18}$$

where $N_*$ is the total number of stars in the mass range $(m_{\rm lo}, m_{\rm up})$ and $n_c(m)$ is the number of Lyman continuum photons emitted by a star of mass $m$. Two convenient expressions for $\log_{10} n_c(m)$, based on data from Panagia (1973) and Maeder (1980), are

$$\log n_c(m) = A + B \log m + C \log\log m \tag{3-19}$$

$$A = 54.066$$

$$B = -8.9232$$

$$C = 45.694,$$

where $n_c(m)$ is in photons $\sec^{-1}$ and $m$ is in solar masses, and

$$\log n_c(m) = A + Bm + Cm^{1/2} + Dm^{1/3} \tag{3-20}$$

$$A = 5.6240$$

$$B = 0.30747$$

$$C = -20.278$$

$$D = 46.614.$$

Both expressions apply to the mass range $8\,M_\odot < m < 100\,M_\odot$. Values of the normalization constant $\chi(m_{lo}, m_{up})$ for the Salpeter IMF and the extended Miller-Scalo IMF are shown in Table E–1 and Table E–2 for several values of $m_{lo}$ and $m_{up}$. Numerical integration was used to determine the total Lyman continuum photon emission rates per star. Values of the integral on the right-hand side of equation (3–18) without the factors in front are listed in Table 3–9 for the two initial mass functions. Dividing the value in Table 3–9 by the appropriate normalization from Table E–1 or Table E–2 will yield the average Lyman continuum photon emission rate per star in the mass range defined by the normalization constant used. Equation (3–19) was used to construct Table 3–9; Lyman continuum emission from stars less massive than $8\,M_\odot$ was ignored. From equation (3–14), the total number of stars $N_*$ in the mass range $(m_{lo}, m_{up})$ is related to the H$\alpha$ flux by

$$N_* = (1.313 \times 10^{62})\, D^2_{Mpc}\, f_{H\alpha}(\mathrm{erg\,cm^{-2}\,sec^{-1}}) \left[\frac{1}{\chi}\int_{m_{lo}}^{m_{up}} n_c(m)\xi(m)\,dm\right]^{-1}. \qquad (3-21)$$

If $D_{Mpc} = 15.7$, $m_{lo} = 8\,M_\odot$, and $m_{up} = 60\,M_\odot$, then

$$N_* = (2.216 \times 10^{16})\, f_{H\alpha}(\mathrm{erg\,cm^{-2}\,sec^{-1}}) \qquad (3-22)$$

for the extended Miller-Scalo IMF, from which the number of OB stars may be estimated. Values of the normalized mass integral, $\frac{1}{\chi}\int_{m_{lo}}^{m_{up}} m\,\xi(m)\,dm$, that is, the average stellar mass, for the two initial mass functions are shown in Table E–3 and Table E–4. The total mass in stars is

$$M_* = \frac{N_*}{\chi}\int m\,\xi(m)\,dm = N_*\,\langle m\rangle. \qquad (3-23)$$

If $D_{\rm Mpc} = 15.7$, $m_{\rm lo} = 8\,{\rm M}_\odot$, and $m_{\rm up} = 60\,{\rm M}_\odot$, then for an extended Miller-Scalo IMF, the total mass of high mass ($> 8\,{\rm M}_\odot$) stars is

$$M_* = (3.549 \times 10^{17})\ f_{\rm H\alpha}({\rm erg\,cm^{-2}\,sec^{-1}})\ {\rm M}_\odot. \qquad (3-24)$$

TABLE 3–9.
Ly c EMISSION RATE PER STAR[a]

| $m_{\rm up}$ | Rate ($10^{45}$ photons sec$^{-1}$) | |
|---|---|---|
| | Salpeter | Miller-Scalo |
| 30 | 9.86 | 6.09 |
| 40 | 28.1 | 16.8 |
| 50 | 50.1 | 29.2 |
| 60 | 71.5 | 40.9 |
| 80 | 108 | 60.4 |
| 100 | 142 | 77.8 |

[a] Not normalized. Divide by $\chi$ from Table E–1 or Table E–2 for desired mass range.

### 3.2.6. The Current Star Formation Rate

The present star formation rate can be estimated from the H$\alpha$ flux. Let $n_c(m)$ be the number of Lyman continuum photons per unit time produced by a main sequence star of mass $m$, and let $t(m)$ be its lifetime on the main sequence. The total number of Lyman continuum photons produced by the star during its lifetime is $n_c(m)\,t(m)$. The lifetime total number of Lyman continuum photons produced per star in a population of stars obeying an initial mass function $\xi(m)$ is

$$\frac{1}{\chi(m_{\rm lo}, m_{\rm up})} \int_{m_{\rm lo}}^{m_{\rm up}} n_c(m)\,t(m)\,\xi(m)\,dm. \qquad (3-25)$$

If $r$ is the rate of star formation in numbers of stars per unit time, then the total rate of production of Lyman continuum photons is

$$N_{\rm Ly\,c} = \frac{r}{\chi(m_{\rm lo}, m_{\rm up})} \int_{m_{\rm lo}}^{m_{\rm up}} n_c(m) t(m) \xi(m)\,dm. \qquad (3-26)$$

The steady state rate of star formation, $r_{\mathrm{stars\,yr^{-1}}}$, is converted to the mass rate of production, $R_{\mathrm{M_\odot\,yr^{-1}}}$, through multiplication by the average mass value from Table E–3 or Table E–4. An empirical approximation to $t(m)$ for a main sequence star of composition $(Y, Z) = (0.28, 0.02)$ may be derived by inverting an expression in Renzini and Buzzoni (1986):

$$\log t(m) = 11.9892 \left(1 - 0.1789\sqrt{1 + 3.894 \log m}\right), \qquad (3-27)$$

where $t$ is in years and $m$ is in solar masses. Table 3–10 shows values of the integral (without the factors on the right-hand side of equation (3–26) that is used to calculate the average number of photons per star produced in a star's lifetime. The present rate of star formation is

$$R = \frac{N_{\mathrm{Ly\,c}}}{\frac{1}{\chi}\int n_c\, t\, \xi\, dm}\, \langle m \rangle. \qquad (3-28)$$

For a population following an extended Miller-Scalo IMF with $m_{\mathrm{lo}} = 0.1\,\mathrm{M_\odot}$, $m_{\mathrm{up}} = 60\,\mathrm{M_\odot}$, and distance $D_{\mathrm{Mpc}} = 15.7$, the present-day star formation rate is

$$\begin{aligned} R &= \frac{(1.313 \times 10^{62})\, D^2_{\mathrm{Mpc}}\, f_{\mathrm{H}\alpha}(\mathrm{erg\,cm^{-2}\,sec^{-1}})}{(2.344 \times 10^{60}\,\mathrm{phot})/4.445} \cdot \frac{3.1558 \times 10^7\,\mathrm{sec}}{\mathrm{yr}} \cdot 0.673\,\mathrm{M_\odot\,yr^{-1}} \\ &= (1.304 \times 10^{12})\, f_{\mathrm{H}\alpha}(\mathrm{erg\,cm^{-2}\,sec^{-1}})\ \mathrm{M_\odot\,yr^{-1}}. \end{aligned} \qquad (3-29)$$

This formula is about a factor of two different from that in Gallagher, Hunter, and Tutukov (1984), mainly because of the different formula used to compute $N_{\mathrm{Ly\,c}}$.

TABLE 3–10.
AVERAGE LIFETIME NUMBER OF Ly c PHOTONS[a]

| $m_{up}$ | $10^{60}$ photons | |
|---|---|---|
| | Salpeter | Miller-Scalo |
| 30 | 1.170 | 0.7299 |
| 40 | 2.342 | 1.418 |
| 50 | 3.309 | 1.965 |
| 60 | 3.999 | 2.344 |
| 80 | 4.844 | 2.792 |
| 100 | 5.381 | 3.065 |

[a] Values are per star, unnormalized. Divide by $\chi$ from Table E–1 or Table E–2 for desired mass range.

## References

Allen, C. W. 1973, *Astrophysical Quantities* (London: The Athlone Press).

Bloemen, J. B. G. M., Strong, A. W., Blitz, L., Cohen, R. S., Dame, T. M., Grabelsky, D. A., Hermsen, W., Lebrun, F., Mayer-Hasselwander, H. A., and Thaddeus, P. 1986, *Astron. Ap.*, **154**, 25.

Burstein, D., and Raychaudhury, S. 1989, *Ap. J.*, **343**, 18.

Cousins, A. W. J. 1976, *Mem. R. Astron. Soc.*, **81**, 25.

Dickman, R. L., Snell, R. L., and Schloerb, F. P. 1986, *Ap. J.*, **309**, 326.

Frerking, M. A., Langer, W. D., and Wilson, R. W. 1982, *Ap. J.*, **262**, 590.

Gallagher, J. H., III, Hunter, D. A., and Tutukov, A. V. 1984, *Ap. J.*, **284**, 544.

Genzel, R., Harris, A. I., Jaffe, D. T., and Wild, W. 1990, *Ap. J.*, **348**, 434.

Johnson, H. L. 1965, *Comm. Lunar Planet. Lab.*, **3**, 73.

Johnson, H. L., Mitchell, R. I., Irarte, B., and Wisniewski, W. Z. 1966, *Comm. Lunar Planet. Lab.*, **4**, 99.

Kennicutt, R. C., Jr. 1983, *Ap. J.*, **272**, 54.

Kennicutt, R. C., Jr, and Kent, S. M. 1983, *A. J.*, **88**, 1094.

Kutner, M. L., and Leung, C. M. 1985, *Ap. J.*, **291**, 188.

Landolt, A. U. 1973, *A. J.*, **78**, 959.

Landolt, A. U. 1983, *A. J.*, **88**, 439.

Maeder, A. 1980, *Astron. Astrophys.*, **92**, 101.

Maloney, P., and Black, J. H. 1988, *Ap. J.*, **325**, 389.

Osterbrock, D. E. 1974, *Astrophysics of Gaseous Nebulae* (San Francisco: W. H. Freeman).

Panagia, N. 1973, *A. J.*, **78**, 929.

Pierce, M., and Tully, R. B. 1988, *Ap. J.*, **330**, 579.

Renzini, A., and Buzzoni, A. 1986, *Spectral Evolution of Galaxies* (Holland: D. Reidel), p. 195.

Sandage, A., and Smith, L. L. 1963, *Ap. J.*, **137**, 1057.

Sanders, D. B., Solomon, P. M., and Scoville, N. Z. 1984, *Ap. J.*, **276**, 182.

Scoville, N. Z., and Good, J. C. 1989, *Ap. J.*, **339**, 149.

Scoville, N. Z., and Solomon, P. M. 1975, *Ap. J. (Letters)*, **199**, L105.

Solomon, P. M., and Sanders, D. B. 1985, in *Protostars and Planets II*, ed. D. C. Black and M. S. Matthews (Tucson: University of Arizona Press), p. 59.

Taylor, B. J. 1986, *Ap. J. Suppl.*, **60**, 577.

Thuan, T. X., and Gunn, J. E. 1976, *P.A.S.P.*, **88**, 543.

Wade, R. A., Hoessel, J. G., and Elias, J. H. 1979, *P.A.S.P.*, **91**, 35.

Wilson, C. D., and Scoville, N. 1990, *Ap. J.*, in press.

Woody, D. P., Miller, R. E., and Wengler, M. J. 1985, *IEEE Trans. Microwave Th. Tech.*, **33**, 90.

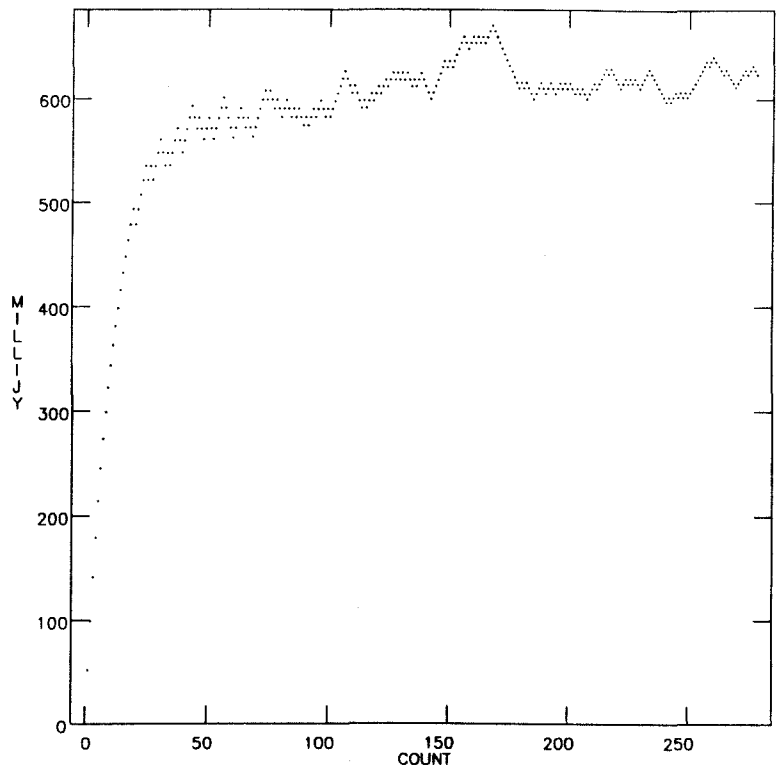


Figure 3–1. Graph of total cleaned flux versus clean component number for channel 14, a flux-containing channel of the NGC 4654 data.

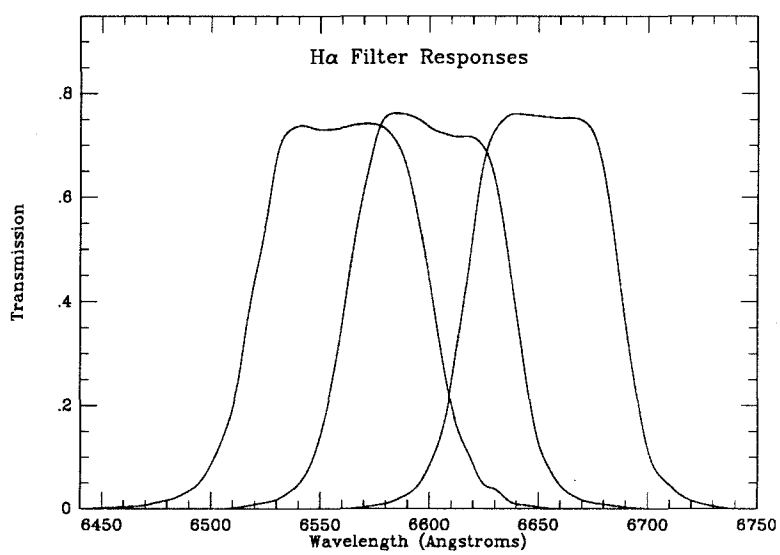


Figure 3–2. Transmission profiles of the three filters used in H$\alpha$ imaging. From left to right, they are referred to in the text as the "6563" filter, the "6600," and the "6675."

# Chapter 4
# Interpretation of Optical and Radio Images

## 4.1. Introduction

Each of the program spirals will be presented individually in the following sections. Table 4–1 lists the spirals and their morphological types (de Vaucouleurs *et al.* 1976). The description and interpretation of the morphological features of each galaxy will rely mostly on images in $B$-band, $i$-band, H$\alpha$ emission, and CO emission. The $B$-band images, and particularly the H$\alpha$ images, trace regions of active star formation. The $i$-band images, which are less susceptible to extinction, indicate the general spiral structure. Because of resolution effects of the interferometer, CO images trace the concentrations of molecular gas like the tips of icebergs. $B-V$ color images are useful to show areas with high extinction or with very young stars.

Figure 4–1 shows a mosaic of $i$-band CCD images of seven of the eight program spirals. (CCD imagery of NGC 4654 was not obtained.) All of the images are to the same scale: each frame is 5.′44 on a side, or 24.9 kpc. North is to the top and east is to the left. Figure 4–2 shows a mosaic of contour maps of the same $i$-band images as in Figure 4–1; the spatial scale is also the same. The contours are in increments of 0.5 $i$ mag arcsec$^{-2}$. Legends at the base of each frame indicate the lowest and highest contour levels and the step (0.5 mag) between each level. Figure 4–3 is a mosaic of CCD images of continuum-subtracted H$\alpha$ emission from seven of the program spirals. The spatial scale is the same as in the preceding two figures. Figure 4–4 is a mosaic of $B-V$ color maps of the program spirals. Redder $B-V$ color is represented as lighter shades, while bluer $B-V$ color is shown as darker shades.

TABLE 4–1. PROGRAM SPIRALS

| NGC | Type[a] | NGC | Type |
|---|---|---|---|
| 4254 | Sc | 4535 | Sc |
| 4303 | Sbc | 4536 | Sbc |
| 4321 | Sbc | 4569 | Sab |
| 4501 | Sb | 4654 | Scd |

[a]de Vaucouleurs *et al.* (1976).

Details of the central regions of the program spirals are shown in Figure 4–5 through Figure 4–9. Each frame in a mosaic is 64″ on a side, or 4.9 kpc. North is to the top and east is to the left. The contours are drawn at levels which are fixed fractions of the peak emission in the frame; a legend at the base of each frame indicates the contour levels and spacing in percent. The contours were chosen to emphasize source structure. Figure 4–5 shows Johnson $B$-band CCD images; Figure 4–6, Thuan-Gunn $i$-band CCD images; Figure 4–7, continuum-subtracted H$\alpha$ emission; Figure 4–8, integrated CO emission interferometer maps; and Figure 4–9, $B-V$, where redder $B-V$ color is in lighter shades and bluer $B-V$ is darker. The H$\alpha$ emission image of NGC 4654 in Figure 4–7 is from Pogge (1989).

The remaining figures in this chapter are overlays of CO emission contour maps with grayscale images in $B$-band, $i$-band, H$\alpha$, and $B-V$. The grayscale images are the same as the images displayed in Figure 4–5 through Figure 4–9. All frames are 64″ on a side, or 4.9 kpc; north is to the top and east is to the left. Coordinates are epoch 1950.

## 4.2. The Galaxies

### 4.2.1. NGC 4254

The appearance of NGC 4254 is typical for an Sc galaxy except for a large, very

prominent spiral arm which loops away from the main body of the galaxy (Figure 4–1). An H I map (Cayatte *et al.* 1990) shows an asymmetric distribution of the atomic gas and a ridge associated with the large, dominant spiral arm. There are three main arms, and all three fork into two arms each; arm spurs are also common. Radio continuum emission at 1465 MHz (Condon 1983) is bright over the optical disk and shows some concentration along spiral arms.

The $i$-band image (Figure 4–11) shows a very nearly circularly symmetric central region with a small nucleus. Three spiral arms can be identified and traced nearly to the center in both $B$ and $i$ bands. In contrast to $B$- and $i$-band emission, the H$\alpha$ emission (Figure 4–12) shows no distinct central concentration at all. Instead, H$\alpha$ emission from the central region is knotty and traces the three arms all the way to the center. There is also significant H$\alpha$ emission between the spiral arms. It is interesting, and judging from the sample studied here, relatively rare, that spiral structure can be continuously traced to the nucleus.

Very broad, red arms have $B - V \approx 0.8$ (Figure 4–4), which indicates a lack of star formation for at least $5 \times 10^8$ years (see Larson and Tinsley 1978). Along spiral arm ridge lines, colors decrease to $B - V = 0.0$–$0.2$, indicative of recent ($\lesssim 10^8$ years ago) star formation. In a photometric study of several bright spirals, Schweizer (1976) found that the blue colors of young, massive stars in the spiral arms of NGC 4254 are exceptionally strong atop the underlying, red disk.

There is not much emission in the interferometric CO map (Figure 4–8) despite the fact that NGC 4254 is one of the brightest sources of CO emission among Virgo spirals (Kenney 1987). Most of the central CO emission must therefore vary only on spatial scales of $\gtrsim 30''$ and so be resolved out by the interferometer. The map of CO emission from NGC 4254 was one of the first made, and the relatively large noise renders the interferometer image marginal. Even so, it appears that the CO emission

and the H$\alpha$ emission share the same topology: both are composed of discrete sources of localized emission. The CO distribution apparently follows the inner edge of H$\alpha$ emission from the dominant arm. A passing spiral density wave could bring about high-mass star formation by inducing cloud-cloud collisions within the wave. The displacement between CO and H$\alpha$ emission may be expected on kinematic grounds because of the speed of the density wave and the finite time for stars to collapse and begin to shine. NGC 4254 is unusual in comparison with the other program galaxies in one sense: there is no central concentration of CO emission, nor of H$\alpha$ emission, despite the fact that there is a definite, bright, central core in the optical continuum.

### 4.2.2. NGC 4303

NGC 4303 is an Sbc galaxy with two main spiral arms that originate at opposite ends of a bar which, as will be discussed below, appears as an oval at low resolution (Figure 4–1). The mid-disk arms seem to be strung together curiously from straight pieces, while the outer disk arms are smoothly curved. Judging from the characteristics of spiral structure in the middle and outer disk, it seems that there are two regimes of spiral arm formation in the disk of NGC 4303. The H I map (Cayatte *et al.* 1990) shows a central depression (lack of flux) inside a large, broken ring of emission, which is in turn surrounded by uniform, symmetrical emission. It is possible that some physical characteristic of the interstellar medium, perhaps related to gas surface density, changes considerably in the outer disk and so alters the morphological and star-forming properties of spiral waves. It may also be that the mid-disk arms are subject to perturbation by the bar, while the outer arms are not.

The *B*-band image (Figure 4–14) shows a very bright, circularly symmetric, slightly extended nucleus superposed on a much fainter, narrow bar. The bar is only 750 pc across and 3 kpc long and has a position angle of about 20°. A spiral arm emerges very clearly from the north end of the bar, turns sharply south along the

eastern length of the bar, and may be traced to the western mid-disk arm. Another inner arm arises in a symmetrical fashion from the south end of the bar and turns sharply north, where it is traced to the eastern mid-disk arm. The fat central oval is illusory and its appearance is due to the combined widths of the narrow bar and two closely spaced, inner spiral arms. There is no sign of the bar feature in $B - V$ color (Figure 4–17), implying that stellar orbits in the inner disk are well mixed rather than trapped in the bar potential.

H$\alpha$ emission from NGC 4303 shows a bright nuclear core surrounded by a remarkable dearth of star formation out to a radius of 2 kpc (Figure 4–3). There is no sign of the small stellar bar in H$\alpha$ emission at all (Figure 4–16). Large associations of H II regions appear throughout most of the middle disk and confuse the spiral arms. H$\alpha$ emission resembles very much a fat, star-forming annulus with a bright core in the central hole.

CO observations of the central region of NGC 4303 reveal molecular gas that is moving in a slow-moving bar potential (Figure 4–8). The position angle of the gas bar is approximately $-40°$, which is quite different from the position angle of the optical bar. If the stellar bar pattern rotates in the same sense as the stars in the disk, then the molecular gas bar *leads* the stellar bar. A geometry in which the gas bar leads the stellar bar has been found in particle simulations of molecular clouds in barred galaxies (Combes and Gerin 1985). For such a situation to occur, the bar must be weak. The short length of stellar bar and the lack of obvious shocks or dust lanes indicates that the bar is, indeed, weak. Numerical models (Combes 1988) also predict spiral structure in the gas inside the radius of the bar, which is marginally apparent as curvature at the ends of the CO bar. This model will be discussed in more detail in Chapter 6, where rotation curve data will be used to locate the positions of dynamical resonances. Combes's (1988) simulations also predict a small ring of

gas, which is not shown in the CO observations, just outside the gas bar; however, the field of view may be too small to show the ring, if it exists. There is a large area of CO emission near the edge of the field to the south whose physical nature is unexplained by Combes's simulations.

There is a ring of very red color ($B - V \approx 1.0$) which is just at the radius of the gas bar (Figure 4–17). The red color may be caused by extinction due to gas and dust, although the extinction is not more severe along the gas bar, where the gas is concentrated. The lack of strong H$\alpha$ emission between the nucleus and the mid-disk H$\alpha$ annulus may be a result of the collection of molecular gas through the action of the central bar at the expense of the middle disk.

### 4.2.3. NGC 4321

NGC 4321 is an Sbc galaxy with a strong spiral pattern. Two fairly thick but well-defined spiral arms unwind from near the nuclear region (Figure 4–1). H I maps by Warmels (1986) and by Cayatte *et al.* (1990) show a central depression in the H I distribution and enhanced emission along the spiral arms. The H I velocity field is fairly regular but shows perturbations related to the spiral arms (Guhathakurta *et al.* 1989), which must be due to strong density waves.

The nuclear region is somewhat elongated in $i$-band (Figure 4–19) in the direction of the spiral arm attachment points. The elongation is revealed in the $B$-band image (Figure 4–18) to be due to a more complex, pinwheel-shaped structure. There is a central hot spot surrounded by four small arms, canted outward, which are best seen in the H$\alpha$ image (Figure 4–20). The four small H$\alpha$ arms are very prominent, the north and south arms being more pronounced than the east and west arms. The small north arm points directly to the origination of the western main arm and is connected to it by a string of H$\alpha$ regions.

The spiral structure of NGC 4321 shows up very well in its $B-V$ image (Figure 4–

4). The interarm disk has colors from $B - V = 0.9$ to about 1.0, while the arms are characterized by $B - V = 0.5$ to 0.7. Of considerable interest is the small blue ring with $B-V = 0.5$ to 0.7 encircling the nucleus (Figure 4–21). This ring was noticed by Arsenault *et al.* (1988), who interpreted it as a ring of high-mass star formation (see also Pogge 1989). It is, of course, associated with the four-armed structure evident in the H$\alpha$ and $B$-band images. The four-armed nuclear structure is apparently a long-lived feature, and the ring probably results from the azimuthal spreading of orbits of stellar groups created by star formation in the small arms. Rotation times at the radius of the blue ring (about 1 kpc) are around $5 \times 10^7$ years, so young stars can make many orbits before they die.

Very interesting structure is shown in the CO emission from the central region (Figure 4–8). There are five bright cores of CO emission that are correlated with the bright center and four-armed pinwheel seen in H$\alpha$ emission. The north and south CO emission cores lie outside of the small north and south H$\alpha$ arms. The east and west CO cores are coincident with their H$\alpha$ counterparts. The two main spiral arms arise from the east and west small arms of the four-armed structure.

The strong spiral arm pattern in the disk and the detailed morphology of the nuclear region suggest that the spiral density waves propagate through the disk all the way to the center of NGC 4321. In a stellar disk with an inner Lindblad resonance, spiral density waves cannot propagate across the entire disk but are absorbed at the resonance (Binney and Tremaine 1987, p. 369). However, in a disk with a pattern speed too large to admit an inner Lindblad resonance, spiral waves can propagate all the way to the center of the disk. Trailing waves propagating inward are turned into leading waves as they reflect from the center. The interference of leading and trailing waves produces density patterns such as shown in Figure 12 in Toomre (1981) (see also Binney and Tremaine 1987, p. 383), which closely resemble the four-armed pattern in

the nuclear region. Very similar interference patterns are also expected in the modal theory of spiral structure (Bertin *et al.* 1989). The absence of an inner Lindblad resonance solves the problem of finding a source of fresh leading waves for swing amplification to work on. The swing amplifier works on leading waves, which are turned into trailing waves with a density amplitude which is enhanced considerably. Reflection at the corotation radius turns the direction of propagation of trailing waves inward to the center, where they may be reflected and emerge as leading waves. The feedback loop is closed by swing amplification of the emergent leading waves as they shear to trailing waves (see Goldreich 1988 for further discussion of the process). The strength of the spiral arms in NGC 4321 may be due to the standing wave pattern which can be maintained through the process outlined above.

It is likely that gas will accumulate at the peaks of the interference pattern and that stars will form at the nodes (where there are large density gradients and perhaps shocks) and then migrate with the wave motion. High-mass star formation is undoubtedly fueled by molecular gas from the four-core CO structure. Because of the similar CO and H$\alpha$ geometries, the stars and gas are probably subject to the same dynamical phenomenon, and the position of young stars relative to gas indicates the direction of the flow or density gradient.

### 4.2.4. NGC 4501

NGC 4501 is an Sb galaxy which has many, tightly-wound spiral arms. The arms are very short, being traceable only about 90° in azimuth around the disk, and have a feathery appearance. The H$\alpha$ image of NGC 4501 (Figure 4–3) shows a disk in which the H II region distribution is surprisingly asymmetrical. In general, the H$\alpha$ emission from the disk is not very strong and the H II regions are not very bright. The northwest half of the disk has many H II associations and at least three major arms can be traced by them. The southeast side of the disk has about one-half the

extent in H$\alpha$ emission as the northwest side.

The spiral arms are particularly prominent in the $B-V$ image (Figure 4–4). The arms are almost uniformly of color $B-V \approx 1.0$ except for the arm ridge lines, which have $B-V \approx 0.8$. Despite the rather small absolute difference in color, the arm-interarm boundaries are sharp and contrasting in color. The $B-V$ color of 0.8 does not imply a large amount of recent star formation. In fact, the arms of NGC 4501 are the reddest of the galaxies in this study.

Whorls of spiral structure can be seen in $B$-band quite close to the nucleus, which is round and not prominent (Figure 4–22). A small core of H$\alpha$ emission at the nucleus is surrounded, at quite some distance, by a patchy ring of emission which may be emergent spiral arms (Figure 4–7) at about 2 kpc radius. Within this ring-like distribution of H$\alpha$ emission there is very little flux except from the nucleus. Though still a relatively weak H$\alpha$ source, the nucleus is by far the brightest H$\alpha$ source in the galaxy. Spectrophotometry of the nuclear region by Keel (1983) indicates a LINER (low ionization) spectrum. The nucleus is very red (Figure 4–9), with $B-V \approx 1.2$ indicating a long hiatus since stars were actively formed in large numbers.

CO emission from the central region is weak (Figure 4–8). There is a relatively bright CO core at the nucleus and a lot of marginal emission surrounding the nucleus. Because of the doubtful nature of the CO emission outside the very center, not much can be said relating the CO map with optical data. Comparison with $B$-band (Figure 4–22) and H$\alpha$ (Figure 4–24) images suggests that CO emission is coincident with the ridge of the innermost eastern spiral arm, which is quite bright. The very red color of the nuclear region may be caused by large amounts of dust associated with the molecular gas.

### 4.2.5. NGC 4535

NGC 4535 is an Sc galaxy with two spiral arms in its inner disk (Figure 4–1); they

become less smooth and well defined in the outer disk and degrade into thick arms highlighted by large, bright H II associations (Figure 4–3). H I emission is extensive and complex (Cayatte *et al.* 1990), the main features being a central hole typical of earlier-type spirals and concentrated knots of emission along the spiral arms and arm spurs in the outer disk. There are only two spiral arms in the inner disk, and they are the only sign of spiral structure until radii beyond 4 kpc are reached. Such dominance of the inner disk by two arms is not seen in any of the other galaxies studied, not even the strong-armed spiral NGC 4321. The dichotomy in appearance between arms in the inner and outer disk is similar to NGC 4303.

In the inner disk, the spiral arms are delineated by small, closely-spaced H II regions (Figure 4–3). The width of the inner arms is very small, less than 500 pc across, as estimated from the extent of H II regions. Upon entering the outer disk, the arms often fork and new arms erupt in the interarm regions. The most ferociously active regions of massive star formation, judging from the account of H$\alpha$ flux and its extent, occur in the outer disk. Locations of spiral arms are evident in the $B-V$ image (Figure 4–4). The arms are rather red and have $B-V \approx 0.7$–$0.8$ except where large H II associations are located, where high-mass stars bring the color down to $B-V \approx 0.3$–$0.5$.

The $i$-band image shows that two spiral arms extend to the nucleus (Figure 4–6). A narrow dust lane, seen best in $B$-band, cuts across the nucleus, bisecting it into north and south halves (Figure 4–26). After cutting across the nucleus, the dust lane curves sharply and follows the inner edge (smaller radius) of both arms. The west arm joins the north lobe of the nucleus, and the east arm joins the south lobe (Figure 4–26). The organized spiral arms and narrow, distinct dust lane on the inner side of the spiral arms imply that a very strong spiral wave is present.

CO emission from the nuclear region of the galaxy is centrally concentrated and

shows little structure (Figure 4–8). There is a slight extension in the CO emission to the south. The H$\alpha$ emission is centrally concentrated (Figure 4–28), even more so than the CO emission; there is also a southern extension of more diffuse H$\alpha$ emission. The nucleus has a blue color, $B - V = 0.5$. There is no indication that the CO emission is associated with the central dust lane, as might be expected if a significant number of the molecular clouds in the region were associated with the dust. Although it could be the case that there is weak, undetected CO emission from molecular clouds in the dust lane, the correlation between CO and H$\alpha$ emission morphology is more apparent.

### 4.2.6. NGC 4536

NGC 4536 is an Sbc galaxy with two major spiral arms and two other strong, easily identifiable arms. The four spiral arms are best seen in H$\alpha$ emission (Figure 4–3). This galaxy is far from the Virgo Cluster center and properly belongs to the Southern Extension of Virgo (Binggeli, Sandage, and Tammann 1985). Its membership in the Virgo Cluster is supported by its recession velocity, angular size, and the resolution of disk features.

H II associations dot the spiral arms, which are well defined and rather thin (Figure 4–3). Aside from the few H II regions which pepper the inner disk, nearly all of the H$\alpha$ emission in the galaxy can be assigned to one of the four spiral arms. The four-armed morphology of NGC 4536 is unique among the spirals studied here. The underlying disk has color $B - V \approx 0.8$ to 0.9 (Figure 4–4). The arms in the inner disk are not very strongly delineated in color, while the arms in the outer disk are strikingly blue, with knots of $B - V$ as blue as about 0.3. In this respect, NGC 4536 resembles NGC 4535: blue arms distinguished by their $B - V$ color are found only in the outer disk.

The elongation of the nucleus in $i$-band (Figure 4–6) is probably due to projection

effects and the high inclination of this galaxy. A concentration of dust on the northeast side of the nucleus, best seen in $B$-band (Figure 4–30), obscures part of the spiral arm that originates to the north. Extinction causes the dust region to have a very red $B-V$ color of about 1.2 (Figure 4–33). The $B$-band image of the nuclear region (Figure 4–5) shows two "ears" of emission at the connection points of two spiral arms. An infrared map at 10.8 $\mu$m (Hawarden *et al.* 1987) shows emission from the center elongated along the major axis of the galaxy. A map at 1413 MHz (Condon *et al.* 1982) also shows similar elongation and some structure that may be associated with the emergent spiral arms. The two pairs of spiral arms are shown in the H$\alpha$ image (Figure 4–7) of the nuclear region, with the arms in each pair originating at points diametrically opposite each other across the nucleus. Coincidence of the infrared and radio maps suggests that the nuclear radio emission is due to a large abundance of supernovae following high-mass star formation. The nuclear emission spectrum (Keel 1983) is consistent with emission dominated by H II regions.

CO emission from the nuclear region is extended and some structure can be seen in the relatively high signal-to-noise map (Figure 4–8). CO emission extends from the northwest and southeast ends of the main, elongated structure and may lead into two of the spiral arms (compare with the H$\alpha$ image, Figure 4–7). Two smaller extensions along the minor axis of the main CO structure may mark the emergence of the two other spiral arms. The pairwise, symmetrical way the spiral arms are arranged about the nucleus is unique among the spiral galaxies studied here and is rare among spirals. There is no indication that CO emission is asssociated with the dust to the northeast of the nucleus, but rather the nuclear CO morphology does resemble the H$\alpha$ morphology.

### 4.2.7. NGC 4569

NGC 4569 is an Sab-type galaxy with a smooth disk and ill-defined, fat spiral arms

(Figure 4–1). NGC 4569 is very close to the center of the Virgo Cluster and interaction with the cluster environment may have had an effect on its disk appearance. Indeed, its disk is notably deficient in H I for a spiral of its size and type (Giovanelli and Haynes 1983), which indicates a strong interaction with the intercluster medium. The negative heliocentric velocity of NGC 4569 strongly suggests that it is near the Virgo Cluster core (Stauffer, Kenney, and Young 1986). The H I disk is small compared with the optical disk, and has an irregular appearance (Warmels 1986; Cayatte *et al.* 1990). A 2.8 cm map by Urbanik, Klein, and Gräve (1986) also shows the radio emission localized within the inner disk.

H$\alpha$ emission from the disk of NGC 4569 (Figure 4–3) is weak and is confined to the very inner part of the disk. Only two spiral arms are evident from the pattern of H$\alpha$ emission, and they reach only about 5 kpc from the center. Nonetheless, small H II regions and some larger H II associations are visible in the arms. The two H$\alpha$ arms and the connected weaker emission encircle the nucleus in an inclined, thin ring of H$\alpha$ emission. The inner disk is almost uniformly of color $B - V \approx 1.0$ to 1.1. If atomic gas has been stripped from the disk, then perhaps the gas surface density has been lowered everywhere, except the inner disk, to below the threshold for high-mass star formation (Kennicutt 1989). It is possible that the thick and poorly delineated spiral arms of NGC 4569 are mainly "old arms" comprised principally of low mass stars.

Its nucleus is extremely bright and blue, with $B - V \approx 0.3$ (Figure 4–4). Spectrophotometry by Keel (1983) shows that the nucleus of NGC 4569 has a LINER (low-ionization) spectrum. A very red feature with $B - V \approx 1.3$ extends southward from just west of the nucleus, on the inner edge of an H$\alpha$ arm. Its $B - V$ color is probably due to extinction by dust. In contrast to the compact appearance of the nucleus in continuum optical bands (Figure 4–5 and Figure 4–6), H$\alpha$ emission from

the central region is rather extended (Figure 4–7).

CO emission from the nucleus is also very strong and compact (Figure 4–8). Marginally reliable CO emission forms an arc south of the nucleus and a core to the north, both of which appear to be associated with regions of extinction (Figure 4–37). The regions of exinction and the low-level CO emission lie along the inner edges of the two main spiral arms, so NGC 4569 may be the only example in this study where molecular gas is associated with a dust lane.

### 4.2.8. NGC 4654

NGC 4654 is an Scd galaxy with chaotic-looking, fragmented spiral structure. CCD imagery of this galaxy was not obtained because of time constraints at the Palomar 60-inch. Discussion of the optical morphology of this galaxy will rely heavily on the reproduction in Sandage and Bedke (1988) of a blue (103a0) plate taken with the Las Campanas du Pont 100-inch reflector. The dye-transfer print reproduced in Wray (1988), the IIIa-J plate reproduction in Warmels (1986) and the IIa-O $B$-band reproduction in Takase *et al.* (1984) are also useful.

The swept appearance of the western side of the galaxy suggests that it is the leading edge of the galaxy as it moves through the cluster. The most prominent spiral arm winds around this side. A radio continuum map at 1465 MHz (Condon 1983) shows emission over the optical disk centered on the nucleus, with a bright spot near the northwest edge that may be emission associated with star formation induced by interaction with the cluster environment. The H I distribution (Cayatte *et al.* 1990) is markedly asymmetrical. There is a central hole and a large concentration of H I emission near the sharp ridge delineated by the bright spiral arm at the northwest edge of the disk.

The inner disk of the galaxy is marked by a narrow, short, bar-like center. The central bar is very bright compared to any other feature in the disk. The total length

of the optical bar is only 2 kpc. The major axis of the bar is very well aligned with the major axis of the galaxy. The H I velocity field (Cayatte *et al.* 1990) is very regular and shows no sign of distortion, as might be expected if the apparent bar were a true dynamical bar, or if the mass distribution were seriously asymmetrical. Comparison with the print in Sandage and Bedke indicates that the H$\alpha$ emission to the northeast of the bar is part of an inner spiral arm which connects near the southeast tip of the bar. A similar, curved line of H$\alpha$ emission arises from the other tip of the bar and curves sharply clockwise to the south. There is a ring of star formation with a radius of 2.5–3 kpc which is almost certainly the union, in projection, of the arcs of two inner spiral arms seen in H$\alpha$ emission.

The CO emission map (Figure 4–8), which has exceptionally low noise, shows a bar-like center and significant structure. Bright CO emission extends further than the H$\alpha$ bar and appears to be physically associated with the emergence of spiral arms from opposite ends of the bar. The diffuse CO emission on the west end of the bar coincides with the connection point of an inner spiral arm which winds to the north. Three islands of CO emission lie on the inner boundary of H$\alpha$ emission from the northern, inner spiral arm (but not all knots of H$\alpha$ emission are accompanied by CO emission). Strong CO emission envelops the strong H$\alpha$ emission from the emergent spiral arm on the east end of the bar.

A strange, J-shaped feature hangs from below the bright core of the bar and curves north to join the east end of the bar. A fainter loop of emission extends from the northwest end of the bar and joins the "J" below the bar. The two loops may be the walls of bubbles in the interstellar medium. Such bubbles expand and sweep up gas by ram pressure from supernovae in a young stellar association (McCray 1987). There are several H II regions within the west loop and one or two in the east loop, so both sides have candidate stellar associations which may provide supernovae.

However, neither bubble has an obvious, centrally located H II region.

## 4.3. Dynamics, Morphology, and Star Formation

In many of the program spiral galaxies, the central CO morphology mimics the H$\alpha$ emission distribution. Note, however, that the type of morphology exhibited is quite different among the different cases: there is a knotty geometry in NGC 4254, a centrally concentrated geometry in NGC 4501 and NGC 4569, an extended but generally featureless morphology in NGC 4535 and NGC 4536, a feature with four-fold symmetry in NGC 4321, and a bar-like morphology in NGC 4654. The similarity in distribution of CO and H$\alpha$ emission suggests a causal link between the ordering of concentrations of molecular gas and the locations of young, high-mass stars. The link may be dynamical and follow from the fact that wherever the gas accumulates or is concentrated, that is where stars must form. High-mass star formation may be enhanced by the increased gas density.

A second effect may act in conjunction with the concurrence of gas and star formation. It may even dominate in extreme conditions. This effect is the heating of molecular clouds and the resultant increased CO emissivity of the warmer clouds. Cloud heating may be caused by the ambient ionizing radiation field but possibly also by large-scale turbulence associated with outflows from young stellar objects. Heating by the ambient radiation field may dominate in the nuclei of spiral galaxies where the stellar density is high. CO emission will be enhanced wherever the density of young, high-mass stars, as marked by the amount of H$\alpha$ emission, is high.

Both NGC 4303 and NGC 4321 display very interesting dynamical structures. NGC 4303, which has a short, narrow, stellar bar, has a molecular gas bar. The gas bar is not aligned with the stellar bar and may be part of a central gas spiral pattern. The morphology is consistent with numerical models (Combes and Gerin 1985) of molecular clouds in a weakly barred spiral galaxy with a small pattern speed.

NGC 4321 has four small arms that radiate from a brighter center, all of which are seen in CO, H$\alpha$, and $B$-band emission. Two of the short arms are associated with the two main arms that are prominent in the outer disk. The structure with four-fold symmetry is probably the result of interference between inbound trailing and outbound leading spiral density waves. Both the swing amplification theory and the modal theory of spiral structure predict such patterns with four-fold symmetry, although it is not clear from the numerical models if the structure can form on such a small spatial scale.

Many of the galaxies show evidence for spiral structure that persists at very small distances from their nuclei. Spiral structure winds to the very center of NGC 4254 and is traceable in both stars and, perhaps, molecular gas. Spiral arms begin at the ends of the short stellar bars in NGC 4303 and NGC 4654 and are traced by starlight and gas. A four-armed pattern emerges strongly in NGC 4321, barely 300 pc from its center. Spiral arms emerge from the outskirts of the spheroidal nuclei of both NGC 4535 and NGC 4536. A dust lane associated with the inner edges of the two spiral arms of NGC 4535 even bisects the nucleus.

Are such close approaches of spiral arms to nuclei supported by theories of spiral structure? In the swing amplification theory of spiral structure, spiral arms result from amplification of density waves as they shear from leading to trailing; reflection of waves at corotation is also integral to the theory. However, density waves behave differently at resonances when propagating in gas (fluid) or stellar (collisionless) disks. Density waves are absorbed at the inner Lindblad resonance in a stellar disk, but propagate straight through the resonance to the center in a gaseous disk. Since the production of spiral arms solely by swing amplification requires a steady source of leading waves, inbound trailing waves encountering the center and turning into leading waves provides such a source. Postulation of such a source of leading waves begs the

question of whether the gaseous density wave can leave the stellar wave behind at the inner Lindblad resonance and then recouple to the stellar disk by exciting a density wave after it leaves the center and emerges from inside the resonance. If there were no inner Lindblad resonance, then both stellar and gaseous waves could pass through to the center. This would explain the prominence of spiral structure in close proximity to spiral nuclei. Secular evolution of the mass distribution of spirals may be driven by dynamical processes (Toomre 1981; Lynden-Bell and Kalnajs 1972) such that all spirals have inner Lindblad resonances. If inner Lindblad resonances are prevalent among spirals, then the spiral structure near Virgo spiral nuclei requires an alternative explanation. It may be the case that since stars form where gas is, stars are concentrated within the gaseous density waves inside the inner Lindblad resonance. Such a configuration of stars might not remain coherent very long without the marshalling force of a stellar density wave.

In the modal theory of spiral structure, as in the swing amplifier theory, a reflection process at corotation is important. Inbound short leading waves interfere with outbound long trailing waves to form the observed spiral pattern. Reflection of waves from a barrier outside the inner Lindblad resonance allows inbound and outbound waves to interfere. The condition that reflection of inbound waves occurs before the inner Lindblad resonance is reached depends on a sharp increase in the velocity dispersion as the center is approached. The observation of large central velocity dispersions in spirals (§7.2.3) supports this picture. However, any spiral structure inside the reflection radius is then not excited. Therefore, the modal theory has more trouble than swing amplification does in explaining spiral structure very close to spiral nuclei.

The stochastic star formation theory could explain spiral structure seen near the nuclei of spirals if that structure is not symmetrical or well organized. If the rotation

curve is very nearly linear at small radii, then the differential rotation needed by the theory to sweep star-forming patches into arcs is lacking. Perhaps only the inner spiral structure of NGC 4254 can be explained by this theory, since the spiral arms are not symmetrically arranged. None of the other spirals with symmetrical spiral structure arranged about their nuclei (NGC 4303, NGC 4321, NGC 4535, and NGC 4536) can possibly be dominated by sheared, stochastic star formation.

It is certainly possible that spiral structure forms, in varying degrees, by the processes described in all three theories. NGC 4321 and NGC 4535 are best described by the swing amplification theory with no inner Lindblad resonance. Nuclear structures in both of these galaxies could be caused by interference of leading and trailing spiral waves. NGC 4501 and NGC 4536 are best described by the modal theory if they have inner Lindblad resonances. The inner Lindblad resonance in NGC 4536 would necessarily be very close to the nucleus; however, the modal theory is the only viable option which can explain the four arms of NGC 4536. The lack of spiral structure near the nucleus of NGC 4501 and the tightly wound arms in its disk are explained by the modal theory, which predicts a lack of spiral structure inside the reflection radius. NGC 4303 probably has at least one inner Lindblad resonance, based on numerical models by Combes and Gerin (1985), but their theory has not been related to either the model theory or the swing amplification theory of spiral structure.

## References

Arsenault, R., Boulesteix, J., Georgelin, Y., and Roy, J.-R. 1988, *Astron. Ap.*, **200**, 29.

Bertin, G., Lin, C. C., Lowe, S. A., and Thurstans, R. P. 1989, *Ap. J.*, **338**, 78.

Binggeli, B., Sandage, A., and Tammann, G. A. 1985, *A. J.*, **90**, 1681.

Binney, J., and Tremain, S. 1987, *Galactic Dynamics* (Princeton: Princeton University Press).

Cayatte, V., van Gorkom, J. H., Balkowski, C., and Kotanyi, C. 1990, *A. J.*, in press.

Combes, F. 1988, in *Galactic and Extragalactic Star Formation*, ed. R. E. Pudritz and M. Fich (Dordrecht: Kluwer Academic Publishers).

Combes, F., and Gerin, M. 1985, *Astron. Ap.*, **150**, 327.

Condon, J. J., Condon, M. A., Gisler, G., and Puschell, J. J. 1982, *Ap. J.*, **252**, 102.

Condon, J. J. 1983, *Ap. J. Suppl.*, **53**, 459.

de Vaucouleurs, G., de Vaucouleurs, A., and Corwin, H. 1976, *Second Reference Catalog of Bright Galaxies* (Austin: University of Texas Press).

Giovanelli, R., and Haynes, M. P. 1983, *A. J.*, **88**, 881.

Goldreich, P. 1988, in *Origin, Structure, and Evolution of Galaxies,* ed. Fang Li Zhi (Singapore: World Publishing Co).

Guhathakurta, P., van Gorkon, J. H., Kotanyi, C., and Balkowski, C. 1988, *A. J.*, **96**, 851.

Hawarden, T. G., Mountain, C. M., Puxley, P. J., and Leggett, S. K. 1987, in *Comets to Cosmology,* ed. A. Lawrence (Berlin: Springer-Verlag), p. 246.

Keel, W. C. 1983, *Ap. J. Suppl.*, **52**, 229.

Kenney, J. D. 1987, Ph.D. Thesis, University of Massachusetts.

Kennicutt, R. C., Jr. 199, *Ap. J.*, **344**, 685.

Larson, R. B., and Tinsley, B. M. 1978, *Ap. J.*, **219**, 46.

Lynden-Bell, D., and Kalnajs, A. J. 1972, *M.N.R.A.S.*, **157**, 1.

McCray, R. 1987, in *Physical Processes in Interstellar Clouds,* ed. G. Morfill and M. Scholer (Dordrecht: Reidel).

Pogge, R. W. 1989, *Ap. J. Suppl.*, **71**, 433.

Sandage, A., and Bedke, J. 1988, *Atlas of Galaxies Useful for Measuring the Cosmological Distance Scale* (Washington, D. C.: U. S. Government Printing Office), p. 90.

Schweizer, F. 1976, *Ap. J. Suppl.*, **31**, 313.

Stauffer, J. R., Kenney, J. D., and Young, J. S. 1986, *A. J.*, **91**, 1286.

Takase, B., Kodaira, K., and Okamura, S. 1986, *An Atlas of Selected Galaxies* (Tokyo: University of Tokyo Press), p. 28.

Toomre, A. 1981, in *The Structure and Evolution of Normal Galaxies,* ed. S. M. Fall and D. Lynden-Bell (Cambridge: Cambridge University Press).

Urbanik, M., Klein, U., and Gräve, R. 1986, *Astron. Ap.*, **166**, 107.

Warmels, R. H. 1986, Ph.D. Thesis, University of Groningen.

Wray, J. D. 1988, *The Color Atlas Galaxies* (Cambridge: Cambridge University Press), p. 66.

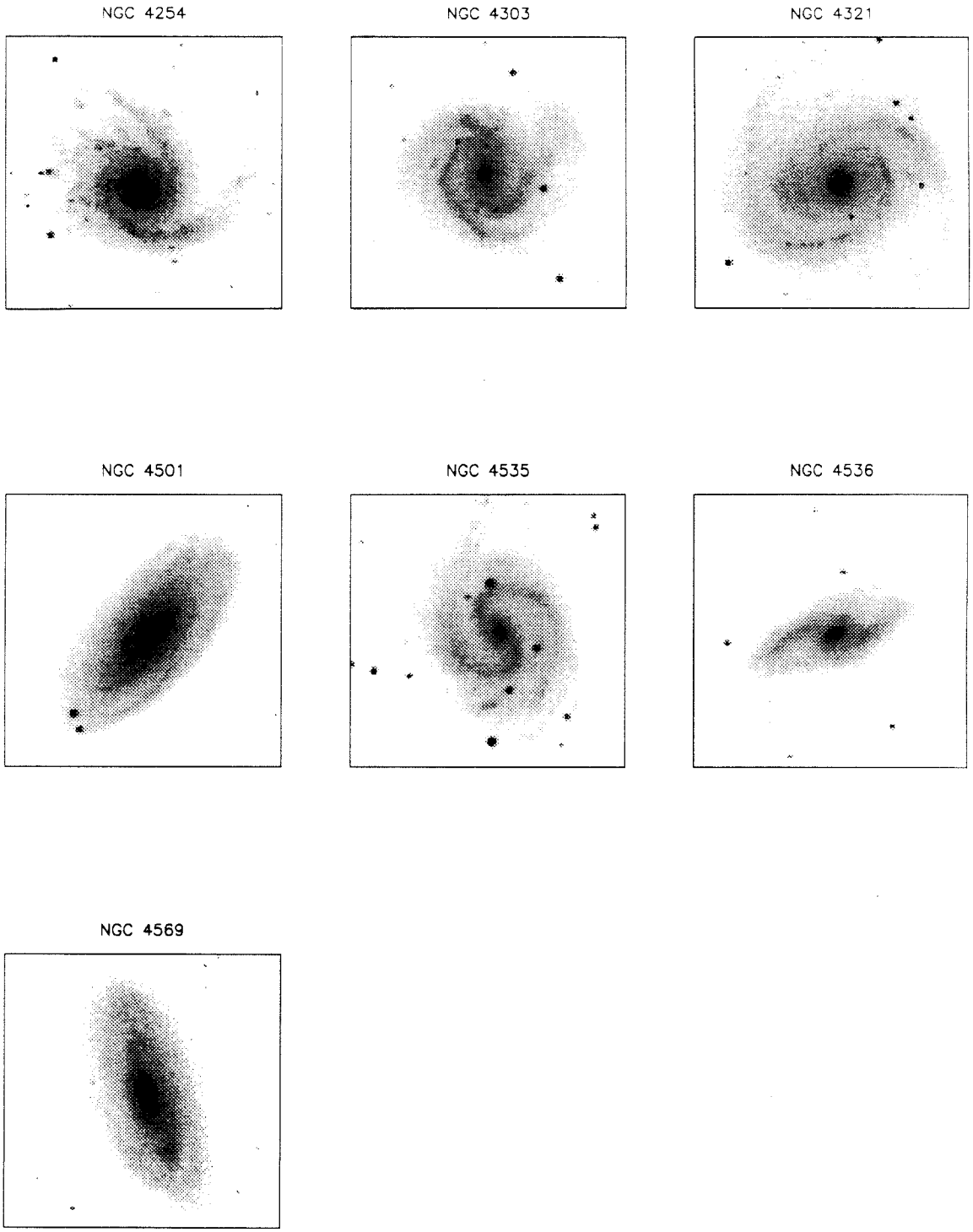


Figure 4–1. Mosaic of Thuan-Gunn $i$-band CCD images of Virgo spiral galaxies. Each frame is $5'.44$ on a side, or 24.85 kpc. North is up and east is to the left.

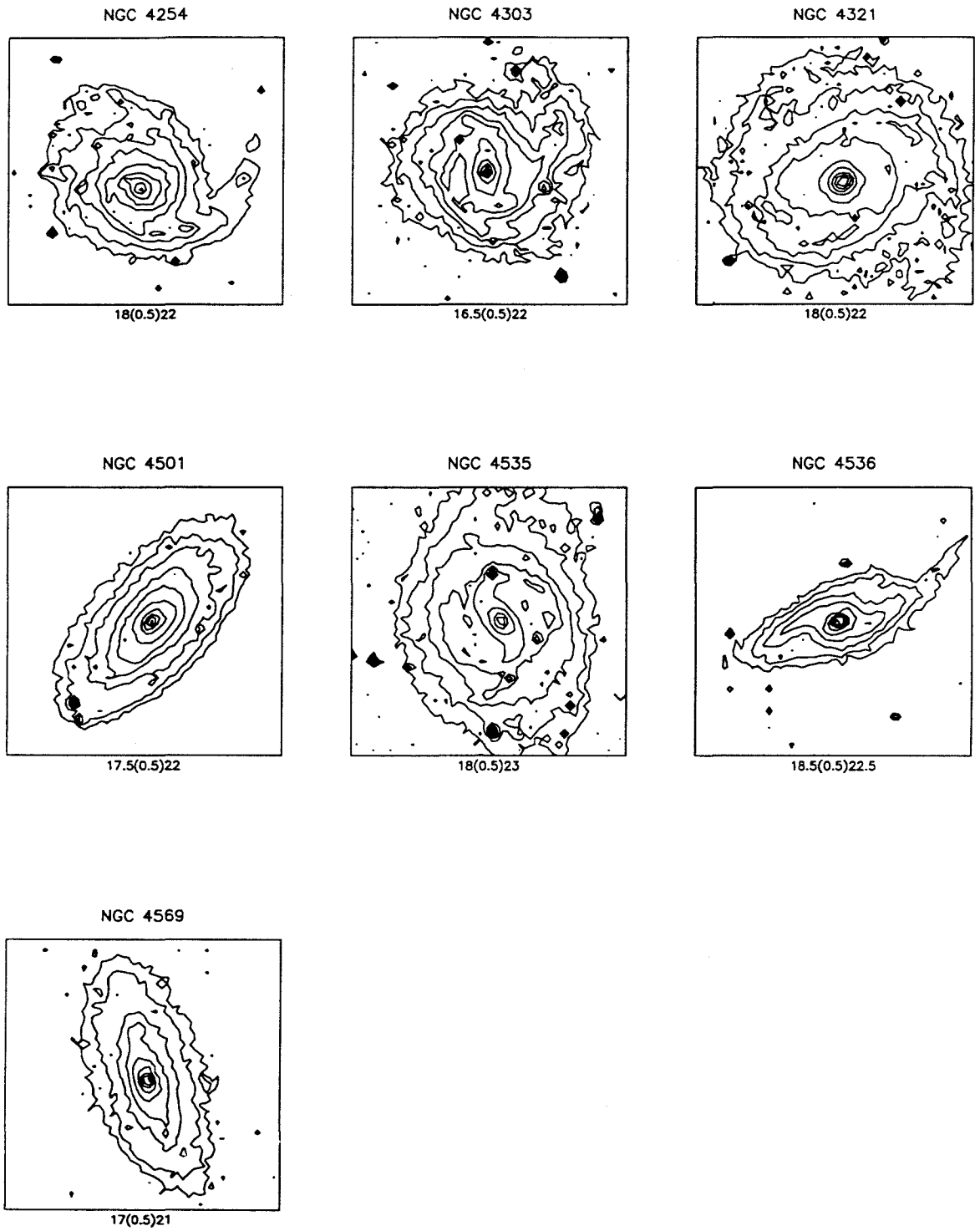


Figure 4–2. Mosaic of contour maps of Thuan-Gunn $i$-band images, shown to the same scale and orientation as Figure 4–1. Contour spacing is $0.5\,i$ mag arcsec$^{-2}$. The lowest and highest contours are listed in the legend of each frame.

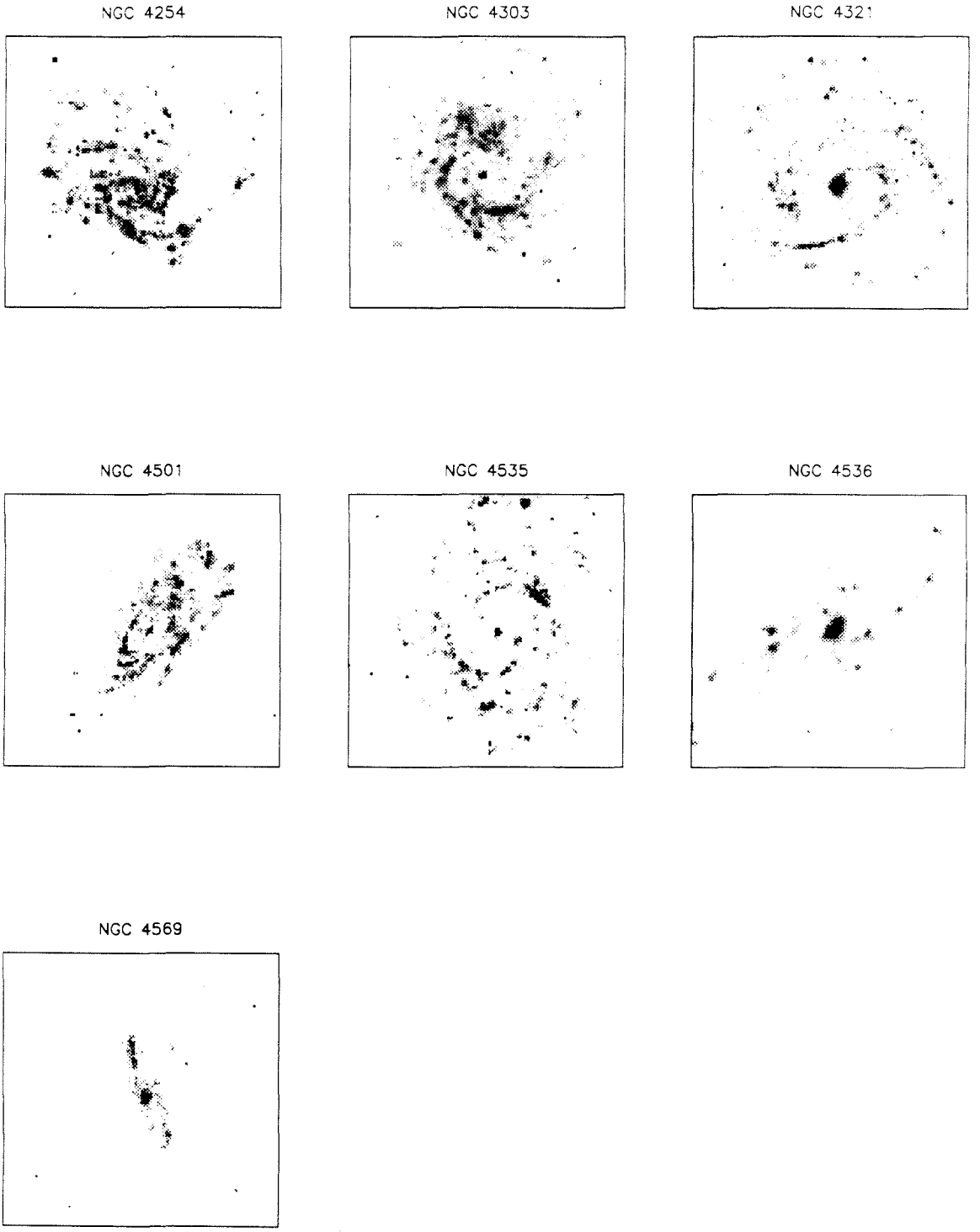


Figure 4–3. Mosaic of H$\alpha$ emission images. Each frame is 5.′44 on a side, or 24.85 kpc. North is up and east is to the left.

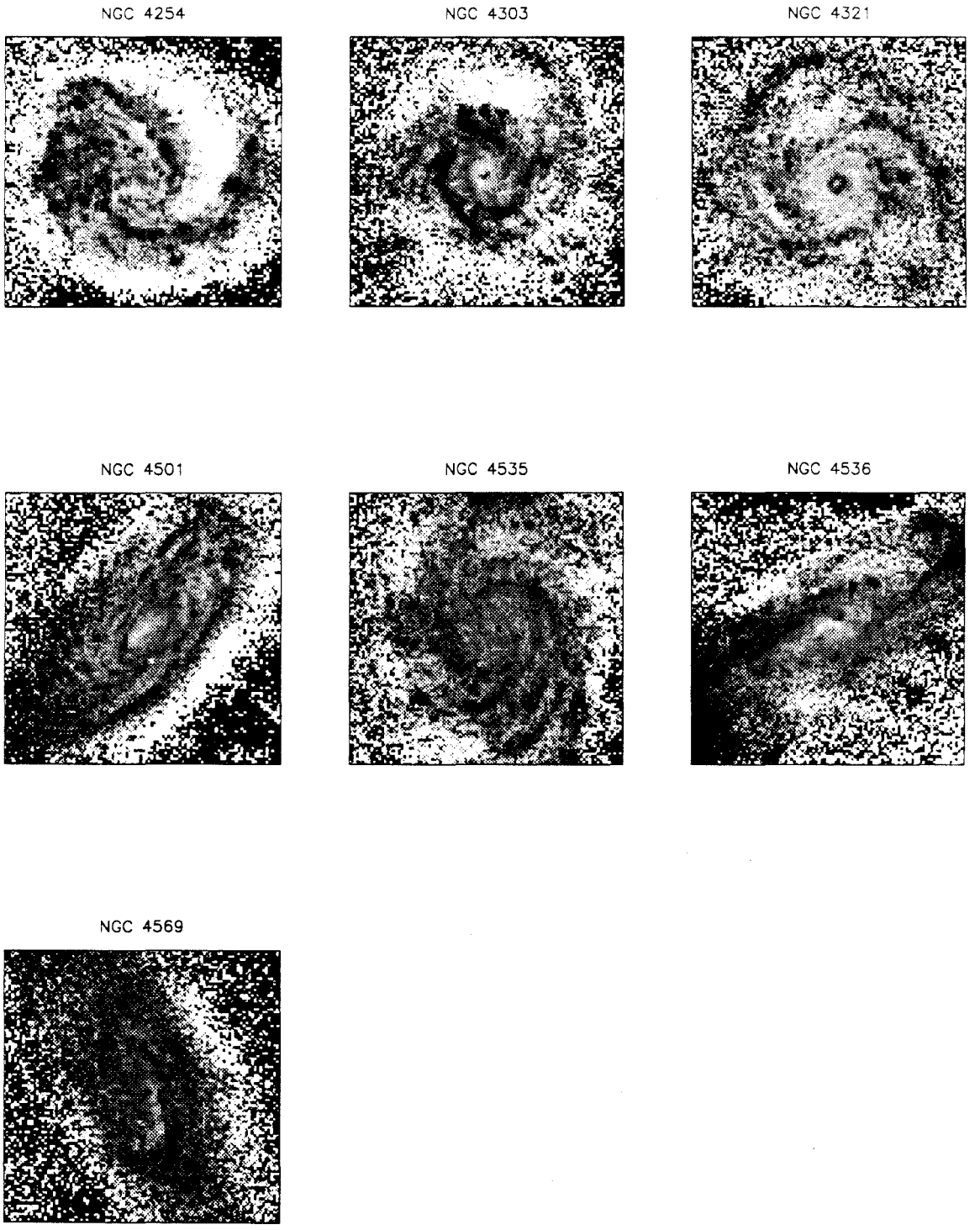


Figure 4–4. Mosaic of $B - V$ color maps of Virgo spiral galaxies. Each frame is $5'.44$ on a side, or 24.85 kpc. North is up and east is to the left. Redder $B - V$ color is represented by lighter shades; bluer $B - V$ color is represented by darker shades.

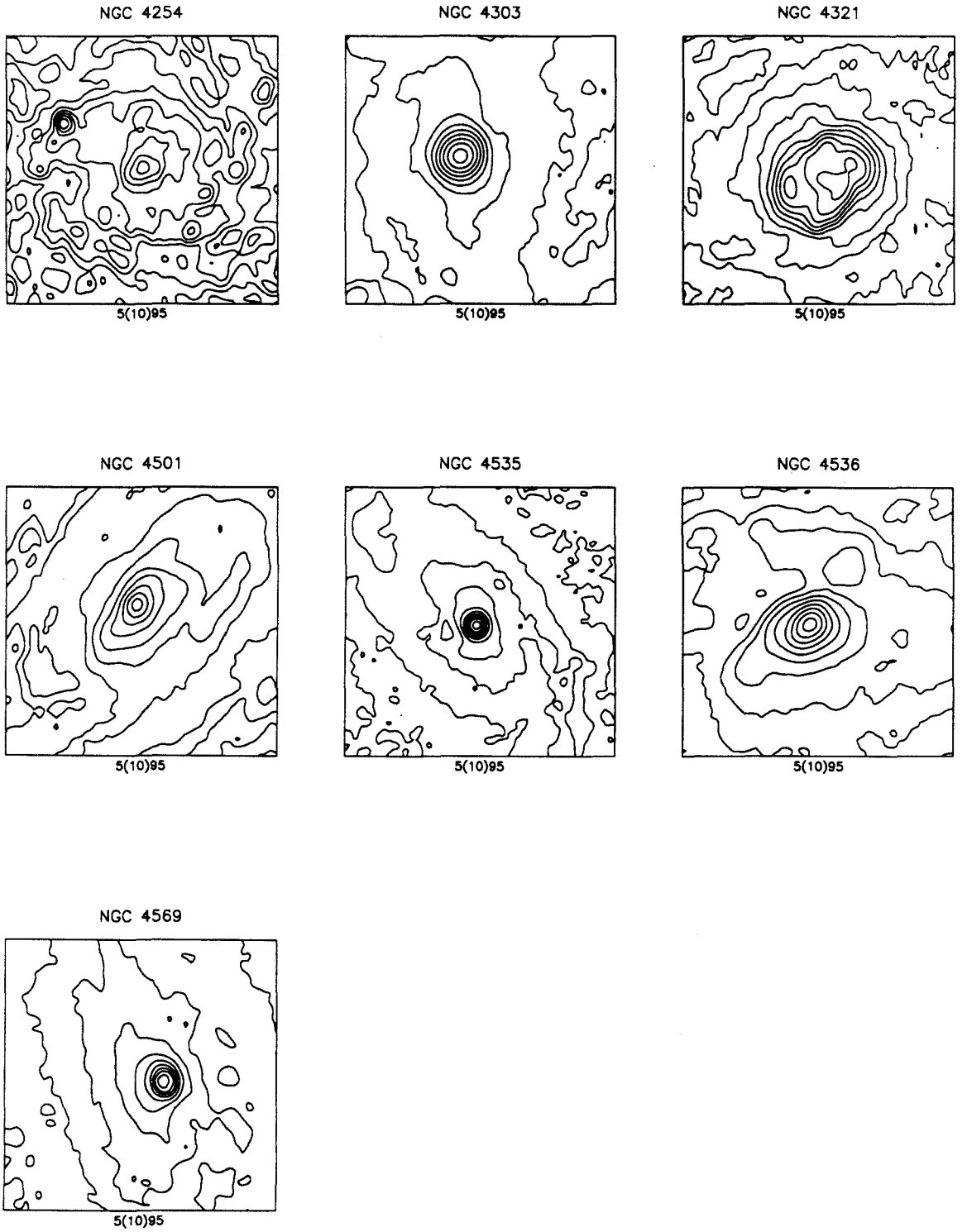


Figure 4–5. Mosaic of Johnson $B$-band images of the central regions of Virgo spiral galaxies. Each frame is $64''$ on a side, or 4.87 kpc. North is up and east is to the left. The lowest and highest contours and the contour spacing as a percentage of the peak is listed in the legend of each frame.

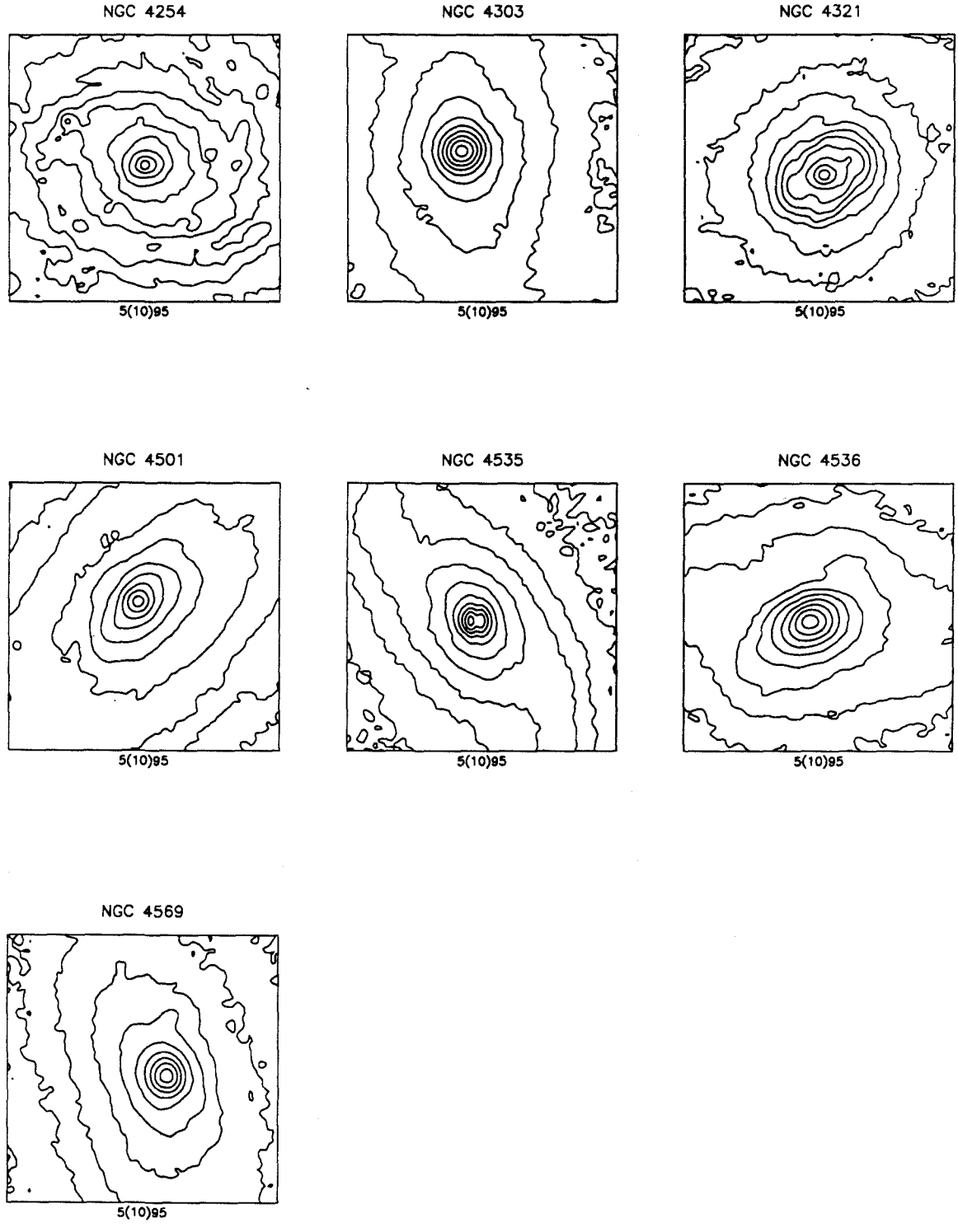


Figure 4–6. Mosaic of Thuan-Gunn $i$-band images of the central regions of Virgo spiral galaxies. Each frame is $64''$ on a side, or 4.87 kpc. North is up and east is to the left. The lowest and highest contours and the contour spacing as a percentage of the peak is listed in the legend of each frame.

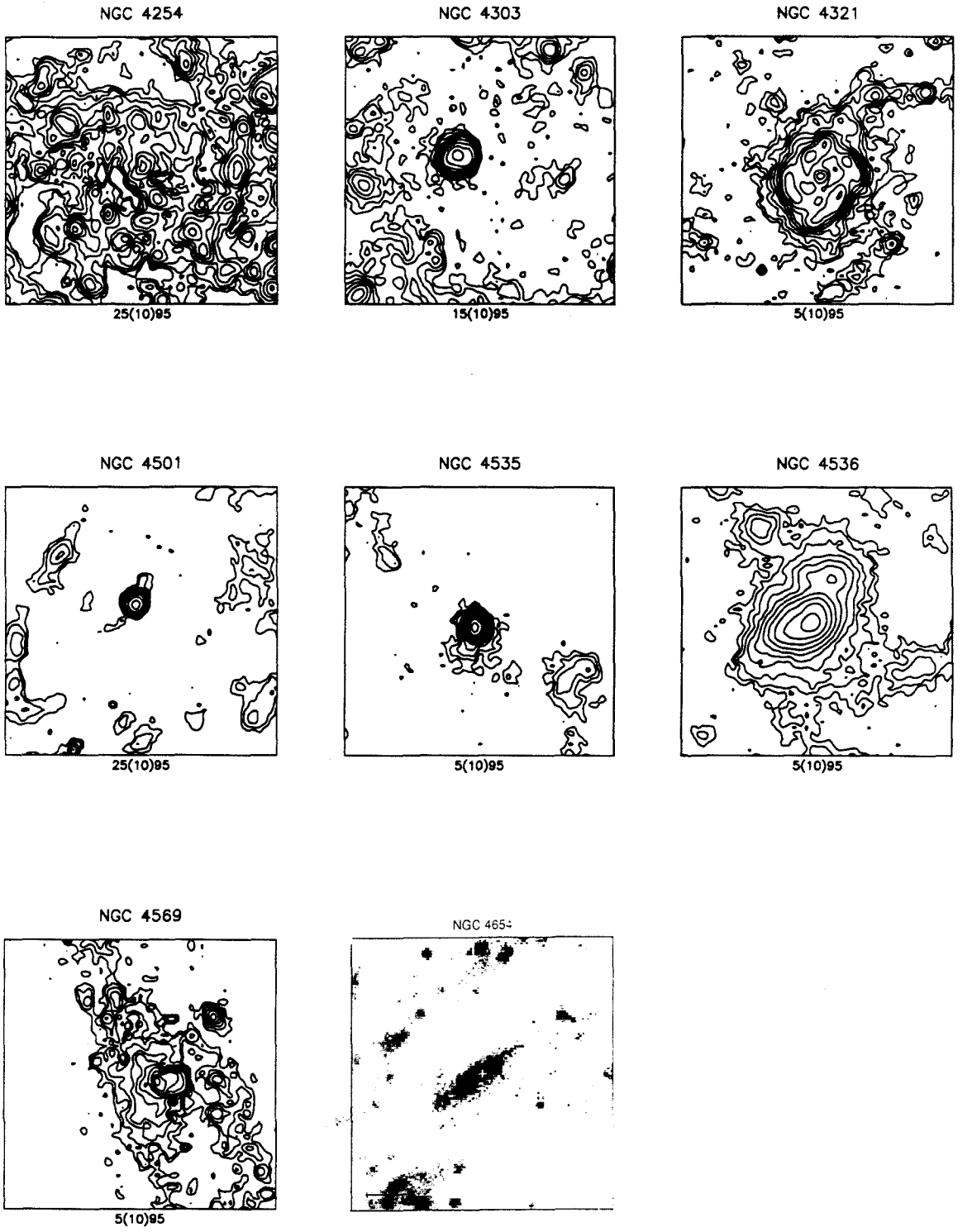


Figure 4–7. Mosaic of H$\alpha$ images of the central regions of Virgo spiral galaxies. Each frame is $64'$ on a side, or 4.87 kpc. North is up and east is to the left. The lowest and highest contours and the contour spacing as a percentage of the peak is listed in the legend of each frame. The image of NGC 4654 is from Pogge (1989).

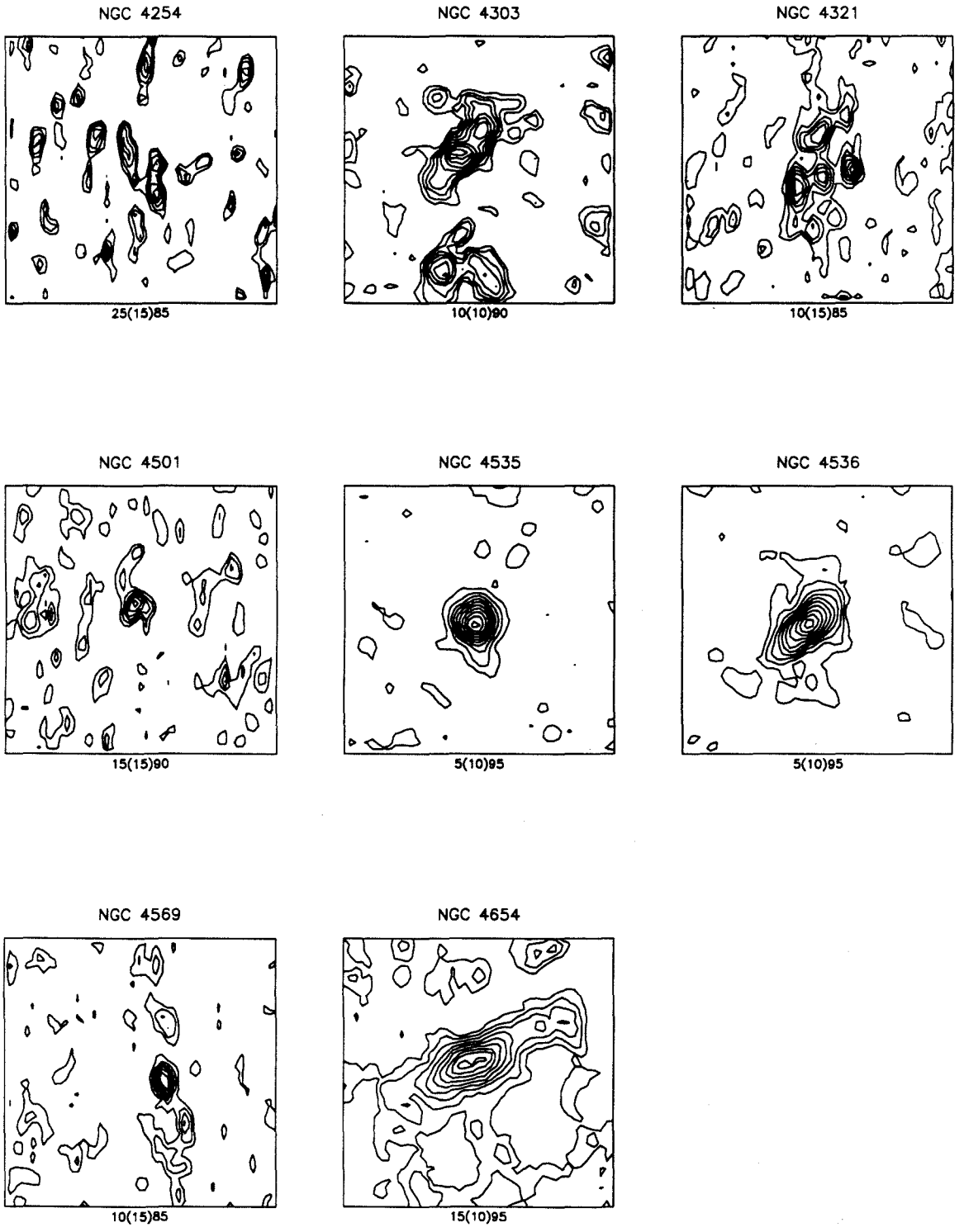


Figure 4–8. Mosaic of CO emission images of the central regions of Virgo spiral galaxies. Each frame is 64″ on a side, or 4.87 kpc, and encompasses the primary beam. North is up and east is to the left. The lowest and highest contours and the contour spacing as a percentage of the peak is listed in the legend of each frame.

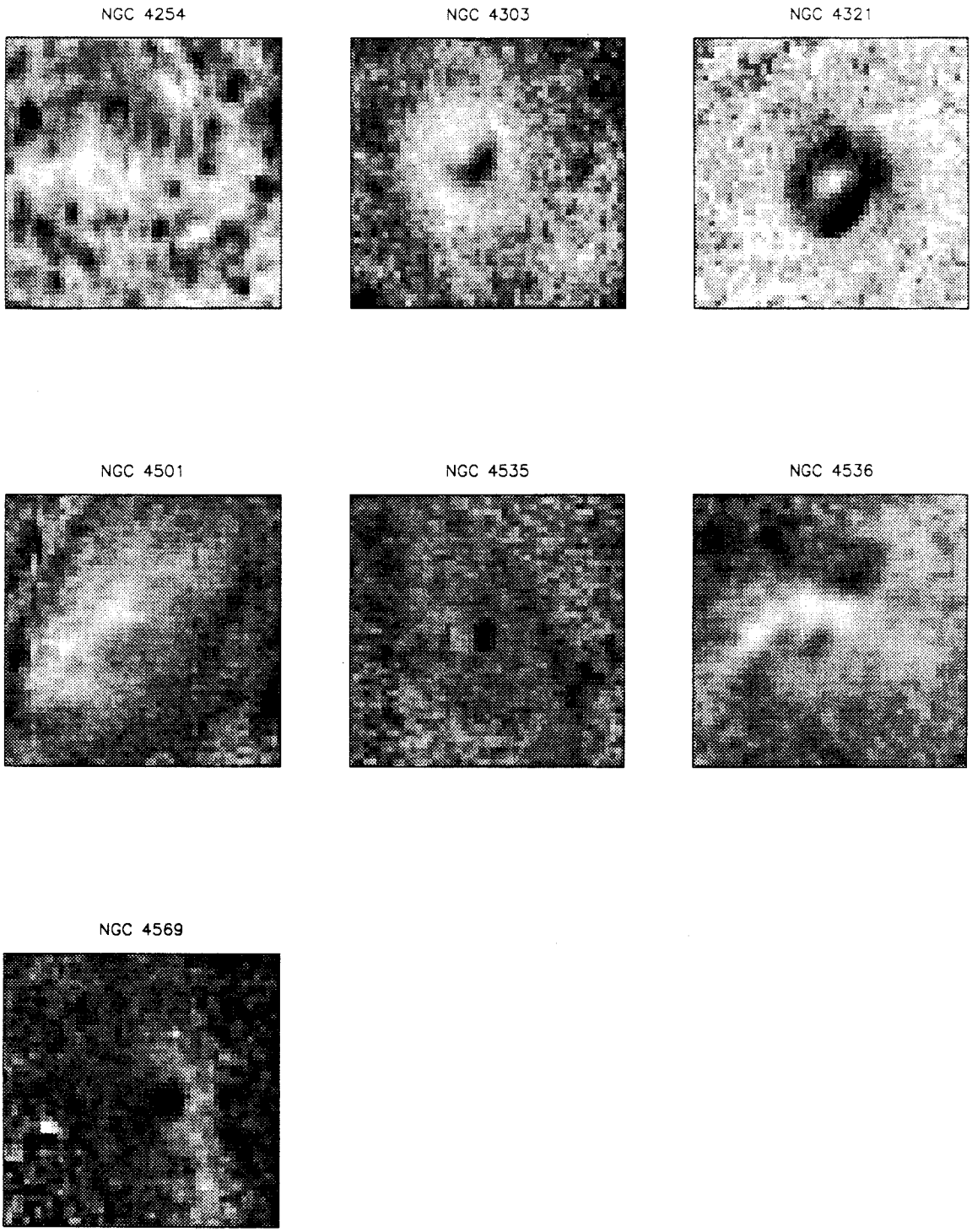


Figure 4–9. Mosaic of $B - V$ color maps of the central regions of Virgo spiral galaxies. Each frame is $64''$ on a side, or 4.87 kpc. North is up and east is to the left. Redder $B - V$ color is shown as lighter shades; bluer $B - V$ color is represented by darker shades.

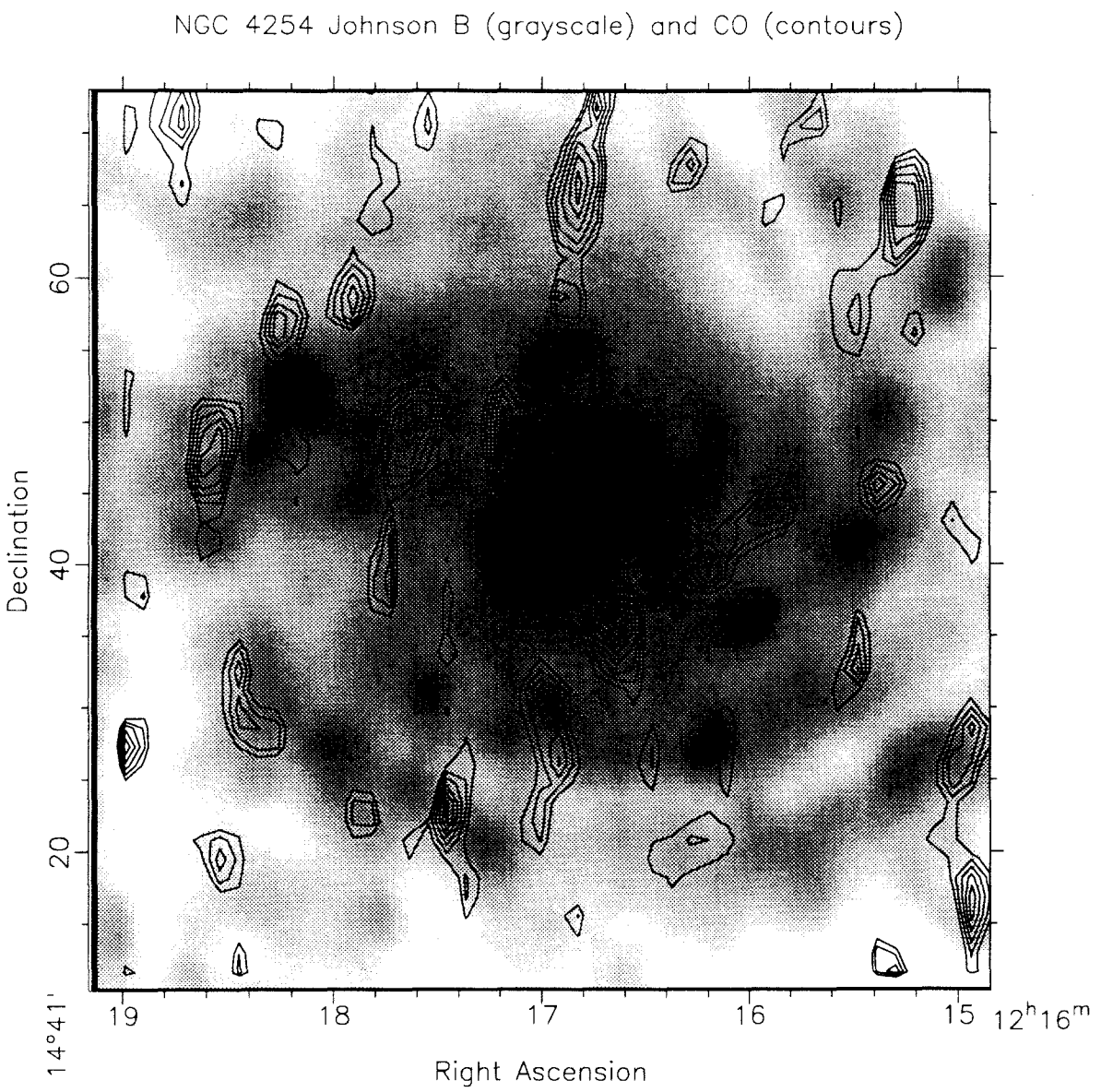


Figure 4–10. NGC 4254. Johnson $B$ (grayscale) and CO (contours).

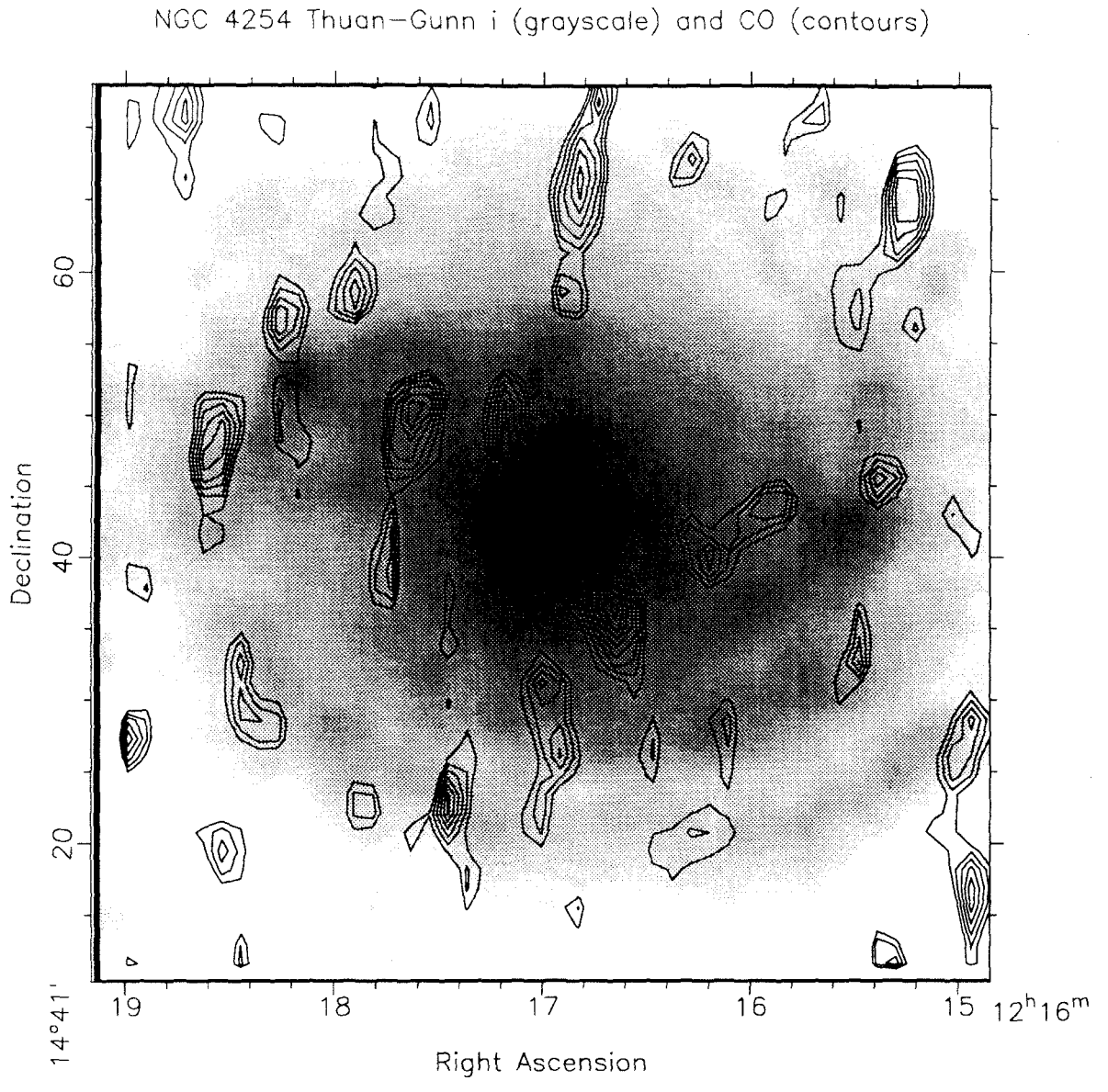


Figure 4–11. NGC 4254. Thuan-Gunn *i* (grayscale) and CO (contours).

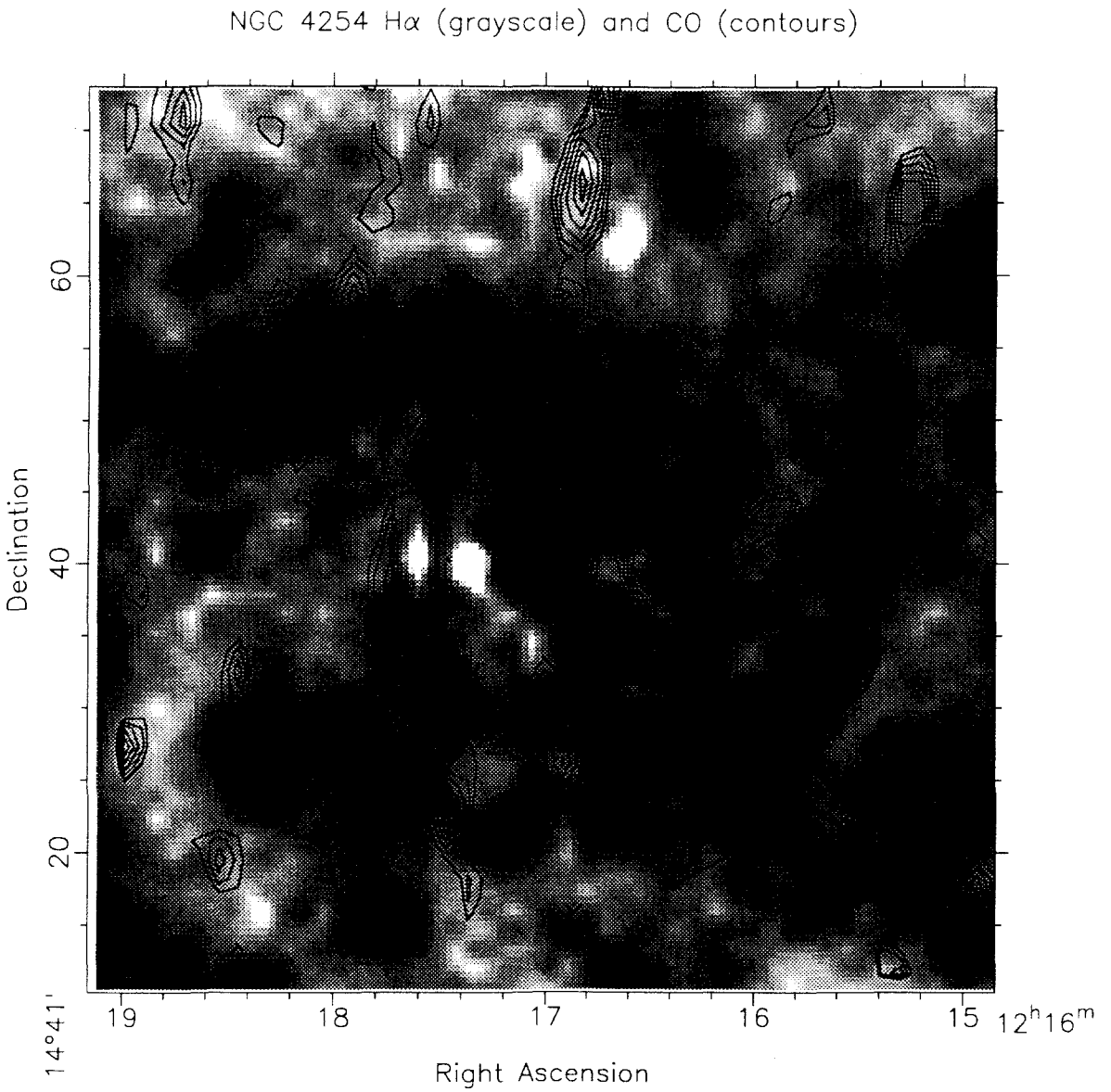


Figure 4–12. NGC 4254. Hα emission (grayscale) and CO (contours).

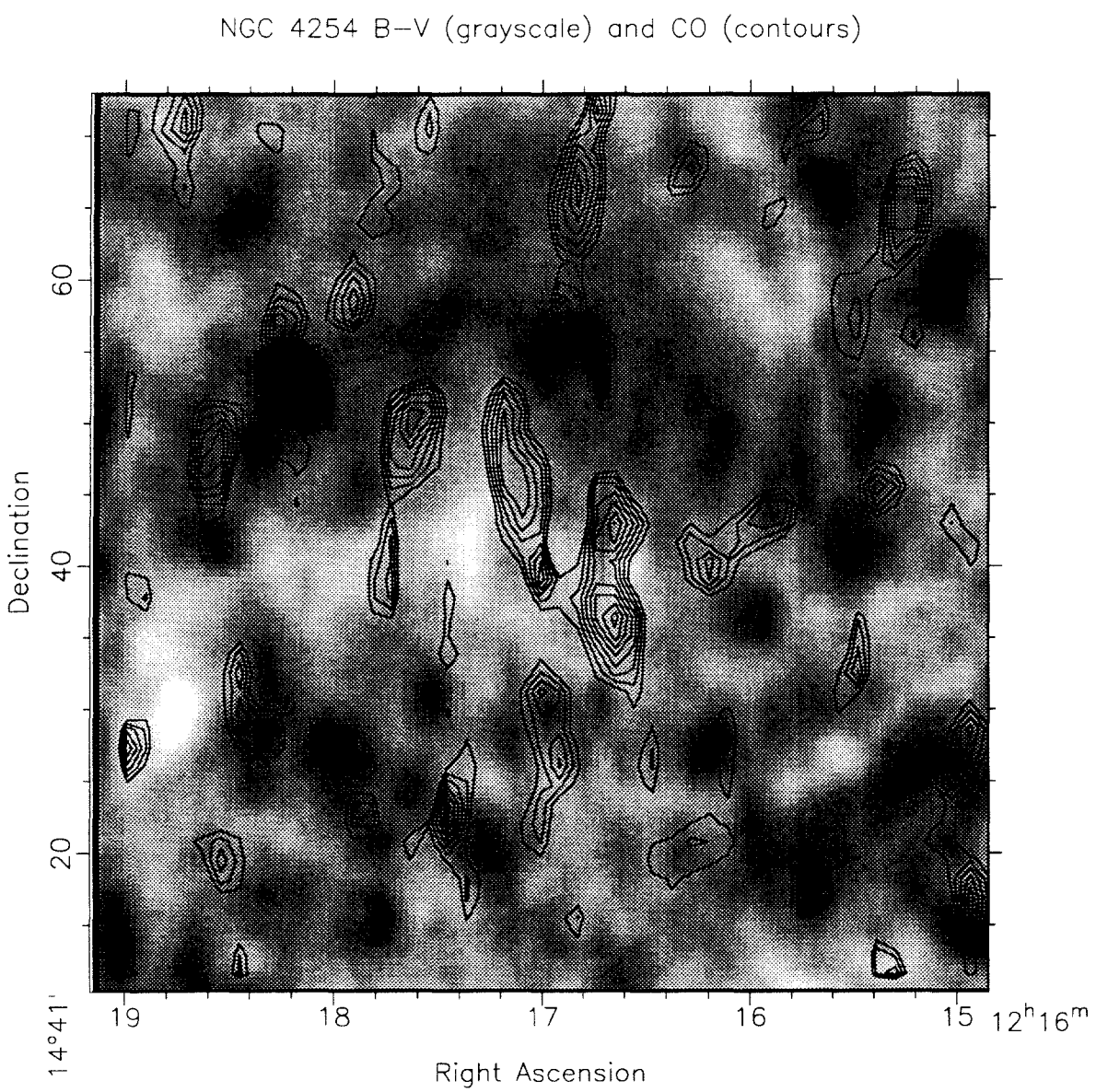


Figure 4–13. NGC 4254. $B - V$ color (grayscale) and CO (contours). Redder $B - V$ is lighter shades; bluer is darker shades.

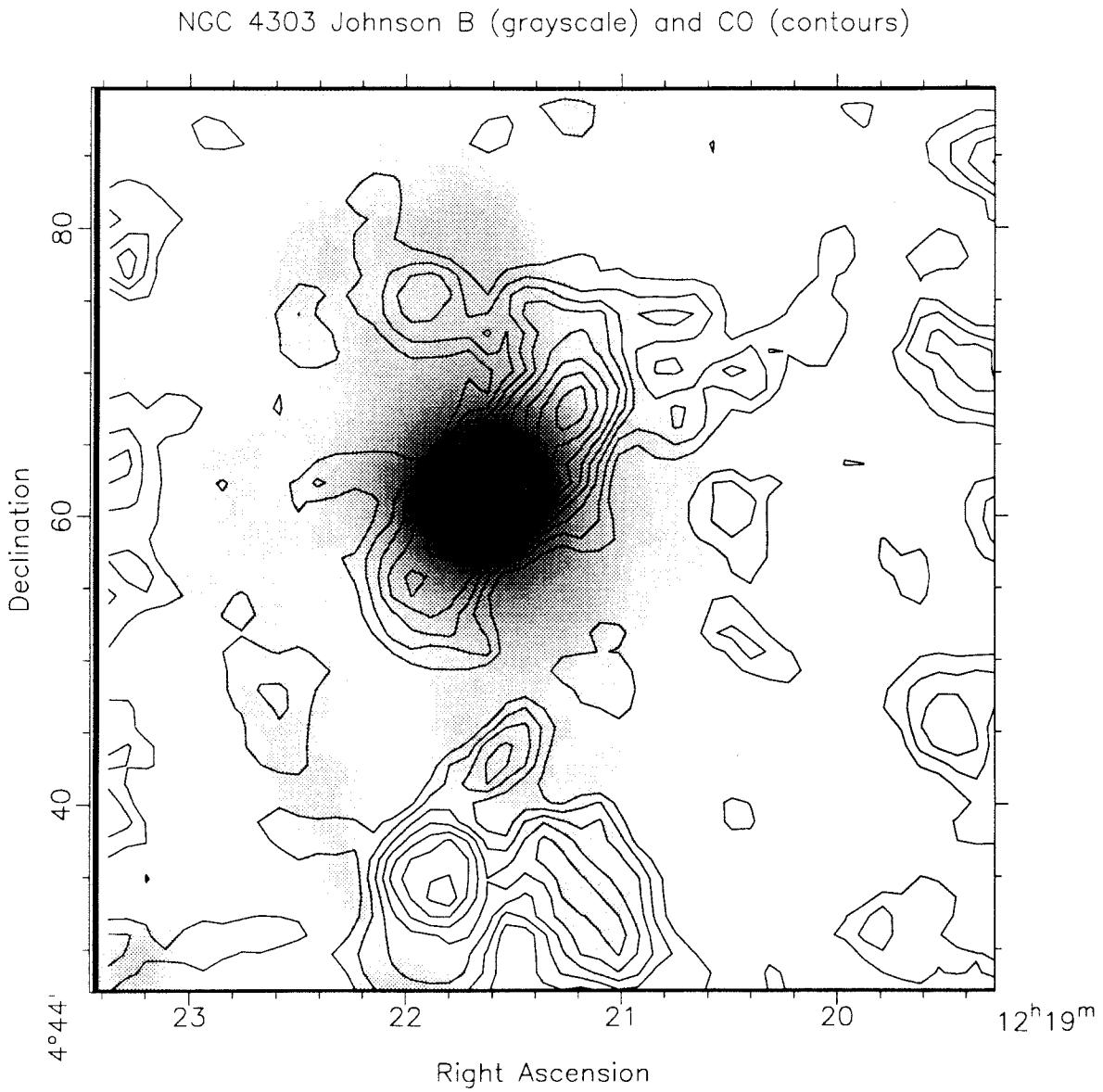


Figure 4–14. NGC 4303. Johnson $B$ (grayscale) and CO (contours).

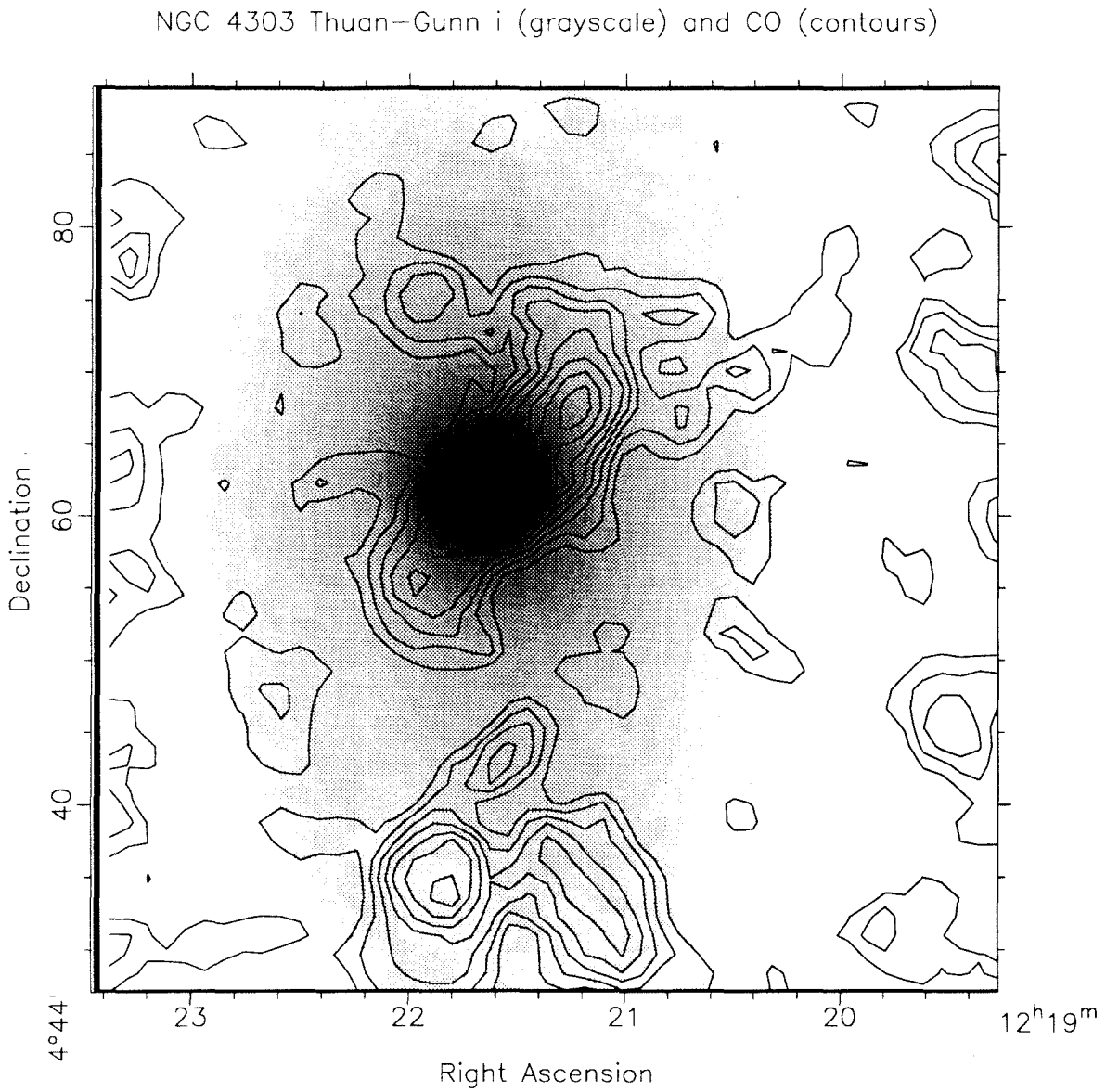


Figure 4–15. NGC 4303. Thuan-Gunn $i$ (grayscale) and CO (contours).

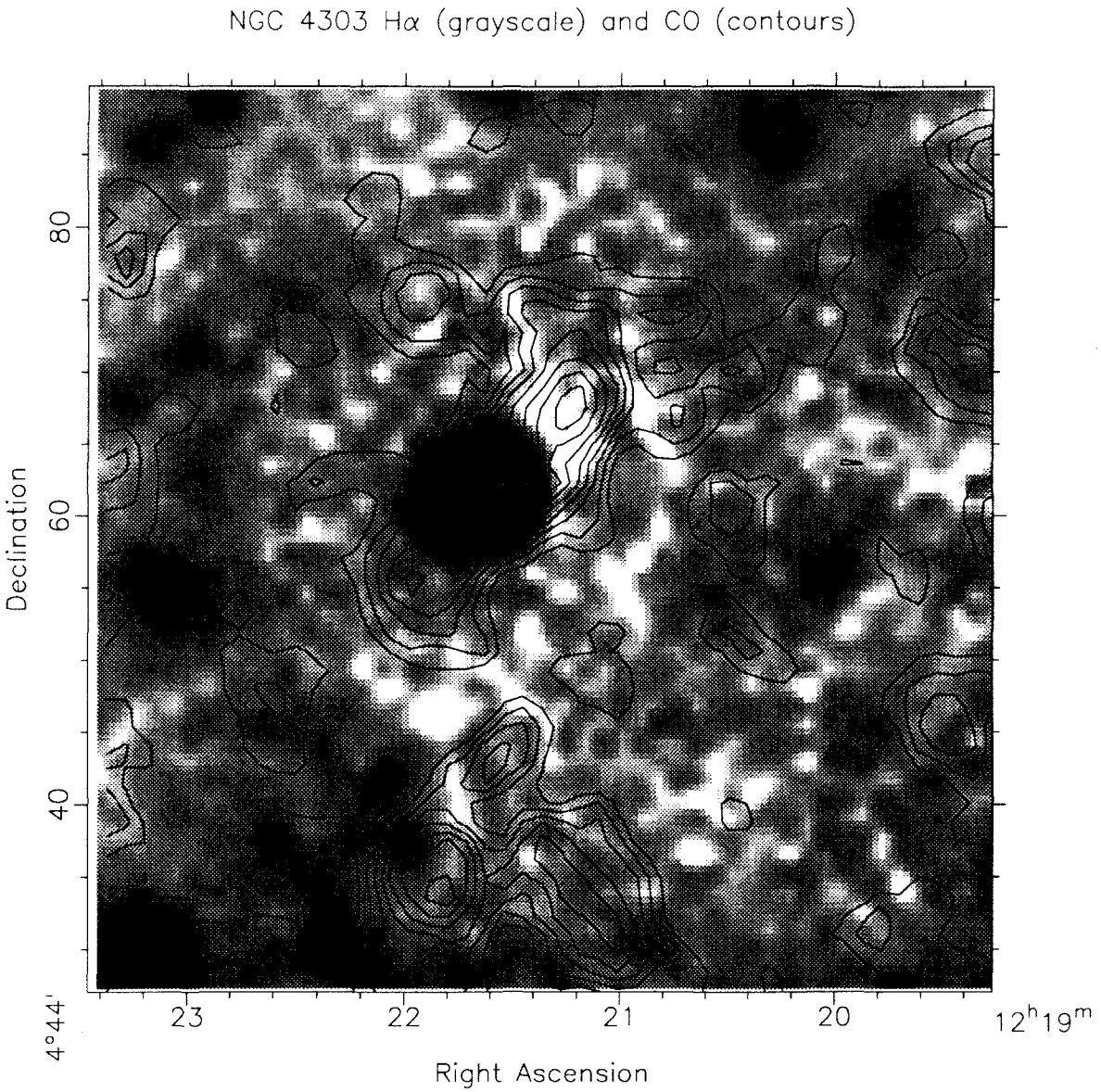


Figure 4–16. NGC 4303. Hα emission (grayscale) and CO (contours).

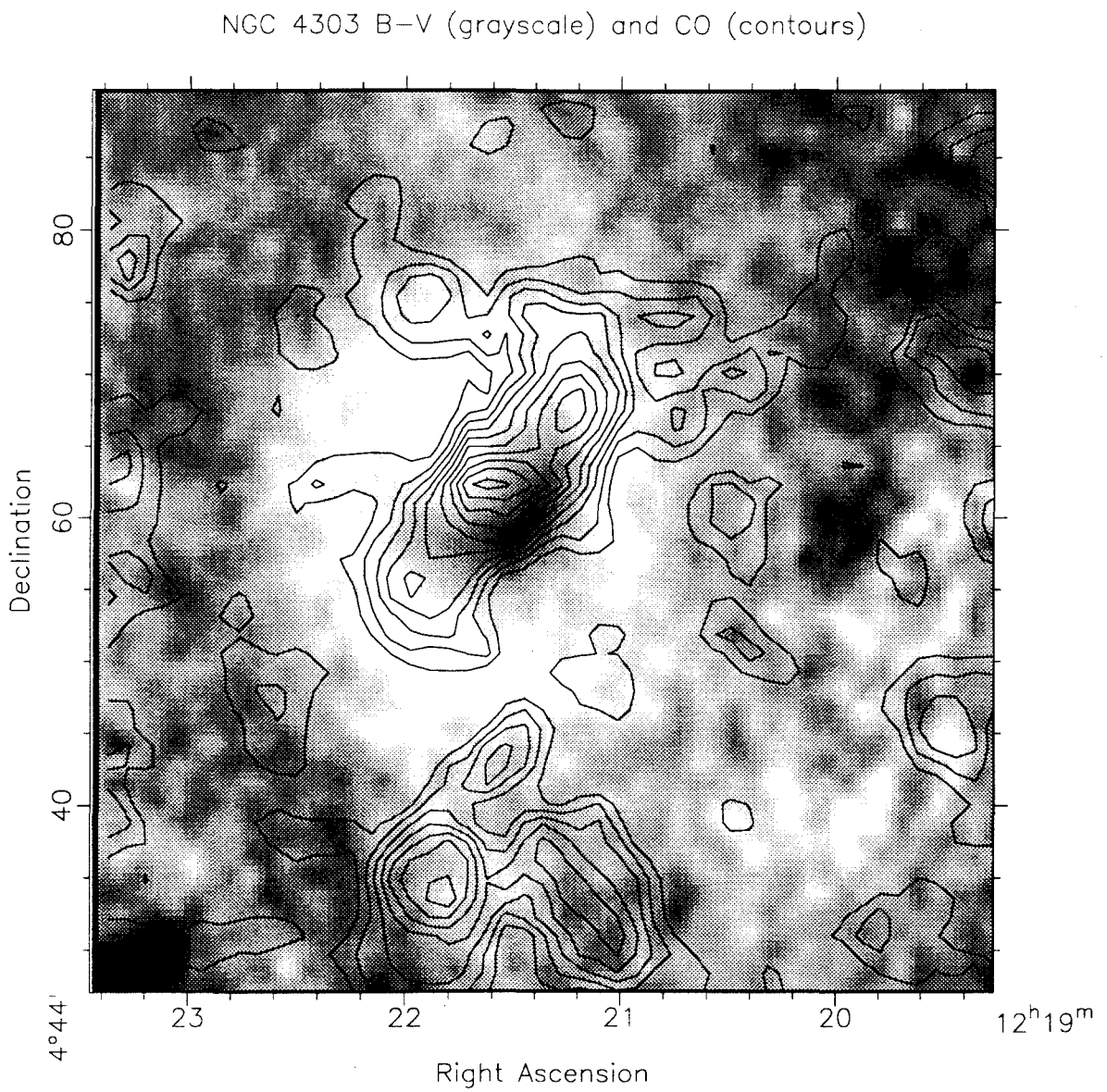


Figure 4–17. NGC 4303. $B - V$ color (grayscale) and CO (contours). Redder $B - V$ is lighter shades; bluer is darker shades.

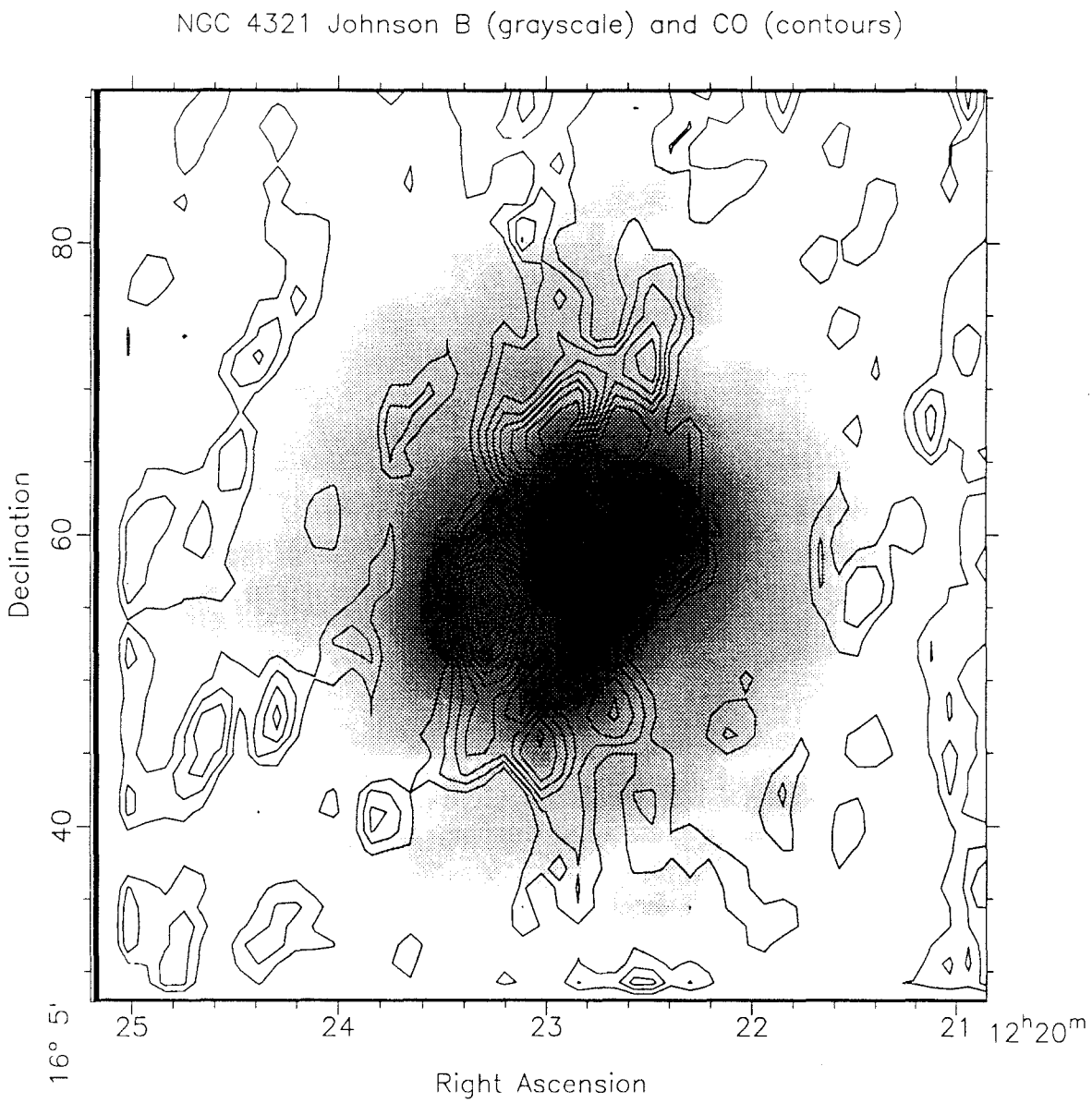


Figure 4–18. NGC 4321. Johnson $B$ (grayscale) and CO (contours).

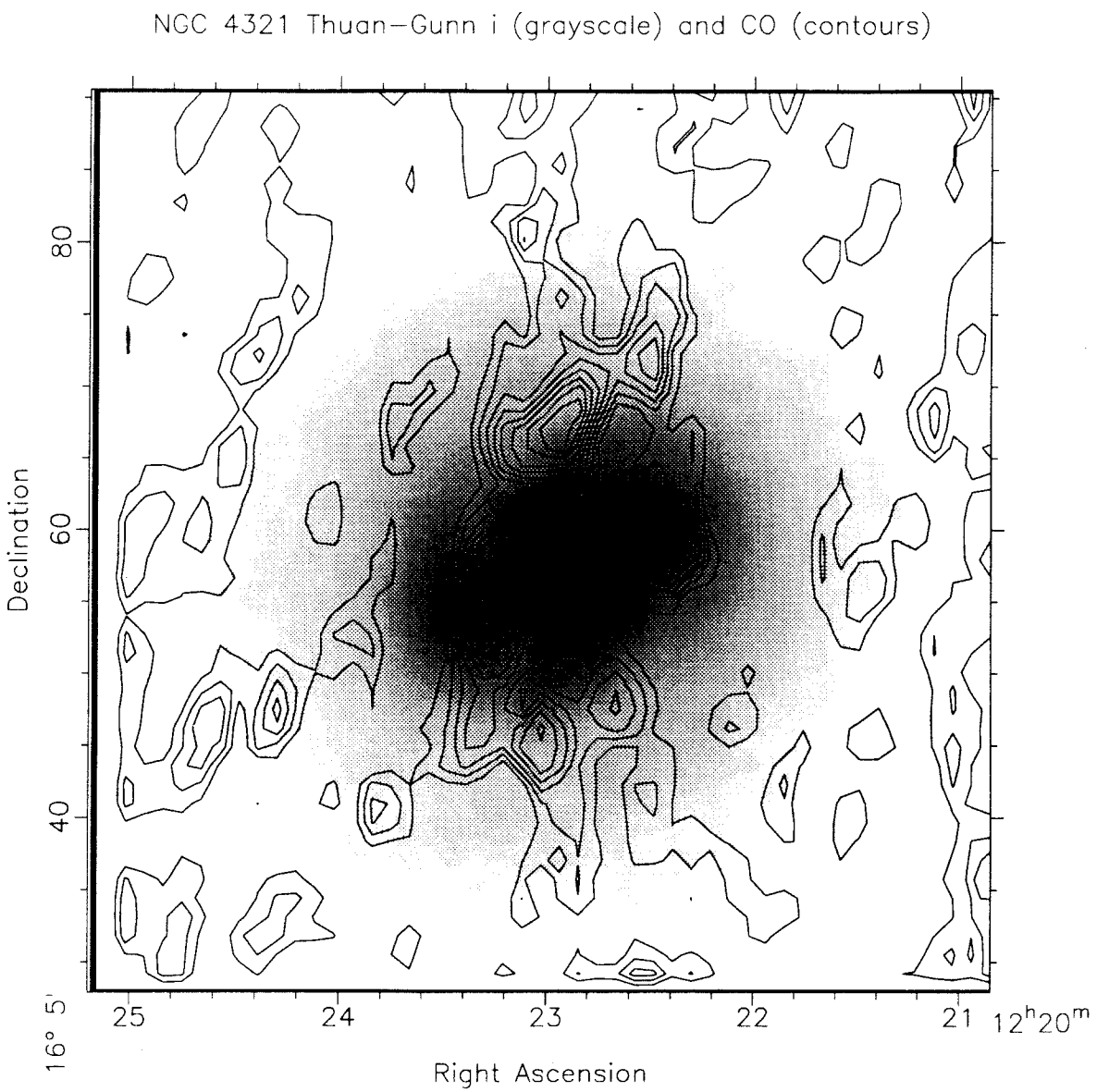


Figure 4–19. NGC 4321. Thuan-Gunn $i$ (grayscale) and CO (contours).

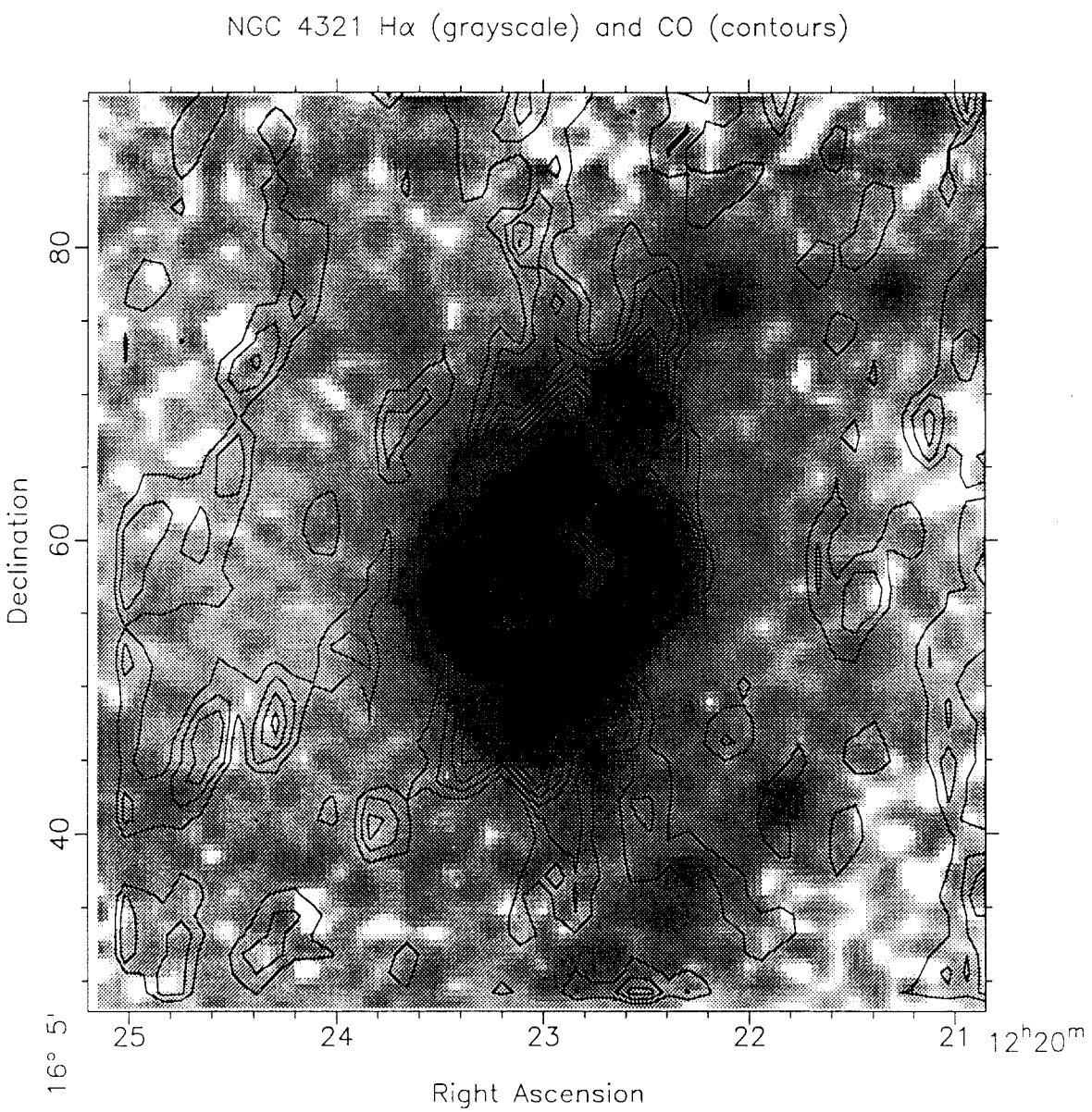


Figure 4–20. NGC 4321. Hα emission (grayscale) and CO (contours).

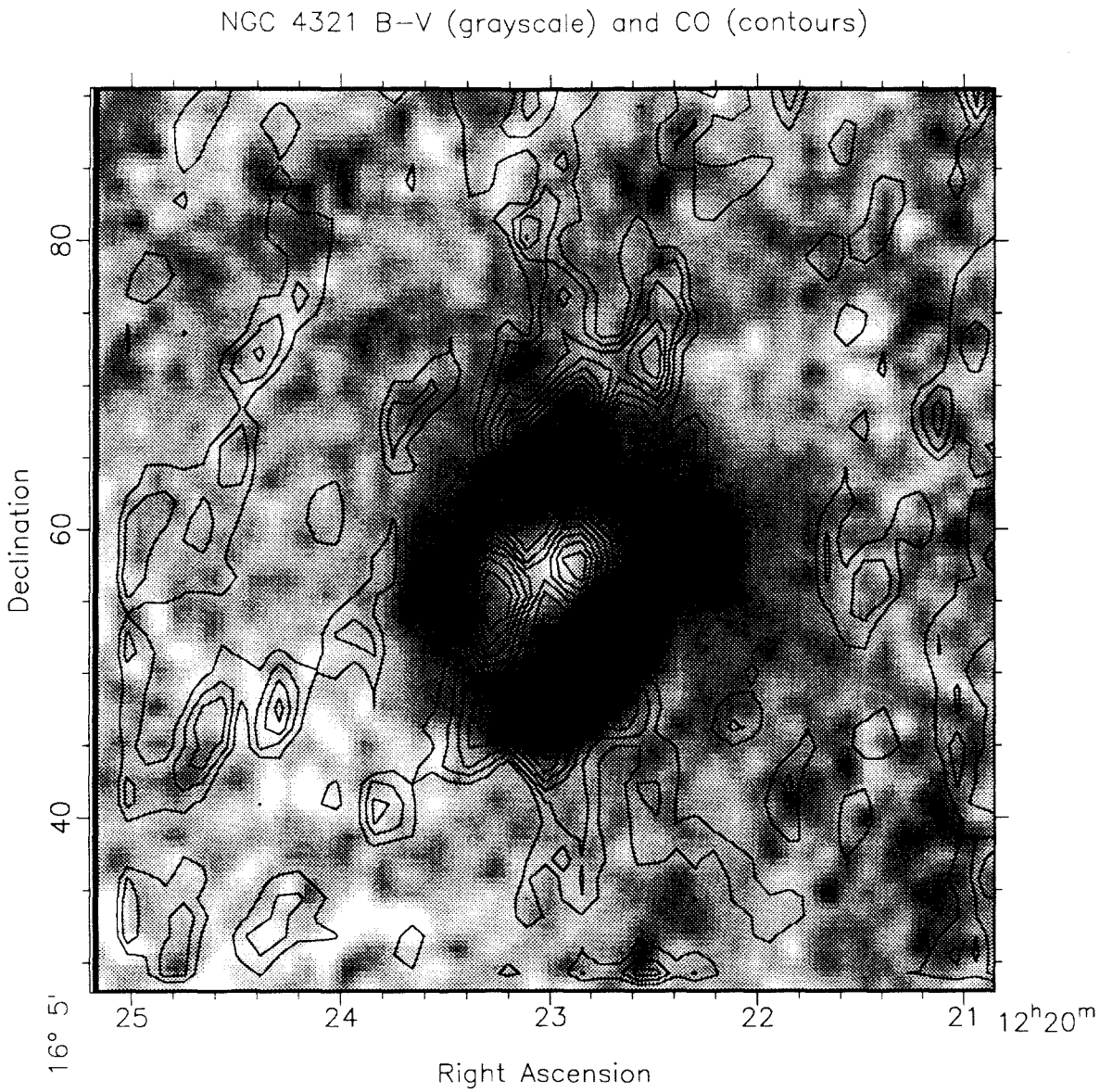


Figure 4–21. NGC 4321. $B - V$ color (grayscale) and CO (contours). Redder $B - V$ is lighter shades; bluer is darker shades.

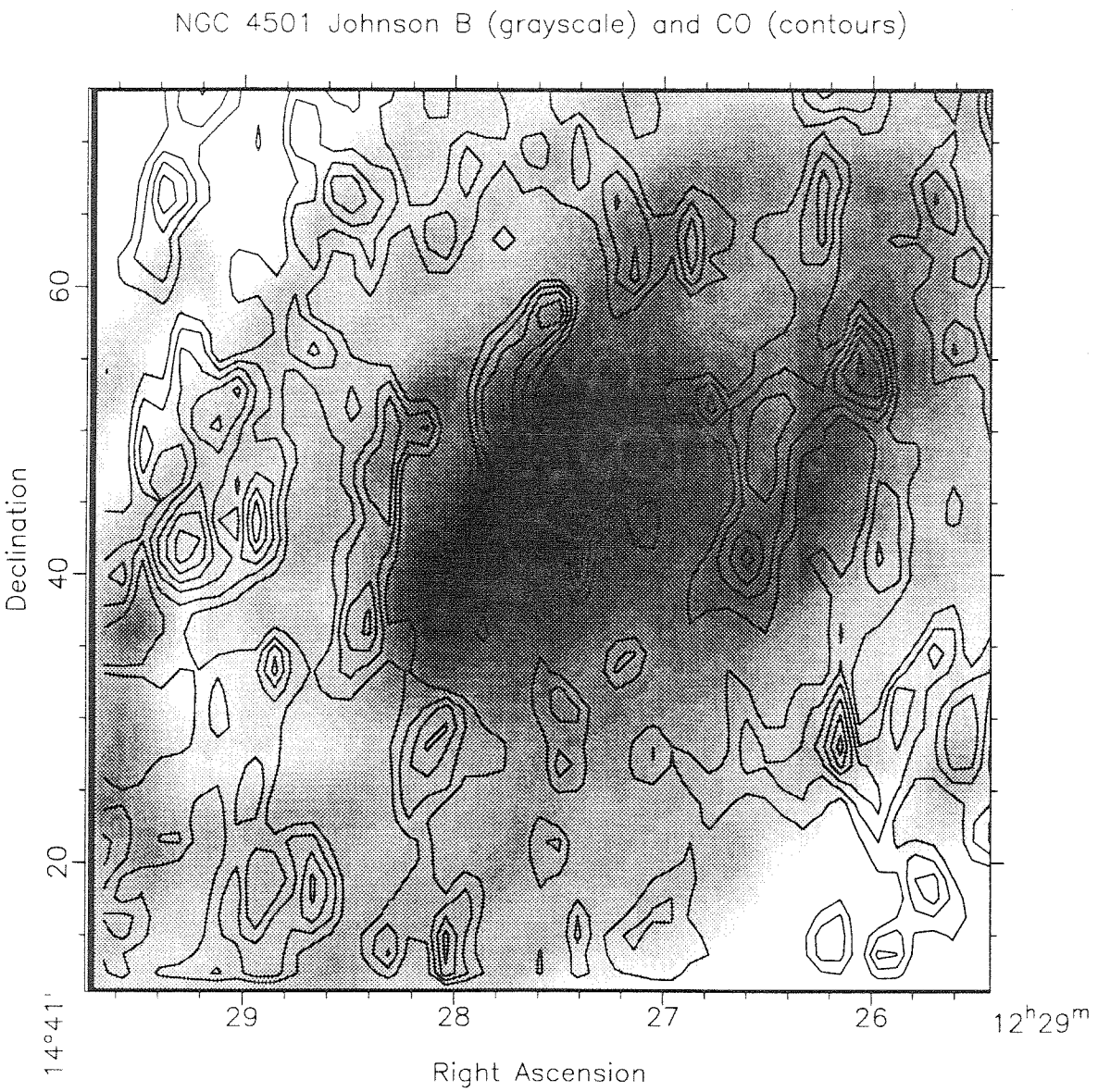


Figure 4–22. NGC 4501. Johnson $B$ (grayscale) and CO (contours).

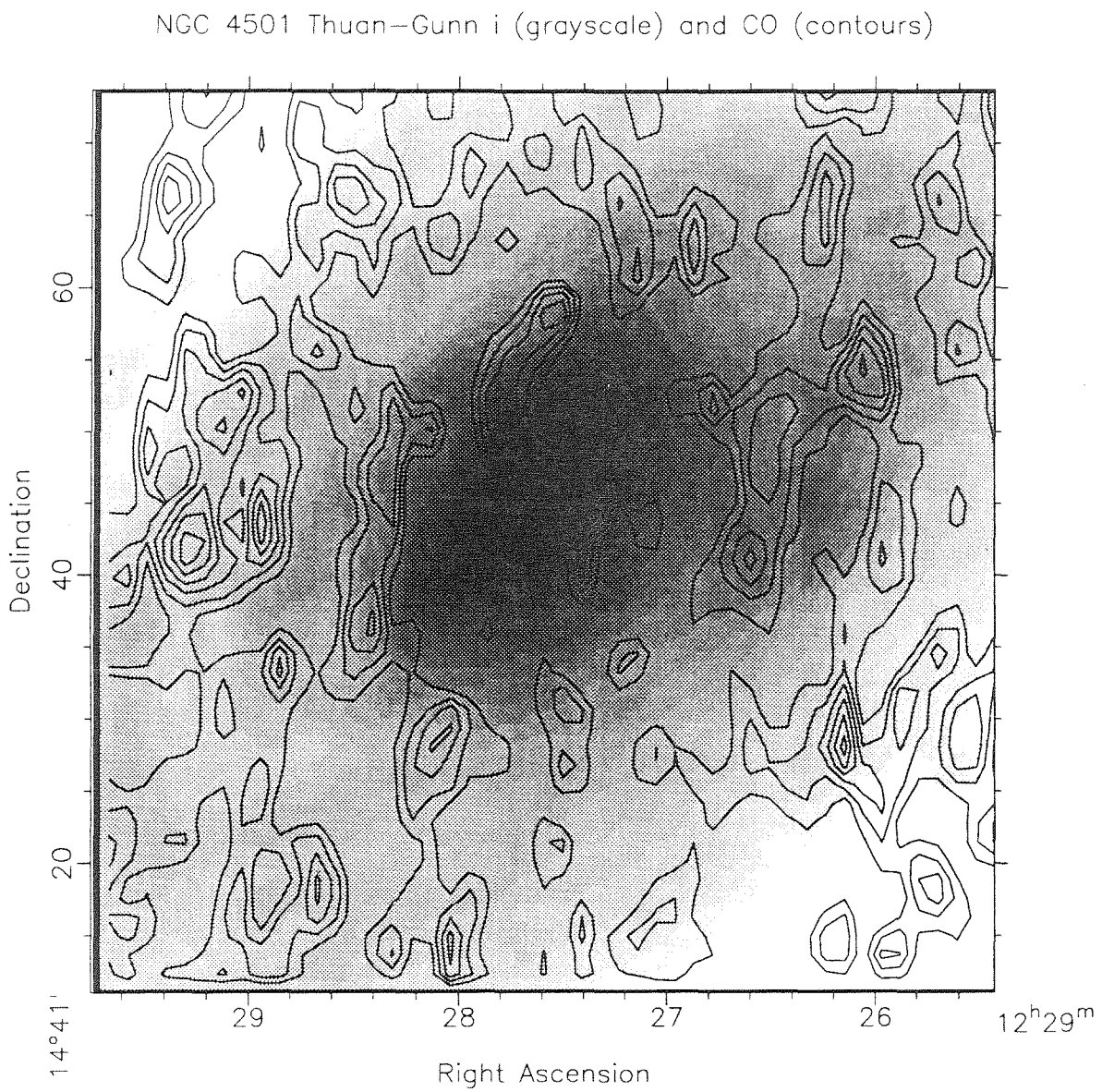


Figure 4–23. NGC 4501. Thuan-Gunn $i$ (grayscale) and CO (contours).

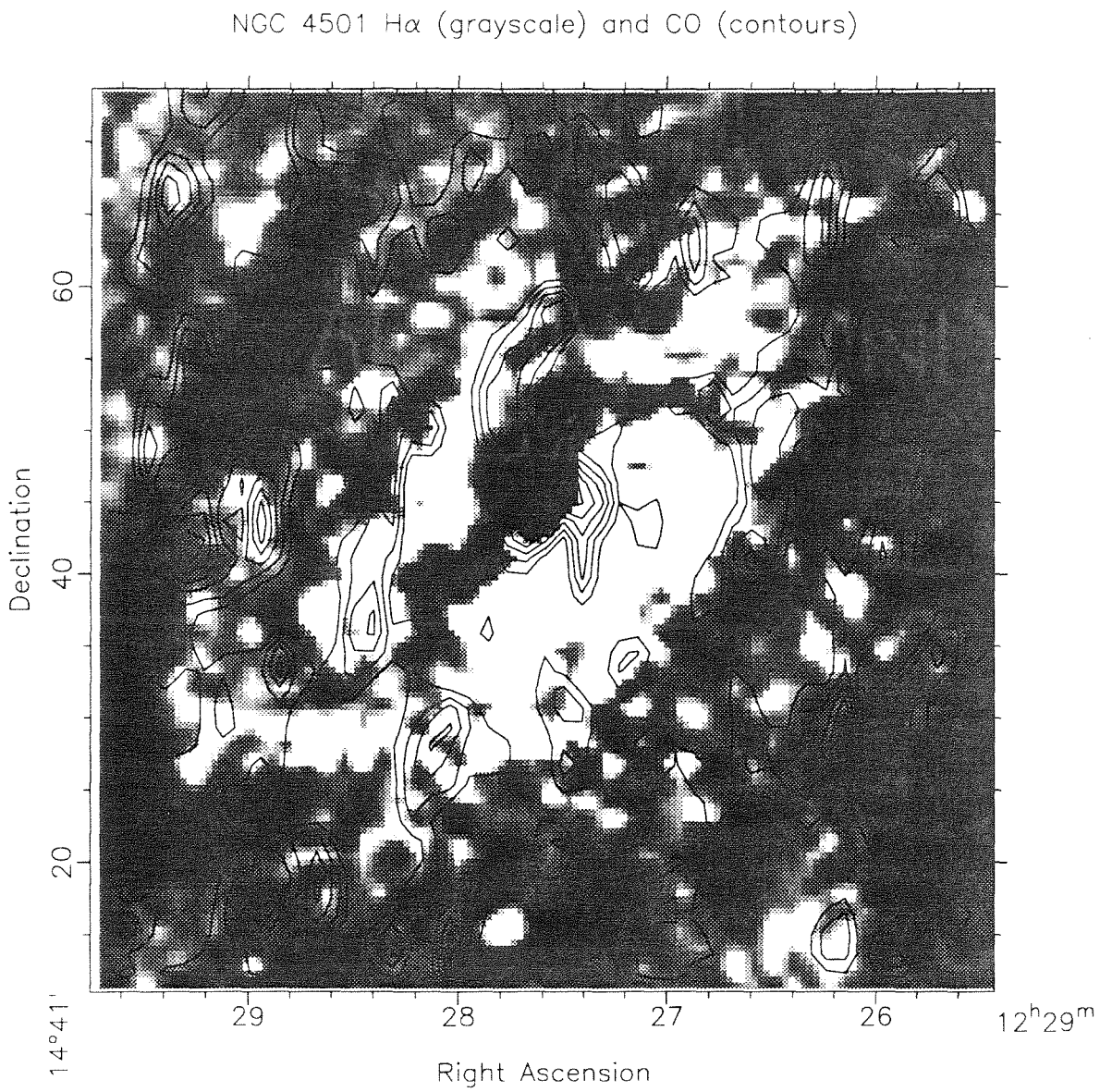


Figure 4–24. NGC 4501. H$\alpha$ emission (grayscale) and CO (contours).

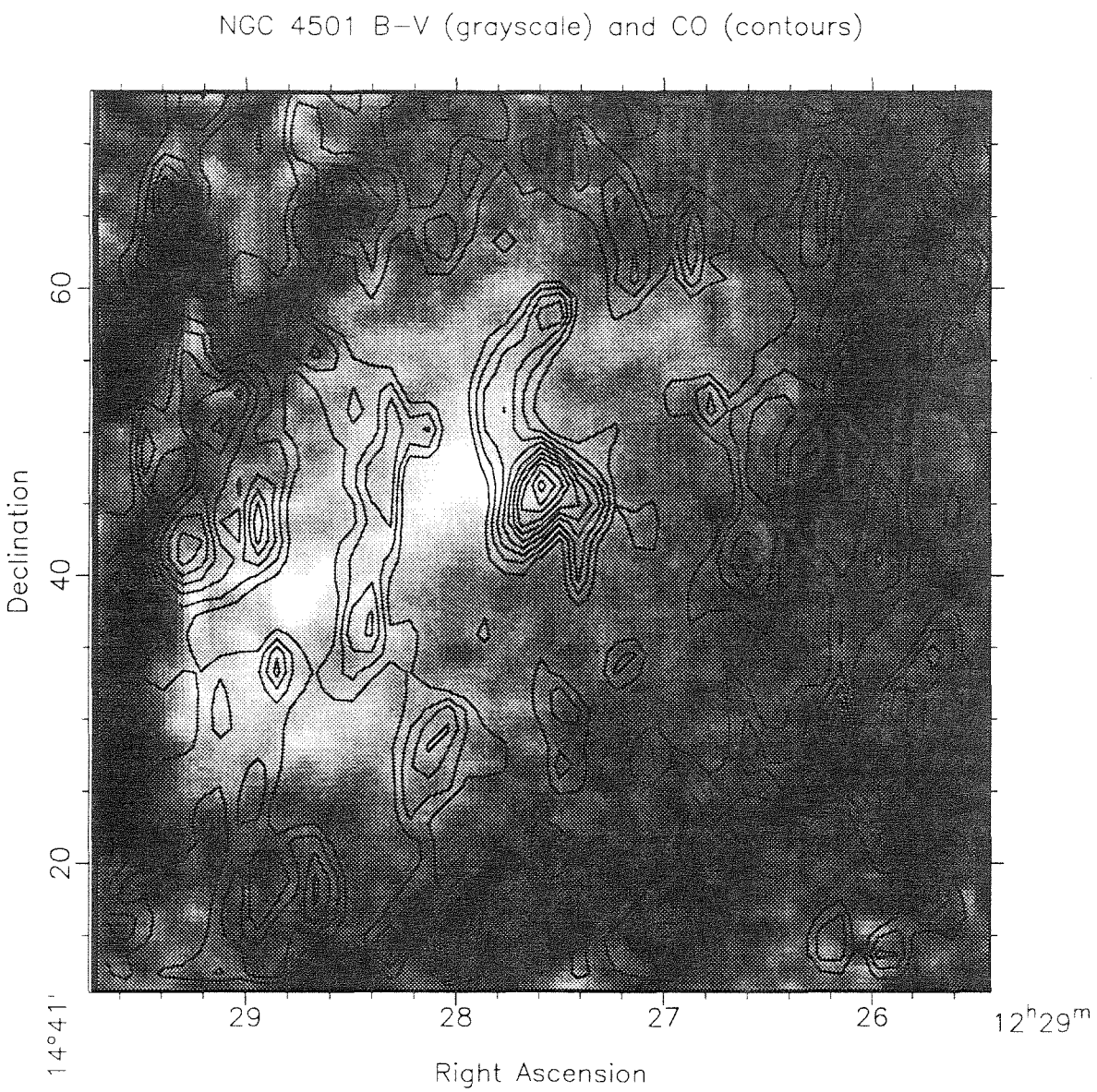


Figure 4–25. NGC 4501. $B - V$ color (grayscale) and CO (contours). Redder $B - V$ is lighter shades; bluer is darker shades.

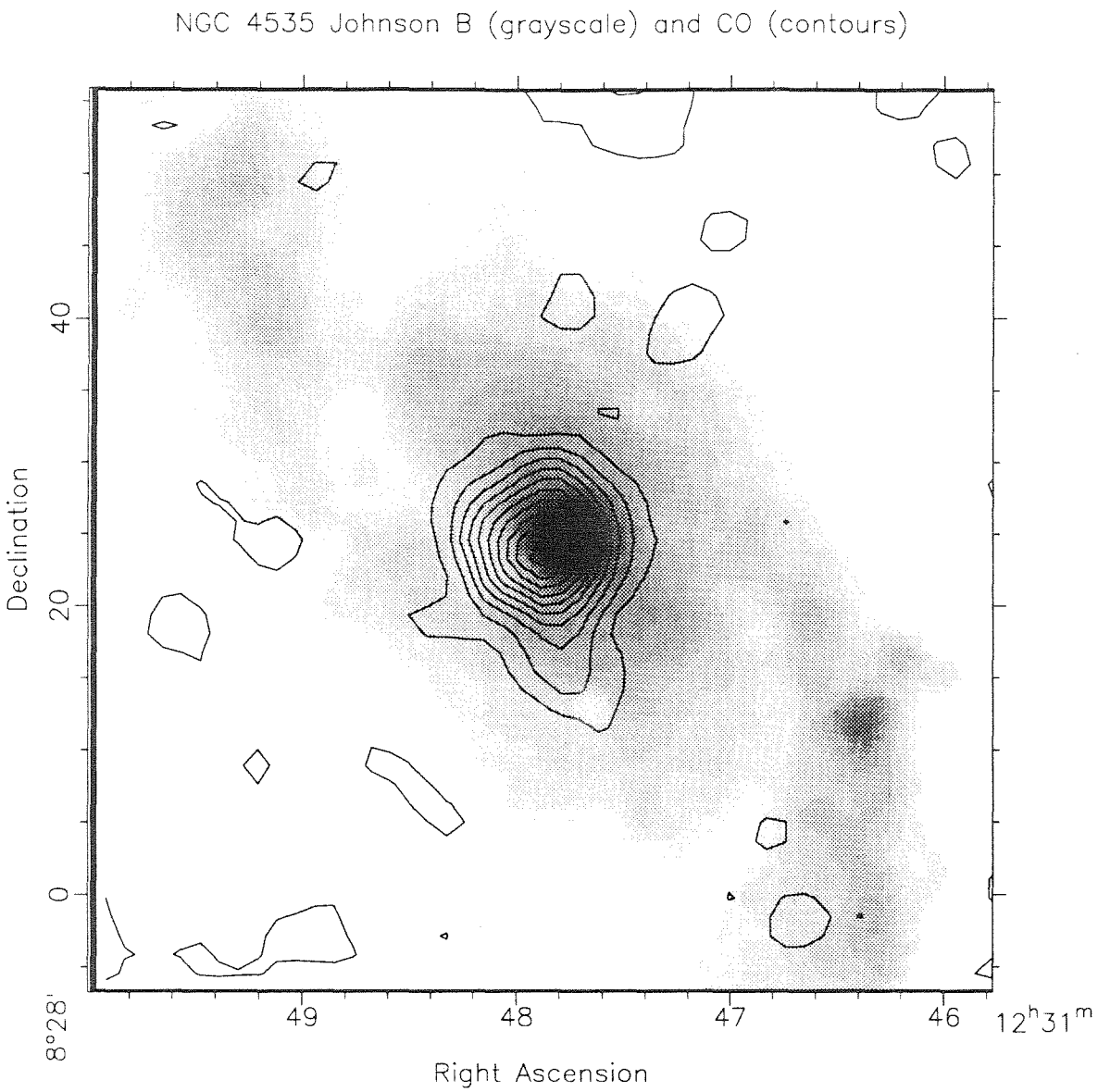


Figure 4–26. NGC 4535. Johnson $B$ (grayscale) and CO (contours).

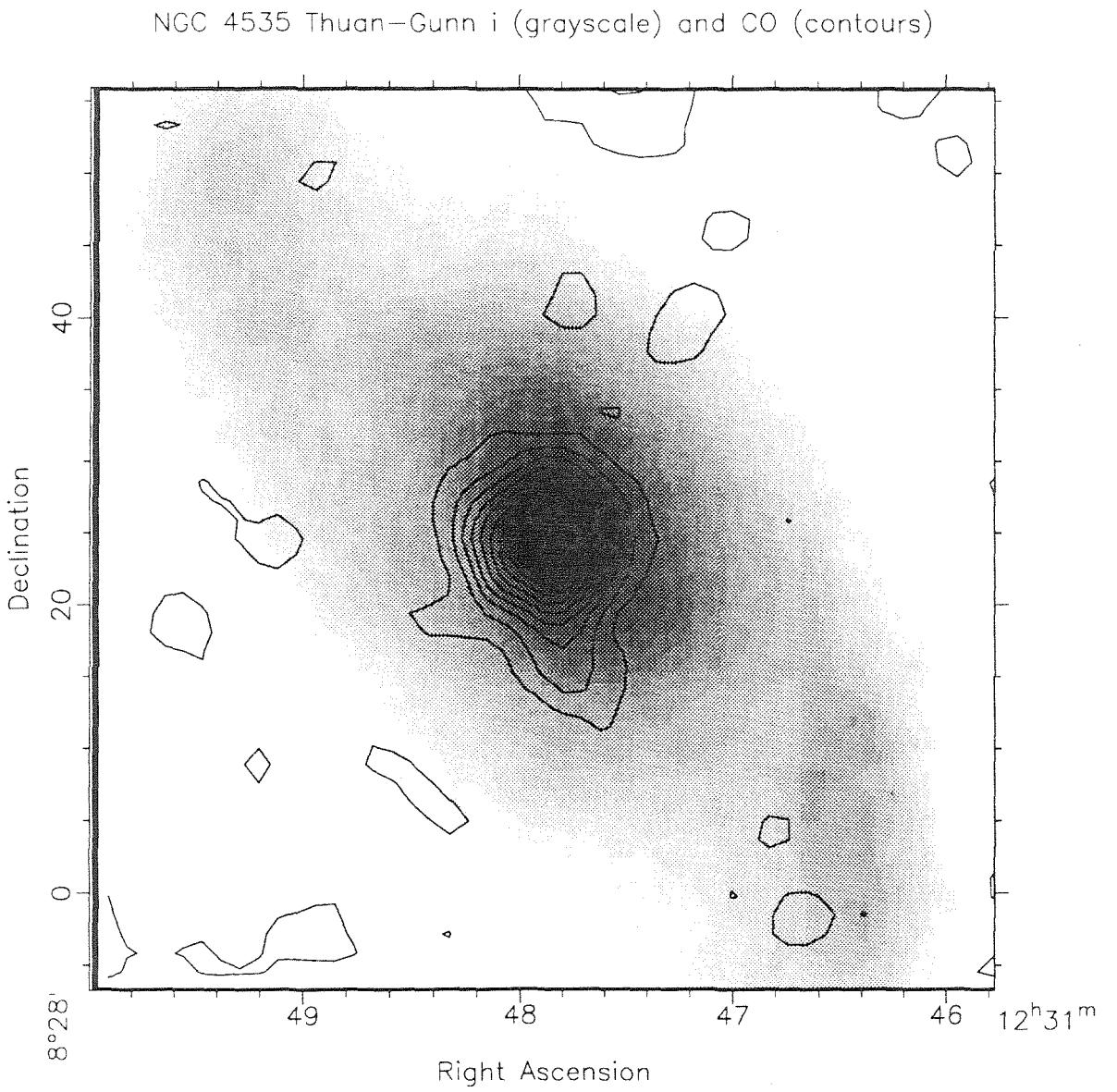


Figure 4–27. NGC 4535. Thuan-Gunn $i$ (grayscale) and CO (contours).

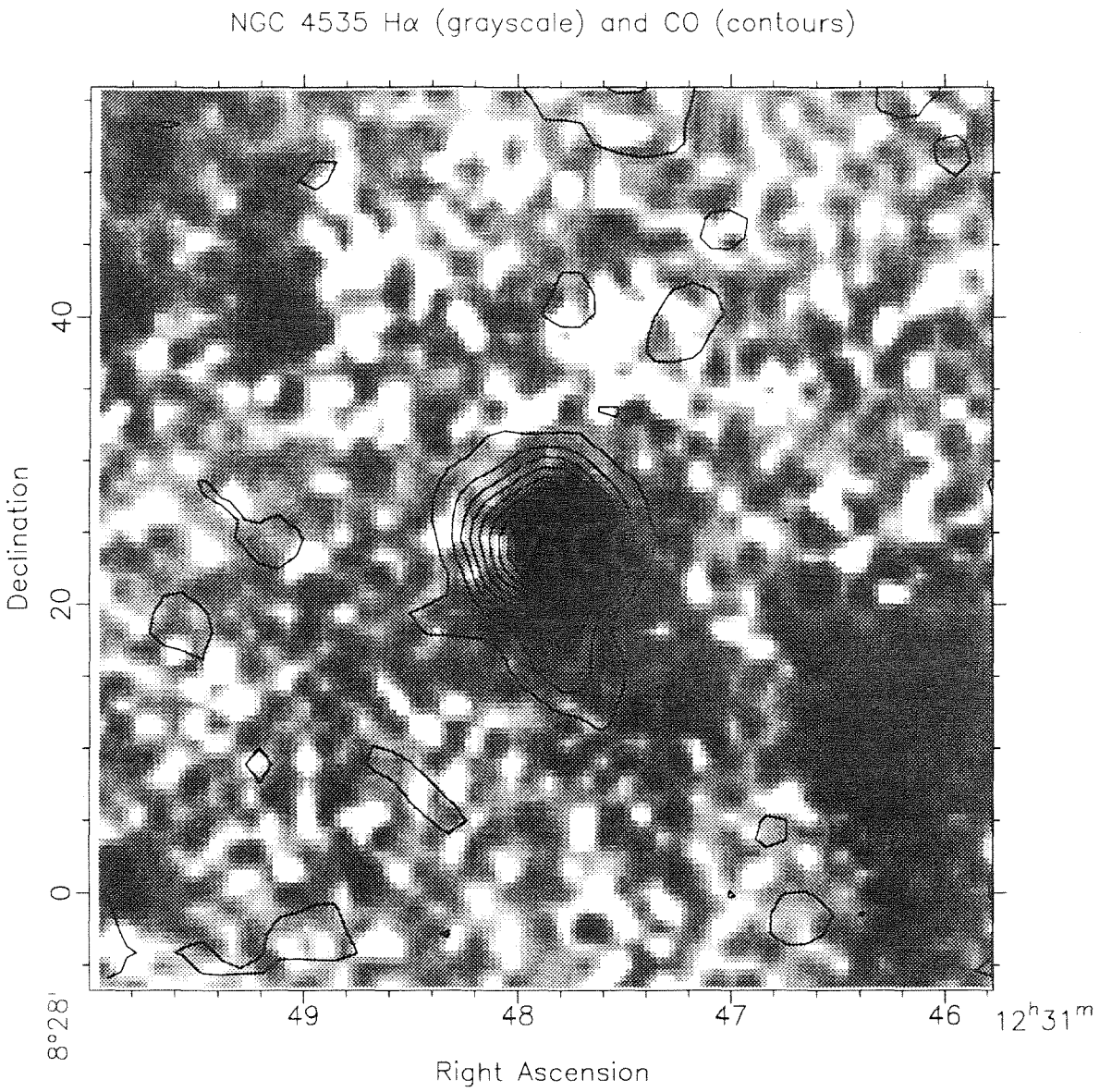


Figure 4–28. NGC 4535. H$\alpha$ emission (grayscale) and CO (contours).

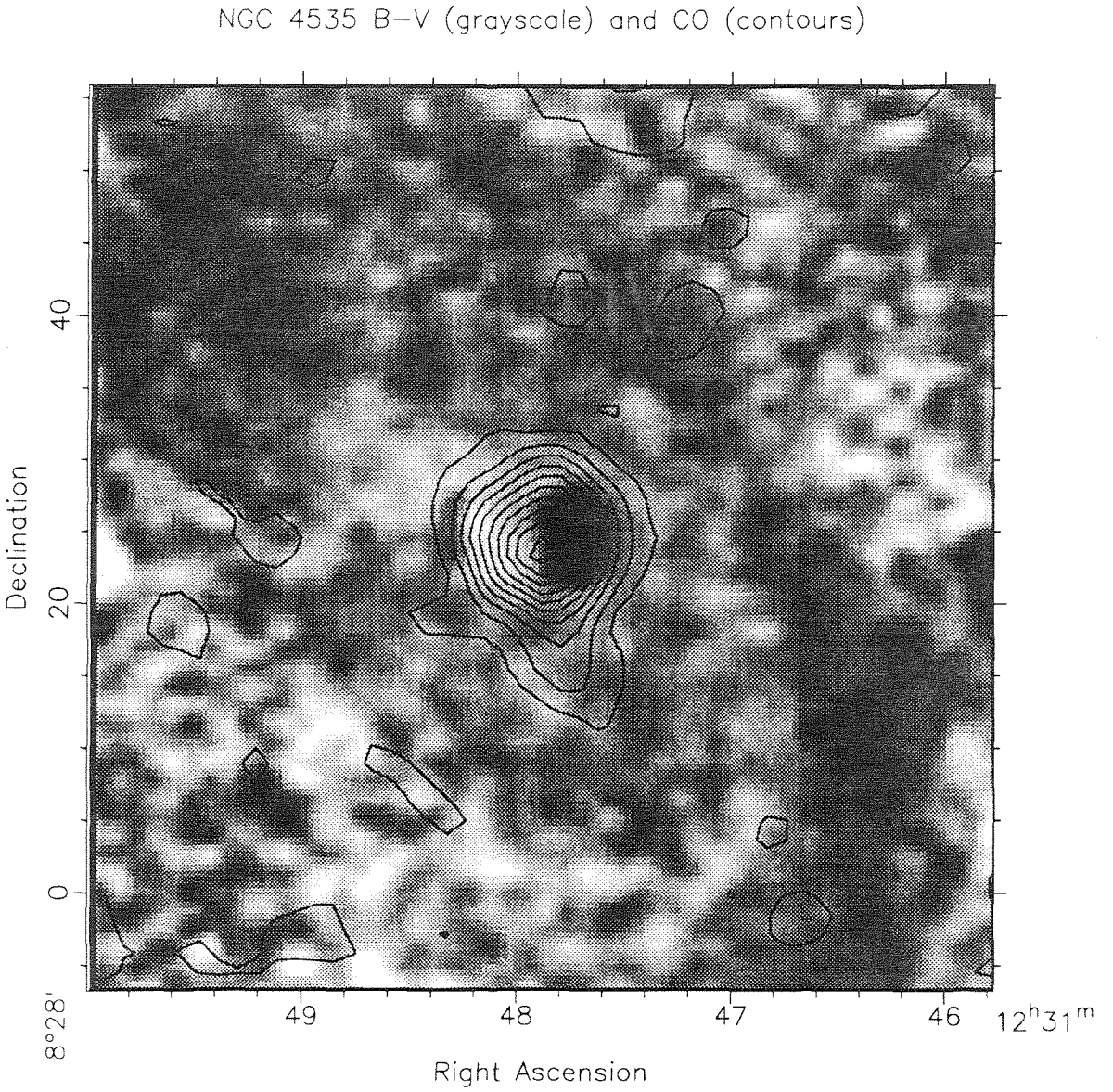


Figure 4–29. NGC 4535. $B - V$ color (grayscale) and CO (contours). Redder $B - V$ is lighter shades; bluer is darker shades.

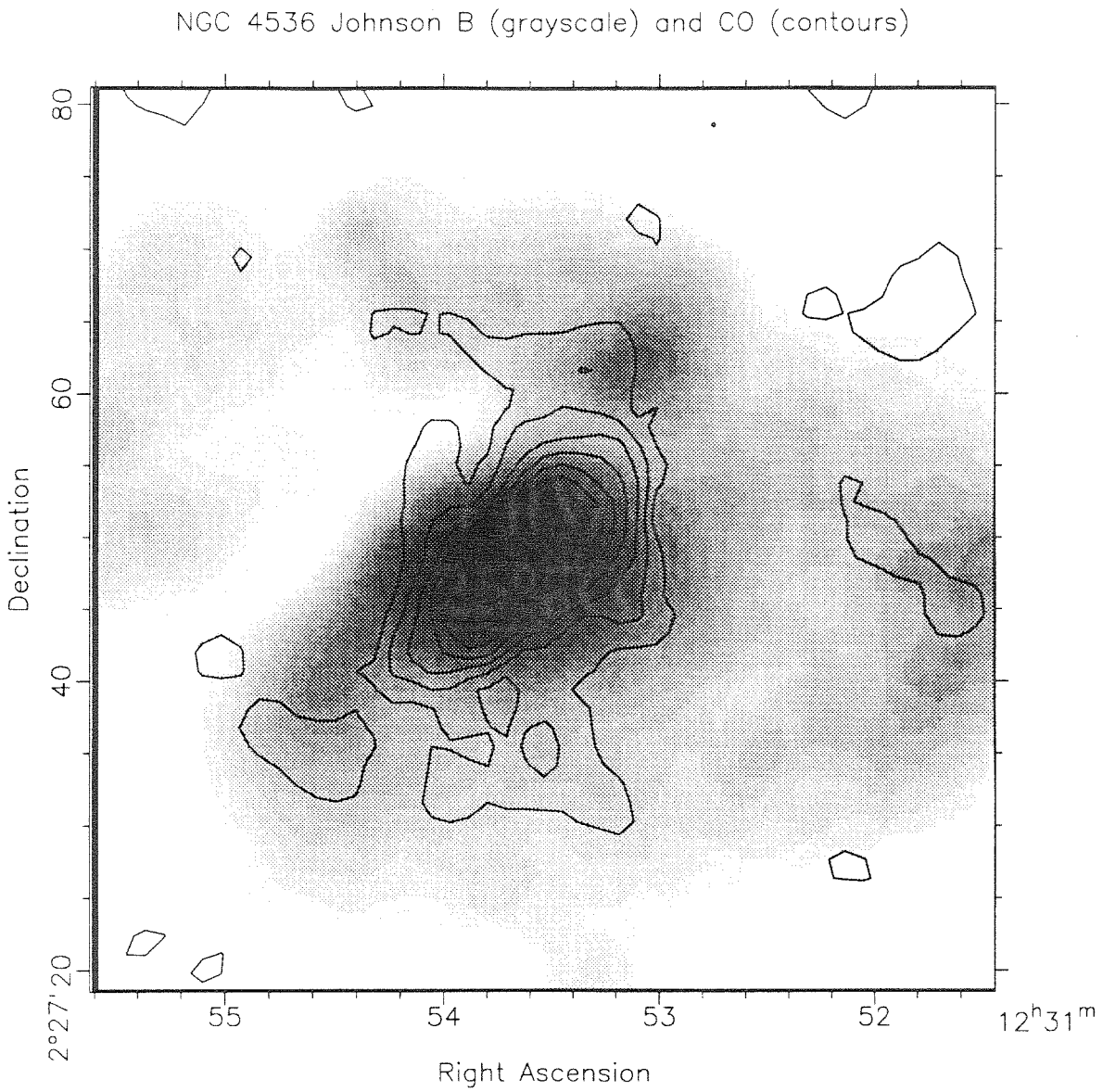


Figure 4-30. NGC 4536. Johnson $B$ (grayscale) and CO (contours).

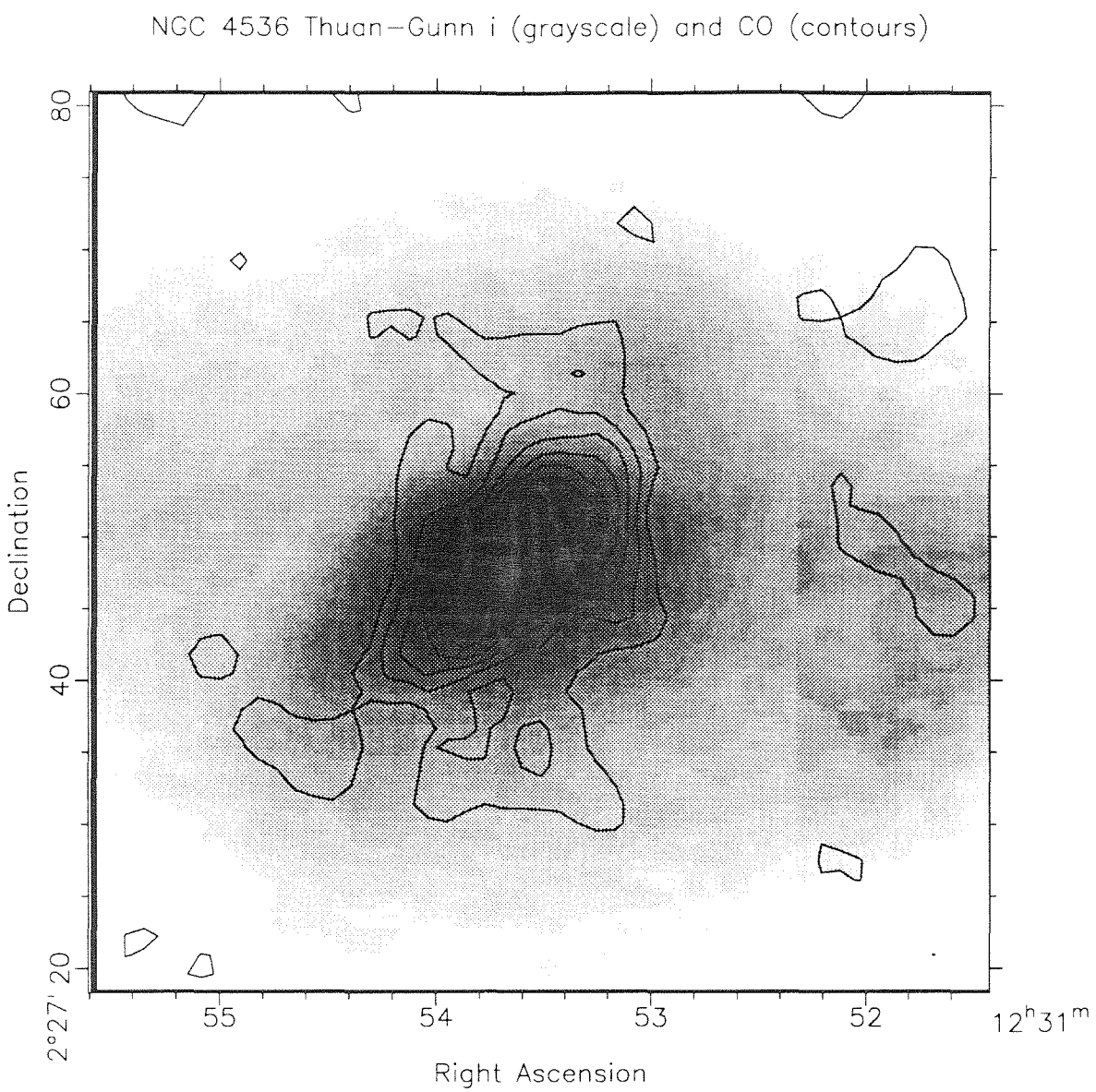


Figure 4-31. NGC 4536. Thuan-Gunn $i$ (grayscale) and CO (contours).

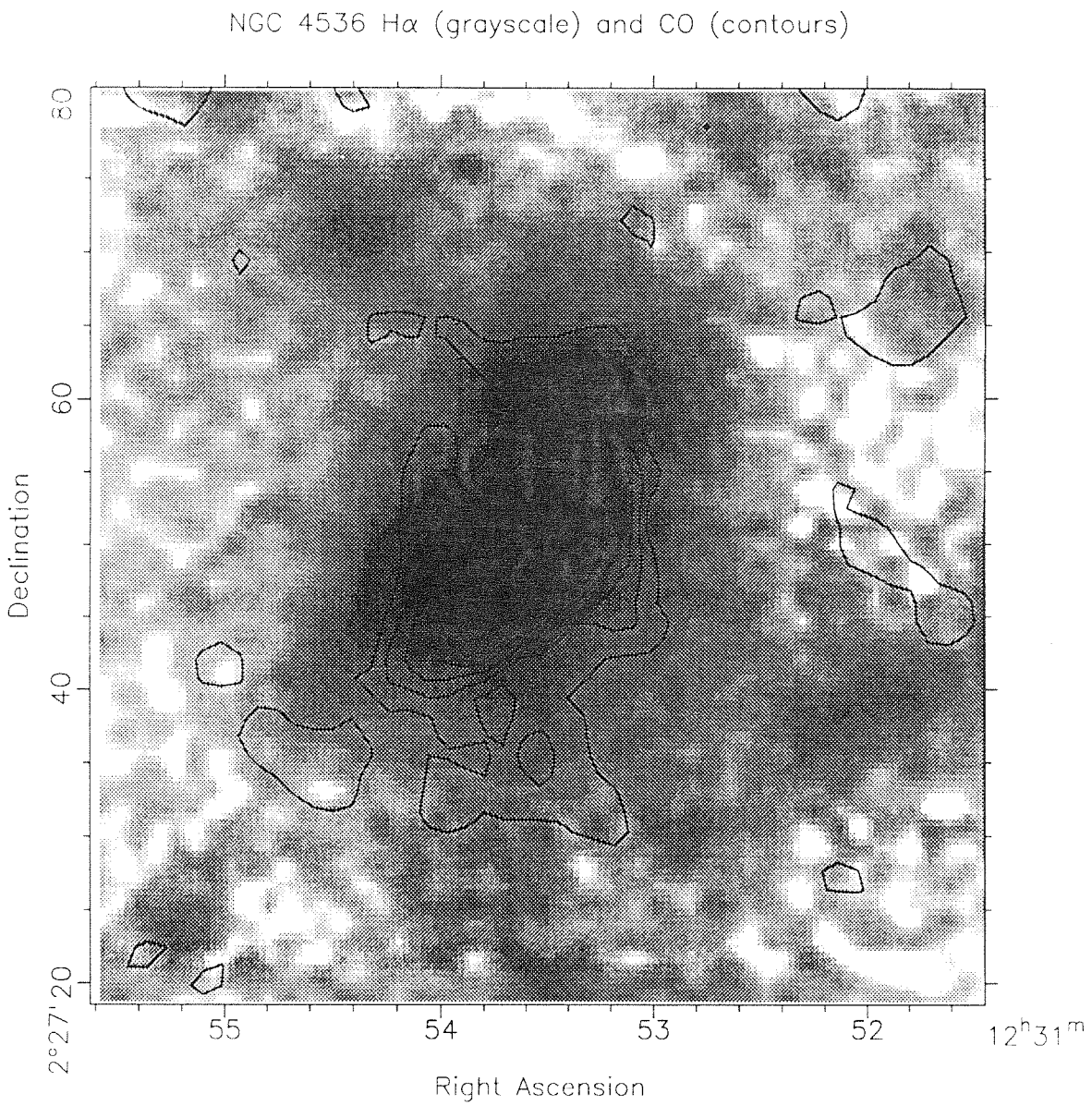


Figure 4–32. NGC 4536. H$\alpha$ emission (grayscale) and CO (contours).

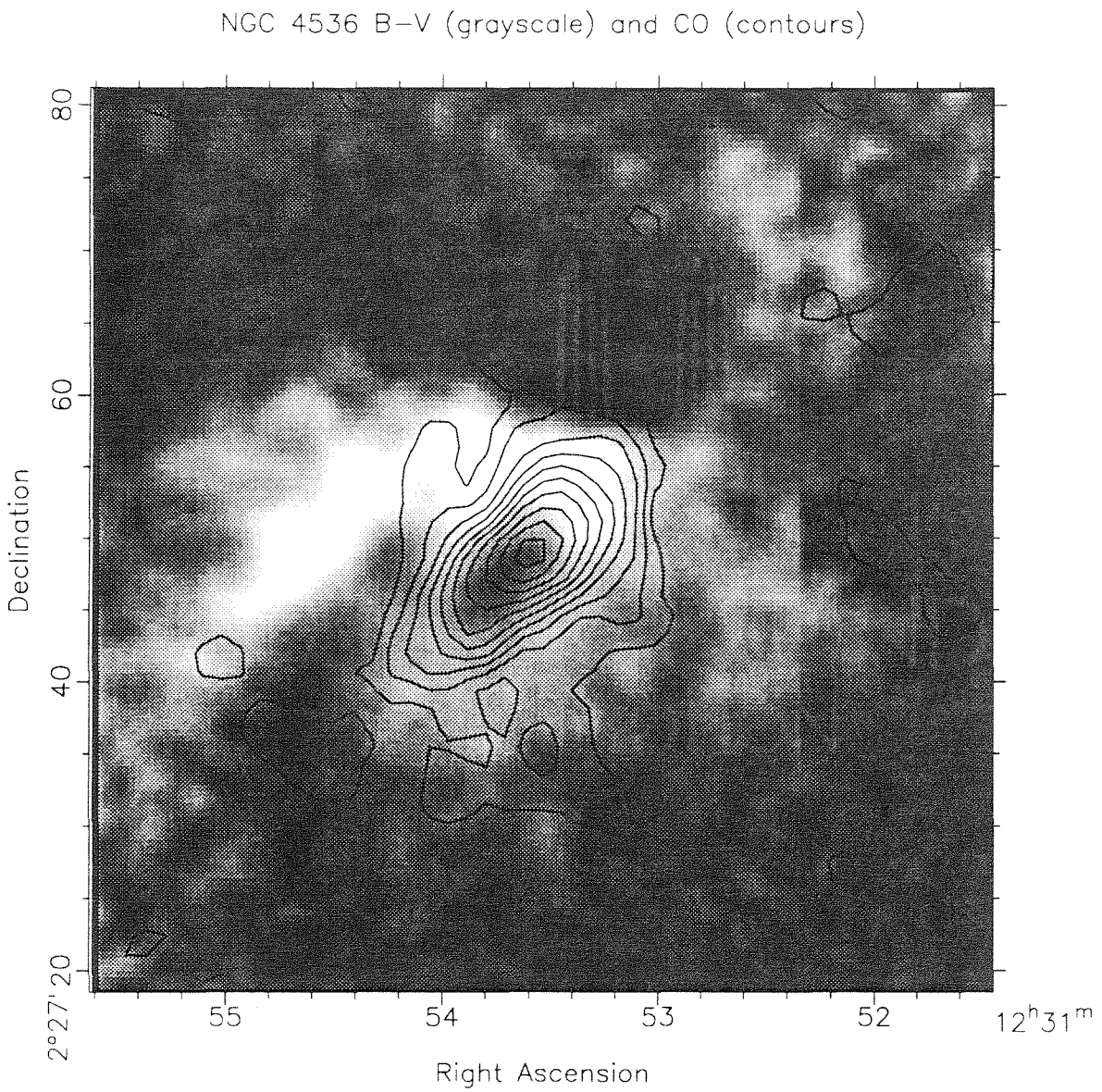


Figure 4–33. NGC 4536. $B-V$ color (grayscale) and CO (contours). Redder $B-V$ is lighter shades; bluer is darker shades.

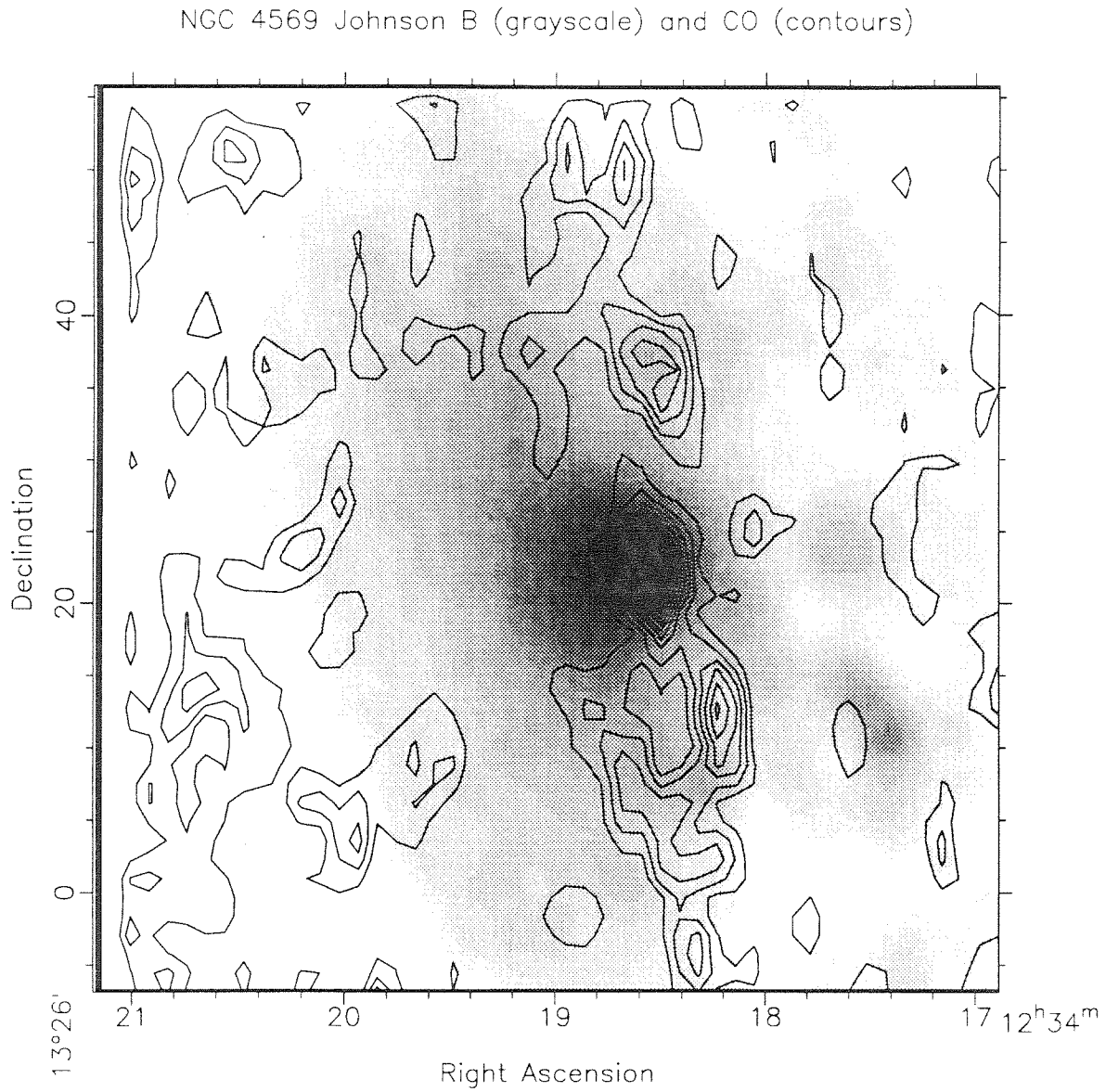


Figure 4–34. NGC 4569. Johnson $B$ (grayscale) and CO (contours).

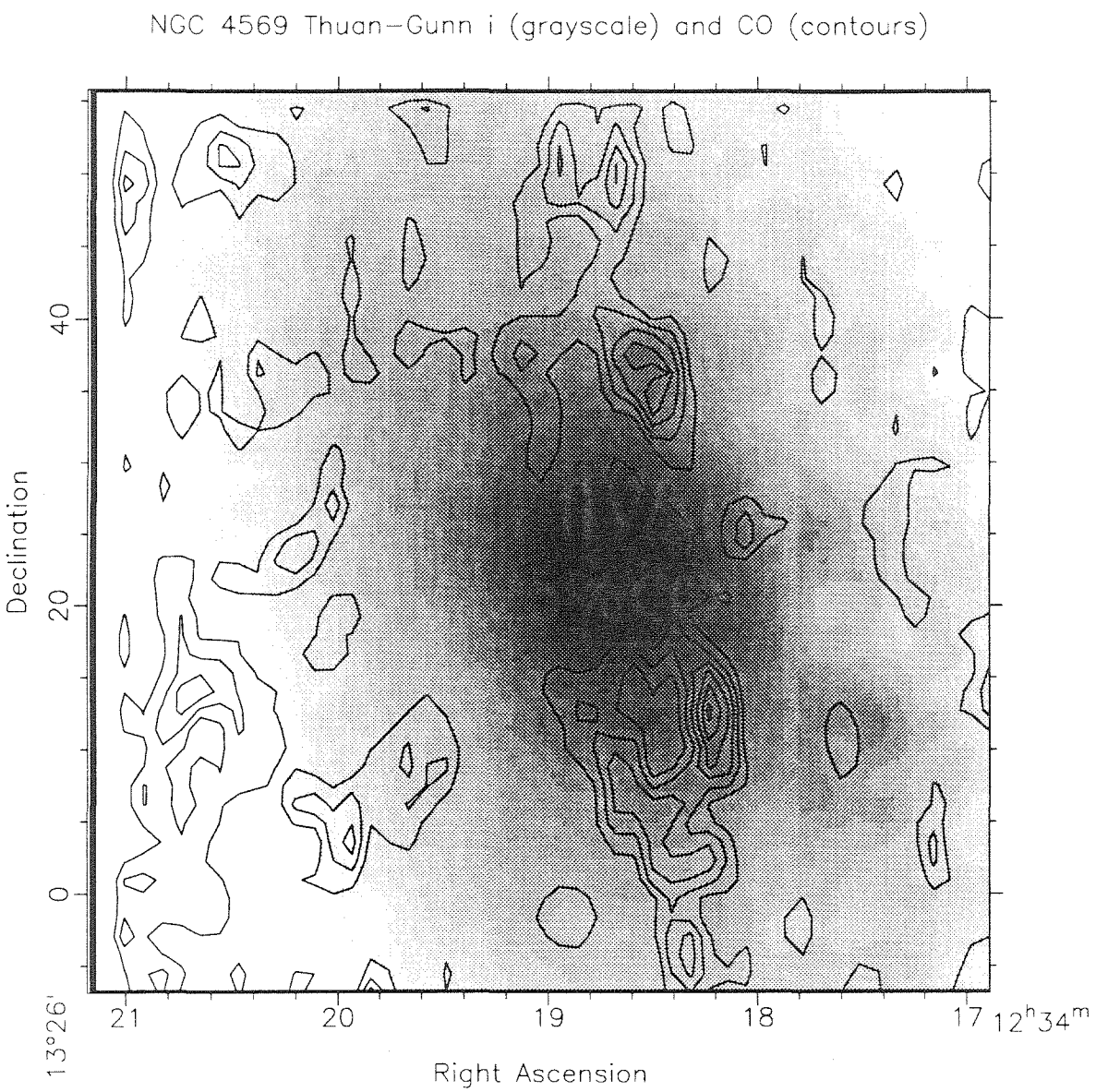


Figure 4–35. NGC 4569. Thuan-Gunn $i$ (grayscale) and CO (contours).

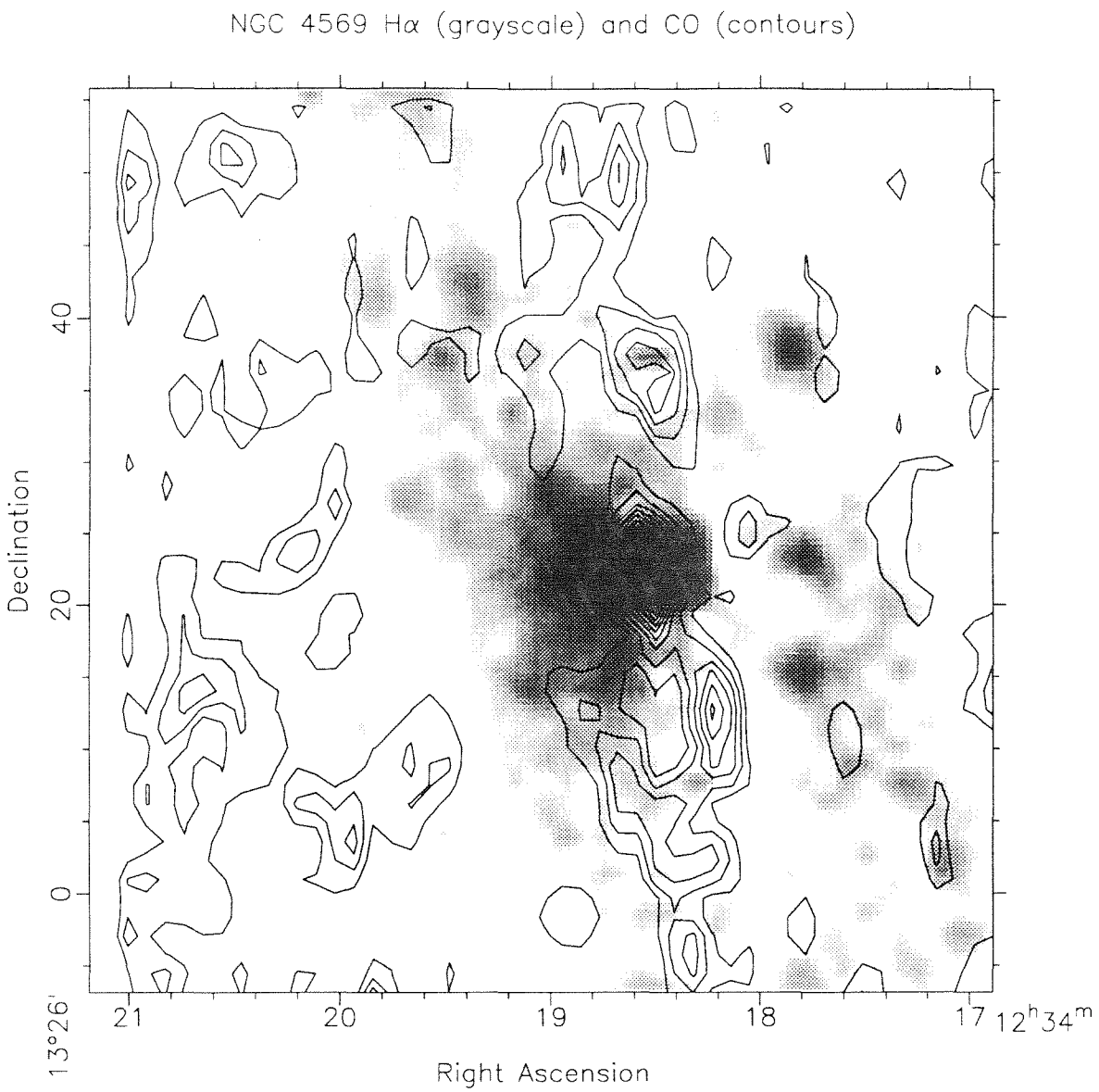


Figure 4–36. NGC 4569. H$\alpha$ emission (grayscale) and CO (contours).

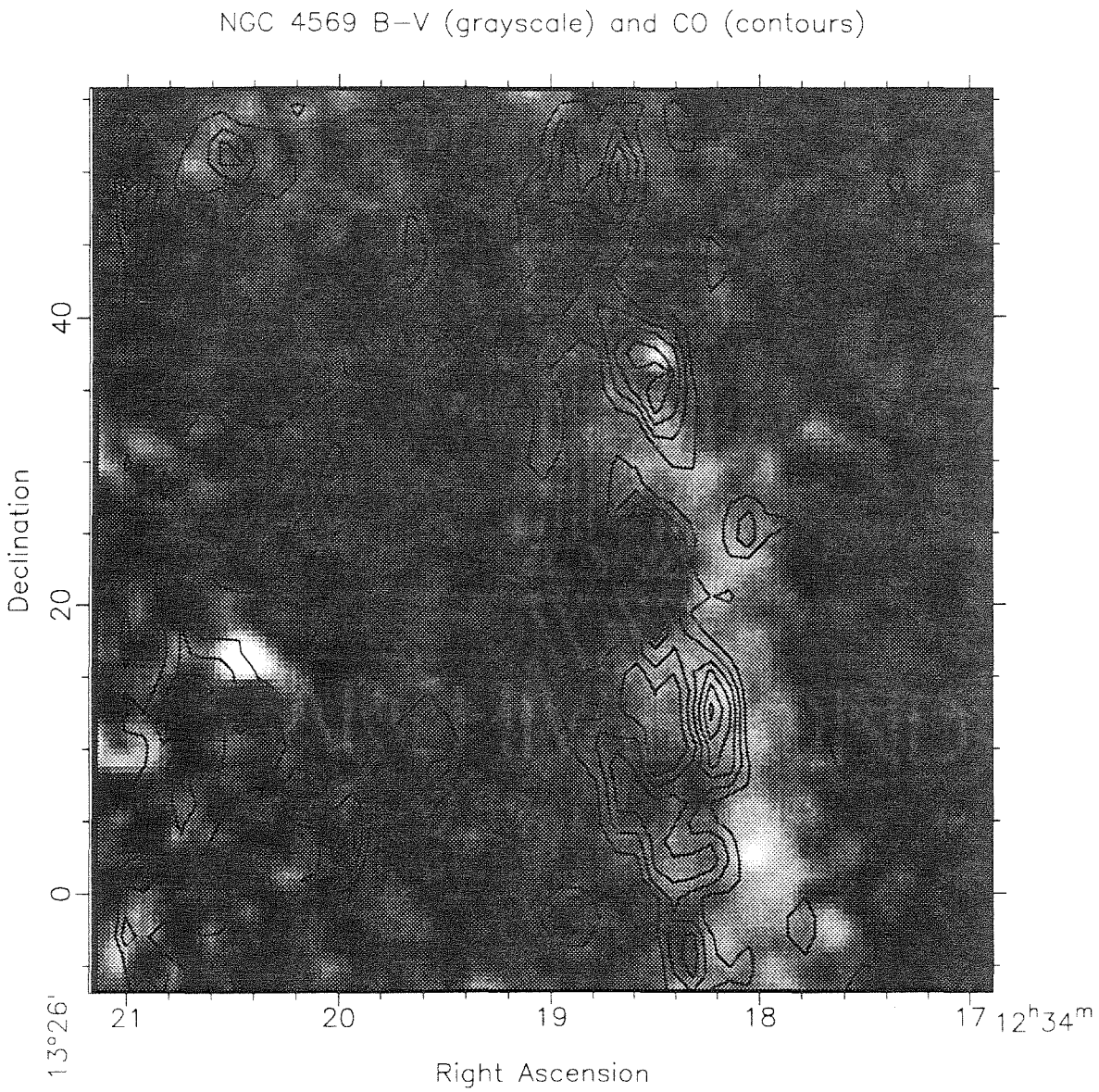


Figure 4–37. NGC 4569. $B - V$ color (grayscale) and CO (contours). Redder $B - V$ is lighter shades; bluer is darker shades.

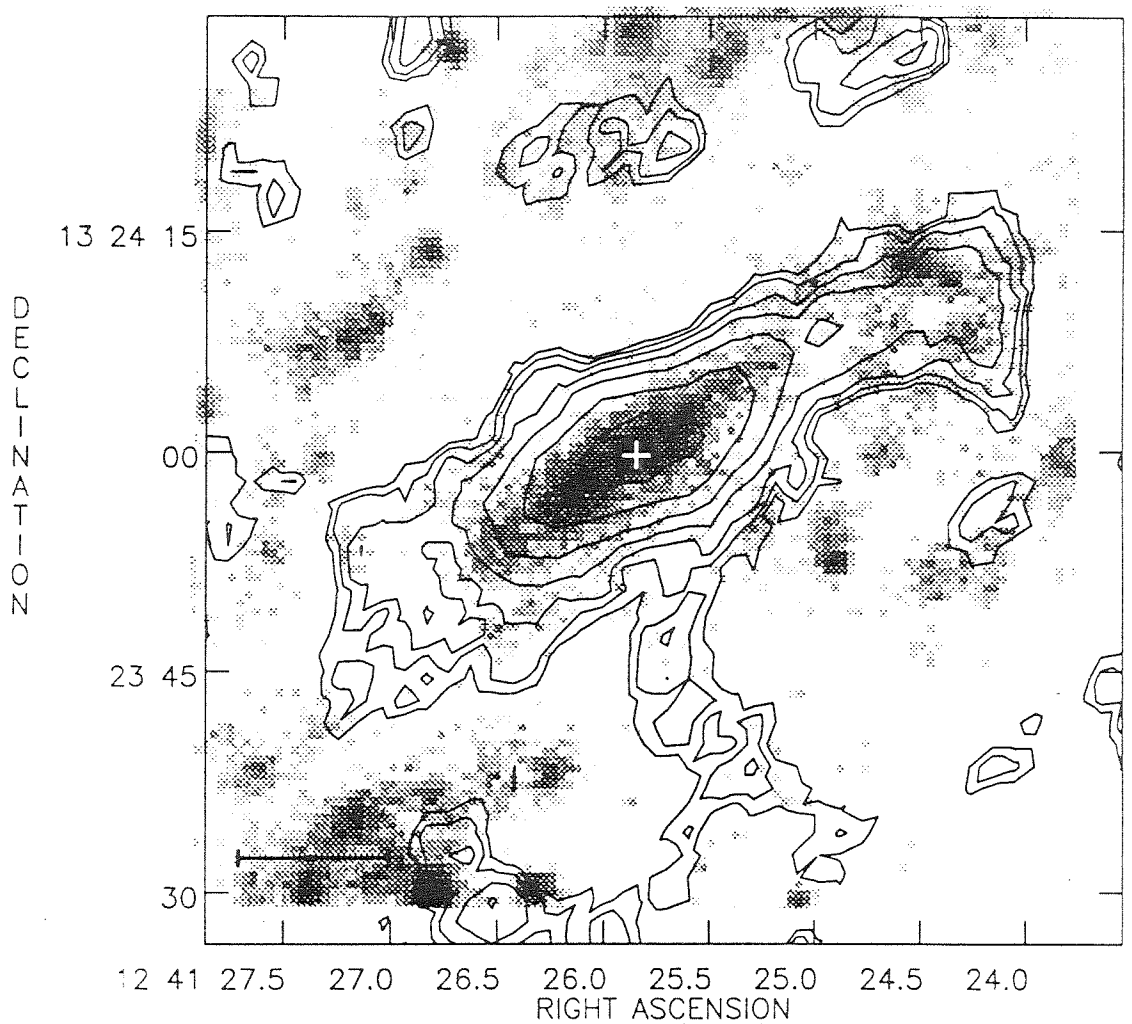


Figure 4–38. NGC 4654. H$\alpha$ emission (grayscale) and CO (contours).

# Chapter 5
# Radial Profiles

## 5.1. Total Magnitudes

Total magnitudes for the program galaxies were computed by converting the data frame units from mag arcsec$^{-2}$ to erg cm$^{-2}$ sec$^{-1}$ arcsec$^{-2}$, computing a surface brightness profile using AIPS, integrating the profile, and converting erg cm$^{-2}$ sec$^{-1}$ to magnitudes. Information in Table 3–7 was used for the conversion. The total magnitudes are listed in Table 5–1 along with total magnitudes from de Vaucouleurs *et al.* (1976). The magnitudes computed from the data are in fairly good agreement with those of de Vaucouleurs *et al.* (1976), although the data generally underestimate the total brightness of the galaxies, probably because of low-level background emission. Also, the de Vaucouleurs *et al.* (1976) values are corrected for internal extinction and reddening. The total H$\alpha$ radiancies of the program galaxies are listed in Table 3–8.

## 5.2. Inner Disk Radial Profiles

### 5.2.1. Observations in Optical Bands and CO

The radial profiles are recorded in Table 5–2 for the optical bands $B$, $i$, and H$\alpha$. Averages within annuli 500 pc wide are listed, and the radius listed is the outer radius of the annulus. The values in the $B-V$ column are averages of $B-V$ color within each annulus; they are not values of $\langle B\rangle - \langle V\rangle$ based on separate photometry of two frames. The average CO surface brightness in annuli measured from interferometer maps is also listed along with the noise in the maps. Note that many of the entries in the CO column at the larger radii are not reliable because of the noise level in the maps. In Figures 5–1 through 5–5, the profiles from Table 5–2 of all program galaxies

TABLE 5–1. TOTAL MAGNITUDES

| NGC | Band | Total Flux $10^{-10}$ erg sec$^{-1}$ cm$^{-2}$ | Total Mag | RC2[a] |
|---|---|---|---|---|
| 4254 | $B$ | 3.271 | 10.84 | 10.42 |
| | $V$ | 4.029 | 9.84 | 9.84 |
| | $r$ | 2.334 | 9.89 | |
| | $i$ | 3.743 | 9.42 | |
| | H$\alpha$ | 0.2621 | 10.58 | 10.91 |
| 4303 | $B$ | 6.159 | 10.15 | 10.21 |
| | $V$ | 7.373 | 9.19 | 9.67 |
| | $r$ | 4.485 | 9.18 | |
| | $i$ | 5.027 | 9.10 | |
| | H$\alpha$ | 0.2375 | 10.62 | 10.85 |
| 4321 | $B$ | 4.907 | 10.39 | 10.10 |
| | $V$ | 7.859 | 9.12 | 9.37 |
| | $r$ | 4.853 | 9.10 | |
| | $i$ | 5.678 | 8.97 | |
| | H$\alpha$ | 0.1405 | 10.85 | 11.05 |
| 4501 | $B$ | 4.291 | 10.54 | 10.27 |
| | $V$ | 4.725 | 9.67 | 9.52 |
| | $r$ | 7.045 | 8.69 | |
| | $i$ | 4.596 | 9.20 | |
| | H$\alpha$ | 0.06193 | 11.21 | 11.50 |
| 4535 | $B$ | 2.404 | 11.17 | 10.66 |
| | $V$ | 2.974 | 10.17 | 9.96 |
| | $r$ | 4.175 | 9.26 | |
| | $i$ | 2.515 | 9.85 | |
| | H$\alpha$ | 0.08612 | 11.06 | 11.43 |
| 4536 | $B$ | 1.504 | 11.68 | 10.99 |
| | $V$ | 1.932 | 10.64 | 10.39 |
| | $r$ | 1.081 | 10.73 | |
| | H$\alpha$ | 0.07075 | 11.15 | 11.48 |
| 4569 | $B$ | 2.855 | 10.98 | 10.23 |
| | $V$ | 3.959 | 9.86 | 9.48 |
| | $r$ | 3.376 | 9.49 | |
| | $i$ | 6.879 | 8.76 | |
| | H$\alpha$ | 0.02416 | 11.62 | 11.62 |

[a] de Vaucouleurs *et al.* (1976), corrected for internal extinction and reddening.

are graphed together for comparison. The surface brightness entries in Table 5–2 were corrected to face-on values by multiplying by $\cos i$, where $i$ is the inclination from Table 2–2. The conversion to mass surface density is

$$(502 \cos i)\, \mathrm{M}_\odot\, \mathrm{pc}^{-2}\, (\mathrm{Jy\, km\, sec}^{-1}\, \mathrm{arcsec}^{-2})^{-1}, \qquad (5-1)$$

using the CO–$H_2$ conversion formula (2–2), which uses the constant in relation (3–4), and the conversion to radiancy is

$$(5.09 \times 10^{48} \cos i)\,\mathrm{erg\,sec^{-1}\,pc^{-2}\,(erg\,sec^{-1}\,cm^{-2}\,arcsec^{-2})^{-1}}. \qquad (5-2)$$

The CO profiles in Figure 5–1 are strikingly similar in form and scale. It appears that an exponential law governs the radial distribution of the gas fairly well in most cases. Scale lengths for the exponentials are rather small, around 5″. Modeling the exact appearance of the CO profiles deduced from the interferometer data will be discussed in §5.3, where quantitative estimates of the scale lengths of the exponentials will be made. Note that NGC 4303, which has a central bar, follows a much steeper exponential law than most of the other galaxies. The increase in $H_2$ surface density at 2.5 kpc radius in NGC 4303 is due to the bright area of CO emission to the south near the edge of the field. The CO emission from NGC 4501 is very peaked and falls off abruptly. Gas detected by the interferometer in all of the other spiral galaxies approximately follows exponential laws.

The *B*-band profiles, shown in Figure 5–2, are uniform in appearance. All profiles have relatively bright, compact centers and more slowly decaying outer regions. The outer regions follow exponential laws very well, all with nearly the same scale length. Of note are the exceptionally bright nucleus of NGC 4569 and the broad, bright center of NGC 4321. The center of NGC 4321 is dominated in *B*-band by the peculiar four-armed structure discussed in Chapter 4. The small arms contribute quite a lot of blue light to the central region of NGC 4321, and only beyond 1 kpc radius does the emission settle into a more conventional exponential distribution.

The *i*-band profiles (Figure 5–3) are striking in their close uniformity. There is only modest brightening of the center relative to the exponential law established at larger radii. All of the galaxies appear to have very similar scale lengths except for NGC 4536, whose light declines on a somewhat shorter scale. The galaxies are divided

TABLE 5–2. SURFACE BRIGHTNESS PROFILES

| NGC | Radius (kpc) | Averages within Annuli CO[a] | $\sigma^a$ | $B^b$ | $i^b$ | H$\alpha^b$ | $B-V$ |
|---|---|---|---|---|---|---|---|
| 4254 | 0.5 | 0.118 | 0.108 | 98.46 | 137.4 | 3.075 | 0.868 |
| | 1.0 | 0.071 | | 56.85 | 71.65 | 2.063 | 0.807 |
| | 1.5 | 0.032 | | 44.32 | 47.75 | 1.928 | 0.723 |
| | 2.0 | 0.021 | | 31.30 | 33.51 | 1.839 | 0.730 |
| | 2.5 | 0.001 | | 22.37 | 24.77 | 1.179 | 0.744 |
| 4303 | 0.5 | 0.430 | 0.064 | 282.3 | 271.0 | 8.020 | 0.824 |
| | 1.0 | 0.120 | | 60.63 | 67.65 | 0.2814 | 0.948 |
| | 1.5 | 0.039 | | 43.14 | 42.90 | 0.2907 | 0.881 |
| | 2.0 | 0.006 | | 38.92 | 32.79 | 0.5244 | 0.788 |
| | 2.5 | 0.032 | | 32.75 | 26.51 | 0.5084 | 0.767 |
| 4321 | 0.5 | 0.426 | 0.073 | 220.4 | 197.4 | 5.548 | 0.746 |
| | 1.0 | 0.294 | | 124.7 | 87.44 | 3.445 | 0.645 |
| | 1.5 | 0.067 | | 37.82 | 37.70 | 0.4609 | 0.880 |
| | 2.0 | 0.014 | | 23.91 | 25.60 | 0.2419 | 0.933 |
| | 2.5 | 0.030 | | 18.96 | 20.26 | 0.1837 | 0.937 |
| 4501 | 0.5 | 0.321 | 0.089 | 171.5 | 266.8 | 4.868 | 1.128 |
| | 1.0 | 0.005 | | 78.50 | 110.9 | 0.0 | 1.090 |
| | 1.5 | 0.054 | | 47.46 | 64.36 | 0.0 | 1.075 |
| | 2.0 | 0.046 | | 36.17 | 46.63 | 0.0264 | 1.051 |
| | 2.5 | 0.046 | | 32.66 | 38.67 | 0.2456 | 0.991 |
| 4535 | 0.5 | 0.635 | 0.026 | 69.46 | 54.78 | 5.630 | 0.882 |
| | 1.0 | 0.077 | | 18.72 | 21.49 | 0.1906 | 0.986 |
| | 1.5 | 0.008 | | 13.40 | 14.00 | 0.1027 | 0.963 |
| | 2.0 | 0.011 | | 10.15 | 10.50 | 0.0865 | 0.979 |
| | 2.5 | 0.016 | | 9.045 | 8.925 | 0.1232 | 0.965 |
| 4536 | 0.5 | 1.755 | 0.065 | 99.01 | 152.7 | 15.94 | 0.986 |
| | 1.0 | 0.761 | | 36.89 | 55.59 | 5.964 | 1.057 |
| | 1.5 | 0.145 | | 19.89 | 24.97 | 2.007 | 0.971 |
| | 2.0 | 0.071 | | 13.79 | 15.62 | 0.7631 | 0.938 |
| | 2.5 | 0.041 | | 10.48 | 11.65 | 0.3702 | 0.944 |
| 4569 | 0.5 | 0.590 | 0.103 | 471.6 | 570.7 | 2.561 | 0.548 |
| | 1.0 | 0.079 | | 58.77 | 169.1 | 0.9330 | 1.049 |
| | 1.5 | 0.086 | | 35.44 | 96.87 | 0.4562 | 1.042 |
| | 2.0 | 0.033 | | 24.93 | 67.76 | 0.3935 | 1.014 |
| | 2.5 | 0.0 | | 21.06 | 53.68 | 0.2725 | 0.962 |
| 4654 | 0.5 | 0.306 | 0.036 | | | | |
| | 1.0 | 0.140 | | | | | |
| | 1.5 | 0.044 | | | | | |
| | 2.0 | 0.017 | | | | | |
| | 2.5 | 0.006 | | | | | |

[a] Units are Jy km sec$^{-1}$ arcsec$^{-2}$.
[b] Units are $10^{-15}$ erg sec$^{-1}$ cm$^{-2}$ arcsec$^{-2}$.

into two classes in $i$-band radiancy, with NGC 4535 and NGC 4536 in one class with a radiancy about an order of magnitude below the other class, which contains the balance of the galaxies. It is probably significant that NGC 4535 and NGC 4536 share many morphological traits: their spiral arms are thin and their spiral structure is very open; their nuclei are round and rather featureless in CO, $B$, $i$, and H$\alpha$ emission; except for the nucleus, their inner disks are relatively devoid of high-mass star formation, which becomes very much more active in their outer disks; their nuclei are very bright in H$\alpha$.

In contrast to the uniform behavior shown by the surface brightness profiles in the other bands, the H$\alpha$ profiles (Figure 5–4) show more diverse forms. The only galaxy which shows an exponential falloff is NGC 4536; H$\alpha$ emission conforms to an exponential law very closely in this galaxy. NGC 4254 is distinguished by the nearly uniform H$\alpha$ emission across its entire central 5 kpc region. NGC 4303 has very strong H$\alpha$ emission at its nucleus; the emission drops rapidly with radius, then climbs slowly outside 1.5 kpc radius where the spiral arms become prominent. The H$\alpha$ profile of NGC 4321 is very similar to its $B$-band profile: evidently, young high-mass stars in the four-armed feature dominate the central light. H$\alpha$ emission from the nucleus dominates the low-level inner disk emission in NGC 4501 and NGC 4535. The radiancy of NGC 4569 roughly follows an exponential law, although its central region is somewhat brighter than would be extrapolated from the exponential law. The H$\alpha$ profile of NGC 4569 is less peaked than would be expected from the stellar appearance of its nucleus in continuum light, but this is expected from the extended morphology of its central H$\alpha$ emission.

There is much similarity among the $B - V$ profiles shown in Figure 5–5. Most galaxies (NGC 4303, NGC 4501, NGC 4535, NGC 4536, and NGC 4569) show a tendency to become bluer with increasing radius, which is reasonable behavior as the

disk light dominates the bulge light at larger radii. Of the galaxies listed, all but NGC 4501 have a much bluer nucleus than would be extrapolated from the color gradient. The blue color of the nucleus is probably a sign of active star formation there; the low level of high-mass star formation in the nucleus of NGC 4501 (from the evidence of H$\alpha$ emission) is unable to make the color of its very red nucleus much bluer. NGC 4321 has a very blue ring between 0.5 and 1 kpc radius, as previously noted by Arsenault *et al.* (1988); its inner disk curiously becomes redder with increasing radius. NGC 4254 has a similar $B - V$ profile with less marked behavior; still, NGC 4254 is bluest in its inner disk between 1 and 1.5 kpc, and its color becomes redder at larger radii. NGC 4254 and NGC 4321 have distinctly different morphologies, so the reason for their similar behavior in color on the 500 pc scale is not known. Both have spiral structure, though of very different forms, in their central regions. Increasing spiral arm strength or width will tend to make the average color bluer at a given radius. At larger and larger radii, spiral arms may cover less and less disk area, which will make the average color at a given radius redder. Since the two effects compete, it is expected that the blue light from spiral arms will dominate over a range in radii. This could explain the blue annuli in NGC 4254 and NGC 4321.

Figures 5–6 through 5–13 show the radial profiles in all bands for each galaxy separately. All profiles are normalized to the same value at the smallest radius so that differences in characteristic length scales will be emphasized. The relative scale is the same for all profiles: one decade represents a change in radiancy (power per unit area) by a factor of ten. Note the similar long-scale exponential behavior of $B$, $i$, and H$\alpha$ emission in NGC 4254 and the slightly shorter-scale CO profile. The very confused appearance of the central region of NGC 4254 yields smooth azimuthal averages of its optical light and CO emission distributions. NGC 4536 also shows smoothly declining profiles in $B$, $i$, H$\alpha$, and CO emission with similar central scale

lengths. In NGC 4536, the CO and H$\alpha$ distribution follow each other closely, and $B$ and $i$ are also similar but with slightly longer scale than the CO and H$\alpha$ beyond 1.5 kpc radius.

Emission from the central region of NGC 4321 is strong in $B$, H$\alpha$ and CO emission out to 1 kpc radius. H$\alpha$ and CO emission then fall precipitously, and a reddening of color accompanies the falling contribution of high-mass stars to the blue light. $B$ and $i$ continuum emission are similar beyond 1.5 kpc. NGC 4303 is more centrally peaked in all bands than NGC 4321 is, but shows similar overall behavior among the radial profiles. $B$ and $i$ emission follow each other very well beyond 1 kpc radius, while H$\alpha$ and CO emission fall very fast outside the central peak. Outside 500 pc radius, the blue color of the very center disappears as it becomes dominated by the redder bulge light. The reddening of $B-V$ color with increasing radius is due to the rapidly decreasing contribution of high-mass stars to the total light, as traced by the H$\alpha$ profile.

NGC 4535 is more extreme in its central concentration of H$\alpha$ and CO emission. Although all bands show a central peak, the $B$ and $i$ band continuum light falls gradually in a long-scale exponential decline, while H$\alpha$ and CO emission plunge very fast outside 500 pc radius. The most extreme example of this behavior is NGC 4501, where H$\alpha$ and CO emission is highly peaked while continuum light in the $B$- and $i$-band falls slowly and smoothly in an approximately exponential fashion. There is some extended CO emission from 1.5 kpc outward which follows the $B$- and $i$-band profiles, but H$\alpha$ emission is at a very low level outside 500 pc radius.

The most striking similarity among most of the radial profiles is the correlation between H$\alpha$ emission and CO emission. (Only NGC 4569 displays behavior which does not show a correlation between CO and H$\alpha$; see below.) The correlation is probably due to the fact that high-mass star formation (which is traced by H$\alpha$ emission)

generally occurs where the concentration of molecular gas is greatest.

There are exceptions to the generalization above exhibited by NGC 4569. As in most of the other galaxies, emission from all bands is centrally peaked; however, the very blue color of the nucleus seems to be due to $B$-band emission, not H$\alpha$ as in NGC 4321 and NGC 4303. It is the large decline in $B$-band emission outside the nucleus, together with the less drastically changing H$\alpha$ profile, which must lead to the red color of the inner disk. Such behavior suggests that the central region houses an aging starburst population. H$\alpha$ emission is surprisingly well correlated with $i$-band emission. The correlation of H$\alpha$ and $i$-band emission may be an indication that high-mass star formation occurs more uniformly throughout the disk of NGC 4569, rather than being concentrated in spiral arms. Then the relative contributions of H$\alpha$ and $i$-band emission would not change drastically with radius as they do in late-type spirals, where the old disk light dominates due to its greater area and dilutes the H$\alpha$ contribution from spiral arms. Note that the variation in CO emission follows the $B$-band emission much better than it follows the H$\alpha$ emission, implying that intermediate mass star formation, rather than high-mass star formation (traced by H$\alpha$ emission), is precipitated by concentration of molecular gas.

Photometry of NGC 4654 was not obtained. The CO profile of this galaxy conforms remarkably well to an exponential law.

### 5.2.2. CO Radial Profiles and Single-Dish Measurements

The position of the centroid of integrated CO emission for each program galaxy is listed in Table 5–3. Also listed are the peak brightness and areal average mean brightness in an individual 5 MHz channel map and the peak CO radiancy in the integrated CO emission interferometer map. The peak brightnesses and radiancies in Table 5–3 are values in a single pixel (2.25 arcsec$^2$), while the average brightnesses are averages over the area containing emission in the brightest channel of the data cube.

Brightness temperatures are computed using the Rayleigh-Jean formula. The peak brightness temperatures are reasonable if the molecular clouds within a pixel area do not completely fill space and have brightness temperatures that are comparable to the brightness temperatures of resolved Galactic molecular clouds (5–10 K). The areal filling factor of molecular clouds *within cloud complexes* at the centers of the Virgo spirals may be estimated from the interferometer maps. The area filling factor is $f_A \approx T_b \sigma_v / T_k \Delta v_{\rm cloud}$, where $T_k$ is the kinetic temperature of the typical molecular cloud, $\Delta v_{\rm cloud}$ is the velocity dispersion of the typical molecular cloud, and $\sigma_v$ is the velocity dispersion of a typical spectral line observation of the Virgo galaxy (excluding the broadening due to rotation of the galaxy). The filling factor will be estimated in Chapter 7, where values of $\sigma_v$ will be presented.

TABLE 5–3. CO EMISSION FROM VIRGO SPIRALS

| NGC | $\alpha_{1950}$ h m s | $\delta_{1950}$ ° ′ ″ | Peak Radiancy[a] | $A_{\rm beam}$ (arcsec$^2$) | Brightness[b] Peak | Brightness[b] Mean | Peak $T_b$(K) | Mean $T_b$(K) |
|---|---|---|---|---|---|---|---|---|
| 4254 | 12 16 16.77 | +14 41 42.9 | 0.8052 | 32.87 | 0.656 | 0.174 | 2.08 | 0.552 |
| 4303 | 12 19 21.60 | +04 45 02.5 | 0.8936 | 48.89 | 0.774 | 0.257 | 1.65 | 0.548 |
| 4321 | 12 20 22.98 | +16 05 57.2 | 1.3164 | 34.25 | 1.193 | 0.390 | 3.63 | 1.186 |
| 4501 | 12 29 27.72 | +14 41 45.6 | 1.2706 | 29.97 | 0.413 | 0.120 | 1.44 | 0.417 |
| 4535 | 12 31 47.96 | +08 28 23.7 | 1.1809 | 59.36 | 0.743 | 0.241 | 1.30 | 0.423 |
| 4536 | 12 31 53.68 | +02 27 48.9 | 2.1690 | 57.71 | 1.021 | 0.316 | 1.84 | 0.571 |
| 4569 | 12 34 18.63 | +13 26 22.1 | 1.9061 | 31.57 | 0.666 | 0.160 | 2.20 | 0.528 |
| 4654 | 12 41 25.90 | +13 23 59.9 | 0.3771 | 53.46 | 0.530 | 0.155 | 1.03 | 0.302 |

[a] Units are Jy km sec$^{-1}$ arcsec$^{-2}$.
[b] Units are Jy beam$^{-1}$.

The OVRO mm-wave interferometer is sensitive to CO emission which has spatial variations on a scale of $\lesssim 30''$. Consequently, uniform emission within the field will not be recovered in the interferometer maps. To estimate the amount of emission recovered, the integrated CO flux densities from interferometer maps (see §3.1.4) are

compared with single-dish measurements by Kenney (1987) in Table 5–4. Values of $I_{CO}$ in units of K km sec$^{-1}$ in Kenney (1987) have been converted to Jy km sec$^{-1}$ by multiplying by the gain, 41.7 Jy/K($T_A^*$). Factors which model the coupling of the FCRAO beam to the source structure are ignored. Kenney used the 14 m FCRAO telescope, which has a beam width (HPBW) of 45″. Although this is smaller than the primary beam size (65″) for a 10.4 m OVRO antenna, it is large enough to capture most of the emission present in the interferometer maps.

In most cases, the fractions of emission recovered are rather small, indicating that a substantial amount of molecular gas in the centers of these galaxies is distributed on scales of $\gtrsim$ 20″. The galaxies of earliest morphological type, NGC 4501 and NGC 4569, have the lowest recovery rates and molecular gas in these galaxies is presumably distributed more uniformly than in later-type spirals. The molecular gas undetected by the interferometer is probably contained in cloud complexes that are smaller than typical cloud complexes in the interferometer maps. If a galaxy has a molecular cloud mass spectrum with many low mass clouds, then the smaller clouds may be able to disperse more uniformly throughout the disk. This could explain the low recovery of CO emission in early-type spirals. The lack of strong spiral structure in earlier-type spirals may mean that collection of gas in spiral arms, and in the nucleus through loss of angular momentum in collisions, are not important phenomena in early types, and so clouds would more uniformly populate their disks. NGC 4254, a late-type spiral, also has a low recovery rate. The CO emission in its central region is not compact or centrally concentrated but is distributed among many small components; H II regions at the center are similarly distributed (see Chapter 4). The low flux recovery rate in NGC 4254 is probably due to the lack of structural organization of the molecular gas. The very shallow slope of its rotation curve (see Chapter 6) supports this hypothesis, since it implies that dynamical influences, which generally

operate on shorter timescales as the angular velocity increases (see Chapter 8), are not as efficient in NGC 4254. Lastly, it cannot be overlooked that the sensitivity of the interferometer influences the amount of emission recovered: the three galaxies most recently observed (NGC 4535, NGC 4536, and NGC 4654), when the system has become more sensitive, have the highest recovery rates. Smaller cloud complexes may also be undetectable due to the limited sensitivity of the interferometer, which is evident in the noise in the maps.

TABLE 5–4. FLUX RECOVERY

| NGC | $I_{CO}$ (Jy km sec$^{-1}$) | | Fraction |
|---|---|---|---|
| | OVRO | FCRAO | Recovered (%) |
| 4254 | 35.6 | 442 | 12 |
| 4303 | 152.9 | 496 | 31 |
| 4321 | 226.4 | 626 | 36 |
| 4501 | 40.5 | 500 | 8 |
| 4535 | 90.3 | 196 | 46 |
| 4536 | 229.3 | 421 | 54 |
| 4569 | 162.4 | 609 | 27 |
| 4654 | 87.1 | 138 | 63 |

Correlations between the CO and H$\alpha$ radial distributions have been noted in §5.2.1 for seven of the spirals, and the frequent similarity of CO and H$\alpha$ morphology was noted in Chapter 4. Based on the flux recovery rates in Table 5–4, how can the observed CO–H$\alpha$ spatial correlations be assessed? The interferometer maps of CO emission should be regarded as indicating the "tips of icebergs." It should be borne in mind that the largest cloud complexes, which contrast the most with their surroundings, are best represented in the interferometer maps. Where such large numbers of clouds accumulate, the high-mass star formation rate should be highest due to two factors: the enhanced gas density and the increased frequency of cloud

collisions. Based on simple ideas about the relationship between star formation and molecular gas, the spatial correlation of H$\alpha$ emission and CO emission in interferometer maps is expected. High-mass star formation is generally believed to be induced by cloud-cloud collisions (Scoville, Sanders, and Clemens 1986). Concentrations of molecular gas in large cloud complexes, to which the interferometer is most sensitive, should be accompanied by much more high-mass star formation because of the increased probability of collision within the complex. The correlation between CO and H$\alpha$ emission is probably better using interferometer maps than single-dish maps.

## 5.3. Inner Molecular Disks of Spirals

Radial distributions in Figures 5–6 through 5–13 demonstrate that the scale lengths of CO emission are considerably smaller than those of optical continuum light ($B$- or $i$-band). Quantitative verification of this observation is supplied in Table 5–5. Least squares fits of exponentials to the CO profiles and to the continuum light profiles were made; the fitted scale lengths are listed in Table 5–5. In some cases (NGC 4303 and NGC 4535) the very bright, nuclear light (within 500 pc radius) was omitted from the continuum light fits. The continuum light scale lengths are in the range 10–30″, which are somewhat smaller than exponential scale lengths associated with the disks of most large spirals. Rapidly declining bulge light is, no doubt, affecting the continuum light scale length estimates so that small values are measured. $B$-band and $i$-band scale lengths agree well with each other, as expected from the similarity of their radial profiles. The CO scale lengths are nearly an order of magnitude smaller than the continuum light scale lengths, being in the range 2–7″. Only the CO profile of NGC 4254, which has localized sources of CO emission spread around its inner disk, has a relatively large CO scale length of 11″.

What could be the cause of such small CO scale lengths? The range of values is similar to the synthesized beam sizes (Table 3–2), which suggests that there could be

TABLE 5–5. INNER DISK SCALE LENGTHS

| NGC | Band | $r_0$ arcsec | NGC | Band | $r_0$ arcsec |
|---|---|---|---|---|---|
| 4254 | $B$ | 18.4 | 4535 | $B$ | 26.7 |
| | $i$ | 15.7 | | $i$ | 22.5 |
| | CO | 11.0 | | CO | 3.0 |
| 4303 | $B$ | 33.7 | 4536 | $B$ | 15.9 |
| | $i$ | 21.3 | | $i$ | 12.7 |
| | CO | 4.7 | | CO | 6.6 |
| 4321 | $B$ | 10.0 | 4569 | $B$ | 19.1 |
| | $i$ | 11.4 | | $i$ | 17.3 |
| | CO | 5.6 | | CO | 7.7 |
| 4501 | $B$ | 22.6 | 4654 | CO | 6.7 |
| | $i$ | 18.9 | | | |
| | CO | 1.6 | | | |

unresolved CO sources at the centers of many of the spirals. In that case, the CO surface brightness profiles should be Gaussian in shape, and the scale lengths would merely represent the restoring beam sizes. The profiles of NGC 4303, NGC 4535, and NGC 4654 are exponential in shape, as shown by the linear profiles on semi-log graphs in Figure 5–1, and are not Gaussian. Furthermore, the CO in NGC 4303 and NGC 4654 is well resolved and decidedly not Gaussian in shape, nor is there evidence of an unresolved, pointlike center in either of them. The profiles of NGC 4321 and NGC 4536 most resemble Gaussians because of their flat centers, but extended structure is present in these sources (Figure 4–8), which enables the interferometer to recover more emission than if the sources were featureless. NGC 4501 and NGC 4569 are the only galaxies which do have compact centers that are probably unresolved. CO profiles based on interferometer data are listed in Table 5–6.

In his study of Virgo spirals, Kenney (1987) used single-dish major axis scans to

probe the radial dependence of CO emission from disks. He included the inclination of the galaxy and modeled the coupling of the main beam to the CO emission in order to estimate the true CO distribution. The observations were fitted by exponentials, or exponentials plus Gaussians. Scale lengths of the exponentials ranged from 15″ to 72″, with the median length being about 30″; the Gaussians had characteristic radii of 12″ or 15″. Using these models, radial profiles of total CO emission were computed; the values are listed in Table 5–7. In some cases (marked by asterisks), the computed model radiance was *less* than the CO emission detected by the interferometer (Table 5–6). In those cases, it was assumed that the emission recovered by the interferometer represented the true, full amount of CO emission at that radius, and the CO radiancy from the interferometer map was used in the radial profile. Emission representing the difference between the model and the observed CO distribution was subtracted uniformly from an annulus extending 30″ beyond where the interferometer emission exceeded the model. The model for NGC 4654 is unsatisfactory and rather peculiar, probably as a result of its asymmetric distribution of CO emission. The interferometric data which make up the first three measurements probably underestimate the total CO emission.

There is an alternative to the use of the the emission profile models of Kenney (1987). The total emission recovered by the interferometer (Table 3–5) may be compared with the single-dish emission from the same-sized region (say, the OVRO primary beam size). Assuming that the difference (the "unrecovered" emission) is distributed uniformly across the primary beam area, the profile of total CO emission may be approximated as the sum of the OVRO profile and Kenney's profile corrected for the recovered OVRO emission. When this alternative approach was used to estimate the variation of emission with radius, there was generally quite a lot more emission at smaller radii than computed from the models of Kenney (1987). Many

TABLE 5–6. RECOVERED CO EMISSION[a] – OVRO

| NGC | Outer Radius of Annulus (kpc) | | | | |
|---|---|---|---|---|---|
| | 0.5 | 1.0 | 1.5 | 2.0 | 2.5 |
| 4254 | 13.03 | 24.93 | 18.26 | 16.62 | 1.080 |
| 4303 | 50.48 | 42.64 | 23.63 | 4.682 | 29.75 |
| 4321 | 49.34 | 100.7 | 37.54 | 10.84 | 29.41 |
| 4501 | 21.34 | 1.058 | 17.90 | 21.07 | 27.64 |
| 4535 | 63.93 | 22.96 | 3.820 | 7.973 | 13.49 |
| 4536 | 83.73 | 118.0 | 37.00 | 25.35 | 18.60 |
| 4569 | 37.26 | 14.55 | 26.16 | 14.33 | 0.0 |
| 4654 | 22.42 | 33.56 | 17.36 | 9.268 | 4.489 |

[a] Values of $I_{CO}$ in Jy km sec$^{-1}$.

assertions to be made in Chapter 7 depend on the amount of CO emission in the inner disks of the program spirals. Increasing the estimates of the amount of emission would lead to sharper, but less conservative, conclusions in Chapter 7. A more conservative approach is appropriate given the uncertainties in measuring the CO emission and in computing the implied molecular gas mass. The conservative approach adopted here is to use the emission profile models of Kenney (1987) except where the emission in the OVRO maps exceeds that in Kenney's models.

The exponential disk scale lengths employed by Kenney (1987) to describe the radial falloff of CO emission are considerably larger than the CO scale lengths listed in Table 5–5. The necessity of including central Gaussians to adequately model some profiles suggests that in some galaxies there may be central CO sources with radial extents that are very small ($\approx 10''$) compared to the scale lengths of their surrounding disks (typically 1–2′). Morris and Rickard (1982) grouped galaxies into two categories based on the presence or absence of a strong, central CO peak superposed on the

TABLE 5–7. TOTAL (SINGLE-DISH) CO EMISSION[a]

| NGC | Outer Radius of Annulus (kpc) | | | | |
|---|---|---|---|---|---|
| | 0.5 | 1.0 | 1.5 | 2.0 | 2.5 |
| 4254 | 42.99 | 94.76 | 94.63 | 79.90 | 75.40 |
| 4303 | 51.02 | 125.0 | 166.8 | 186.2 | 190.9 |
| 4321 | 81.08 | 177.0 | 172.8 | 140.0 | 125.9 |
| 4501 | 24.48 | 63.93 | 91.44 | 109.7 | 120.7 |
| 4535 | 63.93* | 22.96* | 22.61 | 27.68 | 30.94 |
| 4536 | 87.73 | 118.0 | 117.9 | 107.0 | 89.00 |
| 4569 | 46.91 | 110.5 | 140.9 | 150.4 | 147.3 |
| 4654 | 22.42* | 33.56* | 17.36* | 39.16 | 62.71 |

[a] Values of $I_{CO}$ in Jy km sec$^{-1}$, based on models by Kenney (1987).

* Emission from interferometer map used instead of model.

usual disk emission. Sofue (1988) conjectured that many late-type spirals contain tiny, nuclear molecular disks characterized by high gas densities and large velocity dispersions. The hypothesized bright CO cores of spirals could not be demonstrated clearly from the single-dish maps available to Morris and Rickard (1982) and Sofue (1988). The interferometer maps presented in this thesis demonstrate the existence of nuclear CO concentrations. Small scale lengths and distinct central concentrations of CO emission are present in many of the interferometer images. It appears that nearly all spiral galaxies contain central regions of CO emission which are distinctly brighter and more centrally concentrated than a simple extrapolation of the outer disk gas exponential law would imply.

The problem of flux recovery given incomplete coverage of the *uv* plane is particularly troublesome in the case of an exponential source distribution, such as found in galactic disks. The interferometer has trouble with exponentials because the

Fourier transform of an exponential has considerable power at low spatial frequencies. Consider, for illustrative simplicity, the one-dimensional exponential function $f(x) = e^{-|x|}$. This function is shown with its Fourier transform,

$$F(s) = \int_{-\infty}^{\infty} f(x)\, e^{-2\pi i x s}\, dx = \frac{2}{1 + (2\pi s)^2}, \qquad (5-3)$$

in Figure 5–14. Note the relatively large amount of power at low spatial frequencies. The "hole" in the center of interferometric coverage of the *uv* plane prevents the recovery of large-scale source structure. Figure 5–14 motivates the idea that the central CO peaks in interferometer maps are the pointed centers of exponential disks with large scale lengths and that most of the large-scale emission has been resolved out by the interferometer, leaving only the pointed center in the interferometer maps. In the remainder of this section, it will be shown that the small scale lengths of the central CO distributions in interferometer maps are *intrinsic* and are not artifacts of resolution.

To determine if the observed interferometric CO profiles are consistent with the effect of resolution on extended exponential profiles, analytic modeling of interferometric observation of exponential disks was done. In the analysis, the model galaxy was assumed to be face-on. The sampling of the *uv* plane by the interferometer was modeled as a filled annulus with inner and outer radii corresponding to the shortest and longest projected baselines attained. In practice, the sampling of the *uv* plane is along elliptical arcs. A nonlinear algorithm such as MX effectively interpolates between the arcs to estimate the visibilities at unmeasured spatial frequencies in the *uv* plane. The assumption that the galaxy is face-on simplifies the analysis greatly and should not seriously affect the applicability of the models except in the cases of large galactic inclination. In those cases, the interferometer would be expected to recover somewhat more of the emission. The analysis should be regarded as a test of the viability of the hypothesis that small CO peaks result from interferometric observation

of extended exponential disks.

A detailed description of the analysis is included in Appendix D. Results of the modeling are shown in Table 5–8. The parameters $q_{\rm min}$ and $q_{\rm max}$ are Fourier conjugate ($uv$ plane) coordinates corresponding to $b_{\rm min}$ and $b_{\rm max}$, the minimum and maximum baselines. For the OVRO interferometer, the minimum projected baseline length is $b_{\rm min} = 10.4\,{\rm m}$; the typical maximum projected baseline length for the Virgo spiral observations (see Table 3–1) is $b_{\rm max} \approx 60\,{\rm m}$. The baseline lengths 10.4 m and 60 m correspond to values of $q$ of

$$\begin{aligned} q_{\rm min} &= \frac{1}{\lambda/b_{\rm min}} = 4000\,{\rm rad}^{-1} = 0.0194\,{\rm arcsec}^{-1}, \\ q_{\rm max} &= 0.112\,{\rm arcsec}^{-1}. \end{aligned} \qquad (5-4)$$

In some observations, $b_{\rm max}$ may be as large as 80 m, which is $q_{\rm max} = 0.1492\,{\rm arcsec}^{-1}$. In the modeling, nonlinear least squares fits of a resolved exponential function (see Appendix D) were made to the observed CO profiles. Three parameters were varied in the optimization: $q_{\rm min}$, $q_{\rm max}$, and the scale length, $a$. The goal was minimizing the $\chi^2$ of the fit and achieving a flux recovery rate close to the observed recovery ratio (Table 5–4). The vertical scale was freely adjustable in the fit.

TABLE 5–8. MODEL PARAMETERS

| NGC | $a$ | $q_{\rm min}$ | $q_{\rm max}$ | % |
|---|---|---|---|---|
| | arcsec | arcsec$^{-1}$ | arcsec$^{-1}$ | Recovered |
| 4303 | 7.7 | 0.0140 | 0.1120 | 32 |
| 4501 | 9.3 | 0.0280 | 0.1492 | 9 |
| 4535 | 5.0 | 0.0140 | 0.1000 | 46 |
| 4536 | 8.5 | 0.0070 | 0.0900 | 53 |
| 4569 | 8.0 | 0.0194 | 0.1421 | 26 |
| 4654 | 9.0 | 0.0070 | 0.0800 | 60 |

The most important deduction to be made from the values in Table 5–8 is that the exponential scale lengths are small, from 5″–10″ (350 pc to 750 pc). Therefore, the CO observations are consistent with the hypothesis that many spirals have central CO emission concentrations which are peaked on much smaller scales than the outer disk exponentials, with scale lengths 15″–72″ (1 kpc to 5.5 kpc), would imply. The scale lengths in Table 5–8 are somewhat larger than the estimates listed in Table 5–5, but those are measurements of profiles which are affected by resolution, whereas the model scale lengths reflect the true exponential shape, which is necessarily somewhat broader. The target flux recovery rates from Table 5–4 were matched very well by the models. The values of $q_{\rm min}$ and $q_{\rm max}$ that were necessary to match the observed profile shapes are reasonably close to the values of $q$ expected from the possible range of projected baselines. Note that source structure could affect both the flux recovery rate and the shape of the radial surface brightness profile.

Graphs of the observed surface brightness profiles together with the fitted model profiles are shown in Figures 5–15 to 5–20. Surface brightness data are crosses, the model profile is drawn with a solid line, and the original exponential function is a dashed line. The model profile fits only the inner part of NGC 4303 very well. Extra emission from emergent spiral arms and a larger cloud of emission near the edge of the field add to the average surface brightness at larger radii, causing deviation from the profile expected from a smoother distribution. Note that the fitted profile of NGC 4303 takes on negative values over quite a range of intermediate radii. Many of the other fitted profiles also have negative wells outside the central peak. Unphysical, negative emission is not included in the integrated emission maps (see §3.1.3). Therefore, the model profiles (which may have negative wells surrounding bright peaks) cannot fit the observed profiles (constructed only from positive emission) at all radii. However, regions of negative emission are frequently seen surrounding or adjacent to

the central peaks in single channel interferometer maps. The analysis in Appendix D provides a simple explanation of the negative wells as artifacts of finite coverage of the $uv$ plane.

The fit to NGC 4501 is fairly good in the inner part but suffers from the negative well in the fitting function. The low rate of emission recovery forced the $q_{\rm min}$ model parameter to take on a rather large value. There is probably a nearly uniform component of CO emission that is augmented with a CO peak, which would lead to the same flux recovery rate with a more reasonable $q_{\rm min}$ value.

The fit to NGC 4535 works very well with a rather short scale length. The fit to NGC 4536, which has a similar appearance, is good but does not work as well as NGC 4535. The large inclination of NGC 4536 and the CO source structure enable more emission to be detected interferometrically than predicted from a smooth exponential source distribution. This leads to the rather small $q_{\rm min}$ in the model, which allows more emission to be recovered.

Fair approximation to the data is made by the model of NGC 4569 with exactly the expected values of $q_{\rm min}$ and $q_{\rm max}$. Accurate fitting outside the central peak is made impossible by the negative well of the fitting function. A good fit is made to the NGC 4654 profile, but the larger flux recovery rate forces $q_{\rm min}$ to take a rather small value. The large amount of structure in the CO emission increases the amount of emission recovered by the interferometer.

NGC 4254 was not included in the modeling because it lacks a strong central source upon which to base the model. Fits of the NGC 4321 profile were attempted but abandoned: its radial surface brightness profile is shaped too differently to be interpretable as a resolved exponential. The great deal of source structure in NGC 4321 is at the root of the modeling problem.

The assumption that the centrally peaked CO profiles are exponentials was made

to simplify the mathematical analysis (Appendix D) and to provide a measure of the scale length of the peaks. The fact that the observed profiles are well fitted by mathematical models of the resolution of exponential peaks by an interferometer does not prove that the peaks are, indeed, exponentials. Any sufficiently pointy function (a Gaussian with small scale length, for instance) would, in fact, lead to similar results. The important point is that the scale lengths of the central peaks in CO emission are much smaller than typical disk scale lengths, independent of the choice of function to model their shapes. The small scale lengths suggest that the gas in the central regions of spirals is a distinct dynamical component, separate from the disk. It is possible that an increase in molecular cloud CO emissivity toward the centers of spirals contributes to the peaked nature of the central CO profiles. This possibility will be explored in Chapter 7. It is also likely that some physical process is actively transporting gas to the centers of spirals, which will be discussed in Chapter 8.

## References

Arsenault, R., Boulesteix, J., Georgelin, Y., and Roy, J.-R. 1988, *Astron. Ap.*, **200**, 29.

de Vaucouleurs, G., de Vaucouleurs, A., and Corwin, H. G., Jr. 1976, *Second Reference Catalogue of Bright Galaxies* (Austin: University of Texas Press).

Kenney, J. D. 1987, Ph.D. Thesis, University of Massachusetts.

Morris, M., and Rickard, L. J. 1982, *Ann. Rev. Astron. Ap.*, **20**, 517.

Scoville, N. Z., Sanders, D. B., and Clemens, D. P. 1986, *Ap. J.*, **310**, L77.

Sofue, Y. 1988, in *Molecular Clouds in the Milky Way and External Galaxies*, ed. R. L. Dickman, R. L. Snell, and J. S. Young (Berlin: Springer-Verlag), p. 375.

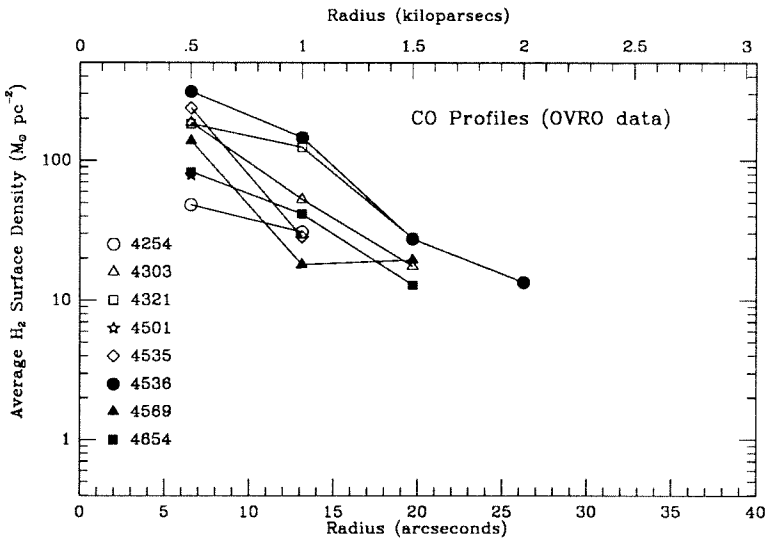


Figure 5–1. Radial profiles of CO emission converted to $H_2$ mass surface density using equation (3–3) and equation (3–4). All values are based on emission from interferometer maps alone, and represent averages within the central disk of radius 500 pc or surrounding annuli 500 pc wide. Data that are unreliable due to noise are not graphed.

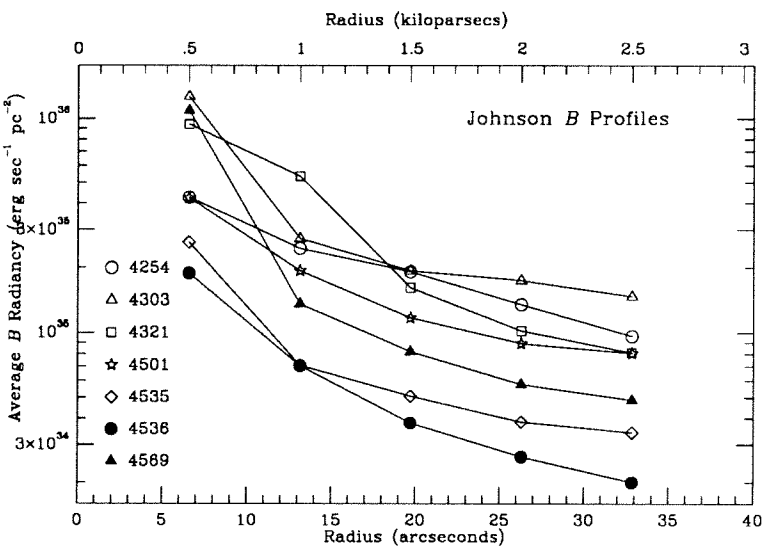


Figure 5–2. Radial profiles of $B$-band radiancy for Virgo spiral galaxies. All values are averages within the central disk of radius 500 pc or in surrounding annuli 500 pc wide.

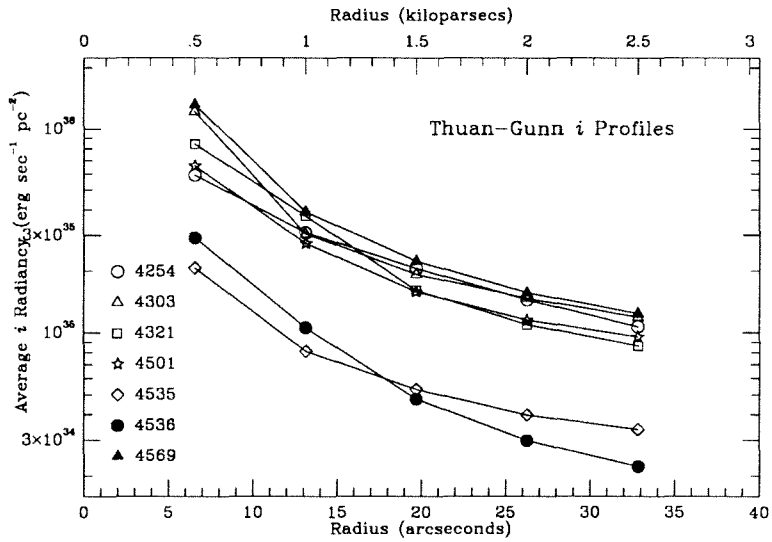


Figure 5–3. Radial profiles of Thuan-Gunn $i$-band radiancy for Virgo spiral galaxies. All values are averages within the central disk of radius 500 pc or in surrounding annuli 500 pc wide.

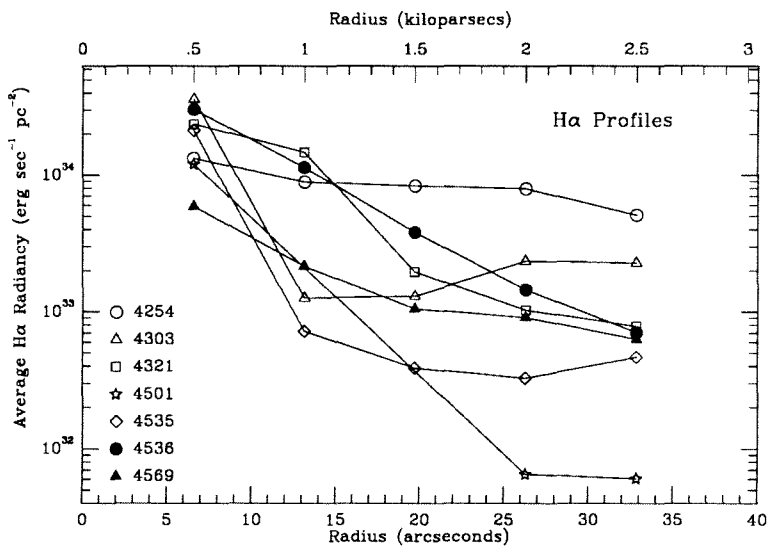


Figure 5–4. Radial profiles of H$\alpha$ radiancy for Virgo spiral galaxies. All values are averages within the central disk of radius 500 pc or in surrounding annuli 500 pc wide.

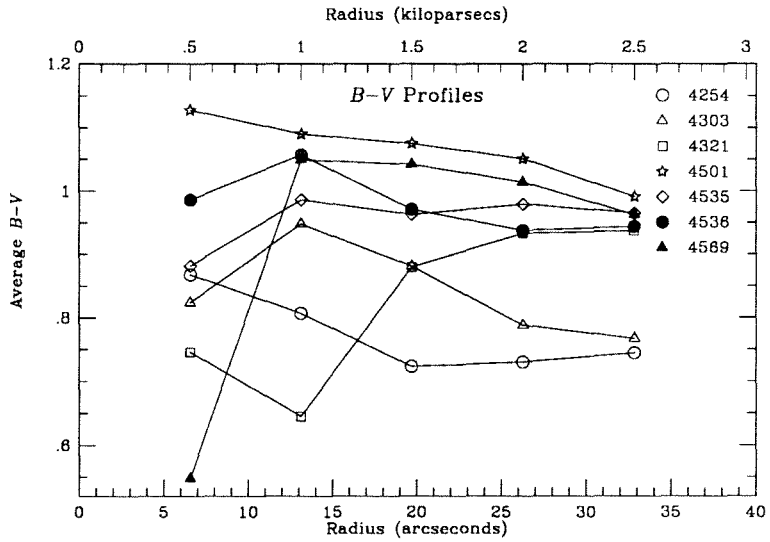


Figure 5–5. Radial profiles of $B-V$ color for Virgo spiral galaxies. All values are averages of $B-V$ color within the central disk of radius 500 pc or in surrounding annuli 500 pc wide.

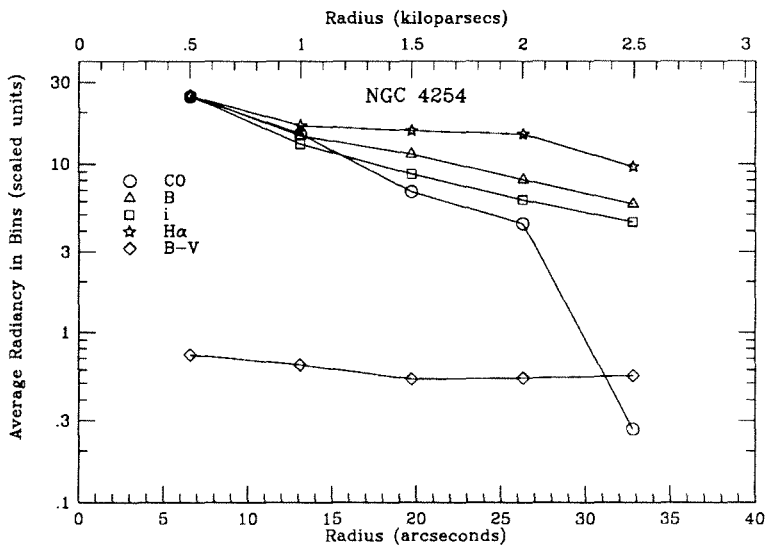


Figure 5–6. NGC 4254. Radial profiles of CO, Johnson $B$, Thuan-Gunn $i$, and H$\alpha$ radiancy with arbitrary normalization and $B-V$ color. Values are averages in the central disk of radius 500 pc or in annuli 500 pc wide.

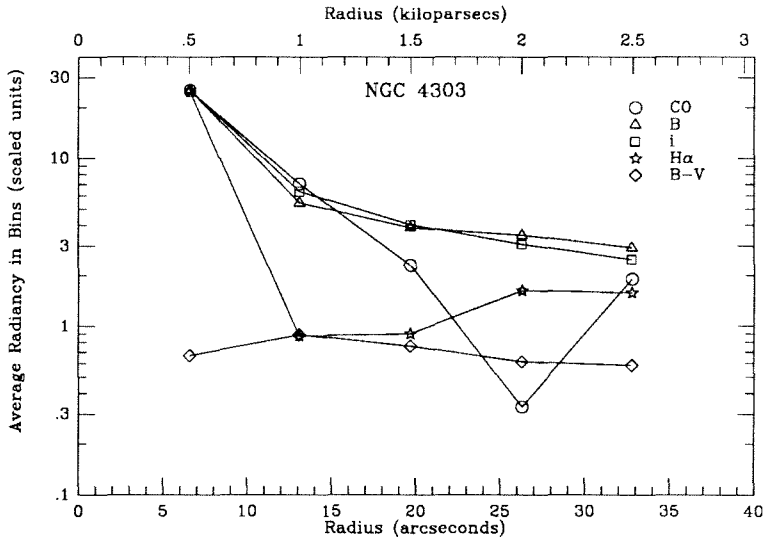


Figure 5–7. NGC 4303. Radial profiles of CO, Johnson $B$, Thuan-Gunn $i$, and H$\alpha$ radiancy with arbitrary normalization and $B-V$ color. Values are averages in the central disk of radius 500 pc or in annuli 500 pc wide.

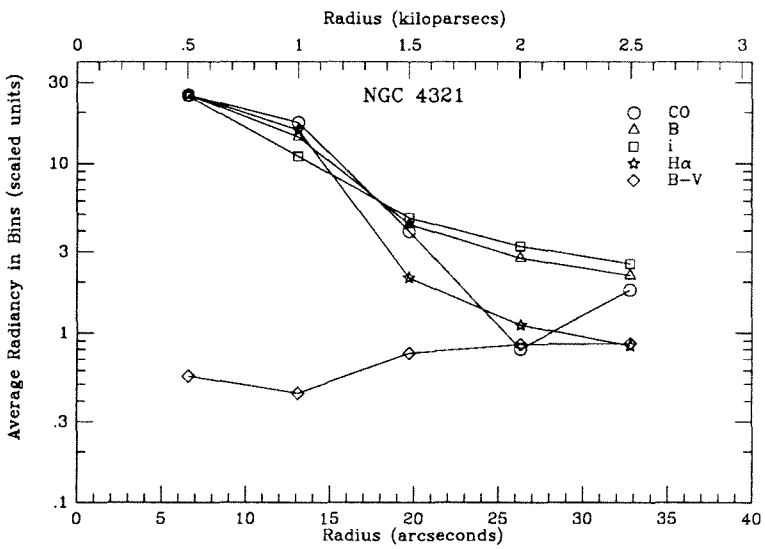


Figure 5–8. NGC 4321. Radial profiles of CO, Johnson $B$, Thuan-Gunn $i$, and H$\alpha$ radiancy with arbitrary normalization and $B-V$ color. Values are averages in the central disk of radius 500 pc or in annuli 500 pc wide.

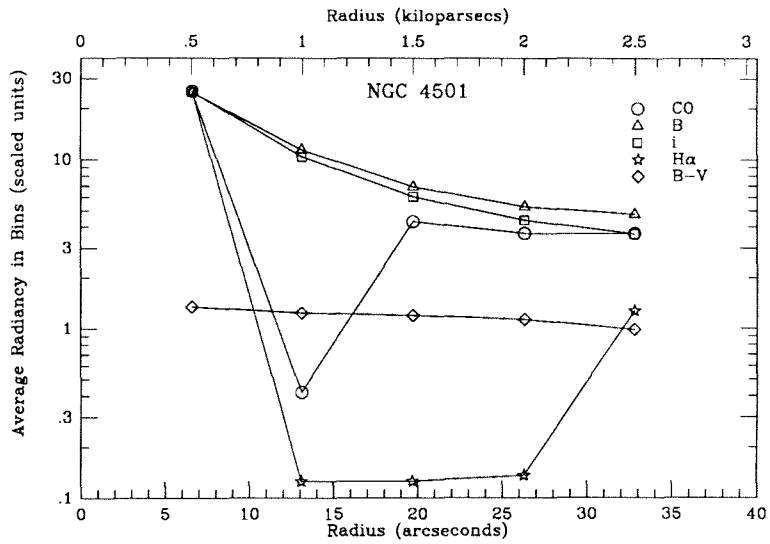


Figure 5–9. NGC 4501. Radial profiles of CO, Johnson $B$, Thuan-Gunn $i$, and H$\alpha$ radiancy with arbitrary normalization and $B-V$ color. Values are averages in the central disk of radius 500 pc or in annuli 500 pc wide.

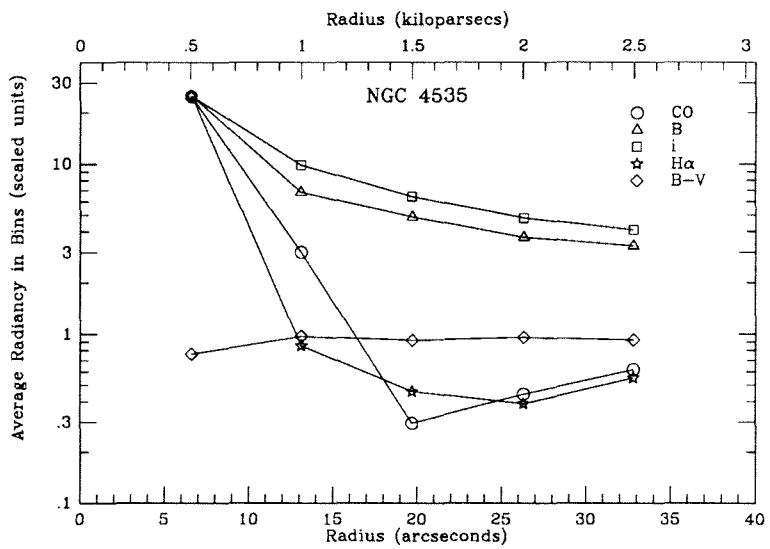


Figure 5–10. NGC 4535. Radial profiles of CO, Johnson $B$, Thuan-Gunn $i$, and H$\alpha$ radiancy with arbitrary normalization and $B-V$ color. Values are averages in the central disk of radius 500 pc or in annuli 500 pc wide.

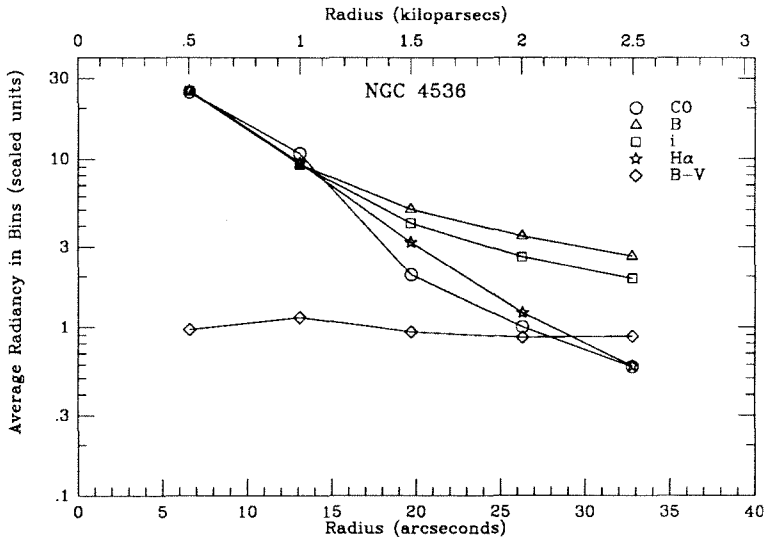


Figure 5–11. NGC 4536. Radial profiles of CO, Johnson $B$, Thuan-Gunn $i$, and H$\alpha$ radiancy with arbitrary normalization and $B-V$ color. Values are averages in the central disk of radius 500 pc or in annuli 500 pc wide.

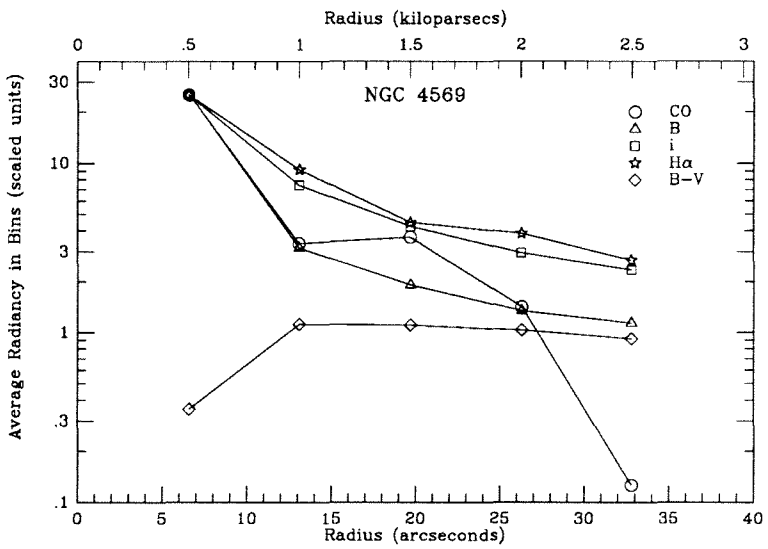


Figure 5–12. NGC 4569. Radial profiles of CO, Johnson $B$, Thuan-Gunn $i$, and H$\alpha$ radiancy with arbitrary normalization and $B-V$ color. Values are averages in the central disk of radius 500 pc or in annuli 500 pc wide.

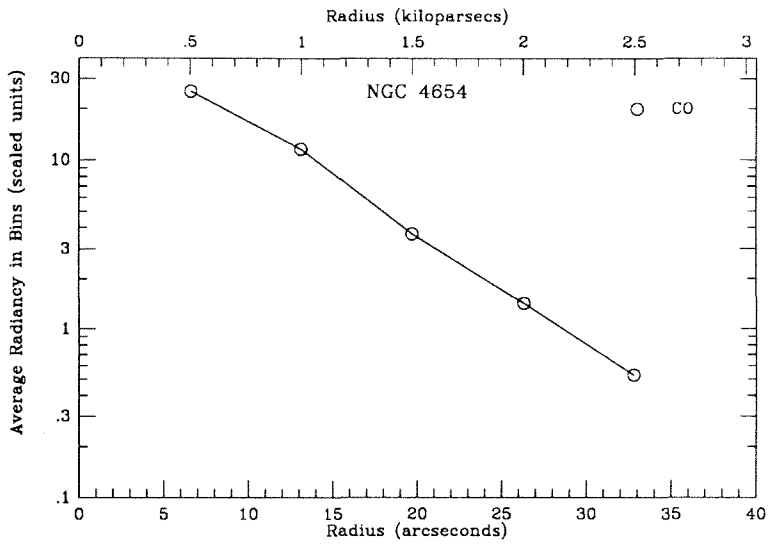


Figure 5–13. NGC 4654. Radial profile of CO radiancy with arbitrary normalization. Values are averages in the central disk of radius 500 pc or in annuli 500 pc wide.

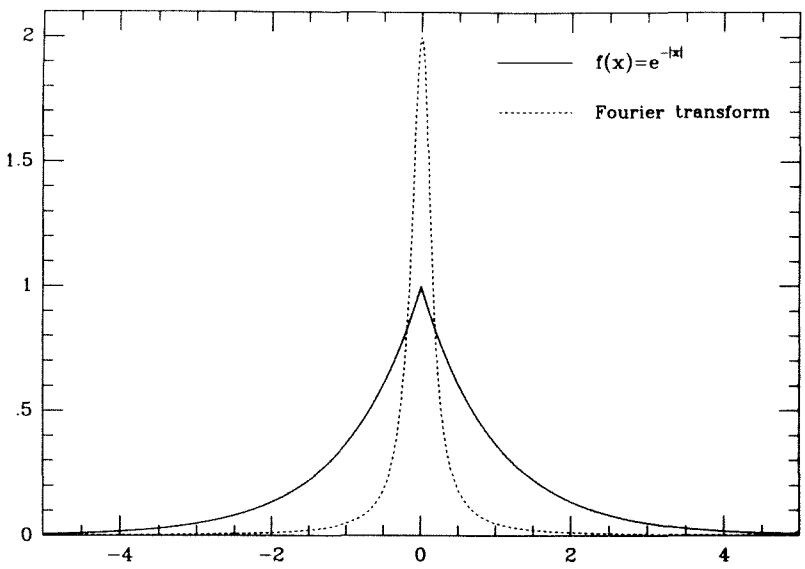


Figure 5–14. Exponential function and its Fourier transform. Note the large amount of power at low spatial frequencies (large scale lengths).

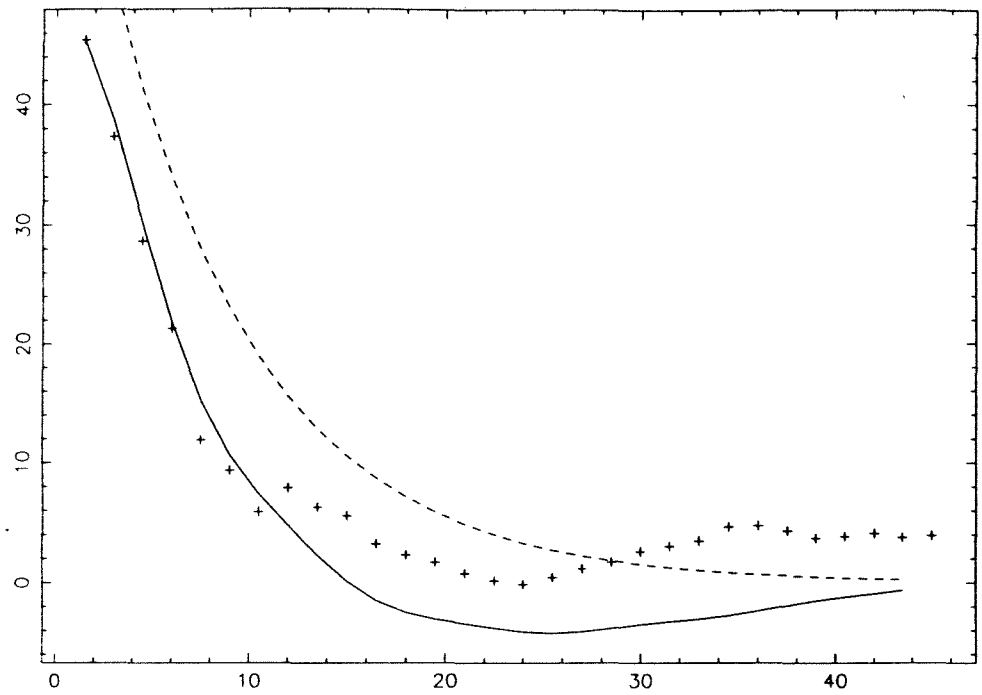


Figure 5–15. NGC 4303. CO radial emission profile (+) and fitted model profile (solid line) based on resolution of the exponential disk (dashed line) by the interferometer.

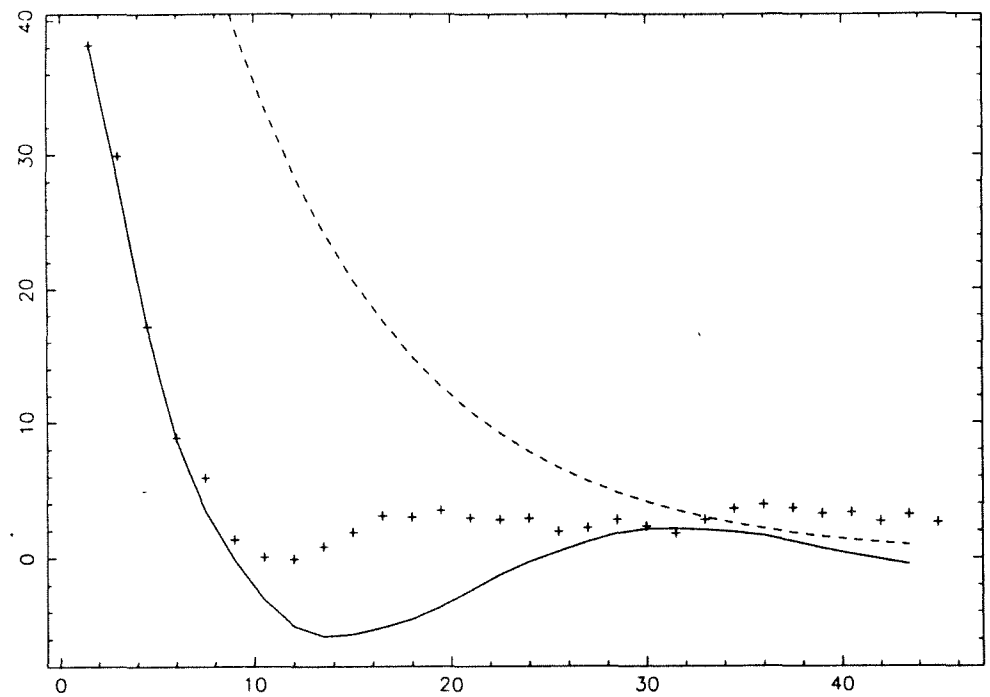


Figure 5–16. NGC 4501. CO radial emission profile (+) and fitted model profile (solid line) based on resolution of the exponential disk (dashed line) by the interferometer.

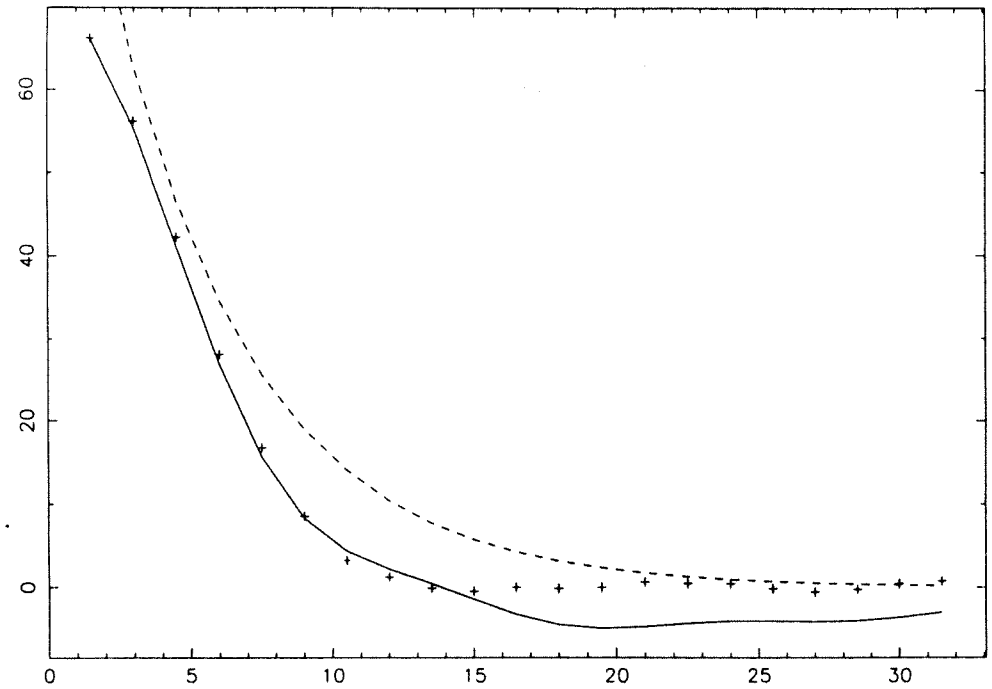


Figure 5–17. NGC 4535. CO radial emission profile (+) and fitted model profile (solid line) based on resolution of the exponential disk (dashed line) by the interferometer.

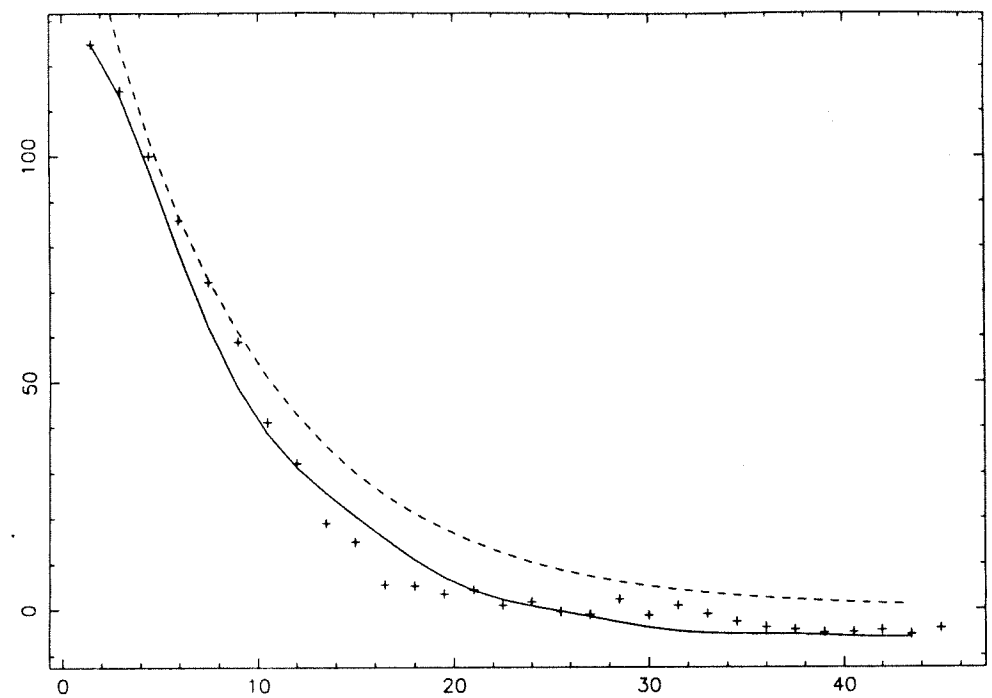


Figure 5–18. NGC 4536. CO radial emission profile (+) and fitted model profile (solid line) based on resolution of the exponential disk (dashed line) by the interferometer.

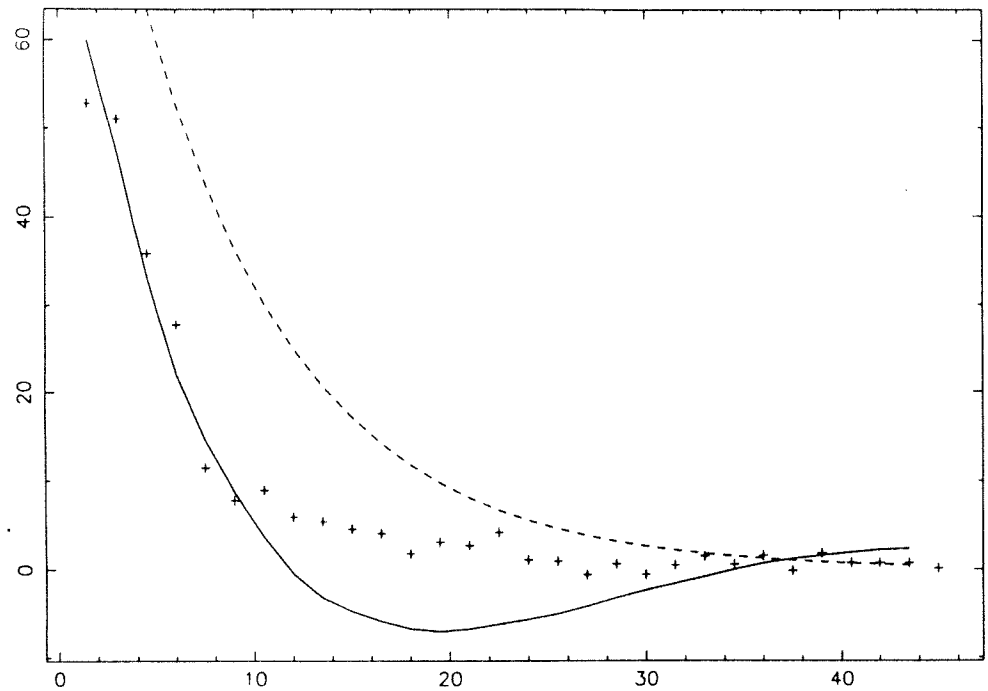


Figure 5–19. NGC 4569. CO radial emission profile (+) and fitted model profile (solid line) based on resolution of the exponential disk (dashed line) by the interferometer.

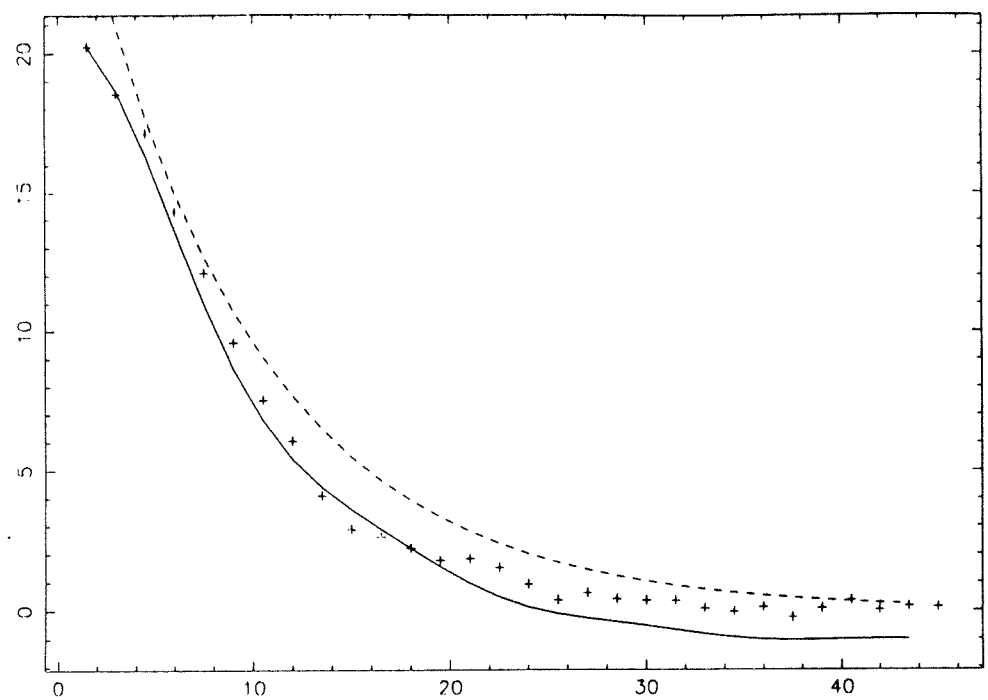


Figure 5–20. NGC 4654. CO radial emission profile (+) and fitted model profile (solid line) based on resolution of the exponential disk (dashed line) by the interferometer.

# Chapter 6
# Velocity Fields

The primary reason to measure the velocity fields of molecular gas in Virgo spiral galaxies is to derive rotation curves. If the gas moves in approximately circular orbits, then the rotation speed provides a means to estimate the total mass within the radius of the orbit. The ratio of gas mass to the total mass is an interesting quantity, for if it is large, then the dynamics are significantly affected by the gas. If the radial mass distribution is known, then the mass-to-light ratio can be computed from radial light profiles. The mass-to-light ratio roughly indicates the average lifetime star formation rate, if it has been monotonic. Further analysis of the mass of gas in the disks of Virgo spiral galaxies and its relation to the total disk mass will be explored in Chapter 7.

## 6.1. Construction of Velocity Fields from CO Spectra

### 6.1.1. Justification of Method

The multichannel images, or "data cubes," which emerge from the MX routine in AIPS contain information about the gas kinematics. The data in a cube may be thought of as spectra shot through the galaxy at each pixel position. Each spectrum may be viewed as a distribution of flux density with velocity. Under the assumption of uniform emissivity of all molecular clouds within a pixel, the spectrum indicates the distribution of velocities of molecular clouds within a pixel. Gas turbulence within individual clouds broadens the distribution, but the magnitude of cloud internal velocity dispersion ($\sigma_v \lesssim 3\,\mathrm{km\,sec^{-1}}$) is not noticeable in the data for this thesis because of the coarser resolution of the filterbank ($\approx 13\,\mathrm{km\,sec^{-1}}$).

A measurement of the mean velocity in the disk midplane along each line of

sight is made by estimating the peak of the velocity distribution. Why is the peak of the distribution used? Other analyses (Warmels 1986, for example) have used the maximum velocity or a windowing and averaging procedure. To address this question, imagine the synthesized beam superimposed on the target galaxy at an arbitrary position in the disk. The extremes in velocity sampled by the beam will lie somewhere along the beam edge and will have little weight (contribute only to the tail of the distribution). Emission from gas located near the center of the beam will be incorporated into the distribution with greatest weight. Under the assumptions that the gas emissivity is constant across the synthesized beam and that turbulent gas motions have a symmetric, centrally peaked distribution, it follows that the best estimate for the velocity of gas at the center of the pixel is the peak of the velocity distribution, or spectrum. To deal with the finite signal-to-noise ratio of spectral data, a Gaussian fit to the data near the peak of the line profile provides a good estimate of the peak.

CO spectra are not necessarily Gaussian in shape, and are usually not even symmetrical. Asymmetry may be caused by a variety of factors. Source structure will certainly contribute to an asymmetry in the emission profile. That is, variation in the gas distribution on scales smaller than the synthesized beam, assuming uniform emissivity, will affect the shape of the emission profile. The shape of the rotation curve within the synthesized beam may also affect the profile shape. If the slope of the rotation curve is constant across the beam, then all velocities will be sampled evenly across the beam. In this case, the rotation curve shape causes no velocity distribution asymmetries. If, however, the slope of the rotation curve changes across the beam, then asymmetries in the velocity distribution are likely to be seen. Velocities will be sampled more heavily where the rotation curve is flatter. These more heavily-sampled velocities will enter the distribution with larger weight, skewing it appreciably unless

brightness variations swamp the effect of the rotation curve. An illustration of this rotation curve effect is depicted in Figure 6–1. The velocity sampling function is flat for the inner, linear part of the rotation curve but becomes strongly peaked for velocities near the elbow of the rotation curve. Since the primary beam of an OVRO interferometer dish covers only the inner part of a typical Virgo spiral, where the rotation curve is approximately linear, this effect is not important in contributing to the skewing of CO emission profiles in this work.

The finite thickness of the molecular gas disk of a spiral galaxy also affects the profile shape. The line of sight through an inclined disk of finite thickness intersects circular orbits having a range of radii. Sampling a range of radii, and hence of circular speeds, results in a broad emission profile. In fact, the profile is also asymmetric, having a high peak corresponding to the heavy sampling of the midplane (highest velocity) gas and a long tail from lower-projected-velocity gas at larger radii in and out of the midplane. Results of modeling the velocity sampling of a typical synthesized beam on a galactic disk for two values of the disk inclination are shown in Figure 6–2. The effect is not very important except for large inclinations ($i \gtrsim 70°$), in which case the tail of the velocity distribution is able to shift the peak of the observed spectrum. The spectra in Figure 6–2 are modeled CO observations of a galactic disk with thickness 305 pc ($4''$ at the distance of Virgo). Perhaps 100 pc is a better estimate for the thickness of the CO layer in the inner part of a disk galaxy (Knapp 1987). The rotation curve of the model galaxy is linearly rising. Much broadening of the line results from the intercloud velocity dispersion, taken to be $10\,\mathrm{km\,sec^{-1}}$. The synthesized beam has dimensions $7''.9 \times 6''.4$, which is the beam size for observations of NGC 4536 reported in this thesis. Little asymmetry is apparent in the line profile of an identical disk viewed at an inclination of 30°. A comparison with selected spectra of NGC 4536 (Figure 6–3) helps to confirm the reality of the effect of finite disk

thickness on profile shapes.

The preceding analysis of profile shapes suggests that the weighted mean does not always accurately estimate the velocity at the peak of emission. The peak of emission corresponds most closely to the mean velocity of gas at a position along the line of sight in the midplane of the galaxy. Accurate estimation of the mean velocity is necessary to construct a rotation curve. The AIPS task MOMNT is commonly used to compute a velocity field from a data cube. MOMNT computes "moments" of an image; in particular, the first moment of a data cube is the emission-weighted mean velocity. The use of a flux threshold helps MOMNT to ignore noise and concentrate on peaks. A weighted mean will usually not locate the peak in the case of an asymmetric profile. Only when the flux threshold is chosen very high, thus tightly windowing the peak, will a weighted mean accurately locate the peak of a skewed profile. The use of a high threshold is not advantageous in practice because the velocity at low-flux pixels cannot then be calculated. Noise spikes and emission near the edges of the filterbank bias the weighted mean toward velocities closer to the center of the filterbank, which leads to a flattened rotation curve. MOMNT is inadequate for constructing velocity fields near the centers of spiral galaxies

### 6.1.2. Method for Measuring Velocity Fields

A FORTRAN program was written to replace MOMNT for computing velocity fields from data cubes. The program fits Gaussian profiles plus baselines to all spectra in a data cube. It uses a nonlinear least squares routine adapted from Bevington (1969). Noise statistics are computed from the fitted curve and the data and allow the selective display of all spectra that pass a signal-to-noise criterion. The spectra that are well fit by the program are interactively selected and poor fits and false signals are rejected. Pixel positions, centroid velocities, and profile widths from the Gaussian fits are the output of the program. The procedure is somewhat tedious

but is subjective only for the most noisy spectra. All numerical data concerning the velocity fields and rotation curves of Virgo spirals were produced with this program. Contour maps of the better CO velocity fields are shown in Figures 6–5 through 6–8.

Examination of the integrated CO emission images (Figure 4–8) shows that the source of emission is very compact for some galaxies (NGC 4501 and NGC 4569, for example). Indeed, the extent of the emission is on the order of the beam size, suggesting that the nuclear sources are nearly unresolved. While the source of emission may be unresolved in a single channel map, some degree of additional resolution is possible with many frequency channels. Because of the inherent rotation of the source of emission, the slope of the rotation curve and the inclination of the plane of the galactic disk work together to separate emission into different velocity channels. Emission from two points within one synthesized beam width would be blended in a wide-band image but are separated into different velocity channels by virtue of disk rotation. Although the resolution in each channel image is limited by the synthesized beam size, the spatial centroid of the emission is well defined. A velocity field can thus be constructed even across an emission region the size of the synthesized beam. Greater disk inclination helps to separate gas at different velocities more clearly. The limit of spatial resolution attainable in a velocity field is determined by phase error and the signal-to-noise ratio. Phase errors are generally kept within $\pm 30°$ at OVRO through calibration with a strong point source, yielding 1/6-beam spatial resolution in a velocity field. For the observations discussed here, this is about $1''$ or 76 pc at the distance of the Virgo Cluster.

Quite a bit of information about a galaxy can be gained from analysis of its velocity field. The most basic facts to be learned concern the galaxy's orientation: the kinematic center of rotation, the systemic velocity, the position angle of the line of nodes, and the inclination to the line of sight. Estimation of these parameters for disk

galaxies may be accomplished using optical methods. Measuring these orientation parameters using the velocity field relies on the assumption, as do direct optical methods, that the galaxy is a flat, smooth, circular disk. In the analysis of velocity fields, the inclination will be adopted from optical measurements of outer isophotes (Table 2–2). All other orientation parameters will be derived from the CO data.

A schematic velocity field for a typical spiral is depicted in Figure 6–4. This figure shows a disk at moderate inclination; the lines are isovelocity contours. The schematic velocity field contains only the rotational signature of the galaxy; perturbations due to streaming motions associated with spiral arms are omitted. Two main features are illustrated in the figure: the linear rise of velocity with radius in the inner disk and the constant velocity in the outer disk. The evenly spaced, straight isovelocity contours near the center are an indication of a linearly rising rotation curve. They result from the fact that the projected rotation velocity

$$V_{\rm proj} = V_c(r)\cos\theta\sin i = \alpha x \sin i, \qquad (6-1)$$

where the rotation velocity in the plane of the inner disk is $V_c(r) = \alpha r$, $\theta$ is the angle from the major axis (so $\cos\theta = x/r$), and $i$ is the inclination. The lack of dependence on $\theta$ implies straight isovelocity contours. In the outer part of the disk where the rotation speed is constant, the dependence of $V_{\rm proj}$ on $\theta$ leads to curved isovelocity contours.

The fit to the velocity field by the orientation parameters $x_0$, $y_0$, $V_{\rm sys}$, and PA is optimized by a procedure due to Warner, Wright, and Baldwin (1973), assuming the adopted inclination, $i$. A nonlinear least squares optimization routine based on a gradient search algorithm in Bevington (1969) is used. The procedure utilizes the entire velocity field. Initial guesses of the parameters serve to divide the velocity field into concentric elliptical annuli centered at the guessed $(x_0, y_0)$ with major axes along the guessed PA and axial ratios according to the adopted $i$. The weighted mean

velocity of all points lying within an elliptical, annular bin of width $2\,dr$ at radius $r$,

$$V(r) = \frac{1}{\sin i} \cdot \frac{\sum_{\theta} \sum_{r-dr}^{r+dr} W(r,\theta)\,|\cos\theta|\,(V_{\rm obs}(r,\theta) - V_{\rm sys})/\cos\theta}{\sum_{\theta} \sum_{r-dr}^{r+dr} W(r,\theta)\,|\cos\theta|}, \qquad (6-2)$$

is the best guess of the rotation velocity in the plane of the disk at radius $r$. Here, $\theta$ is the angle subtended by the ray from the origin to the pixel position $(x, y)$ and the positive branch of the major axis. $W(r,\theta)$ is the weight function, which is taken to be the peak value in the spectrum. Velocities based on low signal-to-noise spectra are given low weight. The factor $|\cos\theta|$ places small weight on velocities near the minor axis, where the geometric correction, $\sec\theta$, is large. The rms deviation from the mean, $\Delta V(r)$, is also computed for each annular bin. The weighted sum of these deviations is calculated as

$$G = \frac{\sum_{r=0}^{r_{\rm max}} \left\{ \sum_{\theta} W(r,\theta)\,|\cos\theta| \right\} [\Delta V(r)]^2}{\sum_{r=0}^{r_{\rm max}} \sum_{\theta} W(r,\theta)\,|\cos\theta|}. \qquad (6-3)$$

It is the purpose of the nonlinear least squares algorithm to minimize $G$, and hence minimize the deviation of velocities within each bin, through varying $x_0$, $y_0$, $V_{\rm sys}$, and PA.

Since the CO data consist only of the inner disk velocity field, there is little information in the isovelocity contours to guide the choice of $x_0$, $y_0$, and $V_{\rm sys}$. Absolutely straight, regularly spaced isovelocity contours hold no clue by which preferred values of $x_0$, $y_0$, and $V_{\rm sys}$ may be deduced. To aid the nonlinear least squares search algorithm, points are weighted within the search algorithm by the integrated emission at that position. This "center-weighting" scheme biases the program to find $(x_0, y_0)$ near the peak of emission and helps to stabilize the search algorithm. Table 6–1 presents the orientation parameters deduced from CO velocity fields using the opti-

TABLE 6–1.
ORIENTATION PARAMETERS FROM CO KINEMATICS

| Object NGC | $\alpha_{1950}$ | $\delta_{1950}$ | $V_{LSR}$ km sec$^{-1}$ | PA degrees |
|---|---|---|---|---|
| 4254 | $12^h\ 16^m\ 17^s.3$ | $14°\ 41'\ 47''$ | 2393.8 | 60.6 |
| 4303 | 12 19 21.6 | 04 45 01 | 1543.7 | −42.8 |
| 4321 | 12 20 23.3 | 16 05 56 | 1580.1 | 150.6 |
| 4501 | 12 29 27.7 | 14 41 45 | 2245.4 | 144.1 |
| 4535 | 12 31 48.0 | 08 28 22 | 1996.0 | 173.0 |
| 4536 | 12 31 53.4 | 02 27 52 | 1858.4 | −56.5 |
| 4569 | 12 34 18.9 | 13 26 20 | −186.9 | 21.9 |
| 4654 | 12 41 25.9 | 13 23 59 | 1069.0 | 120.6 |

mization equation (6–3). These compare very favorably with values adopted from the literature presented in Table 2–2 and Table 5–3.

## 6.2. Description of Velocity Fields

### 6.2.1. NGC 4254

The CO data for NGC 4254 do not have a very large signal-to-noise ratio. The most which can be reliably asserted is that the central velocity field is consistent with solid body rotation of the gas. To the northeast is where there is the most extensive continuous area of measured gas velocities. There is a chain of kinks in the isovelocity contours in the northeast which appears to be associated with the strong spiral arm that winds through that region. The kinks lie inside the spiral arm as marked by H$\alpha$ emission but coincide with the inner edge of CO emission. As noted in Chapter 4, the CO emission from NGC 4254 follows the H$\alpha$ arms but is interior to them. The amplitude of the velocity perturbation indicated by the kinks is about 10 km sec$^{-1}$. Given the small inclination of this galaxy (32°), this is a reasonable value according to density wave theory (see Visser 1980, and Warner, Wright, and

Baldwin 1973, for comparison with M81 and M33). The velocity contour kinks are due to the discontinous change in the velocity of gas clouds as they bunch up upon entering the density wave. The kinks are expected to be on the inner edge of the spiral arm. The amplitude of the velocity perturbation depends on the pattern speed and the velocity dispersion. In view of the marginal reliability of the data, further analysis is not warranted.

### 6.2.2 NGC 4303

The velocity field of the molecular gas in NGC 4303 is very interesting. The isovelocity contours are closely spaced near the very center of the galaxy, indicating a large mass concentration in the central 350 pc. Their appearance is consistent with solid body rotation of the central region. As discussed in Chapter 4, the gas is concentrated in a bar with curving ends which are probably incipient spiral arms. The isovelocity contours are perpendicular to the long axis of the gas bar, which coincides with the major axis of the galaxy. Outside the central solid body zone, the isovelocity contours turn to lie perpendicular to the spiral arms which curve away from the gas bar ends. That is, the contours are perpendicular to the ridgeline of the gas like the segments of an earthworm. The geometry of the gas isovelocity contours is not consistent with the usual pattern found for strong bars in numerical simulations (van Albada and Roberts 1981; Sanders and Tubbs 1980). Simulations of gas flow in strongly barred spirals indicates that the isovelocity contours in the barred region are oriented along the bar due to streaming motion. As discussed in Chapter 4, the bar in NGC 4303 is probably a weak bar with low pattern speed. The velocity gradient in the barred region of the simulations is more nearly perpendicular to the bar major axis, rather than parallel to it as seen in NGC 4303.

A highly conjectural hypothesis by Shlosman, Frank, and Begelman (1989) of a "bar within a bar" may also be consistent with the NGC 4303 observations. They

propose that a small, dynamically distinct gas disk may arise in the high-density, central region of a larger, normal bar. The gas disk would also be subject to the bar-mode instability, but kinematics of the gas flow have not been worked out.

CO velocities in the bright, amorphous region to the south of the molecular gas bar are uncertain due to the decreased sensitivity near the edge of the primary beam. The isovelocity contours run nearly along the major axis of the narrow stellar bar. It may be that this gas moves as expected for gas in a barred potential, although it is not clear how to connect its motion to that of the central gas.

### 6.2.3. NGC 4321

The velocity field of NGC 4321 is complex. The contours in the central part, corresponding to gas in the central and eastern bright CO features, are rather straight and parallel and very generally indicate solid body rotation. However, even in this relatively well-behaved area, there are velocity perturbations on the order of 20–30 $\mathrm{km\,sec^{-1}}$. Elsewhere, the velocity field is scarcely tractable at all. The spiral arm-like extensions to the north and south display isovelocity contours which bend like a slinky and are oriented perpendicular to the ridge lines of the arms. Similar behavior was noted in the curved elbows of the CO bar in NGC 4303. The bending of the contours is probably a manifestation of the velocity perturbation caused by a strong spiral density wave. Cayatte *et al.* (1990) mention the perturbations in the H I velocity field caused by the spiral arms, which must result from an exceptionally strong density wave. The rest of the CO velocity field is very confused and presents a forbidding problem of interpretation. In Chapter 4, a theory was proposed which explained the four-armed H$\alpha$ morphology as the result of interference of leading and trailing spiral waves. The extreme noncircularity of motions in the inner disk of NGC 4321 makes estimation of the total mass in the region from the rotation curve uncertain.

### 6.2.4. NGC 4501

There is very little CO emission from NGC 4501 with which to construct a velocity field. All that can be said is that the isovelocity contours are fairly straight and parallel and are consistent with solid body rotation of the centermost region, about 500 pc across. The central velocity gradient is rather steep.

### 6.2.5. NGC 4535

The velocity field of NGC 4535 is very regular and the isovelocity contours are parallel, indicating that the central region (about 800 pc in size) rotates as a solid body. The velocity gradient across the center is very steep, which indicates a large central mass concentration. At the northern and southern ends of the CO emission, the isovelocity contours first widen and then the indicated velocities decrease. This behavior causes the initially steep inner rotation curve to turn over abruptly and then dip. The decrease in apparent rotation speed may be due to the streaming motions in the spiral arms emerging from the north and south ends of the central gas concentration.

### 6.2.6. NGC 4536

The central velocity gradient of NGC 4536 is exceptionally steep. The isovelocity contours are straight and parallel, indicating solid body rotation for the central region. A slight widening of the isovelocity contours at the eastern and western ends causes the rotation curve to begin to turn over, although the turnover radius is not achieved yet at the farthest extent of the CO velocity data. There is a suggestion of an S-shape for the isovelocity contours crossing the central region. S-shaped contours are normally associated with strong bars (van Albada and Roberts 1981). If there is a central bar, then it is oriented with its major axis pointed nearly along the line of sight. Streaming motions of gas along the length of the bar could cause the large central velocity gradient. However, the central morphology is also consistent with

being a spheroidal feature seen in projection. An alternative interpretation of the velocity field geometry is that the central region exhibits solid body rotation and perturbations of the velocities are caused by the spiral arms which originate to the north and south. Selection between these alternatives is impossible without a more extensive velocity field.

### 6.2.7. NGC 4569

The CO emission from NGC 4569 is not very extensive, so there is little information upon which to create a velocity field and little structure can be discerned from the isovelocity contours across the compact, central CO source. Curvature of the contours is not entirely consistent with solid-body rotation, but there could be anomalous velocities caused by a weak signal. Gas motions associated with the central source that gives rise to the LINER spectrum (see Chapter 4) could have a significant noncircular component. The peculiar, low-brightness CO feature to the south has a strange velocity field. It has a velocity gradient of $70\,\mathrm{km\,sec^{-1}}$ over about 400 pc in the direction of the minor axis. Given the weak signal in the feature, the significance of the velocities there is marginal. The entire H I velocity field measured by Cayatte *et al.* (1990) is disturbed and nonuniform, which may be as much due to the low level of H I emission as it is to the peculiar spiral structure of the galaxy.

### 6.2.8. NGC 4654

The velocity field of NGC 4654 is very regular, with rather straight and uniformly spaced isovelocity contours. There is a velocity gradient at the very center (the peak of CO emission) which is slightly steeper than the uniform gradients to the east and to the west. Except for the innermost 300 pc, solid body rotation for the entire extent of the CO emission is indicated by the evenly spaced isovelocity contours. Interpretation of the central feature as a bar is not supported by the geometry of the gas velocity field. There is a perturbation on the order of $30\,\mathrm{km\,sec^{-1}}$ in the velocities just south

of the peak of CO emission. A peculiar spur of CO emission emerges from that point, and was conjectured in Chapter 4 to be due to molecular gas swept up by an expanding supershell. The signal from the CO feature to the south is unfortunately too small to permit construction of a velocity field.

## 6.3. Rotation Curves

### 6.3.1. Construction of Rotation Curves

Once the kinematic parameters are found, analysis of the velocity field may proceed with the derivation of a rotation curve. The rotation curve of a galaxy is the relation between mean rotation speed of the disk and radius. The values of $x_0$, $y_0$, and $V_{\rm sys}$ from the CO kinematics (Table 6–1) were used along with the adopted values of PA and $i$ (Table 2–2) based on optical and radio studies in the literature. A correct choice of $x_0$ and $y_0$ symmetrizes the rotation curve and eliminates anomalous curvature at small radii, while the correct choice of $V_{\rm sys}$ ensures that the pieces of the rotation curve on both sides of the minor axis are identical. These purposes are best served if $x_0$, $y_0$, and $V_{\rm sys}$ are values derived from the velocity field itself by the least squares minimization of errors described in §6.1.2. Values of PA and $i$ adopted from the literature are used for reasons of consistency. The values of PA deduced from the CO data are in excellent agreement with those adopted from the literature.

Computation of the rotation curve begins with a list of pixel positions and velocities. The pixel spacing was chosen to be $4''.5$ to roughly agree with a typical synthesized beam size (and therefore not to oversample the data) and to increase signal-to-noise over the AIPS images with $1''.5$ pixels. Only pixels with positions within 30° of the position angle of the major axis are included in the deprojection computation (described below), except for the most highly inclined galaxies (NGC 4501, NGC 4536, and NGC 4569), for which points within 45° were accepted. This selection criterion is used so that points with the greater deprojection corrections, and

hence larger uncertainties, are excluded.

To compute a rotation curve from observed positions and velocities at those positions, correction for projection effects must be made. The deprojection transformations are fully described in Appendix C. The equations used to compute the rotation curve data are written out explicitly here. Let

$$pa = 90° + \mathrm{PA}, \tag{6-4}$$

so $pa$ is an angular measure corresponding to the mathematical convention of naming angles as a counterclockwise rotation from the (horizontal) $x$-axis. Let $(x, y)$ be the position of a pixel in the same system which is used to specify the kinematic center $(x_0, y_0)$. The $x$-coordinate requires a rotation correction,

$$x_{\mathrm{real}} = (x - x_0)\cos pa + (y - y_0)\sin pa, \tag{6-5}$$

while the $y$-coordinate requires correction for rotation and inclination,

$$y_{\mathrm{real}} = [(y - y_0)\cos pa - (x - x_0)\sin pa]/\cos i. \tag{6-6}$$

The deprojected radius is then

$$r_{\mathrm{real}} = \sqrt{x^2_{\mathrm{real}} + y^2_{\mathrm{real}}}. \tag{6-7}$$

The deprojected angle between the pixel position and the major axis is

$$\theta_{\mathrm{real}} = \arctan(y_{\mathrm{real}}/x_{\mathrm{real}}). \tag{6-8}$$

Only pixels for which $\theta_{\mathrm{real}}$ satisfies the selection criterion ($\pm 30°$ or $\pm 45°$ for larger $i$) are included in the rotation curve. The circular velocity $V_c(r_{\mathrm{real}})$ at radius $r_{\mathrm{real}}$ is

$$V_c(r_{\mathrm{real}}) = (V_{\mathrm{obs}} - V_{\mathrm{sys}})/\sin i \cos\theta_{\mathrm{real}}. \tag{6-9}$$

A list of $(r_{\mathrm{real}}, V_c(r_{\mathrm{real}}))$ pairs constitutes the rotation curve.

### 6.3.2. Description of the Rotation Curves

The CO data are a valuable addition to optical and H I data. The CO data have high spatial resolution and are not subject to extinction. Accurate rotation curves for the inner regions of the program spirals enables accurate estimation of the central dynamical masses. Rotation curve data were sought from recently published literature so that CO rotation curve data could be compared with data derived from motions of other gas constituents of Virgo spirals. H$\alpha$ emission line data were found, sometimes included with [N II] and [S II] data (Afanas'ev *et al.* 1988; Chincarini and de Souza 1985; Rubin *et al.* 1985; Rubin *et al.* 1989; Woods *et al.* 1990), and excellent H I data were found (Guhathakurta *et al.* 1988). In most cases, the position angle and inclination that were used to construct the rotation curves were at variance with the adopted values used in this study. In those cases, corrections were made to both the radius and the rotation speed by first deprojecting using the position angle and inclination in the literature and then reprojecting using the adopted parameters in Table 2–2. In this manner, the data were made as homogeneous as possible and comparisons could be made directly. There is usually no way of knowing the kinematic center that was used in the published studies, so no correction for misalignment, such as an off-center slit position, was made. Figure 6–9 and Figure 6–10 display all of the rotation curves together for comparison.

Before launching into detailed discussion of individual rotation curves, one general remark about the quality of the data will be made. It is noted that the emission line data reported by Chincarini and de Souza (1985) are generally at variance with all other comparison data reported here, even after correction for the adopted position angle and inclination, in the sense that their rotation speeds are systematically lower than other data shows. The reason for this discrepancy may be an off-center slit position. In that case, lower rotation speeds would result, especially at and beyond

the turnover region of the rotation curve. Due to this systematic discrepancy, data from Chincarini and de Souza (1985) were ignored in rotation curve analyses and do not contribute to the following discussion.

**NGC 4254**

NGC 4254 is a large, late-type Sc spiral with much high-mass star formation in its disk. Its rotation curve (Figure 6–11) has a moderately steep rise which gives it an average central mass concentration with respect to the other spirals studied. The rotation curve turns over around 50″ radius (4 kpc), which is about the extent of the main star-forming disk. Outside this radius, star formation is apparently more sparse along the arms. There is a jog in the rotation curve at 160″ radius (12 kpc) which coincides with the edge of the actively star-forming disk. The rotation curve continues to rise to at least 225″ radius (17 kpc); a single datum beyond this, of lower rotational speed, may indicate the flattening or decline of the rotation curve. The rotation speed at the largest measured radius is modest, about 210 km sec$^{-1}$, placing NGC 4254 at the low end of asymptotic rotation speeds for the eight Virgo spirals studied. The CO velocity data, although scant, agree very well with the H I data.

**NGC 4303**

NGC 4303 is an interesting Sbc-type spiral. The inner rotation curve rises very sharply, having one of the steepest central velocity gradients of all the spirals studied here (Figure 6–12). A very large, centrally concentrated mass is indicated by the steepness of the inner rotation curve. The CO data, with better resolution than the H I data, indicate a turnover and decline in the rotation speed beyond 8″ radius (600 pc), while the H I data are inconclusive about the shape of the rotation curve inside 30″ radius (2 kpc). The turnover in the CO rotation curve (Figure 6–13) is due to the velocity contours following the ridge-line of the curving spiral arms at the ends of the gas bar, and probably does not indicate a drastic decrease of the local mass

surface density. After its rapid rise and decline, the rotation curve rises again and remains approximately flat to 315″ radius (24 kpc) at least. There is a single ripple in the H I rotation curve around 150″ radius (11 kpc) that roughly coincides with the radii of the two outermost spiral arms, which appear to be nearly circular. The asymptotic rotation speed is only about 150 km sec$^{-1}$, the lowest of the eight spirals studied.

Figure 6–14 shows graphs of the angular frequency, $\Omega$, along with the angular frequencies $\Omega+\kappa/2$ and $\Omega-\kappa/2$. All quantities are computed from the data except where derivatives are required; then the rational function fit (Table 6–2) is used. Curves through the data are computed solely from the rational function fit. The position of an inner Lindbald resonance occurs where the pattern speed $\Omega_p = \Omega - \kappa/2$, and of the outer Lindblad resonance where $\Omega_p = \Omega + \kappa/2$. Current wisdom places corotation, which is where $\Omega = \Omega_p$, at the bar ends, which is 1.7 kpc radius in NGC 4303. Reading from Figure 6–14, this implies a pattern speed of $\Omega_p \approx 75$ km sec$^{-1}$ kpc$^{-1}$, which will just barely lead to an inner Lindblad resonance at a very small radius, probably within 500 pc. The outer Lindblad resonance is at 3.2 kpc radius, which coincides with the radius at which the spiral arms begin to open out (that is, where the pitch angle increases). This agrees with the qualitative behavior predicted by Combes and Gerin (1985), although the pattern speed of 75 km sec$^{-1}$ kpc$^{-1}$ is faster than expected.

### NGC 4321

NGC 4321 is a large Sbc spiral. Its inner rotation curve rises with about average slope compared with the other spirals studied. The CO data is somewhat at variance with the H$\alpha$ data (Figure 6–15), but there is much scatter in the CO velocities. A likely cause of the scatter is strong noncircular motion, even near the center of the galaxy, due to velocity structure across the arms of a strong spiral wave. The H$\alpha$

data data strongly indicate a bend in the rotation curve at 40″ radius (3.5 kpc) in the transition region between the inner (solid body plus spiral perturbation) and outer (asymptotic speed) regions. This is the radius at which the outer spiral arms emerge. Between 50″ and 80″ radius (4 and 6 kpc) there is disagreement by as much as 30 km sec$^{-1}$ between the H$\alpha$ and H I rotation speed data. It is conceivable that the H$\alpha$ data is errant, since there is no strong H$\alpha$ emission for this range of radii along the slit position, which falls in an interarm region. However, the H I data are subject to beam-smearing and would be strongly affected by the noncircular motions in the inner disk. Both H$\alpha$ and H I rotation curves subsequently converge and continue to rise out to 165″ radius (13 kpc), which is the edge of the actively star-forming disk. Beyond that radius, only H I data exist, and there is an unquestionable drop in rotation speed out to 255″ radius (19 kpc). The asymptotic rotation speed, until the drop-off at 13 kpc, is about 225 km sec$^{-1}$, placing it around the median asymptotic speed among the spirals studied.

**NGC 4501**

NGC 4501 is an early-type (Sb) spiral with tightly-wound, short spiral arms. Its rotation curve (Figure 6–16) rises with modest slope, being near the median of the spirals studied. The CO data, though scant because of the limited extent of the CO emission, agree well with H$\alpha$ data. The H I data are at consistently smaller rotation speeds than the H$\alpha$ data.The rotation curve gradually makes a transition between the inner (solid body) and outer (asymptotic) regions between 30″ and 40″ radius (2 to 3 kpc). This region corresponds to the innermost approach of active high-mass star formation in the disk. NGC 4501 is apparently very massive, for the asymptotic rotation speed achieved by the H I data is nearly 300 km sec$^{-1}$ at 225″ radius (17 kpc), which is by far the largest rotation speed measured among the spirals surveyed (but see the discussions of NGC 4536 and NGC 4569).

**NGC 4535**

NGC 4535 is a very large Sc-type spiral. CO, H$\alpha$, and H I rotation curve data are all in excellent agreement (Figure 6–17). The inner rotation curve has one of the steepest slopes among the spirals studied, indicating a massive center. The rise is steep and linear to nearly 10″ radius (750 pc), at which point there is an abrupt break, followed by a curve with much shallower slope, still approximately linear. The transition region in the rotation curve seems to correspond with the edge of the small, bright nucleus. The scatter in the H$\alpha$ data between 10″ and 50″ radius (750 pc to 4 kpc) is probably due to the absence of strong H$\alpha$ emission in that region. The rotation curve is still rising at 255″ radius (19 kpc), where the rotation speed is about 260 km sec$^{-1}$, which is average for the spirals studied. The linear portions of the curve combine with the abrupt break at 10″ to give the curve a very peculiar appearance. A jog in the H I rotation curve at about 120″ radius (9 kpc) cannot definitely be associated with any disk feature, being in the interarm region just inside the outermost spiral arms.

**NGC 4536**

NGC 4536 is a very inclined Sbc-type spiral. The CO rotation curve data (Figure 6–18) have good signal-to-noise and come from a well-ordered velocity field. Unfortunately, the only data available for comparison are H$\alpha$ emission line data (Afanas'ev *et al.* 1988) that display such aberrant behavior that their credibility is questionable (Figure 6–19). Its large inclination makes it probable that extinction in the disk midplane hides emission and that the questionable H$\alpha$ spectroscopy is sampling foreground gas velocities. One distinct problem with the spectroscopy is that the slit was placed 34° away from the major axis of the galaxy, thereby increasing the effect of projection on the data and the correction needed to convert to rotation speed in the plane of the disk. For a galaxy with large inclination, the

correction is substantial even for small angular departures from the major axis, and it is somewhat reassuring that the H$\alpha$ rotation curve data agree with the CO data in the inner region. The central velocity gradient of NGC 4536 is the steepest of the spirals studied. A large, central concentration of mass is indicated by the steep inner rotation curve. The transition from solid body rotation to the asymptotic region occurs at about 20″ radius (1.5 kpc), which is at the edge of the bright, extended nuclear region. Although the H$\alpha$ data are suspect, they indicate reasonable rotation speeds around 120″ (9 kpc) from the center, about 200 km sec$^{-1}$, making NGC 4536 one of the more massive of the spirals studied.

**NGC 4569**

NGC 4569 is the earliest type of spiral studied, being an Sab galaxy. It has a very blue nucleus, but is classed as an early-type due to its thick, ill-defined spiral arms. Depletion of neutral hydrogen in this galaxy's outer disk (Kenney and Young 1988) has possibly contributed to the disk appearance. This galaxy has been studied extensively, and the CO data agree well with other rotation curve data (Figure 6–20), although the CO data favor a slightly larger central velocity gradient. The slope of the inner rotation curve is the least among all the spirals studied, indicating very little central mass concentration. Despite its initially shallow slope, the rotation curve continues to rise out to the last measured point (only 105″, or 8 kpc radius), where the rotation speed is a substantial 240 km sec$^{-1}$, second only to the asymptotic speed of NGC 4501. Extrapolating the rotation curve to larger radii indicates a large mass for NGC 4569, although H I stripping in the outer disk may have removed enough mass to cause the outer rotation curve to turn down.

**NGC 4654**

NGC 4654 is the latest-type spiral of those studied, being an Scd galaxy. The CO data are of excellent quality and their agreement with optical rotation curve

data is excellent (Figure 6–21). Solid body rotation for the inner 30″ radius (2 kpc) is implied by the linearly-rising rotation curve. There is then a sharp break in the optical rotation curve data, similar to the case of NGC 4535. The slope of the inner rotation curve is relatively small, exceeding only that of NGC 4569. A comparatively small mass for the inner disk of NGC 4654 is indicated by the small slope. The behavior of the outer rotation curve is uncertain and its measurement is made difficult by the asymmetric distribution of stars and gas in this galaxy (Cayatte *et al.* 1990). The H I data indicate lower rotation speeds relative to the optical and CO data because they were prepared as averages between speeds on approaching and receding sides of the galaxy, and the H I velocity field for NGC 4654 is very asymmetric (Cayatte *et al.* 1990). The asymptotic rotation speed of NGC 4654 is probably relatively small, $200\,\mathrm{km\,sec^{-1}}$ or less, which is among the lowest asymptotic speeds in the spirals studied.

### 6.3.3. Synopsis and Comparison

Features of rotation curves, such as the location of the transition region (between the linear inner curve and the flat outer curve) and waves or jogs in the asymptotic (flat) region, can often be associated with features in the optical or star-forming disk. The transition region may mark the outer edge of the nucleus or bright, central, star-forming region, as in NGC 4535 and NGC 4536. The transition region has also been noted to mark the inner edge of high-mass star formation or spiral arm origination in the disk, as in NGC 4321 and NGC 4501. The transition region marks the outer edge of the most active part of the star-forming disk in NGC 4254. Ripples or waves in the asymptotic region mark the outer edge of high-mass star formation or the outer spiral arm radii in NGC 4254 and NGC 4303. A decline in the rotation curve, whether it is a dip in the inner rotation curve or a decline in the outer rotation curve, indicates a lack of or end to high-mass star formation in NGC 4303 and NGC 4321.

Sometimes, the rotation curve is fairly featureless and modestly curved, as in the case of NGC 4569, and so draws attention to no region in particular. In other cases, there is no conspicuous disk feature associated with a rotation curve feature, as for NGC 4654 (although the lack of a high-resolution image of the entire galaxy impedes identification in this case).

The observation that the shapes of rotation curves often reflect optical disk morphology is not surprising. The shape of a rotation curve indicates the rate at which the mass distribution in a galaxy is changing with radius. The rate, or even the incidence, of star formation has long been connected with the local gas density (Schmidt 1959). The rate of massive star formation has been linked recently by Kennicutt (1989) to the detailed shape of the rotation curve (through the epicyclic frequency) and the local gas surface density. Quite a diverse list of optical disk features were noted above, and the same feature in different rotation curves was often associated with a different disk feature. For instance, sometimes the transition region of the rotation curve marked an inner boundary and sometimes an outer boundary. Based on Kennicutt's recent analysis (1989), it is possible that the onset of high-mass star formation in a disk, or its decline, depends in detail not only on the local gas density but on the total mass, as well, and on how fast the mass surface density is changing locally. With such complex behavior, it is no wonder that diverse disk features may be connected with similar rotation curve features.

## 6.4. Mass Distributions from Rotation Curves

The variation of total mass with radius may be computed from the rotation curve and a model of the mass distribution. For a spherically symmetric distribution of mass, the mass $M(r)$ within radius $r$ depends on the circular speed $V(r)$ through

$$M(r) = (2.313 \times 10^5)\, V^2_{\mathrm{km\,sec^{-1}}}\, r_{\mathrm{kpc}}, \qquad (6-10)$$

where $M(r)$ is in solar masses. The distribution of mass in a thin disk may be computed from the rotation curve, $V(r)$, using the method of Nordsieck (1973). His formula contains an error term for estimating the contribution to the circular speed by the unknown mass distribution beyond the last measurement of $V(r)$, and is designed for easy numerical handling of singularities in the integrals. Nordsieck's formula (10) for the mass surface density $\mu(r)$ is

$$\mu(r) = \frac{1}{2\pi G}\left(\int_r^R \frac{V^2(u)}{u^2}\,du + \int_0^{r-\Delta r_1} \frac{dV^2}{du}\frac{2}{\pi r}\left[K\left(\frac{u}{r}\right) - \frac{\pi}{2}\right] du + \right.$$
$$+ \frac{dV^2(r)}{dr}\left[S_1(\Delta r_1) + S_2(\Delta r_2)\right] + \int_{r+\Delta r_2}^R \frac{dV^2}{du}\frac{2}{\pi u}\left[K\left(\frac{r}{u}\right) - \frac{\pi}{2}\right] du + ,$$
$$\left. + \frac{V^2(R)}{R}\left\{0.55 - 0.05\left(\frac{r}{R}\right)^2\left[1 + \left(\frac{r}{R}\right)^4\right] \pm 0.20\right\}\right) \qquad (6-11)$$

where $r < R$ and $R$ is the radius of the outermost measured point, $G$ is the gravitational constant, $K$ is the complete elliptic function of the first kind, $\Delta r_1$ and $\Delta r_2$ are small compared to $r$, and $S_1$ and $S_2$ are functions tabulated by Nordsieck (1973). The final term takes care of the error in $\mu(r)$ due to the unknown contribution to $V(r)$ by the mass beyond $R$. The first term in equation (6–11) has been corrected for a typographical error in Nordsieck's original paper. The range in mass spanned between estimates computed by assuming spherical symmetry or a thin disk geometry approximates the total range within which the true mass must lie. A factor of two or more may separate the two mass estimates at small radii, with the thin disk carrying more mass, but the estimates approach each other at large radii. The mass distribution of a real galaxy, which is variously dominated by bulge, disk, and halo components at different radii, falls within the extremes marked by the spherical and thin disk mass models.

Use of either equation (6–10) or (6–11) requires at least an estimate of the characteristic circular speed $V(r)$ at radii of interest; moreover, the thin disk mass model

formula (6–11) requires a differentiable estimate. A rational function of form

$$V(r) = \frac{a_3 r^3 + a_2 r^2 + a_1 r}{b_3 r^3 + b_2 r^2 + b_1 r + b_0}, \qquad (6-12)$$

where the $a_i$ and $b_i$ are numerical coefficients, is fitted to the rotation curve data for each galaxy using a nonlinear least squares algorithm. The form (6–12) has three desirable properties that make it far superior to polynomial approximations to rotation curve data: for small radii, the function is nearly linear; for large radii, the function is asymptotically flat; and local peaks or inflections at moderate radii may be reproduced without affecting the behavior at large and small radii. Derivatives of the functional form (6–12) are easily computed for use in equation (6–11) for the mass density. Table 6–2 lists the coefficients of rational functions fitted to rotation curve data, and the maximum radii in arcseconds to which the fits are reliable. All have been normalized to $b_0 \equiv 1$. For $r$ in arcseconds, formula (6–12) yields $V(r)$ in $\mathrm{km\,sec^{-1}}$ using coefficients from Table 6–2. The asymptotic circular speed is the limit

$$V_\infty = \lim_{r\to\infty} V(r) = \frac{a_3}{b_3}\ \mathrm{km\,sec^{-1}}, \qquad (6-13)$$

and the central velocity gradient is

$$V'(0) = \lim_{r\to 0} V(r) = \frac{a_1}{b_0} \equiv a_1\ \mathrm{km\,sec^{-1}\,arcsec^{-1}}, \qquad (6-14)$$

if $V''(0) < 0 \iff a_2 - a_1 b_1 < 0$, so that $a_1$ dominates the behavior near $r = 0$. Table 6–3 lists the values of $V'(0)$ for the Virgo spirals studied here. A distance of 15.7 Mpc is assumed in computing $V'(0)$. The values are computed either using equation (6–14) or linear fits to the inner rotation curve (typically CO) data, as appropriate.

The dynamical mass within the central sphere of radius 500 pc and concentric shells of width 0.5 kpc with outer radius increasing to 2.5 kpc are listed in Table 6–4. These values are graphed in Figure 6–22. The computations are done using equation (6–10), which assumes a spherically symmetric mass distribution. Integration of

TABLE 6–2. COEFFICIENTS OF RATIONAL FUNCTION FITS

| NGC | $a_3$ | $a_2$ | $a_1$ | $b_3$ | $b_2$ | $b_1$ | $r_{max}('')$ |
|---|---|---|---|---|---|---|---|
| 4254 | 3.0717(−3) | −0.11681 | 13.988 | 1.1470(−5) | 3.0293(−4) | 4.9791(−2) | 230 |
| 4303 | 1.1591(−3) | 1.9962 | 79.499 | 6.8925(−6) | 1.3092(−2) | 0.68284 | 320 |
| 4321 | 9.3460 | 1.3739 | 14.422 | 3.9778(−2) | 0.44326 | 0.84235 | 170 |
| 4501 | 7.3529(−4) | −0.11199 | 10.113 | 1.4766(−6) | −2.8605(−5) | 4.9990(−5) | 230 |
| 4535 | 1.9954(−2) | 5.6188(−5) | 20.439 | 6.0812(−5) | 6.2073(−3) | 1.8731(−4) | 210 |
| 4536 | 7.7098(−3) | 4.0307(−3) | 27.409 | 1.4377(−5) | 3.2401(−3) | 4.1082(−4) | 130 |
| 4569 | 0.24461 | 9.1570(−4) | 7.5451 | 5.4117(−4) | 5.1830(−2) | 8.2352(−3) | 105 |
| 4654 | 0.94890 | 0.98847 | 7.6564 | 4.4059(−3) | 0.12801 | 2.2307(−2) | 200 |

TABLE 6–3. CENTRAL VELOCITY GRADIENTS

| NGC | $V'(0)$ $\mathrm{km\,sec^{-1}\,pc^{-1}}$ |
|---|---|
| 4254 | 0.184 |
| 4303 | 0.269 |
| 4321 | 0.180 |
| 4501 | 0.133 |
| 4535 | 0.269 |
| 4536 | 0.360 |
| 4569 | 0.099 |
| 4654 | 0.101 |

the mass surface density in formula (6–11) yields the dynamical mass within a given radius for a thin disk mass distribution. The dynamical mass within the central disk of 500 pc radius and concentric annuli of width 0.5 kpc for a thin disk are listed in Table 6–5 and are graphed in Figure 6–23. Ignorance of the exact mass distributions of these galaxies prevents making any firm statement about the dependence of central mass with morphological type. Where the bulge dominates, the mass distribution is probably closer to being spherically symmetric than a thin disk, although late-type

spirals may be well approximated as disks even near their nuclei. The thin disk mass distribution values in Table 6–5 indicate a tendency for the earlier types to have the most massive cores; the spherical mass distribution values do not show this tendency. Note that these direct mass comparisons do not take into account a scaling by a total mass or characteristic mass; it is not clear how to assign a characteristic mass given an asymptotically flat rotation curve, anyway.

TABLE 6–4.

MASS[a] WITHIN SHELLS—SPHERICAL SYMMETRY

| NGC | Outer Radius[b] (kpc) | | | | |
|---|---|---|---|---|---|
| | 0.5 | 1.0 | 1.5 | 2.0 | 2.5 |
| 4254 | 4.93 | 17.5 | 24.3 | 26.4 | 26.6 |
| 4303 | 11.7 | 18.2 | 20.1 | 21.3 | 22.3 |
| 4321 | 6.07 | 26.4 | 39.9 | 47.5 | 52.1 |
| 4501 | 4.40 | 25.8 | 56.2 | 85.1 | 105 |
| 4535 | 13.7 | 32.9 | 24.6 | 20.4 | 21.6 |
| 4536 | 29.3 | 101 | 92.0 | 58.1 | 38.8 |
| 4569 | 1.38 | 6.43 | 14.2 | 23.6 | 33.7 |
| 4654 | 2.23 | 9.74 | 17.2 | 23.4 | 28.3 |

[a] Mass unit is $10^8\,M_\odot$.

[b] Assumes a distance 15.7 Mpc.

TABLE 6–5.
MASS[a] WITHIN ANNULI — THIN DISK

| NGC | Outer Radius[b] (kpc) | | | | |
|---|---|---|---|---|---|
| | 0.5 | 1.0 | 1.5 | 2.0 | 2.5 |
| 4254 | 9.76 | 21.0 | 25.9 | 28.0 | 29.2 |
| 4303 | 14.7 | 19.7 | 21.1 | 21.9 | 22.3 |
| 4321 | 14.0 | 32.9 | 42.0 | 46.4 | 48.8 |
| 4501 | 19.0 | 50.9 | 76.5 | 95.3 | 107 |
| 4535 | 18.5 | 30.6 | 29.1 | 29.0 | 30.6 |
| 4536 | 42.8 | 79.6 | 71.1 | 56.3 | 47.3 |
| 4569 | 5.95 | 16.0 | 24.8 | 32.5 | 38.9 |
| 4654 | 6.45 | 15.9 | 22.2 | 26.6 | 29.7 |

[a] Mass unit is $10^8\,M_\odot$.

[b] Assumes a distance 15.7 Mpc.

## References

Afanas'ev, V. F., Burenkov, A. N., Zasov, A. V., and Sil'chenko, O. K. 1988, *Astrofizika*, **29**, 155.

Bevington, P. R. 1969, *Data Reduction and Error Analysis for the Physical Sciences*, (New York: McGraw Hill).

Cayatte, V., van Gorkom, J. H., Balkowski, C., and Kotanyi, C. 1990, *A. J.*, in press.

Chicarini, G., and de Souza, R. 1985, *Astron. Ap.*, **153**, 218.

Combes, F., and Gerin, M. 1985, *Astron. Ap.*, **150**, 327.

Guhathakurta, P., van Gorkom, J. H., Kotanyi, C. G., and Balkowski, C. 1988, *A. J.*, **96**, 851.

Kenney, J. D., and Young, J. S. 1988, *Ap. J. Suppl.*, **66**, 261.

Kennicutt, R. C., Jr. 1989, *Ap. J.*, **344**, 685.

Knapp, G. R. 1987, *P.A.S.P.*, **99**, 1134.

Nordsieck, K. H. 1973, *Ap. J.*, **184**, 719.

Rubin, V. C., Burstein, D., Ford, W. K., Jr., and Thonnard, N. 1985, *Ap. J.*, **289**, 81.

Rubin, V. C., Kenney, J. D., Boss, A. P., and Ford, W. K., Jr. 1989, *A. J.*, **98**, 1246.

Sanders, R. H., and Tubbs, A. D. 1980, *Ap. J.*, **235**, 803.

Schmidt, M. 1959, *Ap. J.*, **129**, 243.

Shlosman, I., Frank, J., and Begelman, M. C. 1989, *Nature*, **338**, 45.

van Albada, G. D., and Roberts, W. W., Jr. 1981, *Ap. J.*, **246**, 740.

Visser, C. D. 1980, *Astron. Ap.*, **88**, 149.

Warmels, R. H. 1986, Ph.D. Thesis, University of Groningen.

Warner, P. J., Wright, M. C. H., and Baldwin, J. E. 1973, *M.N.R.A.S.*, **163**, 163.

Woods, D., Madore, B. F., and Fahlman, G. G. 1990, *Ap. J.*, **353**, 90.

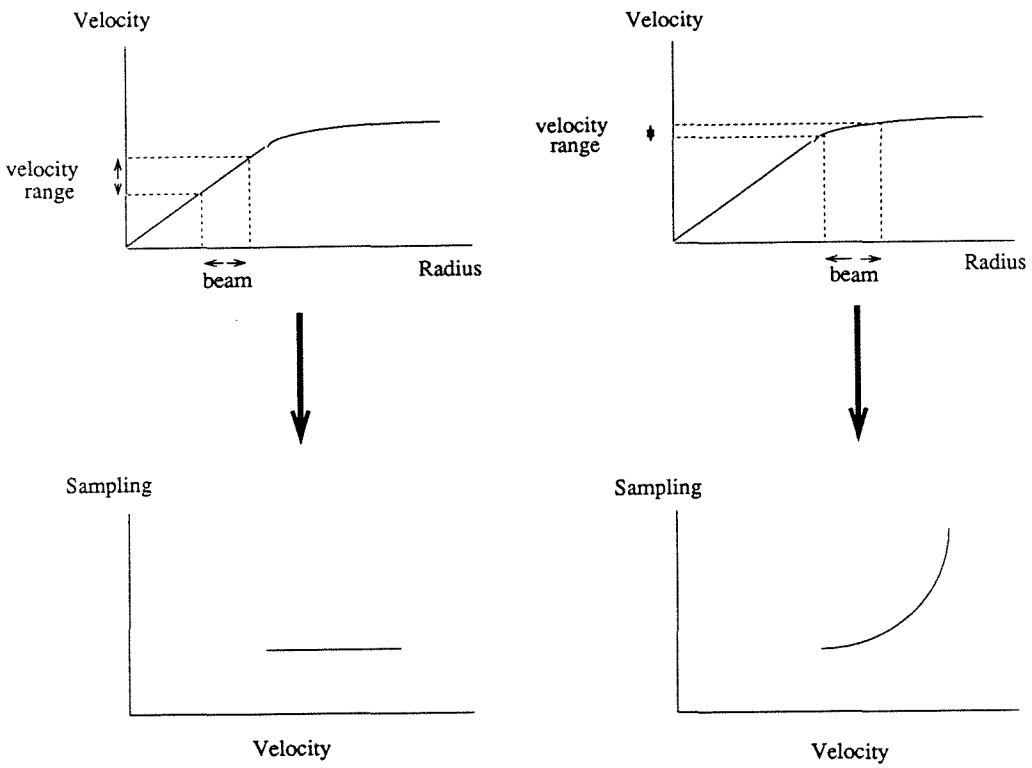


Figure 6–1. The effect of the shape of the rotation curve on the sampling of gas velocities in the disk of a galaxy. A beam placed at a position where the rotation curve is linear will sample velocities uniformly, assuming uniform source brightness. A beam placed where the rotation curve has curvature will result in uneven velocity sampling.

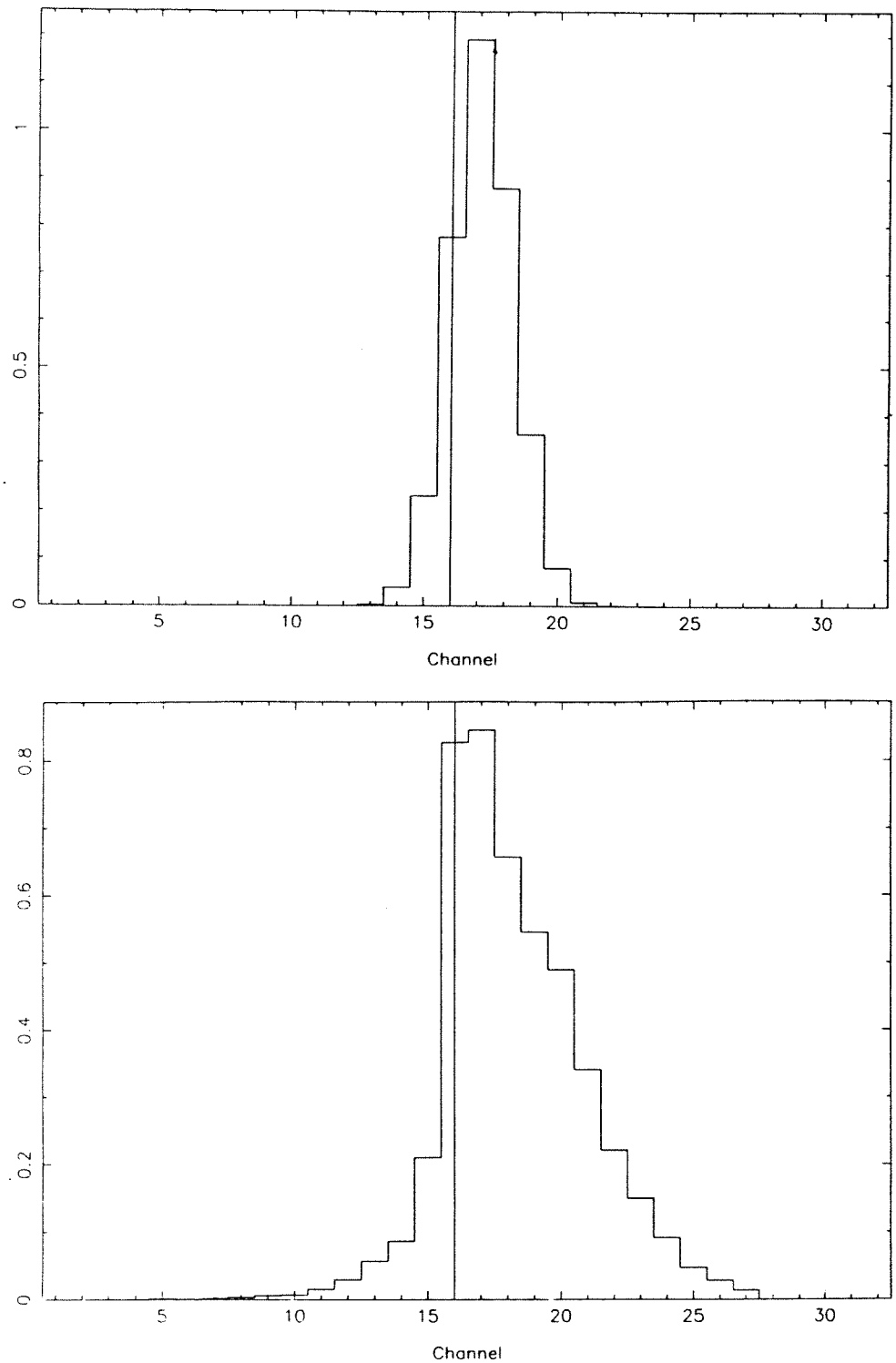


Figure 6–2. (*top*) Model emission profile from gas in a galaxy inclined 30°, with disk thickness 4″, Gaussian beam dimensions 7″.9 × 6″.4, velocity dispersion 10 km sec$^{-1}$, and a linearly rising rotation curve. (*bottom*) Model emission profile for the same disk, inclination 70°.

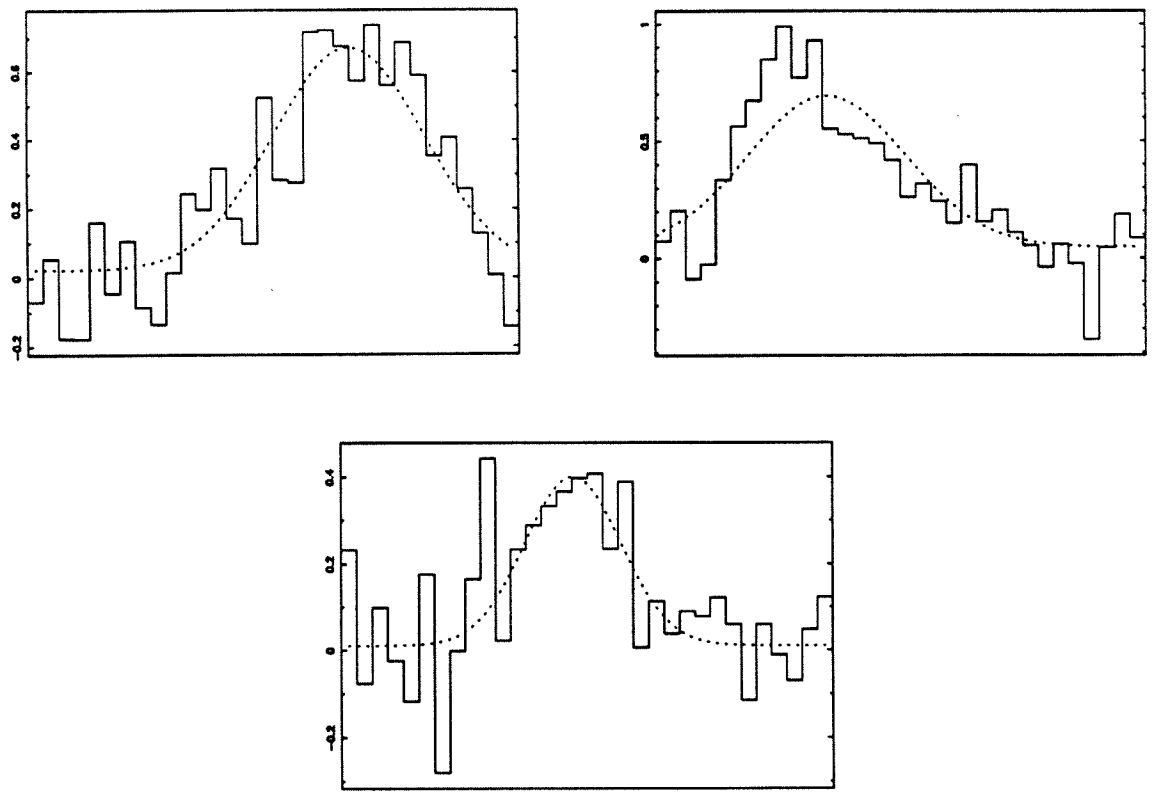

Figure 6–3. Actual spectra of NGC 4536, which has an inclination of 68°, displaying skewed profiles.

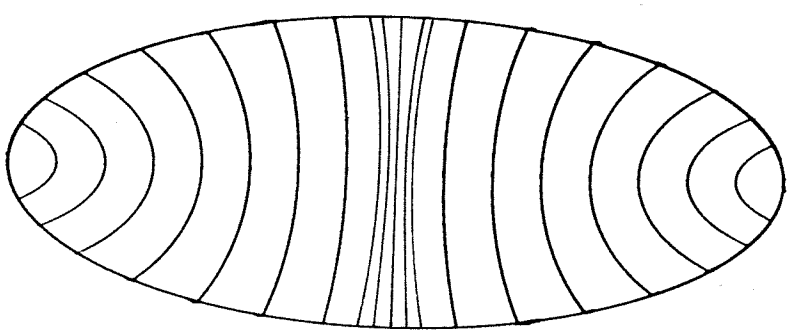

Figure 6–4. Schematic velocity field of a typical spiral galaxy. The lines are isovelocity contours.

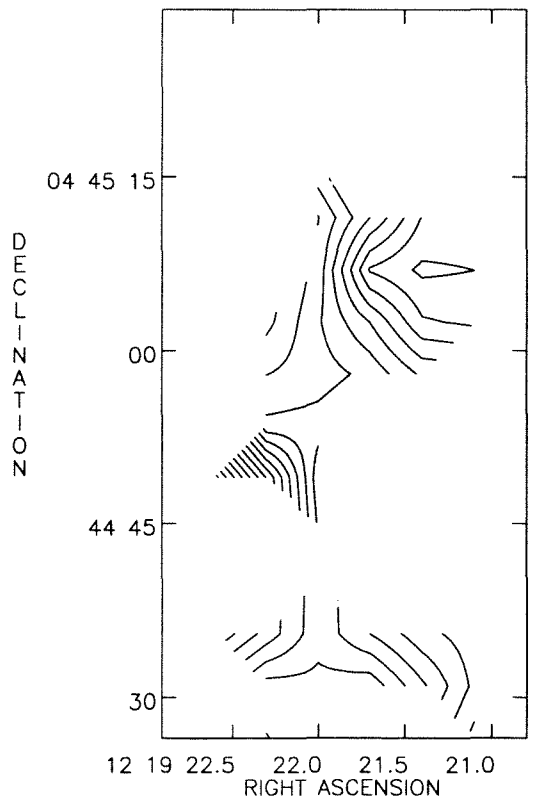


Figure 6–5. NGC 4303. Velocity field.

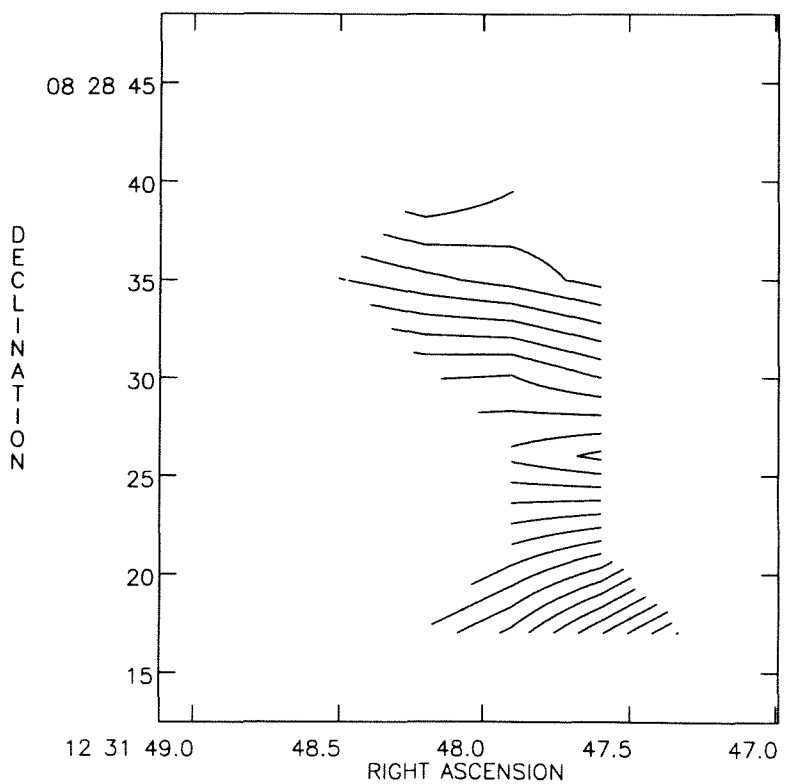


Figure 6–6. NGC 4535. Velocity field.

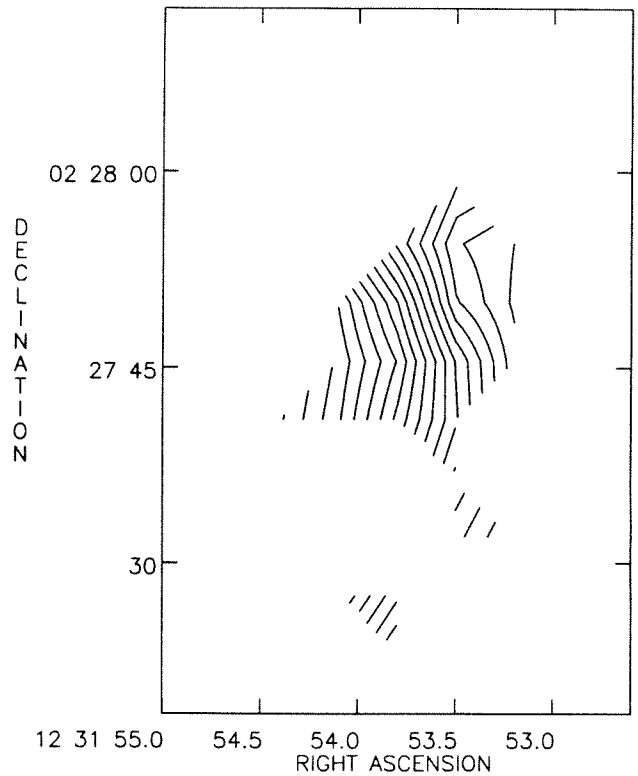


Figure 6–7. NGC 4536. Velocity field.

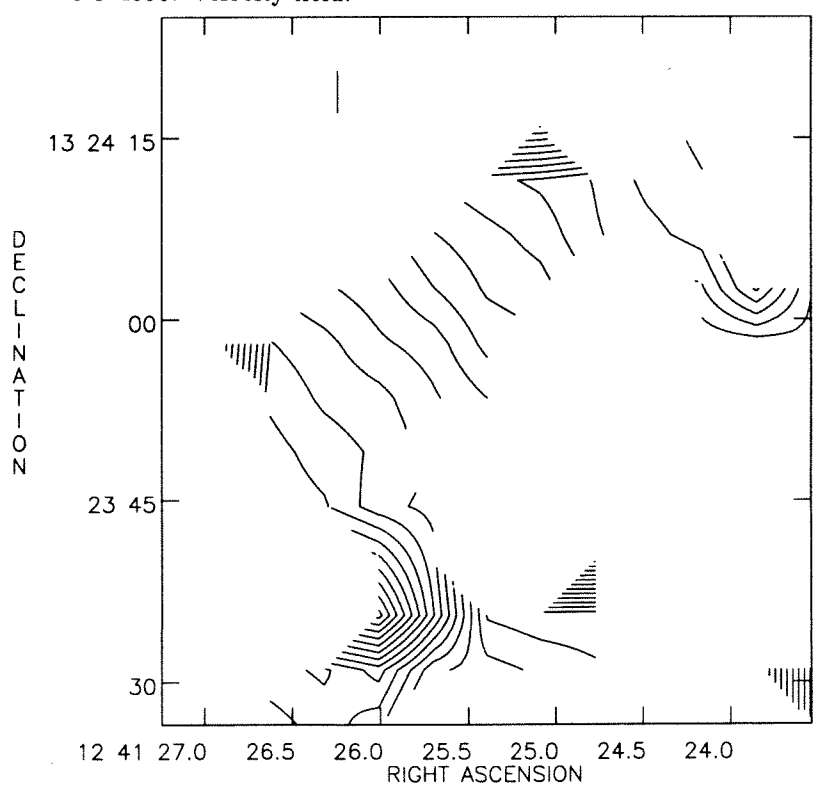


Figure 6–8. NGC 4654. Velocity field.

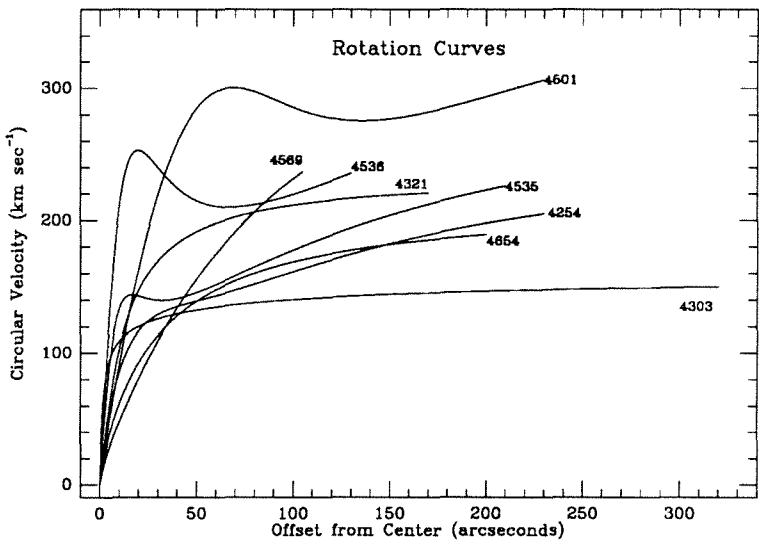


Figure 6–9. Rotation curves of Virgo spiral galaxies.

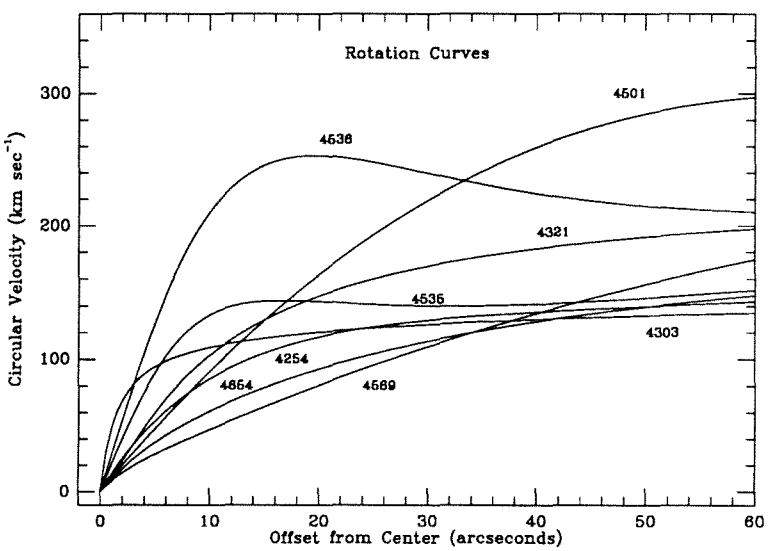


Figure 6–10. Inner rotation curves of Virgo spiral galaxies.

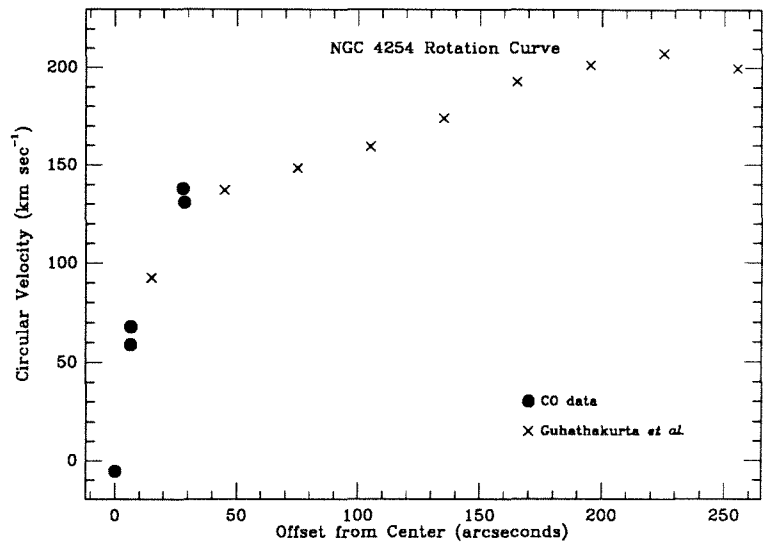


Figure 6–11. NGC 4254. Rotation curve.

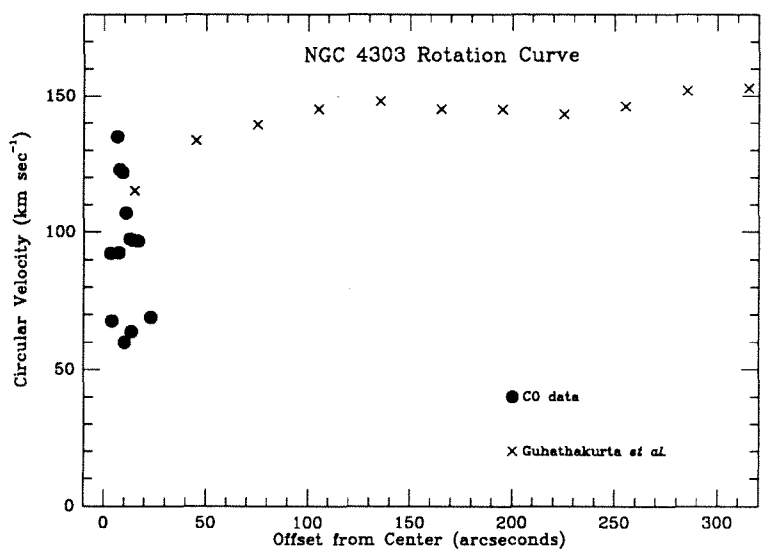


Figure 6–12. NGC 4303. Rotation curve.

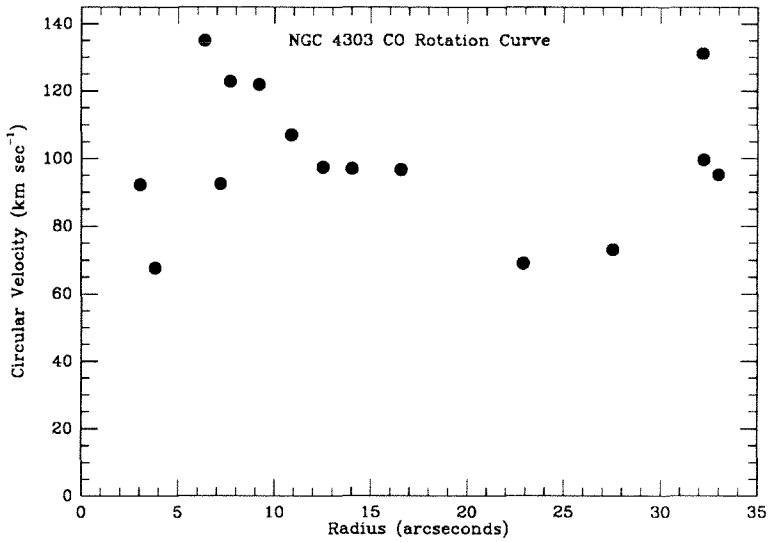


Figure 6–13. NGC 4303. CO rotation curve.

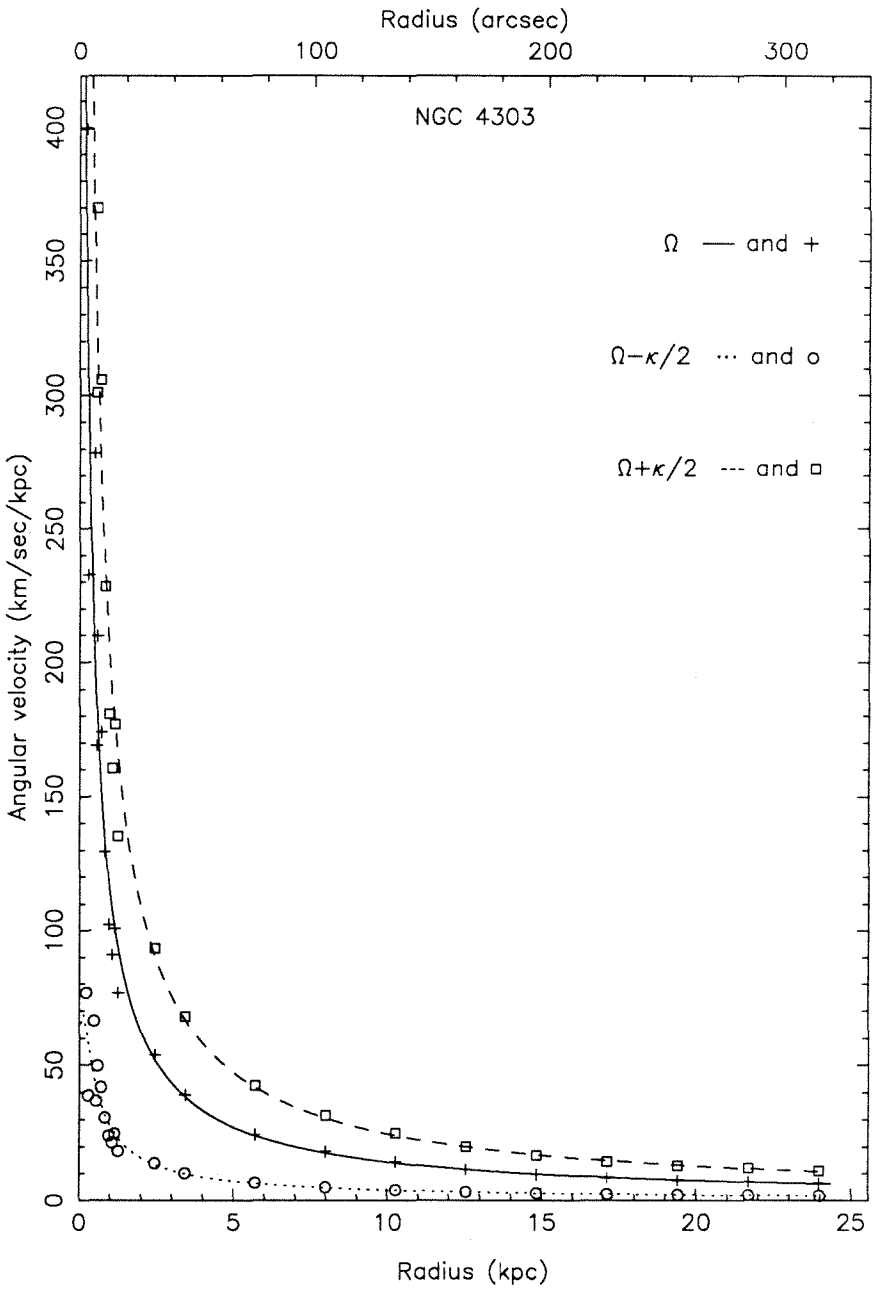


Figure 6–14. NGC 4303. Graph of $\Omega$, $\Omega + \kappa/2$, and $\Omega - \kappa/2$ calculated from data (symbols) and from a rational function fit (curves). A pattern speed of $\Omega_p = 75\,\mathrm{km\,sec^{-1}\,kpc^{-1}}$ places corotation at the bar ends and the outer Lindblad resonance at 3.2 kpc where the spiral arms open up. There is barely a single inner Lindblad resonance at small radius.

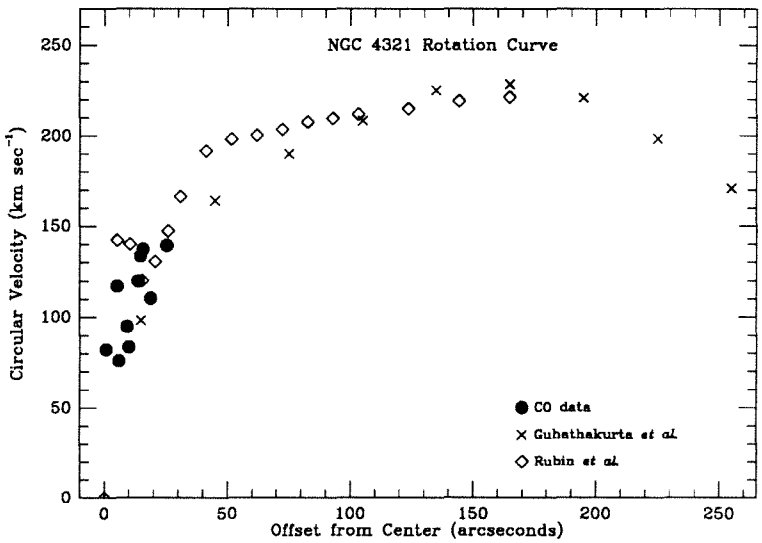


Figure 6–15. NGC 4321. Rotation curve.

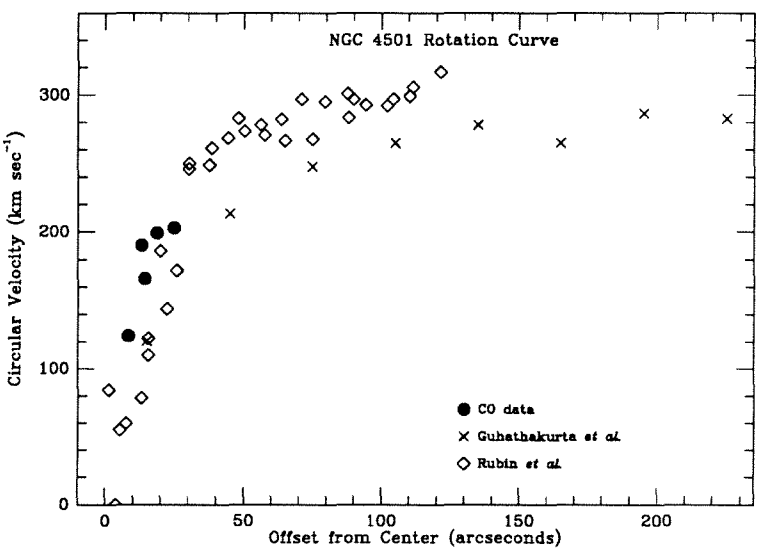


Figure 6–16. NGC 4501. Rotation curve.

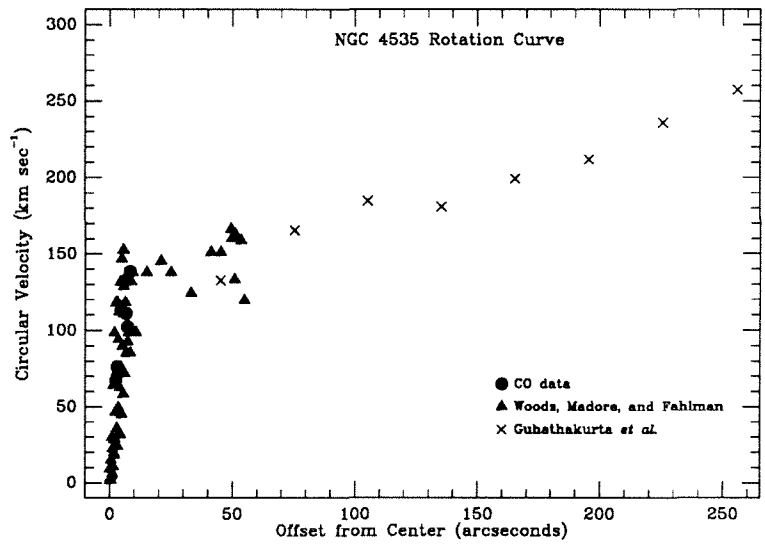


Figure 6–17. NGC 4535. Rotation curve.

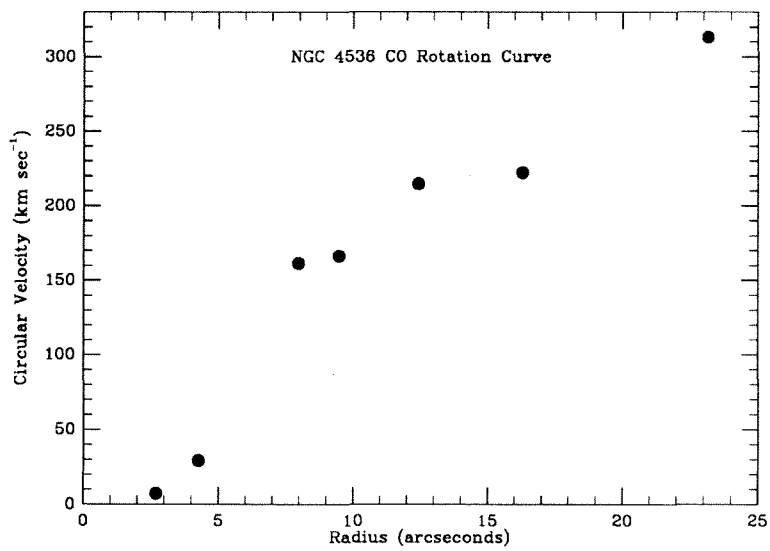


Figure 6–18. NGC 4536. CO rotation curve.

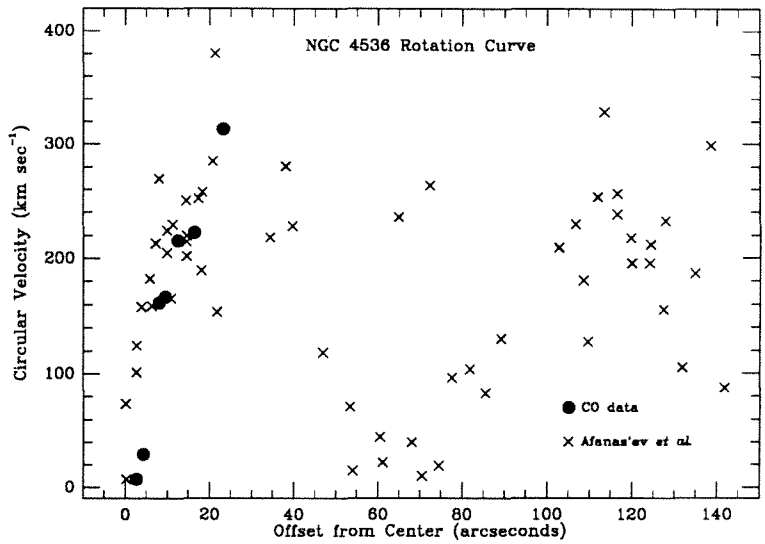


Figure 6–19. NGC 4536. Rotation curve.

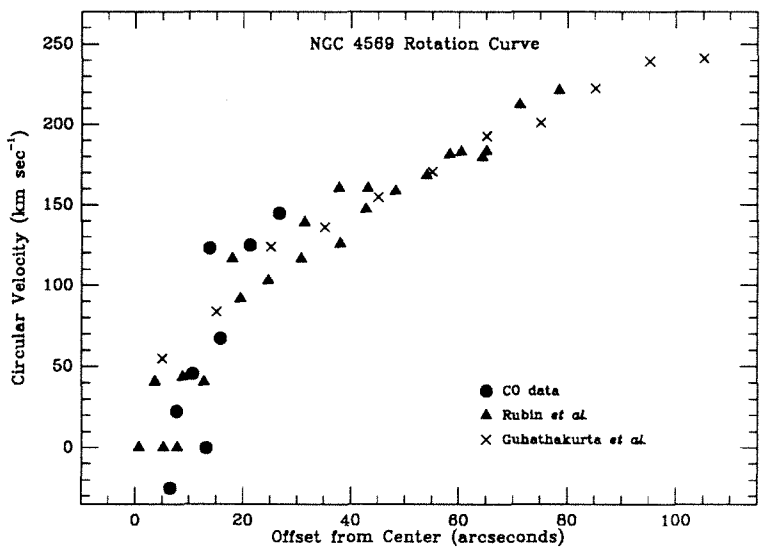


Figure 6–20. NGC 4569. Rotation curve.

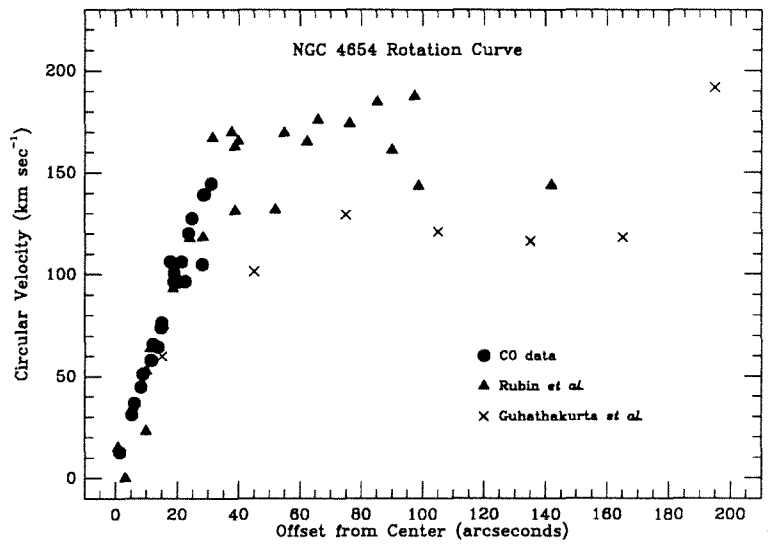


Figure 6–21. NGC 4654. Rotation curve.

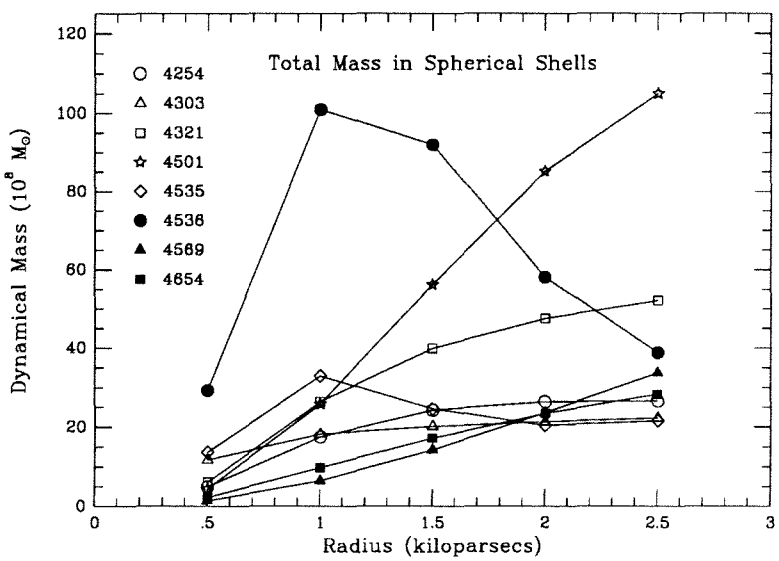


Figure 6–22. Dynamical mass in the central sphere of radius 500 pc and surrounding shells of width 500 pc, assuming a spherically symmetric mass distribution.

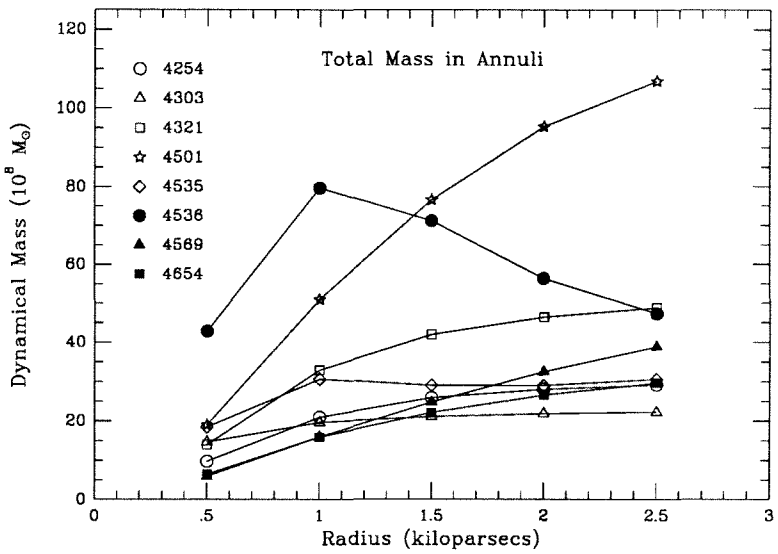


Figure 6–23. Dynamical mass in the central disk of radius 500 pc and surrounding annuli of width 500 pc, assuming a thin disk mass distribution.

# Chapter 7
# The Gas Disks of Spiral Galaxies

## 7.1. Total Gas Mass

There are two phases which contribute significantly to the gaseous mass in spiral galaxy disks. Atomic hydrogen has long been known to be prevalent in spiral disks (see Roberts 1975 for a review), while the importance of molecular hydrogen has been recognized only within the last decade. A significant amount of helium (an additional 36% by mass) is also known to accompany the contribution of hydrogen. Total molecular hydrogen masses based on interferometer data are listed in Table 7–1. The masses refer to roughly the inner 5 kpc diameter regions of the galaxies. Since the interferometer did not recover a significant proportion of the total CO emission (see Table 5–4), the masses in Table 7–1 underestimate the true molecular hydrogen masses. Even so, the masses are substantial. The variation of molecular hydrogen mass with radius is computed using values from Table 5–7 and equation (2–2). These masses within annuli 500 pc wide are listed in Table 7–2, and are derived from a combination of radial models of $I_{CO}$ from Kenney (1987) and interferometer data. The final line lists similar data for our Galaxy using 1 kpc annuli (Sanders, Solomon, and Scoville 1984). Most of the Virgo spirals have amounts of gas in their central regions that are similar to our Galaxy, the greatest difference being only a factor of three more mass in NGC 4321. NGC 4535 has about half the mass of molecular hydrogen in its inner 3 kpc that our Galaxy has.

The variation of atomic hydrogen mass with radius was computed using equation (2–1) and interferometric strip scans by Warmels (1986), who used a nonlinear

TABLE 7–1. TOTAL $H_2$ MASSES

INTERFEROMETER DATA

| NGC | Mass | NGC | Mass |
|---|---|---|---|
| | $10^8\,M_\odot$ | | $10^8\,M_\odot$ |
| 4254 | 1.04 | 4535 | 2.63 |
| 4303 | 4.45 | 4536 | 6.67 |
| 4321 | 6.59 | 4569 | 4.72 |
| 4501 | 1.18 | 4654 | 2.53 |

TABLE 7–2. $H_2$ MASS[a] IN ANNULI

| NGC | Outer Radius (kpc) | | | | |
|---|---|---|---|---|---|
| | 0.5 | 1.0 | 1.5 | 2.0 | 2.5 |
| 4254 | 1.25 | 2.76 | 2.75 | 2.32 | 2.19 |
| 4303 | 1.48 | 3.64 | 4.85 | 5.42 | 5.55 |
| 4321 | 2.36 | 5.15 | 5.03 | 4.07 | 3.66 |
| 4501 | 0.712 | 1.86 | 2.66 | 3.19 | 3.51 |
| 4535 | 1.86 | 0.668 | 0.658 | 0.805 | 0.900 |
| 4536 | 2.55 | 3.43 | 3.43 | 3.11 | 2.59 |
| 4569 | 1.36 | 3.21 | 4.10 | 4.37 | 4.28 |
| 4654 | 0.652 | 0.976 | 0.505 | 1.139 | 1.824 |
| Galaxy | 2.38 | | 2.93 | | 0.42 |

[a] Units are $10^8\,M_\odot$.

algorithm to deconvolve the true surface brightness profile from the data. Spline fits to Warmels' (1986) profiles were integrated to yield the masses of atomic hydrogen within annuli 500 pc wide that are listed in Table 7–3. The final line lists data

for our Galaxy (Sanders, Solomon, and Scoville 1984) for comparison. The data for NGC 4536 were taken from Giovanelli and Haynes (1983), who report single-dish integrated emission at points along the major axis. There are too few data to attempt a deconvolution of the sort applied by Warmels (1986), who did not observe NGC 4536. Because of the high inclination of NGC 4536, the H I masses for NGC 4536 are somewhat inaccurate because of contamination by emission from larger radii within the beam and the possibility that the optical depth $\tau_{\rm H\,I} > 1$.

TABLE 7–3. H I MASS[a] IN ANNULI

| NGC | Outer Radius (kpc) | | | | |
|---|---|---|---|---|---|
| | 0.5 | 1.0 | 1.5 | 2.0 | 2.5 |
| 4254 | 6.20 | 18.1 | 29.0 | 38.5 | 47.0 |
| 4303 | 3.61 | 10.1 | 16.4 | 23.5 | 32.6 |
| 4321 | 2.90 | 9.78 | 17.8 | 26.4 | 34.8 |
| 4501 | 1.57 | 4.85 | 8.48 | 12.6 | 17.7 |
| 4535 | 2.42 | 6.09 | 9.35 | 13.3 | 17.5 |
| 4536 | 2.94 | 8.90 | 14.9 | 21.0 | 27.1 |
| 4569 | 0.616 | 1.76 | 2.95 | 4.46 | 6.59 |
| 4654 | 3.33 | 11.4 | 21.5 | 33.7 | 47.4 |
| Galaxy | | | 10 | | 12.9 |

[a] Units are $10^6\,M_\odot$.

The ratio between molecular and atomic gas mass is interesting. It is well known that molecular hydrogen is more abundant than atomic hydrogen in the inner disks of normal spirals; atomic hydrogen prevails in the outer disks of spirals and becomes the only detectable luminous matter at large radii. Indeed, many spirals have H I profiles which show a central depression, quite unlike the centrally peaked CO profiles noted

here. Table 7–4 lists the molecular to atomic hydrogen mass ratio in annuli 500 pc wide computed from entries in Table 7–2 and Table 7–3. The last line lists values of the ratio for our Galaxy for comparison (Sanders, Solomon, and Scoville 1984).

TABLE 7–4. MASS RATIO $M(H_2)/M(HI)$

| NGC | Outer Radius (kpc) | | | | |
|---|---|---|---|---|---|
| | 0.5 | 1.0 | 1.5 | 2.0 | 2.5 |
| 4254 | 20.2 | 15.3 | 9.48 | 6.02 | 4.66 |
| 4303 | 41.0 | 35.9 | 29.6 | 23.1 | 17.0 |
| 4321 | 81.5 | 52.7 | 28.2 | 15.4 | 10.5 |
| 4501 | 45.5 | 38.4 | 31.4 | 25.2 | 19.9 |
| 4535 | 76.8 | 11.0 | 7.04 | 6.04 | 5.15 |
| 4536 | 86.7 | 38.6 | 23.0 | 14.8 | 9.54 |
| 4569 | 221 | 182 | 139 | 98.1 | 64.9 |
| 4654 | 19.6 | 8.57 | 2.35 | 3.38 | 3.85 |
| Galaxy | | | 50 | | 3.29 |

Values in Table 7–4 show, as expected, that molecular hydrogen is the dominant gas phase species in the inner disks of spirals. The rapid and strictly monotonic (except for the minor aberration of NGC 4654) decline of the molecular to atomic hydrogen ratio with radius results from the very peaked CO distributions. The observed behavior would be more extreme in most cases if the interferometer profiles plus a uniform (resolved) background emission were used in the calculations. The exceptionally large $M(H_2)/M(HI)$ ratios for NGC 4569 exemplify the observation of Kenney (1987) that, although its disk is largely stripped of atomic hydrogen, NGC 4569 has retained its molecular gas. Values of the ratio are not correlated with the amount of high-mass star formation in the galaxy. Galaxies with plenty of high-mass star for-

mation may have large values of the ratio away from the center (NGC 4321) or small ones (NGC 4254 and NGC 4654). Conversely, galaxies with comparatively little high-mass star formation may have large values of the ratio (NGC 4501) or small values (NGC 4535, outside 1 kpc radius). Chapter 8 will explore in detail the relationship between gas density and star formation.

The total gas mass may be computed by summing the corresponding entries in Table 7–2 and Table 7–3 and multiplying by 1.36 to account for the contribution of helium. Values of the total gas mass in 500 pc annuli are listed in Table 7–5. The last line lists data for our Galaxy for comparison. The total gas masses for our Galaxy are estimates of $H_2$ + He only, from Sanders, Solomon, and Scoville (1984), and omit the comparatively small contribution of H I in the inner disk. The gas masses are quite large in general, and it is instructive to compare the gas mass with the dynamical mass within the same region. Dynamical masses within 500 pc annuli are listed in Table 6–4 and Table 6–5. The masses are computed from rotation curves for two mass distribution models: a spherically symmetrical one and a thin disk. Between them, these two mass models approximate the range of possible masses for physically reasonable mass distributions. In the central regions where the bulge dominates the total mass distribution, the dynamical mass estimates that assume spherical symmetry are probably closer approximations to the true mass. Gas mass fractions as a function of radius are listed in Table 7–6, which compares total gas mass ($H_2$ + H I + He) with the mass within a spherically symmetrical mass distribution, and Table 7–7, which compares the total gas mass with the mass in a thin disk. The final line in Table 7–6 lists gas mass fractions for our Galaxy computed using values in Table 7–5 and the rotation curve adopted by Bahcall, Schmidt, and Soneira (1983), assuming a spherically symmetrical mass distribution.

Are the estimated gas mass fractions physically reasonable values? Most of the

TABLE 7–5. TOTAL GAS MASS[a] ($H_2$ + He + H I)

| NGC | Outer Radius (kpc) | | | | |
|---|---|---|---|---|---|
| | 0.5 | 1.0 | 1.5 | 2.0 | 2.5 |
| 4254 | 1.78 | 4.00 | 4.13 | 3.68 | 3.62 |
| 4303 | 2.06 | 5.09 | 6.82 | 7.69 | 7.99 |
| 4321 | 3.25 | 7.14 | 7.08 | 5.89 | 5.45 |
| 4501 | 0.990 | 2.60 | 3.73 | 4.51 | 5.01 |
| 4535 | 2.56 | 0.991 | 1.02 | 1.28 | 1.46 |
| 4536 | 3.51 | 4.79 | 4.87 | 4.52 | 3.89 |
| 4569 | 1.86 | 4.39 | 5.62 | 6.00 | 5.91 |
| 4654 | 0.932 | 1.48 | 0.979 | 2.01 | 3.13 |
| Galaxy[b] | 2.70 | | 3.32 | | 0.48 |

[a] Units are $10^8$ $M_\odot$.

[b] Excludes H I mass.

entries in Table 7–6 and Table 7–7 are rather small, in the range 5% to 10%, but many ratios leap to much larger values at small radii. One mass fraction estimate is physically impossible: the total gas mass estimate exceeds the dynamical mass within 500 pc radius of NGC 4569 if a spherically symmetrical mass distribution is assumed. Many central gas mass fraction estimates are 20% or more, and the gas mass fraction estimates for both NGC 4303 and NGC 4569 are rather large, even out to 2.5 kpc radius. Most of the gas mass fractions are larger than those for our Galaxy. Note, however, that the gas masses in Table 7–5 for our Galaxy are comparable to the masses at the same radii for many Virgo spirals. There is a marked decrease in gas mass in our Galaxy beyond 1.5 kpc. This decrease is probably related to the large amount of gas in the 3 kpc molecular ring in our Galaxy. The ring may have accumulated

gas at the expense of smaller radii. The very small gas mass fractions within 2.5 kpc radius in our Galaxy are not the result of small amounts of gas so much as they are the result of the large dynamical mass in the inner region. The inner rotation curve of our Galaxy (Bahcall, Schmidt, and Soneira 1983) is exceptionally steep, indicating a very large amount of mass in the central region. Many of the Virgo spirals studied here which have central gas masses comparable to that of our Galaxy but have smaller dynamical masses indicated by their rotation curves; hence their gas mass fractions are larger. The very large gas mass fraction in the central region of NGC 4569 suggests the possibility that gas has recently fallen into the center as a result of a merger, but there is no evidence in the optical morphology of the galaxy to indicate a merger or strong dynamical interaction with another galaxy.

TABLE 7–6. GAS MASS FRACTIONS

SPHERICAL SYMMETRY

| NGC | Outer Radius (kpc) | | | | |
|---|---|---|---|---|---|
| | 0.5 | 1.0 | 1.5 | 2.0 | 2.5 |
| 4254 | 0.361 | 0.229 | 0.170 | 0.139 | 0.136 |
| 4303 | 0.176 | 0.280 | 0.340 | 0.361 | 0.359 |
| 4321 | 0.535 | 0.270 | 0.177 | 0.124 | 0.105 |
| 4501 | 0.225 | 0.101 | 0.066 | 0.053 | 0.048 |
| 4535 | 0.187 | 0.030 | 0.042 | 0.063 | 0.068 |
| 4536 | 0.120 | 0.048 | 0.053 | 0.078 | 0.100 |
| 4569 | 1.341 | 0.683 | 0.395 | 0.254 | 0.176 |
| 4654 | 0.418 | 0.152 | 0.057 | 0.086 | 0.110 |
| Galaxy | 0.037 | | 0.031 | | 0.008 |

TABLE 7–7. GAS MASS FRACTIONS

THIN DISK

| NGC | Outer Radius (kpc) | | | | |
|---|---|---|---|---|---|
| | 0.5 | 1.0 | 1.5 | 2.0 | 2.5 |
| 4254 | 0.182 | 0.190 | 0.160 | 0.131 | 0.124 |
| 4303 | 0.140 | 0.258 | 0.324 | 0.352 | 0.358 |
| 4321 | 0.232 | 0.217 | 0.169 | 0.127 | 0.112 |
| 4501 | 0.052 | 0.051 | 0.049 | 0.047 | 0.047 |
| 4535 | 0.139 | 0.032 | 0.035 | 0.044 | 0.048 |
| 4536 | 0.082 | 0.060 | 0.069 | 0.080 | 0.082 |
| 4569 | 0.312 | 0.274 | 0.226 | 0.185 | 0.152 |
| 4654 | 0.144 | 0.093 | 0.044 | 0.076 | 0.105 |

## 7.2. Stability of Gas Disks

### 7.2.1. Numerical Models of Gas Disks

Prompted by the warnings in Table 7–6 that the large estimates of gas mass are not physical, it is natural to wonder if any of the rather large gas mass estimates are realistic. There have been hints from numerical gas hydrodynamical simulations of spiral galaxies that large amounts of gas naturally occur at the centers of spirals. The phase of the gas (molecular, atomic, or ionized) was not considered in any of the simulations. Mulder (1986) modeled gas flow in a galactic potential that included a bar and found a central gas mass surface density 12 times greater than the average outer disk gas mass surface density. The central density gradient was very steep, and the central density in the models was $37\,M_\odot\,pc^{-2}$. The greatest shortcoming of Mulder's models is the neglect of the self-gravity of the gas. Between the center and 2.5 kpc radius, NGC 4535 shows the largest gas mass surface density contrast among

the program spirals: there is nearly 16 times the gas mass surface density at the center as at 2.5 kpc radius, which is similar to the contrast computed by Mulder. However, the central gas mass surface density of NGC 4535 is $326\,M_\odot\,pc^{-2}$ (see Table 7–5), which is much larger than that computed by Mulder. Even the smallest central gas mass surface density, $119\,M_\odot\,pc^{-2}$ for NGC 4654, exceeds Mulder's computation. The self-gravity of the gas was considered in a different hydrodynamical simulation (Huntley 1980), also of a barred spiral. Although problems of a numerical nature made physical interpretation of the gas mass fraction difficult, Huntley found that stable spiral waves were maintained when the local gas mass fraction was between 5% and 15% (and perhaps as much as 28% with liberal interpretation). Most of the gas mass fraction estimates in Table 7–6 and Table 7–7 are, in fact, within this range for the larger radii. As a consequence of simulations such as those discussed above, it has been widely considered that a galactic bar may gather gas through angular momentum loss mechanisms (such as shocks) and sequester the gas at the galactic center. It is therefore surprising, in the light of such models, that the observations reported here indicate such large amounts of gas at the centers of spirals which are not strongly barred at all. Moreover, quantitative estimates of the amount of gas in galactic centers computed from models differ from observed values by about an order of magnitude.

### 7.2.2. Stability Analysis

Because of the large gap between central gas masses and mass fractions computed from models, on the one hand, and from CO observations, on the other, an inquiry into the physical basis for so much gas is warranted. Of primary concern is the question of the stability of a gas disk with as much mass as implied by CO observations. The most serious instability to which rotating disks are subject is a Jeans-type instability. The ordinary Jeans instability for an infinite, homogeneous, nonrotating fluid with

no internal motions occurs when the wavelength of a disturbance satisfies

$$\lambda > \lambda_J = \frac{\pi v_s^2}{G\rho_0}, \qquad (7-1)$$

where $\rho_0$ is the unperturbed density, $G$ is the gravitational constant, and $v_s$ is the sound speed. This is equivalent to the condition that the scale, $r$, of a perturbation is large enough so that the dynamical timescale, $t_{\rm dyn} \approx 1/\sqrt{G\rho_0}$, is shorter than the sound crossing time:

$$t_{\rm dyn} < r/v_s. \qquad (7-2)$$

The source of energy which drives the Jeans instability is gravitational. The enhanced gravitational attraction of the compressed region of a wave-like disturbance outweighs the reduced attraction in the dilated region. Therefore, the gravitational energy density of the disturbance is negative. When $\lambda > \lambda_J$, the net energy density becomes negative, and so the system can lower its energy by allowing the disturbance to grow (Binney and Tremaine 1987, pp. 287ff).

The stability of a rotating sheet is more precarious, because in addition to gravity there is a reservoir of kinetic energy (from the rotation) to feed unstable modes. Bending modes in a thin rotating sheet with uniform surface density and constant angular velocity are always stable. Bending modes satisfy the dispersion relation

$$\omega^2 = 2\pi G\Sigma_0|k|, \qquad (7-3)$$

where $\Sigma_0$ is the unperturbed surface density and $\omega$ and $k$ are the frequency and wavenumber, respectively (Binney and Tremaine 1987, p. 334). Since $\omega$ is never imaginary in equation (7–3), all bending modes are stable. What will now be considered are disturbances only within the plane of the sheet. The dispersion relation for a uniformly rotating sheet is

$$\omega^2 = 4\Omega^2 - 2\pi G\Sigma_0|k| + k^2 v_s^2, \qquad (7-4)$$

where $\Omega$ is the angular speed of the rotation (Binney and Tremaine 1987, p. 312). The sheet is unstable due to a Jeans-type instability if it is not rotating ($\Omega = 0$), for then $\omega^2 < 0$ if

$$|k| < k_J = 2\pi G\Sigma_0/v_s^2. \tag{7-5}$$

Long wavelengths are Jeans unstable due to gravity. There is also instability at short wavelengths if the pressure is nonexistent (so $v_s = 0$): $\omega^2 < 0$ if

$$|k| > 2\Omega^2/\pi G\Sigma_0. \tag{7-6}$$

Both rotation and pressure are needed together to stabilize a rotating sheet. The sheet may be completely stabilized if the quadratic minimum with respect to $|k|$ in equation (7–4) is nonnegative, which places the condition

$$\frac{v_s\Omega}{G\Sigma_0} \geq \frac{\pi}{2} \approx 1.57. \tag{7-7}$$

The stability criterion in equation (7–7) is not changed much if the disk is given a finite thickness. Stability of a uniformly rotating isothermal disk requires that

$$\frac{v_s\Omega}{G\Sigma_0} \geq 1.06 \tag{7-8}$$

(Goldreich and Lynden-Bell 1965).

Although a stellar (collisionless) disk cannot support sound waves, the stability criterion for a stellar disk is very similar to that of a fluid disk. A thin, rotating stellar disk is stabilized by a radial velocity dispersion $\sigma_r$ that satisfies

$$\frac{\sigma_r\Omega}{G\Sigma_0} \geq 1.68, \tag{7-9}$$

(Binney and Tremaine 1987, p. 314), where the numerical value is the result of assuming a Maxwellian distribution of velocities.

The existence of a finite velocity dispersion in a stellar disk or nonzero sound speed (which implies finite pressure) in a gaseous disk is essential to the disk stability.

A cold disk, that is, a disk with zero velocity dispersion or pressure, is violently unstable. This fact was numerically demonstrated in galactic models by Hockney and Brownrigg (1974). Their Figure 1 shows the fragmentation of an unstable disk that had no support from an internal velocity dispersion.

The dispersion relation for a gaseous disk that is not uniformly rotating is

$$(m\Omega - \omega)^2 = \kappa^2 - 2\pi G\Sigma|k| + k^2 v_s^2, \qquad (7-10)$$

where $m$ is the order of the mode and $\kappa$ is the epicyclic frequency

$$\kappa^2 = r\frac{d\Omega^2}{dr} + 4\Omega^2 \qquad (7-11)$$

(Binney and Tremaine 1987, p. 359). If the disk is uniformly rotating, $\kappa = 2\Omega$, and equation (7–10) reduces to the dispersion relation (7–4). A gas disk is locally stable against all nonaxisymmetric ($m \neq 0$) disturbances (Goldreich and Lynden-Bell 1965). Stability with respect to axisymmetric ($m = 0$) disturbances is investigated by solving quadratically for $|k|$ in equation (7–10) and requiring that $\omega^2 \geq 0$ for stability. The result is

$$Q \equiv \frac{v_s \kappa}{\pi G\Sigma} > 1 \qquad (7-12)$$

for stability of a rotating a gas disk to axisymmetric disturbances. The corresponding criterion for stellar disks is

$$Q = \frac{\sigma_r \kappa}{3.36\, G\Sigma} > 1 \qquad (7-13)$$

for stability. $Q$ is the so-called "Toomre parameter" (Toomre 1964). For a mainly stellar disk with 10% embedded gas, the numerical constant in the denominator of equation (7–13) is reduced to 2.9 (in approximate inverse proportion to the amount of gas, cf. Toomre 1974). Introduction of stars, with their inherently large velocity dispersion, has a stabilizing effect on a gaseous disk, as does giving the disk a finite thickness. Disturbances which enter a region with $Q < 1$ will grow while they are in that region.

The stability criteria in relations (7–12) and (7–13) are not constraints on the formation of clouds from the gas. The typical size scale of the instabilities associated with relations (7–12) and (7–13) is much larger than cloud sizes. The characteristic wavelength of the most unstable disturbance in a thin (gaseous or stellar) disk is

$$\lambda_{\rm mu} \approx \frac{2\pi^2 G\Sigma}{\kappa^2} \qquad (7-14)$$

(Binney and Tremaine 1987, pp. 362, 364). For $\kappa_\odot = 36\,{\rm km\,sec^{-1}\,kpc^{-1}}$ and $\Sigma_\odot = 75\,{\rm M_\odot\,pc^{-2}}$ in the vicinity of the Sun, $\lambda_{\rm mu} \approx 5\,{\rm kpc}$. Further hierarchical fragmentation of 5 kpc-sized pieces of a galactic disk could occur as smaller and smaller volumes of the disturbance become Jeans unstable. However, cloud formation is generally believed to take place in a much less violent and less hierarchical manner than through the break-up of a rotating disk. Clouds may more commonly form through accumulation by shocks into filaments; through collisional accretion of smaller clouds or collisional shredding of larger ones; and through instabilities of a thermal or magnetic nature (Parker 1966) which involve Rayleigh-Taylor instability in a two-phase medium.

It is a general requirement of theories of spiral structure that $Q \approx 1$. Swing amplification works well in the regime $Q = 1$–$1.5$; for larger values of $Q$, the gain decreases quite rapidly and spiral structure disappears (Toomre 1981). The modal theory requires marginal stability ($Q = 1$) of the galactic disk. In fact, a process of self-regulation has been hypothesized which maintains $Q \equiv 1$ in galactic disks (Bertin and Romeo 1988). Self regulation proceeds by reducing $Q$ to unity through dissipation of turbulence in the interstellar medium. If $Q$ falls below unity, then dynamical instability initiates vigorous star formation, which increases $Q$ both by heating the interstellar medium and through the dynamical increase in the stellar velocity dispersion. As discussed by Norman (1983), the modal and swing amplification theories are compatible with each other and merely differ concerning the means of amplification

and reflection of traveling waves.

Kennicutt (1989) has noted that the gas disks of many spirals satisfy $Q \gtrsim 1$. This is a reasonable observation, since the disks of most spirals do not appear to be unstable or to house exponentially growing disturbances. In the solar neighborhood, the gas mass surface density is about $5.3\,M_\odot\,pc^{-2}$ (Binney and Tremaine 1987, p. 16). The one-dimensional velocity dispersion of the local Galactic gas is about $5\,km\,sec^{-1}$: it is about $5\,km\,sec^{-1}$ for disk molecular clouds ($4.2 \pm 0.5\,km\,sec^{-1}$, Liszt and Burton 1983; 7–9 $km\,sec^{-1}$, Stark 1984; 2.5–4 $km\,sec^{-1}$, Clemens 1985) and 6–8 $km\,sec^{-1}$ for atomic hydrogen (Burton 1971). This yields $Q \approx 2.7$ for the gas disk in the solar neighborhood, if the velocity dispersions are indicative of average sound speeds in the gas. Turbulent motions in giant molecular clouds, however, are generally supersonic for the observed thermal temperatures (Elmegreen 1985). For all mass contributions to the local disk, $Q \approx 1.7$ from equation (7–13), using the reduced constant 2.9 and $\sigma_r \approx 45\,km\,sec^{-1}$ (cf. Toomre 1974). Thus, the solar neighborhood is safely stable.

### 7.2.3. Computation of Q

Computation of $Q$ for other galaxies requires knowledge of the local velocity dispersion or sound speed, the mass surface density, and the epicyclic frequency. The epicyclic frequency, $\kappa(r)$, may be computed from the rational function fit to the circular speed $V(r)$, equation (6–12), using the formula (7–11) or

$$\kappa(r) = \frac{1}{r}\left(2rV\frac{dV}{dr} + 2V^2\right)^{1/2} \qquad (7-15)$$

Values of the epicyclic frequency at the midpoints of 500 pc-wide annuli are listed in Table 7–8 for the program spirals. The mass surface density for the gaseous component may be computed from Table 7–5, and the total mass surface density may be computed from Table 6–5.

Gas velocity dispersions in the disks in other spirals are probably similar to that of our Galaxy. For example, the average H I velocity dispersion $\sigma_z$ in NGC 628

TABLE 7–8. EPICYCLIC FREQUENCY[a]

| NGC | Radius (kpc) | | | | |
|---|---|---|---|---|---|
| | 0.25 | 0.75 | 1.25 | 1.75 | 2.25 |
| 4254 | 293.7 | 200.2 | 145.3 | 110.9 | 88.41 |
| 4303 | 545.0 | 221.4 | 141.1 | 104.4 | 82.19 |
| 4321 | 295.2 | 242.5 | 183.2 | 145.4 | 120.1 |
| 4501 | 254.0 | 232.5 | 212.7 | 194.0 | 175.8 |
| 4535 | 493.1 | 289.7 | 163.3 | 110.7 | 86.86 |
| 4536 | 685.9 | 489.3 | 301.9 | 191.5 | 133.9 |
| 4569 | 128.0 | 109.2 | 99.82 | 92.69 | 86.70 |
| 4654 | 189.7 | 145.9 | 117.9 | 99.30 | 85.79 |

[a] Units are $\mathrm{km\,sec^{-1}\,kpc^{-1}}$.

is 9–10 $\mathrm{km\,sec^{-1}}$ and drops to 7–8 $\mathrm{km\,sec^{-1}}$ at the optical boundary (Shostak and van der Kruit 1984); in NGC 1058, $\sigma_z = 7.5 \pm 1\,\mathrm{km\,sec^{-1}}$ and is constant across the disk except for an increase to about 10 $\mathrm{km\,sec^{-1}}$ within one kiloparsec of the center (van der Kruit and Shostak 1984); in NGC 3938, $\sigma_z = 10 \pm 2.5\,\mathrm{km\,sec^{-1}}$ and is constant over the disk (van der Kruit and Shostak 1982). The intrinsic velocity dispersion of the H I in our Galaxy is about 7 $\mathrm{km\,sec^{-1}}$ within the solar circle to 850 pc radius; within 850 pc radius, the velocity dispersion increases to a median value around 12 $\mathrm{km\,sec^{-1}}$, although individual measurements of the Galactic center have maxima of $\sigma = 17\,\mathrm{km\,sec^{-1}}$ for $l > 0°$ and even 33 $\mathrm{km\,sec^{-1}}$ for $l < 0°$ (Rohlfs and Kreitschmann 1987). The old disk stars in our Galaxy have a radial velocity dispersion with exponential behavior

$$\sigma_r \propto e^{-R/2h}, \qquad (7-16)$$

where $R$ is Galactocentric distance and the scale length $h \approx 4370$ pc (Lewis and

Freeman 1989), a result which is expected from hydrostatic equilibrium and the assumption $\sigma_r/\sigma_z \approx$ const. $\sigma_r(0) \approx 104\,\mathrm{km\,sec^{-1}}$ for the Lewis and Freeman (1989) data, which implies $\sigma_r(R_\odot) \approx 39\,\mathrm{km\,sec^{-1}}$, which is about right (cf. Toomre 1974).

Widths of CO emission lines are measured from interferometer data by fitting Gaussian profiles to the spectra, as described in §6.1.2. Each spectrum is shot through a pixel 4″.5 on a side. Most of the line profiles are well fitted by Gaussian functions; on rare occasions, the fit is poor because of the very broad, non-Gaussian shape of the profile. Width measurements based on poor fits are omitted from further analysis. As a result, the central width measurements for NGC 4536, which have very broad lines, may be slightly underestimated.

Some of the width of the emission lines is contributed by the finite resolution and the steep rotation curves. The width introduced by rotation of the galaxy can be estimated by assuming that the emission over the beam area is uniform, so that emission at all velocities is represented equally under the beam. Assuming that the beam has uniform response over its effective area, the line width introduced by rotation is just the range of velocities under the beam. The simplifying assumptions used here result in an overestimate of the width introduced by rotation. Attenuation at the edge of the effective beam and the exponentially declining source emission both work to reduce the estimate of rotationally-induced line width. Beam sizes are taken from Table 3–2. The relation between beam FWHM and its variance $\sigma^2$ is

$$\sigma^2 = \frac{\mathrm{FWHM}^2}{8\ln 2}. \qquad (7-17)$$

Model velocity fields are constructed using the orientation parameters in Table 2–2 and Table 6–1 and the rotation curves parameterized by values in Table 6–2. The total variation in velocity across the beam is approximated as the difference in velocity between two ends of the chord, passing through the center of the beam ellipse, that is parallel to the galaxy major axis. The rotational part of the line width is subtracted in

quadrature from the measured width at each position. Corrected widths are averaged azimuthally in elliptical annuli 500 pc wide and are listed in Table 7–9. Values are omitted where there are no data or where the formal error is very large. Typical formal errors are 4–5 km sec$^{-1}$. Where the average estimated rotational line width exceeds the observed width, or where the formal error is exceptionally large, an upper limit is quoted that is the uncorrected line width. The mean velocity dispersions in the final column of Table 7–9 are computed by weighting by the mass in each radial bin.

TABLE 7–9. CORRECTED CO VELOCITY DISPERSIONS[a]

| NGC | Outer Radius (kpc) | | | | | $\langle\sigma_v\rangle$ |
|---|---|---|---|---|---|---|
| | 0.5 | 1.0 | 1.5 | 2.0 | 2.5 | |
| 4254 | 13.5 | 15.8 | 13.3 | 13.9 | 13.5 | 14.3 |
| 4303 | 16.7 | 16.7 | 17.4 | ··· | 19.0 | 17.3 |
| 4321 | 19.3 | <19.4 | <22.1 | 20.2 | 8.6 | 15.9 |
| 4501 | ··· | 16.0 | 20.1 | 17.9 | 15.3 | 17.4 |
| 4535 | 50.0 | 22.8 | ··· | <15.9 | 16.1 | 39.2 |
| 4536 | 51.1 | 44.4 | 23.7 | <19.6 | <19.5 | 43.5 |
| 4569 | 33.5 | 17.5 | ··· | <11.3 | <11.0 | 29.0 |
| 4654 | 13.9 | <13.4 | <10.8 | <11.2 | <12.1 | 13.9 |

[a] Units are km sec$^{-1}$. Values of one-dimensional dispersion $\sigma_v$ corrected for beam smearing are listed. The mean $\sigma_v$ is the average velocity dispersion weighted by the gas mass (from OVRO data) within the radial bin, ignoring upper limits.

Although the sound speed in the interstellar medium of an external galaxy cannot be measured directly, it can be estimated from the velocity dispersion of the gas. Line widths of CO emission from molecular clouds far exceed the width expected for a

thermal velocity distribution. The speed of sound $v_s$ in an ideal gas obeys

$$p_g = \frac{\rho v_s^2}{\gamma}, \qquad (7-18)$$

where $p_g$ is the gas pressure, $\rho$ the gas density, and $\gamma$ is the heat capacity ratio. Turbulence may be approximately taken into account by including a turbulent pressure $p_{\rm turb}$. The pressure is caused by the velocity dispersion of the gas: $p_g = \rho\sigma_v^2$, where $\sigma_v$ is the one-dimensional velocity dispersion. Since the linewidths are supersonic, the turbulent velocity dispersion is far greater than the thermal velocity dispersion and the turbulent pressure is much greater than the thermal pressure. Therefore,

$$p_{\rm tot} = p_g + p_{\rm turb} \approx \rho\sigma_v^2 \qquad (7-19)$$

and so $v_s \approx \sigma_v\sqrt{\gamma}$. For diatomic molecular gas, $1 < \gamma \lesssim 5/3$, with variation depending on temperature and pressure because of excitation of modes of energy storage in the motions of the constituent atoms. The one-dimensional velocity dispersion $\sigma_v$ may be used in equation (7–12) in place of $v_s$ for molecular gas disks with relatively small error.

Values of $Q_{10}$ in 500 pc-wide annuli for the gas disks of Virgo spirals are listed in Table 7–10, where $Q_{10}$ is computed using formula (7–12) with the reduced divisor 2.9, assuming $v_s \equiv 10\,{\rm km\,sec^{-1}}$, and with gas mass surface densities computed from Table 7–5. Values of $Q_{50}$ in 500 pc-wide annuli are listed in Table 7–11, where $Q_{50}$ is computed using formula (7–13) with the reduced divisor 2.9, assuming $\sigma_r \equiv 50\,{\rm km\,sec^{-1}}$, and with total mass surface densities from Table 6–5, which assumes a thin disk mass distribution. Values of $Q_{10}$ for our Galaxy were computed from the gas masses in Table 7–5. Epicyclic frequencies were computed from H I rotation curve data in Rohlfs and Kreitschmann (1987) using the formula

$$\kappa^2 = 4B(B - A) \qquad (7-20)$$

(Binney and Tremaine 1987, p. 122), where $A$ and $B$ are the Oort parameters. Values of $Q_{50}$ for our Galaxy were computed assuming a spherically symmetric mass distribution with the Rohlfs and Kreitschmann (1987) rotation curve data.

TABLE 7–10. $Q_{10}$ FOR GAS DISKS

| NGC | Outer Radius (kpc) | | | | |
|---|---|---|---|---|---|
| | 0.5 | 1.0 | 1.5 | 2.0 | 2.5 |
| 4254 | 1.039 | 0.946 | 1.108 | 1.329 | 1.385 |
| 4303 | 1.667 | 0.822 | 0.652 | 0.599 | 0.583 |
| 4321 | 0.572 | 0.642 | 0.815 | 1.089 | 1.249 |
| 4501 | 1.616 | 1.690 | 1.796 | 1.897 | 1.990 |
| 4535 | 1.213 | 5.525 | 5.043 | 3.814 | 3.373 |
| 4536 | 1.231 | 1.931 | 1.953 | 1.868 | 1.952 |
| 4569 | 0.434 | 0.470 | 0.559 | 0.681 | 0.832 |
| 4654 | 1.282 | 1.863 | 3.793 | 2.179 | 1.554 |
| Galaxy | 3.255 | | 4.565 | | 26.65 |

The values of $Q_{10}$ in Table 7–10 are generally greater than unity, indicating that the gas disks of most of the spirals are locally stable against axisymmetric perturbations at most radii. From the prevalence of values of $Q_{10} > 1$, several deductions may be made. First, $Q_{10}$ was computed for Table 7–10 with the assumption that $v_s \equiv 10\,\mathrm{km\,sec^{-1}}$. Based on H I observations of other galaxies described above, $10\,\mathrm{km\,sec^{-1}}$ may be too large by a factor of two for the outer disk but too small by a factor of about two for the inner 0.5–1.0 kpc. Use of values of $\sigma_v$ from Table 7–9 to compute $Q$ will result in values that are generally larger than the $Q_{10}$ values listed in Table 7–10. Since $Q > 1$ is expected on the observation of stability of normal spiral disks, the prevalence of $Q_{10} > 1$ suggests that $v_s \equiv 10\,\mathrm{km\,sec^{-1}}$ is not a bad as-

TABLE 7–11. $Q_{50}$ FOR GALACTIC DISKS

| NGC | Outer Radius (kpc) | | | | |
|---|---|---|---|---|---|
| | 0.5 | 1.0 | 1.5 | 2.0 | 2.5 |
| 4254 | 0.479 | 0.750 | 0.830 | 0.824 | 0.783 |
| 4303 | 1.168 | 0.980 | 1.004 | 1.025 | 1.043 |
| 4321 | 0.287 | 0.559 | 0.654 | 0.706 | 0.745 |
| 4501 | 0.098 | 0.219 | 0.322 | 0.401 | 0.456 |
| 4535 | 0.624 | 0.961 | 0.748 | 0.593 | 0.568 |
| 4536 | 0.346 | 0.737 | 0.866 | 0.774 | 0.658 |
| 4569 | 0.157 | 0.259 | 0.362 | 0.457 | 0.548 |
| 4654 | 0.320 | 0.532 | 0.648 | 0.724 | 0.779 |
| Galaxy | 0.568 | 0.917 | 0.825 | 1.062 | 1.160 |

sumption. In fact, $Q_{10} \approx 1.5$–$2.0$ around 2.5 kpc radius, suggesting $v_s \approx 5$–$7\,\mathrm{km\,sec^{-1}}$ there. Moreover, since $\sigma_v(\mathrm{H\,I})$ increases near the Galactic center, it is expected that $Q_{10}$ should decrease at small radii if other spirals behave like our Galaxy. $Q_{10}$ does, in fact, decrease at small radii in the spirals with $Q_{10} > 1$. The values of $Q_{10}$ for our Galaxy are rather large, but this is probably due to underestimation of the total gas mass, especially between 1.5 kpc and 2.5 kpc radius. In general, values of $Q_{10}$ indicate that the large gas masses in NGC 4501, NGC 4535, NGC 4536, and NGC 4654 listed in Table 7–2 are not physically forbidden by dynamical considerations.

Recall that local instability implies that a disturbance will grow in amplitude as it passes through the unstable region. Although local axisymmetric stability is not everywhere necessarily mandatory in a normal spiral disk, the reasons for any apparent instabilities should be sought. The values of $Q_{10}$ are rather low at all radii, particularly inside 1.5 kpc, for NGC 4254. A value of $v_s$ rather larger than $10\,\mathrm{km\,sec^{-1}}$

could explain the smallish values of $Q_{10}$, as could a slight overestimate of the gas mass. NGC 4303 has low values of $Q_{10}$ at all radii except the very center. The values of $Q_{10}$ paradoxically decrease with increasing radius, which is not the behavior expected if systematic variation of $v_s$ with radius is the cause of the behavior of $Q_{10}$. It is possible that gas masses have been overestimated out to 2.5 kpc radius. NGC 4303 is the only program spiral with a clear bar at its center that is massive enough to influence gas dynamics. Perhaps large gas velocity dispersions result from the bar, which might explain the uniformly low $Q_{10}$ values if the increased $\sigma_r$ supports a more massive gas disk. Alternatively, the rotation curve may not reflect circular speeds which are the result of mass but rather it may be altered by noncircular motions in the bar velocity field. In such a case, the computed epicyclic frequency may be incorrect. Low values of $Q_{10}$ also pertain to NGC 4321 out to at least 1.5 kpc radius. The behavior of $Q_{10}$ could be explained by an increased sound speed or velocity dispersion near the center of the order 20 km sec$^{-1}$, as suggested by values of $\sigma_v$ in Table 7–9. Values of $Q_{10}$ for NGC 4569 are the most troublesome, being small out to 2.5 kpc radius. If the low $Q_{10}$ values are presumed to be due to underestimating $v_s$, then a value at the center is required that is at least 2.5 times as great as in the disk. Values of $\sigma_v$ from Table 7–9 suggest that $v_s \approx$ 20–30 km sec$^{-1}$. Three other galaxies, NGC 4535, NGC 4536, and NGC 4654, have values of $Q_{10}$ indicating stability at all radii but show anomalous values of $Q_{10}$ at their centers. Compared to the rather large values of $Q_{10}$ at radii beyond 500 pc, the central values of $Q_{10}$ are unexpectedly small. NGC 4535 shows this tendency very strongly. Such behavior may occur if $v_s$ increases dramatically at the very center, as suggested by the large central values of $\sigma_v$ in Table 7–9, or if the central gas masses are somewhat overestimated.

Several galaxies have values of $Q_{10}$ which are at the edge of the numerical range which implies stability within the errors. These galaxies are NGC 4254, NGC 4303,

NGC 4321, and NGC 4569. It is very suggestive that these same galaxies are the ones which have relatively large gas mass fractions, as inspection of Table 7–7 shows. Of the three galaxies with anomalously low values of $Q_{10}$ within 500 pc of their centers, two (NGC 4535 and NGC 4654) have central gas mass fractions which are clearly larger than the values outside 500 pc. Explanations for this behavior will be discussed in §7.3.

Values of $Q_{50}$ in Table 7–11 refer to the stability of the entire disk of gas and stars. Most of the values are less than unity, but this fact does not necessarily imply instability. The central radial velocity dispersion of our Galaxy is $\sigma_r \approx 104\,\mathrm{km\,sec^{-1}}$ (Lewis and Freeman 1989), which falls to $\sigma_r \approx 80\,\mathrm{km\,sec^{-1}}$ at 2.5 kpc radius. Assuming that the Virgo spirals have stellar disks with similar velocity dispersions, the values in Table 7–11 may reasonably be increased by factors of from 1.6 to 2.1, which is enough to boost all of the $Q_{50}$ values to greater than unity except those for NGC 4501. The variation of $Q_{50}$ with radius is rather stable from 1.5 kpc radius outward for each galaxy. The behavior of $Q_{50}$ is moderated by two competing influences: the decrease of $\sigma_r$ with increasing radius and the decrease of $Q$ with the onset of spiral structure. The relatively low values of $Q_{50}$ for NGC 4501 are probably due to a larger central velocity dispersion for this early-type, very massive galaxy. Central values of $Q_{50}$ are also low for NGC 4536 and for our Galaxy, which together with NGC 4501 are the three galaxies with the steepest central velocity gradients. Such great central mass concentrations are probably distributed with spherical symmetry, thereby decreasing the disk midplane surface density, and are probably stabilized by rather larger velocity dispersions. Both effects will increase $Q$. However, NGC 4569 also has a low value of $Q_{50}$, but it has a very small central concentration of mass.

## 7.3. Adjusting Gas Mass Estimates

On the balance of the numerical evidence provided in Tables 7–6, 7–7, and 7–10,

are the molecular gas masses (Table 7–2) computed in the standard way (equation 2–2) physically reasonable? Some of the gas mass fractions are rather large, and some are impossibly large; their values call for revision of the molecular gas mass estimates. Alternatively, most of the values of the stability parameter $Q$ imply that rotating gas disks with such large mass surface densities are locally stable against axisymmetric disturbances, or can arguably be made marginally stable by assigning them reasonable gas velocity dispersions. Values of $Q$ are not so obviously wrong in most cases as to discount the large gas mass estimates. What follows is a discussion of the various factors which influence gas mass and dynamical mass computation and estimation of the stability parameter. The goal will be to dismiss the factors with insignificant effect and to estimate the degree of influence of the major effects.

### 7.3.1. Rotation Curve

If dynamical masses have been underestimated, then large gas mass fraction estimates will result. Dynamical masses may be modified by adjusting the rotation curves to be envelopes of velocity data instead of least squares curves passing through the data. The resulting increased circular speeds $V$ will thereby inflate the dynamical mass approximately as $V^2$. Modifying rotation curves to be envelopes will also increase the stability parameter $Q$ by changing the epicyclic frequency, $\kappa$, which will increase roughly as $V$ (since $dV/dr$ is proportional to the change in $V$ in the linear part of the rotation curve). Consider the most extreme case, NGC 4569, whose computed gas mass fraction lies in the range 31% to 134%. To reduce these estimates to realistic gas mass fractions in the range 5–10% would require at the very least an increase of the rotation speed by a factor of $\sqrt{3} \approx 1.7$, which means boosting the rotation speed at 500 pc from 35 km sec$^{-1}$ to 61 km sec$^{-1}$. Although there is substantial scatter in the rotation curve data (Figure 6–20), the largest admissible outlier speed at 500 pc radius is 55 km sec$^{-1}$. This speed is marginally able to adjust the lower

bound on the gas mass fraction into the reasonable range. However, the marginally acceptable effect is not satisfying, and modification of all rotation speed estimates smacks of posterior reasoning. (See also the discussion of rotation speed estimation in § 6.1.1).

Some of the rotation curves are very closely delineated by the data, such as the case of NGC 4654 (Figure 6–21), which admits a total variation $\Delta V \approx 5\,\mathrm{km\,sec^{-1}}$. Such a well-defined rotation curve does not allow much change of the dynamical mass estimate, so the gas mass fraction must stand between 14% and 42% or else another cause for the large gas mass fraction estimates should be sought. Examination of the spread in velocity data for all rotation curves shows that the greatest increase that can be made in the circular speed at 500 pc radius by drawing the envelope is an extra 50%, which is only sufficient to cut the gas mass fraction estimate in half. Note also that the problem is rather more severe than indicated by the values in Table 7–6 and Table 7–7, since the gas is undoubtedly confined to a thin disk of 50 pc–100 pc width, while the stellar mass is spheroidally distributed with a comparatively large radius. The ratio of volume densities of gas and stars in the disk midplane is therefore much larger than indicated by values of the gas mass fractions in Table 7–6. In the solar neighborhood, gas and stellar volume densities are comparable (Binney and Tremaine 1987, p. 202).

### 7.3.2. Distance Error

If the adopted distance, $D$, to the Virgo Cluster is too great, then all masses will be overestimated. However, the molecular gas mass estimate is proportional to $D^2$ (equation 2–2), while the dynamical mass estimate is proportional to $D$ (equation 2–3), so the gas mass fraction estimate varies in proportion to errors in $D$. It is quite unreasonable, though, that the distance to the Virgo Cluster can be in error by enough to alter gas mass fraction estimates by factors of three to ten. Recent measurements

of the distances to galaxies in the Virgo Cluster are only as low as 13 Mpc (Tonry, Ajhar, and Luppino 1989), while high estimates are as large as 22 Mpc (Harris 1988). The adopted distance, 15.7 Mpc, is already at the low end of the range; clearly, the larger distance estimates will inflate the computed gas masses.

### 7.3.3. Abundances

Abundance variations have both direct and indirect effects on the gas mass estimates. The presence of helium adds an extra 36% to the hydrogen mass. It is difficult to see how helium could be very much less abundant in normal spirals, but even its complete absence would rather negligibly diminish the gas mass estimates to 74% of their reported values. The effects of metal abundance on the gas mass estimate are much more difficult to ascertain.

Spectrophotometry of individual H II regions in nearby spirals (Smith 1975) was used to estimate the metallicities in these galaxies. Smith observed nine galaxies, extended the work of Searle (1971), and reached similar conclusions. Early-type spirals were found to have larger metallicities than late-type spirals. This observation can be understood if it is assumed that the gas mass fraction of a galaxy decreases monotonically over the life of the galaxy after some fiducial time (say, a gas infall time). Then those galaxies with larger gas mass fractions have processed less of their interstellar material and would be expected to have lower metallicities. The differences in metallicity among morphological types are thus linked to their gas mass fractions. The larger metallicity of early-type galaxies should increase the emissivity of their molecular cloud populations.

No correlation was found by Smith to relate metallicity with galactic mass. One implication of this observation is that, if gas enrichment occurs by infall, then the amount of extra star formation is proportional to the amount of extra gas. In this manner, the gas mass fraction and metallicity remain unchanged despite the gain in

mass. The rate of star formation is independent of the mass, and hence rotation speed, of the galaxy in this scenario. This implies that differential rotation does not provide the relative velocities in cloud-cloud collisions that lead to star formation. Alternatively, the lack of a galaxy mass-metallicity correlation may only say that each morphological type may be seen equally in galaxies of all sizes.

Finally, and perhaps most importantly, Smith agreed with Searle and found large-scale abundance gradients across the disks of spirals. [O/H], [Ne/H], and [S/H] were found to drop by a factor of 10 from the nuclei to the outer disk in all types of galaxies. This fact would increase the CO emissivities of molecular clouds at the center of a spiral galaxy relative to those in the disk.

Using models of virialized, magnetized clouds in pressure equilibrium with the surrounding interstellar medium, Elmegreen (1989) showed that the dependence of the CO–$H_2$ conversion factor on metallicity is $\xi \propto z^{-3/8}$. Galaxies with greater metallicity, which are presumably earlier-type galaxies, will have a slightly smaller conversion factor, making them overluminous in CO emission for their $H_2$ mass. The small exponent in the power-law dependence on metallicity means that the variation in $\xi$ due to metallicity will be rather small when applied to spiral galaxies.

### 7.3.4. CO–$H_2$ Conversion Factor

As discussed in §3.1.5, there is some degree of controversy over the correct value of the conversion factor $\xi$ (equation 3–3) between CO radiancy and $H_2$ column density for our Galaxy and for nearby galaxies. Recent observational studies to determine empirically a value of $\xi$ have found values in the range $\xi = (1.8 - 4.8) \times 10^{20}\,\mathrm{cm^{-2}(K\,km\,sec^{-1})^{-1}}$. Based on the scatter in the empirical measurements of $\xi$, the adopted value $\xi = 3 \times 10^{20}\,\mathrm{cm^{-2}\,(K\,km\,sec^{-1})^{-1}}$ will yield molecular hydrogen masses reliable to within a factor of two. If a low value of $\xi$ pertained to the central regions of the Virgo spirals studied here, then the reduction of the estimated gas

masses by one-half would place nearly all of the gas disks comfortably into the stable $Q > 1$ regime. The range of empirical values of $\xi$ is not sufficient to reduce the central gas mass fractions in Table 7–6 (which assumes spherical symmetry) to under 10%, although most of the gas mass fractions in Table 7–7 (thin disk mass distribution) are reasonable after a reduction by one-half.

Analytical models of magnetized molecular clouds in virial equilibrium with the pressure at the cloud surface equal to the ambient pressure of the interstellar medium (Elmegreen 1989) indicate a larger value of $\xi$, not a smaller one, for extragalactic studies. Even if the molecular cloud population in another galaxy is the same as in our Galaxy and follows a mass law

$$n(M)\,dM = n_0(M/M_0)^{-\alpha}\,dM, \qquad (7-21)$$

then the extragalactic conversion factor $\xi_{\rm gal}$ differs from the conversion factor in our Galaxy, $\xi_{\rm local}$, by a factor

$$\frac{\xi_{\rm gal}}{\xi_{\rm local}} = \frac{2.25-\alpha}{2-\alpha} \qquad (7-22)$$

because of the averaging of a telescope beam over an ensemble of clouds. For $\alpha = 1.5$, the factor is 1.5. See Elmegreen (1989) for details. Direct application of this result would *increase* the gas masses in Table 7–5 to nearly half again their values.

Physical mechanisms that will result in a different conversion factor $\xi$ for galactic centers are discussed in the next two sections. The goal will be to see what range of properties could pertain to galactic center clouds and the range of conversion factors that result. At issue is the true amount of molecular hydrogen at the centers of spirals and the degree to which it is reflected by conventional mass estimates.

### 7.3.5. Density

Table 5–3 lists the peak and mean CO brightness for each of the program spiral galaxies. Estimates of the mean molecular hydrogen density within cloud complexes

detected by the interferometer may be made from those values. Using the adopted conversion between CO radiancy and $H_2$ mass, equation (2–2), and assuming that the molecular disk is 50 pc thick, values of the areal-averaged number density, $\bar{n}_{H_2}$, may be computed. These are shown in Table 7–12 along with values of $\bar{n}^*_{H_2}$, which are estimates of the areal-averaged molecular hydrogen density in molecular clouds that are members of cloud complexes detected with the interferometer. The mean density of clouds in complexes is $\bar{n}^* = \bar{n}/f_A$, where $f_A$ is the area filling factor of clouds within cloud complexes estimated from the equation $f_A \approx T_b \sigma_v / T_k \Delta v_{\rm cloud}$, where $T_b$ is the mean brightness temperature listed in Table 5–3, $T_k \approx 10\,{\rm K}$, $\sigma_v$ is the velocity dispersion from Table 7–9, and $\Delta v_{\rm cloud} \approx 5\,{\rm km\,sec^{-1}}$ is the velocity dispersion in a single cloud. The area filling factor would be just the ratio of brightness temperatures except that the velocity dispersion of clouds allows multiple clouds along the line of sight to be spread in velocity space. The ratio of velocity dispersions adjusts the brightness temperature ratio by counting the number of clouds along the line of sight.

TABLE 7–12. AVERAGE $H_2$ DENSITY

| NGC | $\bar{n}_{H_2}\,({\rm cm^{-3}})$ | $f_A$ | $\bar{n}^*_{H_2}\,({\rm cm^{-3}})$ |
|---|---|---|---|
| 4254 | 163 | 0.158 | 1030 |
| 4303 | 181 | 0.190 | 950 |
| 4321 | 267 | 0.377 | 710 |
| 4501 | 258 | 0.145 | 1780 |
| 4535 | 240 | 0.332 | 720 |
| 4536 | 440 | 0.497 | 880 |
| 4569 | 387 | 0.306 | 1260 |
| 4654 | 76 | 0.084 | 910 |

The mean densities in Table 7–12 are averages over 2.25 arcsec$^{-2}$ areas, or regions about 115 pc on a side. The density of the Sgr B2 complex, a very large and bright molecular association at the center of our Galaxy, averaged over a 40–50 pc region, is $\bar{n}_{H_2} = 2 - 3 \times 10^3\,\mathrm{cm}^{-3}$. The value of $\bar{n}$ for Sgr B2 decreases by a factor of a few when averaged over a region a few hundred parsecs in size, because the clouds are discrete and do not completely fill space. The values of the mean molecular hydrogen density for the nuclear regions of Virgo spirals, corrected by the areal filling factor, $\bar{n}^*_{H_2}$, are all comparable to the Sgr B2 density, but are slightly smaller. If cloud temperatures near the centers of Virgo spiral galaxies are larger than the 10 K value used to estimate $f_A$, then the resulting increases in $n^*_{H_2}$ would bring the densities into good agreement with those of Galactic center molecular clouds. CO emission is a reliable indicator of the mass of molecular clouds in the disk of our Galaxy whose mean densities satisfy $10^2\,\mathrm{cm}^{-3} \lesssim \bar{n}_{H_2} \lesssim 10^4\,\mathrm{cm}^{-3}$. Both Sag B2 and the molecular clouds at the centers of Virgo spirals apparently satisfy this relationship, so there is reason to believe the molecular mass estimates if the molecular clouds at the centers of Virgo spirals resemble Galactic disk molecular clouds.

### 7.3.6. Temperature

The effect of molecular cloud temperature on CO emissivity has been modeled both analytically and numerically with similar results. As discussed in §3.1.5, Kutner and Leung (1985) found that

$$\xi \equiv N_{H_2}/I_{CO} \propto T_k^{-1.3} \qquad (7-23)$$

for isothermal clouds, where $T_k$ is the kinetic temperature of the cloud. The nonlinearity in equation (7–23) is produced by the nonlinear coupling between antenna temperature and excitation temperature except when $T_k \gtrsim 30$ K (Maloney and Black 1988). Elmegreen (1989) found, in fact, that

$$\xi \propto T^{-1} \qquad (7-24)$$

for magnetized, virialized clouds in pressure equilibrium with the interstellar medium, where $T$ is the areal-averaged thermal temperature. Since such a strong dependence on temperature is indicated, it would be wise to investigate the sources of heating of molecular clouds and to determine if molecular clouds in the central regions of spirals have different characteristic temperatures than disk molecular clouds. The proper temperature to consider is that of the gas in regions from which observable CO emission arises. Although CO emission is generally optically thick, the region from which it arises is likely to have considerable spatial extent because of Doppler shifts due to turbulent motions in the cloud.

There are many sources of heating for molecular clouds. Based on the noted spatial correlation between CO and H$\alpha$ emission (see Chapter 4), the main source of cloud heating may be expected to be associated with high-mass star formation. Although the direct coupling between gas and an ambient radiation field is weak, the gas may be more efficiently heated by dust grains bathed in the radiation field. Dust may heat the gas through photoelectric emission in a strong ultraviolet field, so this process is important in the outer parts of molecular clouds, especially in their atomic hydrogen envelopes. Any increase in CO emissivity due to a higher temperature from photoelectric heating is partially negated by a decrease in the size of the CO-emitting surface of the cloud. Analysis by Elmegreen (1989) indicates that

$$\xi \propto u^{3/8}, \qquad (7-25)$$

where $u$ is the energy density of the ambient ionizing field, which partially offsets the relation $\xi \propto u^{-1}$ due to temperature.

Within the cloud, collisional heating of the gas by warm dust grains that are heated by infrared radiation is important. However, the dust temperature is very insensitive to the strength of the ambient radiation field. If $F_{\rm IR}$ is the flux of the

ambient infrared radiation field, the temperature of the dust, $T_{\rm dust}$, follows

$$F_{\rm IR} = \epsilon \sigma_{\rm SB} T_{\rm dust}^4, \qquad (7-26)$$

where $\epsilon$ is the dust emissivity and $\sigma_{\rm SB}$ is the Stefan-Boltzmann constant. Therefore, with moderate coupling between gas and dust, a huge increase in the ambient flux is needed to raise the gas temperature appreciably. The mean dust temperature in Sgr B2 is in the range 13–23 K over the range of CO emission, while the temperature deduced from CO emission is about 20 K (Lis and Goldsmith 1990). Approximate agreement between the two temperatures could mean that gas and dust are partially coupled through collisional heating.

The most important source of heating in larger molecular clouds is dissipation of turbulence. Lis and Goldsmith (1990) included photoelectric and collisional heating and heating by turbulence, cosmic rays, and Alfvén waves in their model of Sgr B2 and concluded that turbulence was the dominant heating source. Turbulent heating has also been suggested by Güsten *et al.* (1985) as the dominant heating source for Galactic center molecular clouds. Multitransition observations of ammonia emission by Güsten *et al.* (1985) and Morris *et al.* (1983) indicate even higher temperatures for Galactic center clouds than implied by CO observations. Ammonia observations imply temperatures of $\gtrsim 50$ K for Sgr A, but $T_{\rm dust}$ is only $\approx 35$ K. The reason for higher ammonia temperatures is probably that ammonia emission is concentrated in the warmer, denser cores of the clouds. There is no doubt that Galactic center molecular clouds are much warmer than disk molecular clouds in the radial range 2–10 kpc, whose temperatures are 4 K on average (Solomon *et al.* 1987) but whose warm cores may be 10 K–20 K (Solomon and Sanders 1986). Turbulent heating is the reason suggested by Walmsley (1987), who noted that the CO line widths are about 3 km sec$^{-1}$ for spiral arm molecular clouds but are 10–20 km sec$^{-1}$ for Galactic center clouds.

The heating rate due to dissipation of turbulence derived by Black (1987) is

$$\Gamma_{\rm turb} \propto v_t^3 \, n \, R_{\rm c}^{-1}, \qquad (7-27)$$

where $v_t$ is the turbulent velocity, $n$ is the density, and $R_{\rm c}$ is the size of the region under consideration. Falgarone and Puget (1985) have derived a similar formula with identical dependence on $v_t$ for condensations moving through a more diffuse cloud medium. At high densities, the cooling is dominated by molecular line radiation from thermalized transitions and obeys

$$\Lambda \propto T_k^3 \qquad (7-28)$$

(Scoville, Solomon, and Penzias 1975; Lis and Goldsmith 1990). Equating the heating (equation 7–27) and cooling (equation 7–28) rates leads to the temperature dependence

$$T_k \propto v_t (n/R_{\rm c})^{1/3}, \qquad (7-29)$$

from which the conversion factor dependence follows using equation (7–24):

$$\xi \propto v_t^{-1}. \qquad (7-30)$$

The source of energy to drive the turbulence is not known with certainty. Norman and Silk (1979) note that winds from young stellar objects are common enough to provide a source of turbulence, but the energetics and timescales involved are uncertain. Energy injection by supernovae cannot be ignored, either. Both potential sources of energy to drive the turbulence are associated with star formation inside the molecular cloud or in its vicinity, which fits with the correlation between CO and H$\alpha$ emission.

The increased temperatures of molecular clouds at the centers of spirals are probably connected with the increase in turbulence in such clouds through equation (7–27). The accompanying increase in CO emissivity would lead to CO profiles that are more

strongly peaked than is proportionate to the concentration of molecular hydrogen. Judging from the increase of the H I velocity dispersions at small radii in other spiral galaxies (§7.2), an increase of at least a factor of 1.4 in CO emissivity over that of disk molecular clouds appears commonplace. CO velocity dispersions (Table 7–9) are also larger at the centers of many spiral galaxies. In our Galaxy, for which higher resolution measurements are possible, the possible increase in CO emissivity due to heating by dissipation of turbulence within the central kiloparsec is a factor of 2.4–4.7. These estimates do not include allowances for changes in other physical parameters such as density or metallicity, but such corrections enter as a small (sublinear) power of the changing quantity and probably do not overpower the temperature dependence. Reductions of the molecular hydrogen masses in Table 7–2, of the $H_2$/H I mass ratios in Table 7–3, and of the gas mass fractions in Table 7–6 and Table 7–7 by factors of 2.5 to 5 are reasonable inside 1 kpc radius. Values of the stability parameter $Q$ for the gas will likewise increase by the same factors due to the increased velocity dispersion. Such reductions in gas mass are not so large as to completely invalidate the observations of large central gas masses, but they are sufficient to place all gas mass fractions in the realm of reason and to ensure the stability of gas disks in the central regions of spirals.

All galaxies except NGC 4254 and NGC 4654 show CO velocity dispersions that are significantly greater than $10\,\mathrm{km\,sec^{-1}}$. If the corrected line widths are representative of turbulence in the clouds, then most of the clouds are probably substantially warmer than Galactic disk molecular clouds. Noncircular motions near the nuclei of NGC 4303 and NGC 4321 probably increase their central line widths. Some of the galaxies show a large increase in intrinsic line width at small radii. The width of NGC 4569 increases by a factor of three, while those of NGC 4535 and NGC 4536 increase by factors of at least two. The larger line widths probably indicate greater

cloud turbulence, which implies that the central clouds are warmer than their disk counterparts. Molecular gas masses for the central clouds will be overestimated approximately in proportion to their larger temperatures. Many of the galaxies, however, do not show an increase in CO line width near their centers. Dynamical effects may dominate other factors that influence line width in NGC 4303 and NGC 4321, but the lack of any significant change in the widths for NGC 4254 is puzzling. Lack of data prevents a definite conclusion in the case of NGC 4501. The widths of nearly all lines in NGC 4654 are so narrow that the filterbank does not resolve them with very great accuracy. For all galaxies, the contribution of the missing flux to the line widths is probably substantial. The behavior of CO widths with radius, as shown in Table 7–12, suggests that molecular gas velocity dispersions rise substantially at the centers of many spirals, but the numerical values are not precisely quantitative because of missing flux.

## References

Bahcall, J. N., Schmidt, M., and Soneira, R. M. 1983, *Ap. J.*, **265**, 730.

Bertin, G. and Romeo, A. B. 1988, *Astron. Ap.*, **195**, 105.

Binney, J., and Tremaine, S. 1987, *Galactic Dynamics* (Princeton: Princeton University Press).

Black, J. H. 1987, in *Interstellar Processes,* ed. D. J. Hollenbach and H. A. Thronson, Jr. (Dordrecht: Reidel), p. 731.

Burton, W. B. 1971, *Astron. Ap.*, **10**, 76.

Clemens, D. P. 1985, *Ap. J.*, **295**, 422.

Elmegreen, B. G. 1985, in *Protostars and Planets II,* ed. D. C. Black and M. S. Matthews (Tucson: University of Arizona Press), p. 33.

Elmegreen, B. G. 1989, *Ap. J.*, **338**, 178.

Falgarone, E. and Puget, J. L. 1985, *Astron. Ap.*, **142**, 157.

Giovanelli, R. and Haynes, M. P. 1983, *A. J.*, **88**, 881.

Goldreich, P., and Lynden-Bell, D. 1965, *M.N.R.A.S.*, **130**, 125.

Güsten, R., Walmsley, C. M., Ungerechts, H., and Churchwell, E. 1985, *Astron. Ap.*, **142**, 381.

Harris, W. E. 1988, in *The Extragalactic Distance Scale: Proceedings of the ASP 100th Anniversary,* ed. S. van den Bergh and S. J. Pritchet (ASP Conf. Ser. 4), p. 231.

Hockney, R. W., and Brownrigg, D. R. K. 1974, *M.N.R.A.S.*, **167**, 351.

Huntley, J. M. 1980, *Ap. J.*, **238**, 534.

Kenney, J. D. 1987, Ph.D. Thesis, University of Massachusetts.

Kennicutt, R. C., Jr. 1989, *Ap. J.*, **344**, 685.

Kutner, M. L., and Leung, C. M. 1985, *Ap. J.*, **291**, 188.

Lewis, J. R., and Freeman, K. C. 1989, *A. J.*, **97**, 149.

Lis, D. C., and Goldsmith, P. M. 1990, *Ap. J.*, in press.

Liszt, H. S., and Burton, W. B. 1983, in *Kinematics, Dynamics, and Structure of the Milky Way,* ed. W. L. H. Shuter (Dordrecht: Reidel), p. 135.

Maloney, P., and Black, J. H. 1988, *Ap. J.*, **325**, 389.

Morris, M., Polish, N., Zuckerman, B., and Kaifu, N. 1983, *A. J.*, **88**, 1228.

Mulder, W. A. 1986, *Astron. Ap.*, **156**, 354.

Norman, C. A. and Silk, J. 1979, *Ap. J.*, **228**, 197.

Norman, C. A. 1983, in *Internal Kinematics and Dynamics of Galaxies,* ed. E. Athanassoula (Dordrecht: Reidel), p. 163.

Parker, E. N. 1966, *Ap. J.*, **145**, 811.

Roberts, M. S. 1975, in *Galaxies and the Universe,* ed. A. Sandage, M. Sandage, and J. Kristian (Chicago: University of Chicago Press), p. 309.

Rohlfs, K., and Kreitschmann, J. 1987, *Astron. Ap.*, **178**, 95.

Sanders, D. B., Solomon, P. M., and Scoville, N. Z. 1984, *Ap. J.*, **276**, 182.

Scoville, N. Z., Solomon, P. M., and Penzias, A. A. 1975, *Ap. J.*, **201**, 352.

Searle, L. 1971, *Ap. J.*, **168**, 327.

Shostak, G. S., and van der Kruit, P. C. 1984, *Astron. Ap.*, **132**, 20.

Smith, H. E. 1975, *Ap. J.*, **199**, 591.

Solomon, P. M., and Sanders, D. B. 1985, in *Photostars and Planets II,* ed. D. C. Black and M. S. Matthews (Tucson: University of Arizona Press), p. 59.

Solomon, P. M., Rivolo, A. R., Barrett, J., and Yahil, A. 1987, *Ap. J.*, **319**, 730.

Stark, A. A. 1984, *Ap. J.*, **281**, 624.

Tonry, J. L., Ajhar, E. A., and Luppino, G. A. 1989, *Ap. J. (Letters)*, **346**, L57.

Toomre, A. 1964, *Ap. J.*, **139**, 1217.

Toomre, A. 1974, in *Highlights of Astronomy,* ed. G. Contopoulos (Dordrecht: Reidel), p. 457.

Toomre, A. 1981, in *Structure and Evolution of Normal Galaxies,* ed. J. M. Fall and D. Lynden-Bell (Cambridge: Cambridge University Press), p. 111.

van der Kruit, P. C. and Shostak, G. S. 1982, *Astron. Ap.*, **105**, 351.

van der Kruit, P. C. and Shostak, G. S. 1984, *Astron. Ap.*, **134**, 258.

Walmsley, C. M. 1987, in *Physical Processes in Interstellar Clouds,* ed. G. E. Morfill and M. Scholer (Dordrecht: Reidel), p. 161.

Warmels, R. H. 1986, Ph.D. Thesis, University of Groningen.

# Chapter 8
# Star Formation Rates

## 8.1. Galactic History

### 8.1.1. Lifetime Average

The total mass in stars divided by the age of a galaxy is an approximation to the lifetime average star formation rate of a galaxy. Substantial mass is returned to the interstellar medium over the course of evolution of stars with a wide range of initial masses. Consequently, a more accurate estimate of the lifetime average star formation rate must take account of stellar mass loss. By integrating masses of stellar remnants and comparing them to the masses of the original stars, Gallagher, Hunter, and Tutukov (1984) estimated that a fraction $\beta \approx 0.35$ of the mass in stars is returned to the ISM in each stellar generation. The value of $\beta$ depends somewhat on the slope and cutoff of the stellar initial mass function. Since the gas returned to the ISM will cycle through many stellar generations in the lifetime of a galaxy, the present observed mass in stars should be multiplied by

$$1 + \beta + \beta^2 + \cdots = (1 - \beta)^{-1} \approx 1.54 \qquad (8 - 1)$$

to estimate the total mass of all stars ever formed.

An upper estimate for the current total mass in stars is simply the dynamical mass, since the gas mass is (usually) rather small in comparison to the stellar mass. Dynamical masses are listed in Table 6–4 and Table 6–5 for two mass distribution models. Alternatively, the total gas mass (Table 7–5) may be subtracted from the dynamical mass to estimate the stellar mass. To arrive at a single estimate of the

average lifetime star formation rate, dynamical masses for the two mass models are averaged, and the stellar mass estimates are obtained by subtracting gas masses from average dynamical masses. Multiplication by 1.54 from equation (8–1) and division by $1.5 \times 10^{10}$ years (the adopted age of the galaxies) leads to the values in Table 8–1 for the average lifetime star formation rate per unit area in annuli 500 pc wide. These values are graphed in Figure 8–1. The "error" bars indicate the small range of values obtained by subtracting the gas mass or not subtracting it. It is not the inclusion or omission of gas mass but rather the uncertainty in the appropriate mass model that leads to systematic errors that may be substantial, especially at small radii, but that are typically a factor of two or less.

TABLE 8–1. AVERAGE LIFETIME SFR[a]

| NGC | Outer Radius (kpc) | | | | |
|---|---|---|---|---|---|
| | 0.5 | 1.0 | 1.5 | 2.0 | 2.5 |
| 4254 | 0.084 | 0.075 | 0.060 | 0.047 | 0.038 |
| 4303 | 0.159 | 0.072 | 0.045 | 0.033 | 0.027 |
| 4321 | 0.110 | 0.114 | 0.098 | 0.082 | 0.069 |
| 4501 | 0.146 | 0.161 | 0.169 | 0.164 | 0.151 |
| 4535 | 0.194 | 0.136 | 0.069 | 0.045 | 0.037 |
| 4536 | 0.448 | 0.382 | 0.207 | 0.103 | 0.060 |
| 4569 | 0.051 | 0.039 | 0.044 | 0.047 | 0.048 |
| 4654 | 0.051 | 0.053 | 0.050 | 0.045 | 0.040 |
| Area[b] | 0.79 | 2.36 | 3.93 | 5.50 | 7.07 |

[a]Units are $M_\odot\ yr^{-1}\ kpc^{-2}$.

[b]Area of annulus in $kpc^2$.

Most of the galaxies show average star formation rates per unit area that are

high at their centers and slowly decline with radius, although some have rates that are relatively constant with radius (NGC 4501, NGC 4569, and NGC 4654). The high rate of star formation at the center of NGC 4536 suggests that gas has been fed efficiently to its innermost regions, or that a very efficient star formation process operates between 500 pc and 1.5 kpc radius. Alternatively, perhaps there was initially a large amount of gas at the center of NGC 4536. NGC 4654, in contrast, has had a relatively low rate of star formation throughout its lifetime.

### 8.1.2. Average Over $5 \times 10^9$ years

The optical luminosity of a galaxy provides a measure of the average star formation rate over a range of time shorter than the age of the galaxy. The blue luminosity of a stellar population is dominated by stars produced during the last few $10^9$ years (Larson and Tinsley 1978). Let $L_B(m)$ be the $B$-band luminosity of a star of mass $m$. The proportion of stars in a stellar population with mass between $m$ and $m + dm$ is $\frac{1}{\chi}\xi(m)\,dm$, where $\frac{1}{\chi}\xi(m)$ is the initial mass function with normalization $\chi$. If $r(t)$ is the number rate of star formation at time $t$, then the total number of stars that are still alive with masses between $m$ and $m + dm$ is

$$\frac{1}{\chi}\int_0^{t(m)} r(t)\,\xi(m)\,dm\,dt, \qquad (8-2)$$

where $t(m)$ is the lifetime of a star of mass $m$. The total $B$-band luminosity of a stellar population is

$$L_B(\mathrm{tot}) = \frac{1}{\chi}\int_{m_{\mathrm{lo}}}^{m_{\mathrm{up}}}\int_0^{t(m)} r(t)\,\xi(m)\,L_B(m)\,dt\,dm. \qquad (8-3)$$

Assume that $r(t)$ is constant in time over the last few $10^9$ years, as was found to be approximately true by Gallagher, Hunter, and Tutukov (1984) for a number of spirals. Then the expression for the total $B$-band luminosity is simple:

$$L_B(\mathrm{tot}) = \frac{r}{\chi}\int_{m_{\mathrm{lo}}}^{m_{\mathrm{up}}} t(m)\,\xi(m)\,L_B(m)\,dm. \qquad (8-4)$$

The star formation rate in solar masses per year estimated from the observed $L_B(\mathrm{tot})$ is

$$R_{\mathrm{M}_\odot\,\mathrm{yr}^{-1}} = L_B(\mathrm{tot})\langle m\rangle \left[\frac{1}{\chi}\int_{m_{\mathrm{lo}}}^{m_{\mathrm{up}}} t(m)\,\xi(m)\,L_B(m)\,dm\right]^{-1}, \qquad (8-5)$$

where $\langle m\rangle$ is the average stellar mass for the initial mass function $\xi(m)$. Values of $\langle m\rangle$ are listed in Table E–3 and Table E–4 for the Salpeter IMF and the extended Miller-Scalo IMF (equation 3–16). The latter IMF is favored by Kennicutt (1983) in his study of global star formation rates in spirals. A formula for the main sequence stellar lifetime as a function of stellar mass is shown in equation (3–27). However, Gallagher, Hunter, and Tutukov (1984) list coupled formulae for the effective stellar lifetime $t(m)$ and the *lifetime average* $B$-luminosity $L_B(m)$ for stars of two compositions. For consistency, the latter will be used here. The equations are

$$\log L_B(m) = 0.6 + 2.92\log m - 0.37\log^2 m \qquad (8-6)$$

and

$$\log t(m) = 9.7 - 3.23\log m + 0.84\log^2 m \qquad (8-7)$$

for stars with composition $Y = 0.3$ and $Z = 0.001$, where $m$ is in solar masses, $t(m)$ is in years, and $L_B(m)$ is in solar $B$-band luminosities. The luminosity of the Sun in $B$-band is

$$\mathrm{L}_{B\odot} = 5.48 \times 10^{32}\,\mathrm{erg\,sec}^{-1}, \qquad (8-8)$$

which can be deduced from the absolute $B$ magnitude of the Sun, $M_{B_\odot} = +5.47$ (Allen 1973), and the conversion information in Table 3–7. For stars with composition $Y = 0.3$ and $Z = 0.03$, the formulae are

$$\log L_B(m) = 0.4 + 3.28\log m - 0.51\log^2 m \qquad (8-9)$$

and

$$\log t(m) = 9.8 - 3.43\log m + 0.91\log^2 m. \qquad (8-10)$$

There is not much difference (at most 50%) between the total $B$-band luminosities produced using the two sets of formulae. The equivalent lifetimes in equation (8–7) and equation (8–10) are not much different from the main sequence lifetime in equation (3–27). Table 8–2 lists the total lifetime $B$-band energy produced per star integrated over all stars up to an age $1.5 \times 10^{10}$ years using formula (8–4). Values for both compositions are shown for the Salpeter and extended Miller-Scalo initial mass functions. The lower mass cutoff used throughout is $0.1\,M_\odot$. There is very little dependence on the upper mass cutoff, being only a 2% change over the range $30\,M_\odot$ to $100\,M_\odot$.

TABLE 8–2. LIFETIME B-BAND ENERGY PER STAR[a]

| $Z$ | IMF | $\langle E_B \rangle$ |
|---|---|---|
| 0.03 | Miller-Scalo | 5.81 |
| | Salpeter | 2.04 |
| 0.001 | Miller-Scalo | 8.11 |
| | Salpeter | 3.09 |

[a]Units are $10^{50}$ erg star$^{-1}$.

Using $B$-band surface brightness data from Table 5–2, the $Z = 0.03$ entry for a Miller-Scalo IMF in Table 8–2, the average mass per star from Table E–4, and formula (8–5), the star formation rate can be estimated as a function of radius. As described by Gallagher, Hunter, and Tutukov (1984), stars with masses $1\,M_\odot$ to $2.5\,M_\odot$ make the greatest contribution to the $B$-band luminosity. Their lifetimes are $4 \times 10^8$ years to $6 \times 10^9$ years, so estimation of the star formation rate from $B$-band luminosity is relevant to this time span. A constant rate of star formation and a mass range of $0.1\,M_\odot$ to $60\,M_\odot$ are assumed. Values of the star formation rate deduced from $L_B$

are listed in Table 8–3. Surface brightnesses were converted to luminosities using the formula

$$L_B = (9.291 \times 10^{15})\, f_B\, (\mathrm{erg\,cm^{-2}\,sec^{-1}\,arcsec^{-2}})\, A_{\mathrm{pc}^2}\, \cos i\, \mathrm{L}_{B\odot}, \qquad (8-11)$$

where $i$ is the inclination of the galaxy, $A_{\mathrm{pc}^2}$ is the area of the region in square parsecs, and $\mathrm{L}_{B\odot} = 5.48 \times 10^{32}\,\mathrm{erg\,sec^{-1}}$. Judging from the range of values in Table 8–2, the uncertainty in the star formation rate estimates in Table 8–3 is about a factor of two due to composition changes and perhaps more due to uncertainty in the IMF.

TABLE 8–3. SFR FROM $L_B^a$

| NGC | Outer Radius (kpc) | | | | |
|---|---|---|---|---|---|
| | 0.5 | 1.0 | 1.5 | 2.0 | 2.5 |
| 4254 | 0.108 | 0.062 | 0.049 | 0.034 | 0.025 |
| 4303 | 0.322 | 0.069 | 0.049 | 0.045 | 0.037 |
| 4321 | 0.239 | 0.135 | 0.041 | 0.026 | 0.021 |
| 4501 | 0.108 | 0.049 | 0.030 | 0.023 | 0.021 |
| 4535 | 0.066 | 0.018 | 0.013 | 0.010 | 0.009 |
| 4536 | 0.095 | 0.036 | 0.019 | 0.013 | 0.010 |
| 4569 | 0.278 | 0.034 | 0.021 | 0.015 | 0.012 |
| Area[b] | 0.79 | 2.36 | 3.93 | 5.50 | 7.07 |

[a] Units are $\mathrm{M_\odot\,yr^{-1}\,kpc^{-2}}$.

[b] Area of annulus in $\mathrm{kpc^2}$.

The analysis of $B$-band luminosities in 500 pc-wide annuli presupposes the circularity of stellar orbits. This assumption is supported on morphological grounds based on the circular symmetry of features in $B-V$ images, such as in the central regions of NGC 4303 and NGC 4321. If stellar orbits were not circular, then such features could not persist for long. The analysis of dynamical masses also relies on the assumption of circular orbits.

Much more varied behavior is evident from the star formation rates deduced from $B$-band luminosity than from dynamical masses. Figure 8–2 displays the radial behavior of $B$-band star formation rates, pertaining to $4 \times 10^8$ to $6 \times 10^9$ years ago, for each galaxy. The enhanced star formation in a ring between 500 pc and 1 kpc radius in NGC 4321 is prominent and corresponds to the four-armed dynamical feature near its center. NGC 4535 shows a relatively small star formation rate, which supports the hypothesis that its inner spiral arms are primarily old arms. NGC 4536 also displays rather low star formation rates in its central region, in contrast to the high lifetime average rates computed in the last section. This implies that NGC 4536 has either had much more star formation in its distant past, or else that it is currently forming very many stars. The very bright nucleus of NGC 4569 is prominent for its high rate of star formation relative to the rest of the inner disk; NGC 4303 shows similar behavior.

Comparison of the recent rates with lifetime averages highlights some interesting behavior. Almost all of the galaxies show a smaller recent star formation rate (as estimated from the $B$-band luminosity) compared with their lifetime average rate at the same radius. This generally holds for all radii except the innermost kiloparsec, where the recent star formation rates are generally higher than the lifetime average. Taken at face value, the implication is that most spirals suffered a decline in the star formation rate in their inner regions about $5 \times 10^9$ years ago. Errors of the order of a factor of two in the star formation rates estimated from $L_B$ make the hypothesis of a general declining star formation rate for most galaxies more uncertain. The strongest statement that can be made is that the star formation rate did not increase substantially in the inner regions of most spirals, except in their nuclei, between $15 \times 10^9$ and $5 \times 10^9$ years ago. Uncertainty in the slope at intermediate masses and lower mass cutoff of the initial mass function prevent making a stronger statement.

A hypothesis that is consistent with the observed behavior of the star formation rates in time is that most spirals underwent star formation in their first $10^{10}$ years that was on average more vigorous than that in their last $5 \times 10^9$ years. Early gas infall and processes associated with shifting dynamical equilibrium in young galaxies could have contributed to vigorous early star formation rates.

There are several galaxies that do not show a decreasing star formation rate between $15 \times 10^9$ and about $5 \times 10^9$ years ago somewhere within their disks. For instance, the star formation rate seems to have declined everywhere in the inner 5 kpc of NGC 4569 except in the very center (inside 500 pc radius), where the more active recent star formation rate is evident in the very blue color of the nucleus. Also noteworthy is the entire inner 5 kpc of NGC 4303, which shows a steady rate of star formation from $4 \times 10^8$ to $15 \times 10^9$ years ago. It is possible that the formation of the stellar bar in NGC 4303 could have happened around $5 \times 10^9$ years ago and that the bar has since maintained the star formation rate due to its dynamical effects. Alternatively, a large rate of star formation (for whatever reason) may have continued until $5 \times 10^9$ years ago or less and increased the central mass so much that it became susceptible to a bar mode instability, which led to formation of the small stellar bar seen today. Star formation has increased its pace over the last few $10^9$ years in the inner kiloparsec of NGC 4321, probably because of dynamical effects related to the four-armed feature at its center.

### 8.1.3. Current Star Formation Rate

Formulae for deriving the current star formation rate based on H$\alpha$ emission have been presented in §3.2.5. Using equation (3–29) and the total H$\alpha$ radiancies in Table 3–8, the total current star formation rates for the program spirals may be estimated. These values are presented in Table 8–4, which assumes an extended Miller-Scalo IMF (equation 3–16) and mass limits of $0.1\,M_\odot$ and $60\,M_\odot$. Uncertainties in

the H$\alpha$ radiancy and the form of the initial mass function probably overwhelm the uncertainty introduced by the unknown loss of ionizing photons to absorption by dust or through escape from the galaxy. Estimates of the current star formation rate for NGC 4303 ($\approx 14\,M_\odot\,yr^{-1}$) and NGC 4536 ($7.8\,M_\odot yr^{-1}$) presented by Kennicutt (1983) are in basic agreement with the values in Table 8–4. In general, the earlier-type galaxies have lower global star formation rates than the later-type galaxies.

TABLE 8–4.

TOTAL CURRENT STAR FORMATION RATE

| NGC | $R\,(M_\odot\,yr^{-1})$ | NGC | $R\,(M_\odot\,yr^{-1})$ |
|---|---|---|---|
| 4254 | 34 | 4535 | 11 |
| 4303 | 31 | 4536 | 9.2 |
| 4321 | 18 | 4569 | 3.2 |
| 4501 | 8.1 | | |

Using formula (3–29), the current rate of star formation can be estimated from the surface brightness $\mu\,(erg\,sec^{-1}\,cm^{-2}\,arcsec^{-2})$ as

$$R = (2.251 \times 10^8)\,\mu\,(erg\,sec^{-1}\,cm^{-2}\,arcsec^{-2})\,A_{pc^2}\,\cos\,i\;M_\odot\,yr^{-1}, \qquad (8-12)$$

which assumes an extended Miller-Scalo IMF and a distance $D_{Mpc} = 15.7$. $A_{pc^2}$ is the area of the region in square parsecs and $i$ is the inclination of the galaxy. As for formula (3–29), values of the IMF normalization factor, the average stellar mass along the IMF, and the Lyman continuum photon emission rate were taken from Table E–2, Table E–4, and Table 3–12, respectively. Surface brightnesses as a function of radius are listed in Table 5–2; with equation (8–12), they yield the current star formation rate estimates in annuli 500 pc wide are listed in Table 8–5. Data are lacking for two radii in NGC 4501 due to uncertainties in subtracting the continuum emission.

TABLE 8–5.

CURRENT STAR FORMATION RATES[a]

| NGC | Outer Radius (kpc) | | | | |
|---|---|---|---|---|---|
| | 0.5 | 1.0 | 1.5 | 2.0 | 2.5 |
| 4254 | 0.59 | 0.39 | 0.37 | 0.35 | 0.22 |
| 4303 | 1.59 | 0.055 | 0.059 | 0.10 | 0.10 |
| 4321 | 1.04 | 0.65 | 0.087 | 0.045 | 0.035 |
| 4501 | 0.54 | ··· | ··· | 0.003 | 0.027 |
| 4535 | 0.94 | 0.032 | 0.017 | 0.014 | 0.021 |
| 4536 | 1.35 | 0.51 | 0.17 | 0.064 | 0.031 |
| 4569 | 0.27 | 0.098 | 0.046 | 0.040 | 0.028 |
| Area[b] | 0.79 | 2.36 | 3.93 | 5.50 | 7.07 |

[a] Units are $M_\odot\,yr^{-1}\,kpc^{-2}$.

[b] Area of annulus in $kpc^2$.

Graphs of the values in Table 8–5 are presented in Figure 8–3. Comparison with Figure 8–2 shows that there some similarities in the radial behavior between the current star formation rate and the average over the last $\approx 5 \times 10^9$ years (from $L_B$). The ring of currently active star formation in NGC 4321 between 500 pc and 1 kpc radius has apparently been in such a state for the last $\approx 5 \times 10^9$ years. The current rate of star formation at the centers of both NGC 4303 and NGC 4569 are high relative to their surrounding disks, as it has been for the last $\approx 5 \times 10^9$ years.

Some differences between current and recent star formation rate radial behavior are noteworthy. The inner 1–2 kpc of both NGC 4535 and NGC 4536 are currently forming stars at rates very much above their average rates at larger radii. This observation corresponds to the bright, nuclear H$\alpha$ emission from these two galaxies.

In contrast, the recent average star formation rates (from $L_B$) showed much less marked radial dependence. The star formation rate throughout the central 5 kpc of NGC 4254 is significantly greater now than the average over its recent past.

The most striking difference between recent ($4 \times 10^8$ to $6 \times 10^9$ years ago) and current star formation rates is one of scale. The central regions of most of the program spirals are currently undergoing a star formation renaissance. In the range 2 kpc to 2.5 kpc radius, current star formation rates for most spirals are around $0.03\,M_\odot\,yr^{-1}\,kpc^{-2}$, which is very similar to the average rate over the last $\approx 5 \times 10^9$ years for the same radii, $0.01$–$0.03\,M_\odot\,yr^{-1}\,kpc^{-2}$. Much larger current star formation rates pertain within 2 kpc radius for most spirals. The ring of star formation in NGC 4321 has a current star formation rate of $0.7\,M_\odot\,yr^{-1}\,kpc^{-2}$, which is nearly five times the average rate (from $L_B$) over the last $5 \times 10^9$ years. The median star formation rate within 500 pc radius similarly increased by a factor of five from the average value over the last $\approx 5 \times 10^9$ years, $0.23\,M_\odot\,yr^{-1}\,kpc^{-2}$, to the current median value of around $1.0\,M_\odot\,yr^{-1}\,kpc^{-2}$.

It is possible, though perverse, that the errors in estimating the current star formation rate (a factor of two) and the recent average star formation rate (another factor of two) could have conspired to operate systematically in opposite directions to produce the factor of five median increase in star formation rates. Several arguments suggest that no conspiracy is taking place but, instead, that the central regions of many of the program spirals are undergoing more vigorous star formation now than they have in the last few billion years. The persistent factor of five difference is suggestive of an error in scale, but it is important to note that galaxies do not maintain their relative ranking in central star formation rate for the two timescales. Some, like NGC 4535 and NGC 4536, have much greater relative current star formation rates compared to their recent past rates, while another, NGC 4569, has a greatly

diminished relative current rate. Furthermore, the star formation rates at larger radii are not affected by the factor of five difference, and there the recent and current rates are very similar. Mere scaling has not biased the current star formation rate estimates to appear much larger than the $5 \times 10^9$-year average rates; instead, a real increase in many of the central rates has apparently transpired and real changes in the radial behavior of the star formation rate have occurred.

One explanation for the large current star formation rates is that the galaxies in this sample were chosen primarily on the basis of their CO luminosities, which are high and therefore indicate large amounts of molecular gas. The large current star formation rates can be understood as arising from the large amounts of molecular gas in these galaxies. This explanation begs the question, though, of why there is currently so much gas and concomitant star formation but not as much in the last few $10^9$ years.

It is certainly possible that the stellar initial mass function has changed over the last $5 \times 10^9$ years, and not (necessarily) the star formation rate. Extrapolation of the high-mass star formation rate, which is based on H$\alpha$ emission, to the rate of formation of stars of all masses, most of which do not contribute significantly to the Lyman continuum flux, is a very uncertain process. For instance, if the current IMF has a rather high lower mass cutoff (substantially greater than $0.1\,M_\odot$), then the total mass of stars implied by equation (3–24) would be much less. To account for the factor of five, and thereby to bring the current star formation rate estimate for the centers of the spirals into approximate equality with the average rates over the last $5 \times 10^9$ years, requires a lower mass cutoff $m_{\rm lo}$ satisfying

$$\chi(m_{\rm lo},\, 60\,M_\odot)\,\langle m\rangle\Big|_{m_{\rm lo}}^{60\,M_\odot} = \frac{1}{5}\,\chi\,(0.1\,M_\odot, 60\,M_\odot)\,\langle m\rangle\Big|_{0.1\,M_\odot}^{60\,M_\odot} \qquad (8-13)$$

(see equation 3–23). The solution to equation (8–13) may be calculated easily from the IMF (equation 3–16); it is $m_{\rm lo} = 1.85\,M_\odot$. The suppression of the formation

of lower mass stars has been suggested in the case of galaxies with active nuclei or nuclei with extremely large amounts of gas (cf. Rieke *et al.* 1980, for a discussion of M82 and NGC 253). Observations at infrared and ultraviolet wavelengths would be needed to place more constraints on the form of the initial mass function.

## 8.2. Other Star Formation Indicators

### 8.2.1. B – V Color

The $B-V$ color of a stellar population is an indication of the integrated effects of the star formation history that produced the population. In general, stellar populations redden as they age, although the uncertain contribution of stars that have evolved off the main sequence complicates the relationship between color and age. A fuller description of the star formation history of a stellar population includes both the age of the population and the rate of change of the pace of star formation. Exploration of this two-dimensional descriptive space requires two colors. Stellar population evolution models have been calculated extensively by Larson and Tinsley (1978) for $U-B$ and $B-V$ colors. In principle, any two colors will serve to describe the linear star formation history of a stellar population.

Larson and Tinsely (1978) found that the colors of normal galaxies fall along a single curve in the $(U-B, B-V)$ plane. The position of the galaxy along the curve is almost uniquely determined by the ratio between the average star formation rate over the last $10^8$ years to the average lifetime star formation rate. Therefore, the information from colors is very similar to that from $L_B$ and the dynamical mass. For instance, a recent burst of star formation in a quiescent, red disk leads to different colors than does a burst early in the life of a galaxy that then settles to a quiescent state. Deviations from the standard curve correspond to bursts of star formation that produce greater numbers of stars for larger deviations.

Although $U$-band photometry was not obtained, small-aperture photometry is

available in Longo and de Vaucouleurs (1983), from which the $U-B$ color at various radii may be estimated. Inclination of the galaxy leads to contamination of the light at small radii with that from larger radii. $B-V$ data are listed in Table 5–2. Comparison of the observed colors with the grid of models calculated by Larson and Tinsley (1978) can provide an estimate of the relative star formation rate over the last $10^8$ years. Approximate $U-B$ and $B-V$ colors are listed in Table 8–6. For reference, the empirical normal line colors from Larson and Tinsley (1978) are listed in Table 8–7.

TABLE 8–6.

APPROXIMATE $U-B$ AND $B-V$ COLORS

| NGC | $B-V$ | $U-B$[a] | NGC | $B-V$ | $U-B$ |
|---|---|---|---|---|---|
| 4254 | +0.7, +0.8 | +0.2, +0.3 | 4535 | +0.9, +1.0 | 0.0, +0.25 |
| 4303 | +0.8, +0.9 | +0.2, +0.3 | 4536 | +0.9, +1.1 | +0.3, +0.4 |
| 4321 | +0.6, +0.9 | −0.1, +0.05 | 4569 | +0.5, +1.0 | +0.1, +0.2 |
| 4501 | +1.0, +1.1 | +0.6, +0.7 | | | |

[a] Approximate range of $U-B$.

TABLE 8–7.

LARSON-TINSLEY NORMAL LINE

| $B-V$ | $U-B$ | $B-V$ | $U-B$ |
|---|---|---|---|
| 0.45 | −0.16 | 0.80 | +0.32 |
| 0.50 | −0.09 | 0.90 | +0.50 |
| 0.60 | +0.01 | 0.95 | +0.59 |
| 0.70 | +0.14 | 1.0 | +0.69 |

Galaxy colors that fall on the normal line are indicative of a monotonically declining star formation rate. Some of the program spirals have colors that place them very near or on the normal line. NGC 4501 is notably very red, its color indicating a stellar population at least $5 \times 10^9$ years old, but it is located right on the normal line. A decreasing star formation rate models this galaxy's inner disk history very well. The colors at larger radii, 2–2.5 kpc, are near the normal line and also indicate a declining star formation rate for NGC 4303, NGC 4535, and NGC 4569. NGC 4254 is on the normal line but shows evidence for a weak, recent burst of star formation about 1–2 $\times$ $10^8$ years ago at larger radii. This is consistent with the interpretations of the star formation rates derived in the preceding sections.

There are noteworthy exceptions to the monotonicity of the star formation rates among the program spirals. First, there is some evidence for recent increases in the star formation rate in some galaxies. NGC 4321 has colors between 500 pc and 1 kpc radius that indicate a strong, very young burst of star formation within the last $10^8$ years. This burst is associated with the blue ring of star formation in this galaxy. NGC 4303 also shows the colors of a very young, $\approx 10^8$-year-old burst of star formation at its center. The colors of NGC 4535 indicate a weak nuclear burst of star formation. All this history is corroborated by the star formation rates pictured in Figure 8–1 through Figure 8–3. A much older burst of star formation, now aged 3–5 $\times$ $10^8$ years, is indicated by the nuclear colors of NGC 4569, which is supported by comparison of current and recent past star formation rate data in Figure 8–2 and Figure 8–3.

In addition to the star formation bursts, there is further indication of nonmonotonicity in star formation rates. Several galaxies have colors that place them off the normal line over most of their inner disks: NGC 4321, NGC 4535, NGC 4536, and NGC 4569. These galaxies have colors that place them *above* the normal line. Dis-

placements below the normal line are interpretable as aging bursts of star formation, but displacements above the normal line signify very recent star formation or non-decreasing (even increasing) star formation rates. This observation substantiates the relatively large current star formation rates that were estimated for some galaxies.

### 8.2.2. Mass-to-Light Ratios

Coupled with the color analysis of the previous section is the mass-to-light ratio of a stellar population. Like the $B-V$ color, $M/L_B$ indicates the ratio of the recent star formation rate to the lifetime average rate. As a population ages and reddens, the light becomes dominated by low mass stars and so the mass-to-light ratio increases. Mass-to-light ratios from Larson and Tinsley (1978) for model stellar populations on the normal line are listed in Table 8–8. The values have been multiplied by a factor of two, bringing them into empirical agreement with observations as described by Larson and Tinsley (1978), and have been converted to units of $M_\odot/L_{B\odot}$, where $L_{B\odot} = 5.48 \times 10^{32}\,\mathrm{erg\,sec^{-1}}$. For comparison, mass-to-light ratios have been computed using two mass models, a spherically symmetrical one and a thin disk. Masses within annuli are listed in Table 6–4 and Table 6–5, while $B$-band luminosities were computed from values in Table 5–2. The mass-to-light ratios are listed in Table 8–9 and Table 8–10.

TABLE 8–8.

MASS-TO-LIGHT RATIOS

| $B-V$ | $M/L_B$ | $B-V$ | $M/L_B$ |
|---|---|---|---|
| 0.45 | 0.15 | 0.80 | 1.00 |
| 0.50 | 0.25 | 0.90 | 1.35 |
| 0.60 | 0.49 | 0.95 | 1.52 |
| 0.70 | 0.74 | 1.0 | 3.27 |

Many of the general characteristics of the star formation rate histories that were evident in $B-V$ color are also evident in $M/L_B$. As expected, the mass-to-light ratios for most of the galaxies are consistent with their $B-V$ colors, which supports the assumption of monotonic nonincreasing star formation rates made by Larson and Tinsley (1978) when computing their models. The very red $B-V$ color of NGC 4501 is accompanied by correspondingly large values of $M/L_B$, which are indicative of an old stellar population with little recent star formation. NGC 4569 also has large values of $M/L_B$ which correspond to the colors of its red disk, and has a very small $M/L_B$ inside the central kiloparsec where the $B-V$ color is very blue and where there has been much relatively recent star formation. Both NGC 4254 and NGC 4303 have $M/L_B$ values near the normal line in the range expected based on their $B-V$ colors, although NGC 4254 has slightly larger $M/L_B$ values.

TABLE 8–9. $M/L_B^a$ — SPHERICAL SYMMETRY

| NGC | Outer Radius (kpc) | | | | |
|---|---|---|---|---|---|
| | 0.5 | 1.0 | 1.5 | 2.0 | 2.5 |
| 4254 | 0.81 | 1.66 | 1.77 | 1.95 | 2.14 |
| 4303 | 0.64 | 1.55 | 1.45 | 1.21 | 1.17 |
| 4321 | 0.45 | 1.15 | 3.45 | 4.64 | 4.99 |
| 4501 | 0.73 | 3.09 | 6.69 | 9.51 | 10.1 |
| 4535 | 3.63 | 10.8 | 6.76 | 5.28 | 4.89 |
| 4536 | 10.8 | 33.2 | 33.8 | 22.0 | 15.0 |
| 4569 | 0.088 | 1.10 | 2.42 | 4.08 | 5.36 |

[a] Units are $M_\odot/L_{B\odot}$, where $L_{B\odot} = 5.48 \times 10^{32}$ erg sec$^{-1}$.

In fact, several galaxies have values of $M/L_B$ that are larger than expected from

TABLE 8–10. $M/L_B^a$ — THIN DISK

| NGC | Outer Radius (kpc) | | | | |
|---|---|---|---|---|---|
| | 0.5 | 1.0 | 1.5 | 2.0 | 2.5 |
| 4254 | 1.60 | 1.99 | 1.89 | 2.06 | 2.34 |
| 4303 | 0.81 | 1.68 | 1.52 | 1.25 | 1.18 |
| 4321 | 1.04 | 1.44 | 3.63 | 4.54 | 4.67 |
| 4501 | 3.12 | 6.10 | 9.11 | 10.6 | 10.3 |
| 4535 | 4.90 | 10.1 | 8.00 | 7.52 | 6.94 |
| 4536 | 15.8 | 26.3 | 26.1 | 21.3 | 18.4 |
| 4569 | 0.38 | 2.74 | 4.23 | 5.62 | 6.20 |

their $B - V$ colors. Mass-to-light ratios are rather too large in NGC 4321, and it is surprising that the ring of enhanced star formation is not apparent in the $M/L_B$ values. (The ring of diminished star formation in NGC 4303 is, in fact, evident from a larger $M/L_B$ between 500 pc and 1 kpc radius.) The values of $M/L_B$ for NGC 4535 are much too large for its colors, and those of NGC 4536 are extraordinarily high. The large $M/L_B$ for NGC 4535 and NGC 4536 could be due, at least in part, to the very rapid increase in $M/L_B$ along the normal line when $B - V \gtrsim 1.0$. However, that explanation cannot apply to NGC 4321, whose colors are not near $B - V = 1.0$. Instead, it is likely that the assumption of the monotonicity of the star formation rate is not correct for these galaxies. The same suggestion has already been made in previous sections: these galaxies have much larger current star formation rates in their inner disk than the rates in their recent past. It is probable that the large current star formation activity is occurring atop the very old, red disks of these galaxies, and that they are entering a star formation renaissance after a long hiatus. The appearance of the inner disk of NGC 4535 and perhaps of NGC 4536 suggests that the inner spiral

arms are mainly stellar, "old" arms with little gas.

## 8.3. Comparative Star Formation History

The details of the star formation histories of the program spirals discussed in preceding sections can be neatly summarized in ratio-ratio graphs. This very illustrative method of summarizing star formation histories is due to Gallagher, Hunter, and Tutukov (1984). Figure 8–4 graphs the star formation rate information in Table 8–1, Table 8–3, and Table 8–5 as relationships between the logarithms of the ratios of star formation rates over various timescales. The abscissa is the logarithm of the ratio between the star formation rate deduced from the $B$-band luminosity and the rate deduced from H$\alpha$ emission, so it compares the star formation rate from $4 \times 10^8$ to $6 \times 10^9$ years ago to the current rate. The ordinate compares the lifetime average rate to the average over times $4 \times 10^8$ to $6 \times 10^9$ years ago. The circle encloses an error region which corresponds to errors of factors of two in all rates. Regions which have had a constant or declining star formation rate will be located in the first quadrant. Gallagher, Hunter, and Tutukov (1984) noted that most of the spirals in their study clustered around the $y$-axis, which is consistent with a large global star formation rate in the distant past but smaller, comparable global rates during times within the last $5 \times 10^9$ years.

Some of the central regions of the program spirals are consistent with constant or declining star formation rates. Points within the dotted circle are consistent with an unchanging rate of star formation over the lifetime of the galaxy. Most of the inner 5 kpc of NGC 4303 (all except the inner kiloparsec) has had a roughly constant star formation rate over its lifetime. The same is true for the inner disk of NGC 4321 from 1 kpc to 2.5 kpc radius. Much of the disk of NGC 4569 is consistent with a roughly constant star formation rate, and the disk of NGC 4501 from 2–2.5 kpc has had a monotonically declining rate of star formation.

Most of the points lie outside the dotted circle and are located in the second quadrant, which is where stellar populations undergoing a current burst of star formation are located. The star formation rate within 1.5 kpc radius in NGC 4536 is currently much higher than it has been in the past $5 \times 10^9$ years. NGC 4254 has had a relatively constant rate of star formation until the present, when its star formation rate has increased substantially. The central kiloparsec or so of NGC 4303, NGC 4321, and NGC 4535 are all more actively forming stars now than they have been over the past $5 \times 10^9$ years.

Another way of graphing the star formation history information is to compare both recent and current star formation rates with the lifetime average star formation rate. These data are graphed in Figure 8–5. The dotted circle indicates the range over which errors of a factor of two in each star formation rate estimate could shift the position of a point. Points within the dotted circle are consistent with constant star formation rates over a galactic lifetime. The graph is divided into four sectors that indicate the approximate star formation history. The sector labeled "Increasing" refers to a monotonically increasing star formation rate up to the present. "Post-burst" populations are ones for which the current star formation rate is less than the average rate over the time range $4 \times 10^8$ to $6 \times 10^9$ years ago, which is deduced from the $B$-band luminosity. Points in the "Burst" sector are ones for which the current star formation rate is greater than the rate in the recent past (deduced from $L_B$). Finally, the sector labeled "Decreasing SFR" refers to populations that show a monotonically decreasing star formation rate. NGC 4536 is noteworthy for the burst of star formation in its inner disk. The central regions of NGC 4303, NGC 4321, and NGC 4535, as noted above, show increasing or bursting star formation rates inside 1.5 kpc radius. The very center of NGC 4569 has had an increasing star formation rate over its lifetime, although it may be entering a post-burst state and slowing

its current star formation rate. The very compact cluster of points for NGC 4254 indicates that its entire inner disk has formed stars at coordinated rates, rather than having star formation concentrated over small radial ranges, as is common in the other program spirals. The points for NGC 4536 are also compact, though not to the degree shown by NGC 4254.

Star formation histories seem to be consistent with the presence of dynamical influences, many of which are apparent in the optical or CO morphology. In the case of NGC 4254, the dynamical influence that may drive star formation is the tightly wound, ubiquitous spiral arm pattern in the inner disk. The prominent spiral pattern persists all the way to the center of the galaxy and, by favoring no radius, may advance star formation evenly across the inner disk. The bar in NGC 4303, if it is about as old as the galaxy, may have provided a constant dynamical trap for gas and so fueled a constant star formation rate in the inner disk. If the errors in the star formation rate estimate are taken into account, the bar may have formed later in the life of the galaxy, perhaps over the last $5 \times 10^9$ years, and so caused increasing recent star formation rates by bringing more gas to the center. The four-armed structure that occupies the central 2 kpc of NGC 4321 has had a great influence on the star formation rate in its region, causing it to increase over the last $5 \times 10^9$ years. It probably came into existence about $5 \times 10^9$ years ago or shortly thereafter. The large amount of star formation at the very center of NGC 4569 must have been fueled by large amounts of gas, but no obvious dynamical factor within the galaxy is apparent. However, the negative heliocentric velocity of NGC 4569 and its line of sight proximity to the Virgo Cluster center suggest that NGC 4569 has fallen into the cluster very recently and is now in the vicinity of the core. Environmental effects and dynamical perturbations sustained in the course of making such a passage could have caused clouds in the interstellar medium of NGC 4569 to lose angular momentum

and spiral into its center, fueling the recent burst of star formation there. The near-constant but low star formation rate of the inner 5 kpc of NGC 4535 (except the 1 kpc region around the nucleus) is consistent with the smooth appearance of its inner spiral arms, which are probably old, stellar arms. The inner disk has relatively little gas, except for the nucleus. Gas may have been systematically passed from the inner disk into the nucleus as clouds traversed the spiral arms, lost angular momentum, and spiraled into the center. A very thin dust lane marks the inner edges of the spiral arms, indicating that a rather strong shock accompanies the spiral arms. Gas passing through the shock would lose angular momentum on each passage and eventually end up at the center. The current burst of star formation in NGC 4536 is tantalizingly not readily explainable as the result of dynamical factors. Although the four-armed galaxy morphology of the galaxy is very rare, if not unique, it is highly unlikely that the four arms sprang into existence to coincide with the beginnings of the current burst of star formation. If NGC 4536 is barred, which is a possible but uncertain interpretation of the morphology of this very inclined galaxy, then perhaps the dynamical action of the bar helped to accumulate the gas that precipitated the current nuclear burst of star formation.

## 8.4. Gas and Star Formation

### 8.4.1. Gas Consumption Times

Current star formation rates for the program spirals are listed in Table 8–5. Assuming that the current rate is maintained, how long will the existing gas reservoir last? Total gas masses, which include $H_2$, H I, and He, are listed in Table 7–5. It is certainly possible that the gas will migrate in time and probably sink to smaller radii. However, naively forming the ratio between the available gas mass and the current star formation rate at each radius will provide a rough but instructive estimate of the time to consume the locally available gas in star formation. Gas consumption times

TABLE 8–11. GAS CONSUMPTION TIMES[a]

| NGC | Outer Radius (kpc) | | | | |
|---|---|---|---|---|---|
| | 0.5 | 1.0 | 1.5 | 2.0 | 2.5 |
| 4254 | 3.9 | 4.3 | 2.9 | 1.9 | 2.3 |
| 4303 | 1.6 | 38 | 30 | 13 | 11 |
| 4321 | 3.9 | 4.7 | 21 | 24 | 22 |
| 4501 | 2.4 | ··· | ··· | 280 | 27 |
| 4535 | 3.5 | 13 | 15 | 16 | 10 |
| 4536 | 3.3 | 4.0 | 7.3 | 13 | 18 |
| 4569 | 9.0 | 20 | 31 | 27 | 30 |

[a] Units are $10^8$ years.

are listed in Table 8–11.

The gas consumption timescales for the inner kiloparsec of the program spirals are on the order of a few $10^8$ years. Current star formation rates in many of the nuclei are very high, so the times to deplete the gas are short despite the large amounts of gas in many of the spiral nuclei. If, as discussed in Chapter 7, the gas masses are overestimated in the central regions of spirals, then the gas consumption times should be shortened proportionally. In view of the errors inherent in both estimating the gas mass and in estimating the current star formation rate, the values in Table 8–11 should be considered conservatively to indicate order of magnitude gas consumption times. The timescales increase significantly at larger radii, reaching a few $10^9$ years at 2.5 kpc radius, which is an order of magnitude longer than the timescales for the centermost regions. NGC 4254 is unique among the program spirals in that its gas consumption time does not change much with radius within the central 5 kpc. Characteristic gas depletion times for NGC 4254 are also rather short compared with

those of other spirals at radii beyond 1 kpc. Star formation is apparently proceeding directly in proportion to the gas mass in NGC 4254 so that gas consumption times are roughly constant at all radii. There are no regions with enhanced or depressed star formation rates, as occur in other spirals because of the dynamical influences of localized features. Instead, the ubiquitous spiral pattern in the inner disk of NGC 4254 probably drives star formation with equal efficiency at all radii inside 2.5 kpc.

### 8.4.2. Star Formation Laws

A basic relationship between gas density and the rate of star formation is of the form

$$R \propto \rho^n, \qquad (8-14)$$

where $R$ is the rate of star formation, $\rho$ is the gas density, and $n$ is a small exponent (Schmidt 1959). Recent work by Kennicutt (1989) has expanded on the basic equation (8–14). Through examining many spirals of various morphological types, Kennicutt (1989) proposed that the relationship between gas density and the star formation rate has two regimes: in one regime, a law like equation (8–14) pertains; in the other regime, the behavior is highly nonlinear, with small changes in gas density resulting in large changes in the star formation rate. It was empirically discovered by Kennicutt (1989) that the regime that controls the star formation law is related to the value of the Toomre $Q$-parameter (equation 7–12). Regions with a small value of $Q$ for the gas disk are actively forming stars and obey a law of form

$$R = \alpha \Sigma_{\rm gas}^N, \qquad (8-15)$$

where $\Sigma_{\rm gas}$ is the mass surface density of the gas, $\alpha$ is a scaling constant, and $N$ is a small exponent. When $Q$ increases beyond what appears to be a universal threshold, the star formation rate drops precipitously in a higher nonlinear way. Kennicutt (1989) empirically found that $N = 1.3 \pm 0.3$ for regions in star-forming spirals that

are in the physical regime described by equation (8–15). Under Kennicutt's (1989) model, it is possible that the central regions of spirals are in the nonlinear domain in which small changes in gas density precipitate large changes in the star formation rate. This is because the threshold gas density that separates the Schmidt-law regime (equation 8–15) from the highly nonlinear regime increases steeply toward the centers of spirals, where the epicyclic frequency $\kappa$, which enters into the computation of $Q$, becomes large. Therefore, large amounts of gas may build up at the center of spirals before the density threshold is reached, at which point the star formation will increase dramatically with only a minor increase in the gas density. Much more gas would have to accumulate to push the central disk into the other physical regime where equation (8–15) pertains.

The dependence of Kennicutt's (1989) star formation law model on the Toomre $Q$-parameter provides a quantitative description of a link between star formation and spiral structure which, if not obvious, has been at least suspected for a long time. Kennicutt's (1989) elaboration of the basic star formation law, equation (8–15), is intended to apply to kiloparsec-sized scales. On such scales in galactic disks, the dependence of the form of the star formation law (Schmidt-like or highly nonlinear) on the value of $Q$ suggests that when strong spiral structure is present, the physical processes of star formation lead to a dependence on gas density like equation (8–15). When strong spiral structure is absent, the physical processes leading to equation (8–15) disappear. The physical process in question could very well be compression of gas in a density wave, or effects linked to the passage of a wave. When wave action is absent, other processes such as stochastic or self-propagating star formation may dominate and their relationship with the average local gas density may be highly nonlinear as star formation "turns on and off" with density variations or other influences such as supernovae. The fact that swing amplification of spiral waves is most

efficient when $Q < 1.5$ is very good for Kennicutt's theory, for then spiral structure is expected to be absent when $Q \gtrsim 2$. Kennicutt's theory requires large values of $Q$ in the outer parts of disks beyond the limiting radius where H II regions are found; $Q$ may also have large values at the centers of spirals. The modal theory of spiral structure requires a large $Q$ at the centers of spirals; $Q = 2.5$ is commonly used in numerical calculation of modes (Bertin *et al.* 1989). The requirement of modal theory that $Q = 1$ identically in the disk outside the nucleus is not germane to Kennicutt's (1989) star formation model, though, since then there is no explanation for the star formation cutoff in the outer parts of spirals.

The forms of the star formation law in the centers of the program spirals may be determined using current star formation rates from Table 8–5 and gas masses from Table 7–5 and Table 5–6. The star formation laws using total molecular hydrogen masses are virtually identical to the total gas mass star formation laws, since the $H_2$ mass is dominant in inner disks (see Table 7–4). Figure 8–6 shows the relationship between the gas mass surface density determined from interferometer data and the star formation rate. Figure 8–7 shows the relationship between the total gas mass surface density ($H_2 + H\,I + He$) and the star formation rate. Table 8–13 lists the slopes and intercepts of power-law fits (following equation 8–15) to the star formation laws in Figure 8–7, while Table 8–12 lists the same information for the star formation laws in Figure 8–6. The range in Table 8–12 and Table 8–13 refers to the radii that were included in the fitting. Two of the galaxies, namely NGC 4303 and NGC 4535, show steeply increasing star formation rates in their central kiloparsec regions, so a single power law does not adequately describe the data. The units of $\alpha$ are erg $\mathrm{sec}^{-1}\,\mathrm{pc}^{-2}$.

The exponents in Table 8–13 are, for the most part, near $N = 2$. An exponent of $N = 2$ is expected if cloud-cloud collisions are the main factor that precipitates high-mass star formation (see §8.5). Of the five slopes near $N = 2$, the measured mean

TABLE 8–12

CURRENT STAR FORMATION LAWS

OVRO FLUXES AND Hα

| NGC | $\alpha$ | N | Range (kpc) |
|---|---|---|---|
| 4254 | 33.75 | 0.174 | 0–1 |
| 4303 | 28.55 | 2.64 | 0–1.5 |
| 4303 | 32.81 | 0.518 | 0–2.5 |
| 4321 | 31.49 | 1.27 | 0–2.5 |
| 4501 | 28.97 | 2.69 | 0–2.5 |
| 4535 | 30.54 | 1.59 | 0–1 |
| 4535 | 32.41 | 0.309 | 0.5–2.5 |
| 4536 | 32.08 | 0.955 | 0–2.5 |
| 4569 | 32.37 | 0.648 | 0–2 |

value is $N = 2.0 \pm 0.4$. The exceptions to $N = 2$ are NGC 4254, which has a much shallower exponent, $N \approx 0.5$, and NGC 4501 and the central region of NGC 4303, which have very steep exponents, $N \gtrsim 8$. The very weak dependence of the star formation rate on gas density in NGC 4254 is connected with the ubiquitous H II region associations in its inner disk. High-mass star formation occurs everywhere with frequency in the inner disk of NGC 4254 and is not localized within a certain radius. The behavior of the star formation laws of NGC 4303 and NGC 4501 can be explained with Kennicutt's (1989) theory, which indicates that the gas densities for these galaxies may be near the threshold value. A highly nonlinear dependence of the star formation rate on the gas surface density is expected because of a large $Q$ value. Central $Q_{10}$ values for NGC 4303 and NGC 4501 are, in fact, relatively large compared to other values in Table 7–9. The rather strange radial behavior of the star

TABLE 8–13

CURRENT STAR FORMATION LAWS

TOTAL GAS MASS AND Hα

| NGC | $\alpha$ | N | Range (kpc) |
|---|---|---|---|
| 4254 | 32.91 | 0.498 | 0–2.5 |
| 4303 | 15.22 | 7.88 | 0–1.5 |
| 4303 | 28.48 | 2.24 | 0–2.5 |
| 4321 | 28.65 | 2.17 | 0–2.5 |
| 4501 | 13.30 | 9.85 | 0–2.5 |
| 4535 | 30.51 | 1.51 | 0–2.5 |
| 4536 | 29.67 | 1.85 | 0–2.5 |
| 4569 | 27.91 | 2.43 | 0–2.5 |

formation law for NGC 4303 (the 0.5–2.5 kpc region has a star formation law with a negative slope) may be due to star formation that is forced or driven at some radii by the gas flow around the stellar bar. In addition, radial averaging may obscure the physics operating in a nonaxisymmetric system.

Star formation laws derived using interferometer data show qualitatively similar behavior to the total gas star formation laws, but the relations are not as clean. There is a tendency for the power laws to steepen at smaller radii, which could be an artifact of the missing flux which is lost primarily at larger radii. The effect of missing flux is to cause the power laws to appear less steep, and that is generally the effect seen in the values in Table 8–12.

Star formation laws derived in the same way using $B$-band radiancies instead of Hα radiancies are graphed in Figure 8–8 for $H_2$ masses from OVRO data and in Figure 8–9 for total gas masses. Comparing Figures 8–6 through 8–9, it appears

that H$\alpha$ radiancy is better correlated with molecular hydrogen surface density from OVRO data, and that $B$-band radiancy is better correlated with the total gas mass surface density. Within a single galaxy, the data are very well correlated; scatter among the data for all galaxies is due to vertical displacement of the linear laws for each of the galaxies. There are two probable causes for vertical displacements: variations in extinction and in star forming efficiency. Varying extinction from galaxy to galaxy probably does not completely account for the scatter. The star forming efficiency can vary from galaxy to galaxy due to dynamical effects, such as the number of spiral arm crossings a molecular gas cloud undergoes in an orbit or the rate of dynamically-induced collisions between clouds. In addition, the star formation history also accounts for some of the scatter. NGC 4536, which is currently undergoing a burst of star formation, is well within the middle of the distribution of data in Figure 8–6 (H$\alpha$–OVRO CO star formation laws), but low in Figure 8–8 ($B$-band–OVRO CO star formation laws) because of its low average star formation rate over the past $5 \times 10^9$ years.

Global star formation laws that hold for all spiral galaxies may be deduced using all of the data in Figure 8–6 and Figure 8–9, which exhibit the best correlations. By assimilating all data, variations in star formation efficiency and history among galaxies are ignored, and only the variation of the average star formation rate with the gas density is considered. A linear least squares fit to the data in Figure 8–6, which relates the current density of star formation, $\Sigma_{\rm sfr}$(H$\alpha$), to the concentrations of molecular gas detected by the interferometer, $\Sigma_{\rm H_2}$(OVRO), indicate that

$$\log \Sigma_{\rm sfr}\,({\rm H}\alpha) = 31.97 + 0.955 \log \Sigma_{\rm H_2}\,({\rm OVRO}) \pm 0.44, \qquad (8-16)$$

where $\Sigma_{\rm sfr}\,({\rm H}\alpha)$ is in erg sec$^{-1}$ pc$^{-2}$ and $\Sigma_{\rm H_2}\,({\rm OVRO})$ is in $M_\odot$ pc$^{-2}$. CO interferometer data on NGC 4254, which are marginal, and two measurements of H$\alpha$ in NGC 4501, for which the continuum subtraction was uncertain, are excluded from

the fit (equation 8–16). A linear least squares fit to all $B$-band radiancy and total $H_2$ mass surface density leads to

$$\log \Sigma_{\rm sfr}\,(B) = 33.38 + 0.915 \log\, \Sigma_{\rm H_2}\,({\rm tot}) \pm 0.31, \qquad (8-17)$$

where $\Sigma_{\rm sfr}\,(B)$ is in erg sec$^{-1}$ pc$^{-2}$ and $\Sigma_{\rm H_2}\,({\rm tot})$ is in $M_\odot$ pc$^{-2}$. The other relationships, between $\Sigma_{\rm sfr}\,(H\alpha)$ and $\Sigma_{\rm H_2}\,({\rm tot})$ or between $\Sigma_{\rm sfr}\,(B)$ and $\Sigma_{\rm H_2}\,({\rm OVRO})$, lead to nonlinear exponents (1.34 and 0.44, respectively) and, as discussed above, are not as well correlated as the relations (8–16) and (8–17).

It is not too surprising that the exponents $N$ of the star formation laws $\Sigma_{\rm sfr} \propto \Sigma_{\rm gas}^N$ implied by equation (8–16) and equation (8–17) are nearly unity. Very simply, stars form in proportion to the amount of gas available. This viewpoint assumes that the star formation rate depends only on cloud properties, so that the average rate of star formation is proportional to the average number of clouds, or the average molecular gas density, in a volume of space. Averaging over large areas in the disk of a spiral galaxy, as was done to construct Figures 8–6 through 8–9 and to derive the global star formation laws (8–16) and (8–17), samples many clouds and many star forming regions, is insensitive to the local details of the dependence of star formation on gas density, and ignores the possibility that local effects may dominate the star formation rate in some regions.

There are two general paths by which star formation occurs in molecular clouds. One route is the approximately steady, random appearance of stars due to the collapse of knots in clouds. This method of forming stars may be largely stochastic but may also be partly self-induced and rely on compression or collection of gas by winds, outflows, or stellar ejecta. The second route to star formation is through the influence of other clouds, such as collisions between clouds or supernovae in nearby clouds. Dynamical effects, such as passage through spiral arms, could increase the rate of interaction between molecular clouds by bringing them closer together or in-

creasing their random velocities. The global or large-scale star formation law depends most strongly on the first, "stochastic," path to star formation, which implies a linear dependence between the molecular gas density and star formation rate. The influence of other clouds will be strongest when the density of clouds is highest, where much high-mass star formation is expected. The data in this thesis have sufficient resolution to explore the possibility that the second, "stimulated," path to star formation dominates in some regions. In particular, the interferometer maps identify regions of high concentrations of molecular clouds, so a strong correlation between CO emission in interferometer maps and H$\alpha$ emission is expected if stimulated star formation is important. The morphological similarity between CO and H$\alpha$ emission already has been noted in Chapter 4 and the similarity in radial distribution has been noted in Chapter 5. In contrast, the total CO emission is dominated by the average cloud population, and so is expected to correlate better with the $B$-band emission, which is dominated by lower-mass stars produced more abundantly via the stochastic star formation mode. A simple model for the relationship between the molecular gas density and the stimulated star formation rate is developed in the next section.

### 8.4.3. Stimulated Star Formation

Assume that each star-forming unit, which will be called a cloud, has a sphere of influence of radius $r_a$; a cloud is able to induce star formation in other clouds that enter this sphere of influence. Let extra stars be induced with rate $\epsilon_a$ stars per cloud per unit time, so that the rate of stimulated star formation per cloud is

$$\frac{4\pi}{3}\, r_a^3\, n_{\rm clouds}\, \epsilon_a, \qquad (8-18)$$

where $n_{\rm clouds}$ is the number density of clouds. Formally, the number of clouds within the sphere of influence of a given cloud is $(4\pi r_a^3\, n_{\rm clouds}/3 - 1)$, since the cloud does not stimulate itself (that is the "stochastic" star formation model). Equation (8–18)

is derived in the limit

$$4\pi r_a^3 \, n_{\rm clouds}/3 \gg 1 \qquad (8-19)$$

when stimulated star formation dominates. If $n_{\rm clouds}$ is small or if $r_a$ is small (because clouds are small or weakly interacting) so that equation (8–19) does not hold, then stimulated star formation is unimportant. The stimulated star formation rate per volume is

$$\frac{4\pi}{3} r_a^3 \, n_{\rm clouds}^2 \, \epsilon_a, \qquad (8-20)$$

and the total rate is

$$\frac{4\pi}{3} \int r_a^3 \, n_{\rm clouds}^2 \, \epsilon_a \, dV \qquad (8-21)$$

integrated over the volume of interest. In a disk galaxy,

$$n_{\rm clouds} \propto \frac{\Sigma_{\rm clouds}}{h} \propto \frac{\Sigma_{\rm gas}}{h\langle m_{\rm cloud}\rangle} \propto \frac{S_{\rm CO}}{h\langle m_{\rm cloud}\rangle}, \qquad (8-22)$$

where $\Sigma$ denotes surface density, $h$ is the characteristic thickness of the disk, $\langle m_{\rm cloud}\rangle$ is a characteristic mass per cloud, and $S_{\rm CO}$ is the CO radiancy in Jy km sec$^{-1}$ arcsec$^{-2}$. The total rate integral in equation (8–21) is

$$R_{\rm stim} \propto \frac{4\pi \, r_a^3 \, \epsilon_a \, D^2}{3h\langle m_{\rm cloud}\rangle^2} \int S_{\rm CO}^2 \, d\Omega, \qquad (8-23)$$

where the volume element $dV \approx h \cdot dA \approx D^2 h \, d\Omega$, where $D$ is distance to the source. The dependence on $S_{\rm CO}^2$ in equation (8–23) will emphasize concentrations of molecular gas. This approach differs substantially from past studies of the relationship between star formation and gas density (cf. Kennicutt 1989), which used the mean gas density and compared it with a star formation indicator. The stimulated star formation model, in the guise of equation (8–23), indicates that the square of the local gas density (or the areal average of its square) is the more appropriate quantity to compare with H$\alpha$ emission. A model relating specifically to cloud-cloud collisions worked out in §8.6.3 also arrives at a quadratic dependence of gas surface density

with star formation rate. Equation (8–23) may not be appropriate in low density regions, however, because of the rarity of cloud interactions; some H$\alpha$ emission from regions of low cloud density could be due to OB stars formed at random.

H$\alpha$ and $B$-band photometry was compared with the mean square of both CO emission from OVRO maps and total CO emission. Interferometer maps of integrated CO emission were squared and the mean $S^2_{\rm CO}$ was computed in the central disk of radius 500 pc and surrounding annuli 500 pc wide. The total CO emission was estimated as the sum of the OVRO maps and axisymmetric models by Kenney (1987) based on single-dish measurements; Kenney's models were scaled according to the amount of emission recovered in the interferometer maps (Table 5–4) so that the sum with interferometer maps would equal the total observed CO emission. These composite CO maps contain all of the CO emission and retain as well the information about molecular gas concentrations present in the interferometer maps. The star formation laws relating mean square $H_2$ surface density and star formation are graphed in Figure 8–10 through Figure 8–13 for OVRO or total mean squared CO emission and H$\alpha$ or $B$-band emission.

The mean squared gas density from interferometer maps correlates much better with H$\alpha$ emission than does the mean squared total gas density. This is an expected result if H$\alpha$ emission comes mostly from OB stars produced as a result of interactions between clouds, since such interactions will be more likely where the gas is most concentrated, which is indicated in interferometer maps. The mean squared total molecular gas density correlates best with $B$-band emission. Whenever stimulated star formation dominates, different star formation laws are expected for different galaxies because of the differing kinematics or star formation histories in different galaxies. For instance, the rate $\epsilon_a$ will change depending on the rate of passage of clouds through spiral arms or on the random velocities of clouds. The star formation

rate at times up to $\approx 5 \times 10^9$ years in the past affects the $B$-band radiancy today, so that a phase lag may exist between current locations of concentrations of gas and stars which contribute most to the $B$-band emission. The above factors, in addition to the effects of extinction, contribute to the scatter in the star formation laws in Figure 8–10 through Figure 8–13.

Universal star formation laws relating the mean square gas density to a star formation indicator are computed from the data with the best correlations: H$\alpha$ and interferometer CO, and $B$-band and total CO. Linear least squares fits to all of the data indicate that

$$\log \Sigma_{\rm sfr}\,({\rm H}\alpha) = 31.05 + 0.686 \log\langle \Sigma^2_{\rm gas}\,({\rm OVRO})\rangle \pm 0.27 \qquad (8-24)$$

and

$$\log \Sigma_{\rm sfr}\,(B) = 33.61 + 0.332 \log\langle \Sigma^2_{\rm gas}\,({\rm tot})\rangle \pm 0.19, \qquad (8-25)$$

where $\langle \Sigma^2_{\rm gas}\rangle$ is the local mean square gas density in units of $M^2_\odot\,{\rm pc}^{-4}$ and $\Sigma_{\rm sfr}$ is in units of $\mathrm{erg\,sec^{-1}\,pc^{-2}}$. Data from NGC 4254 were excluded from both fits because of the marginal interferometer map, which does little to highlight gas concentrations. The slopes in equation (8–24) and equation (8–25) are not unity (respectively 0.7 and 0.3). In the case of equation (8–24), the slope of 0.7 implies that stimulated star formation is not the only means of generating OB stars in regions of dense cloud concentration. The much lower exponent (0.3) in equation (8–25) indicates that stimulated star formation does not adequately describe the intermediate mass star formation process in the general population of molecular clouds. The scatter introduced by the different star formation laws for individual galaxies may also have acted to decrease the slopes of the universal fits. The slope could be close to unity for the relation between $\Sigma_{\rm sfr}\,({\rm H}\alpha)$ and $\Sigma_{\rm gas}\,({\rm OVRO})$, which is consistent with stimulated star formation dominating in cloud complexes, and close to 0.5 for $\Sigma_{\rm sfr}\,(B)$ and $\Sigma_{\rm gas}\,({\rm tot})$,

which is consistent with stochastic star formation dominating in the general cloud population.

## 8.5. Star Formation and Galaxy Rotation

Examination of the star formation laws graphed in Figure 8–6 and Figure 8–7 reveals that the star formation laws vary from galaxy to galaxy. Some headway can be made toward understanding one aspect of the reason for variation of the star formation law among disks by examining the innermost kiloparsec of the program spirals. Figure 8–14 shows the relationship between the current star formation rate (from Table 8–5) and the slope of the inner rotation curve (from Table 6–3) for the central kiloparsec of the program spirals. The data are well fitted by a straight line that passes very nearly through the origin:

$$\Sigma_{\rm sfr}(0) = 4.33\, V'(0) - 0.0255, \qquad (8-26)$$

where $\Sigma_{\rm sfr}(0)$ is the average current star formation rate within 500 pc radius in units of $M_\odot\,{\rm yr}^{-1}\,{\rm kpc}^{-2}$ and $V'(0)$ is the central rotation curve slope in units of $\rm km\,sec^{-1}\,pc^{-1}$. It is a pity that the relationship does not continue to hold as well when larger areas are considered. At distances from the nucleus greater than about 500 pc, dynamical effects related to morphology evidently begin to dominate the star-forming tendency of a rotating disk. Notice, for instance, that the star formation rates of NGC 4303 and NGC 4321 are both greater than implied by the linear fit in Figure 8–14, and that the fit would be much better if these two points were excluded. The bar in NGC 4303 and the four-armed structure near 1 kpc radius in NGC 4321 are two dynamical constructions that greatly influence the local star formation rate. Their influences are probably responsible for the elevated positions of the data points in Figure 8–14.

The source of the correlation between star formation rate and rotation curve slope

is probably linked with the great concentrations of molecular gas at the centers of spirals. Figure 8–15 shows the relationship between the total gas ($H_2 + H\,I + He$) mass surface density within the central kiloparsec of the program spirals and the slopes of their inner rotation curves. The linear fit to the data is good and follows

$$\Sigma_{gas}(0) = 953\,V'(0) + 79.7, \qquad (8-27)$$

where $\Sigma_{gas}(0)$ is the average gas mass surface density within 500 pc radius in units of $M_\odot\,pc^{-2}$ and $V'(0)$ is the central rotation curve slope in units of $km\,sec^{-1}\,pc^{-1}$.

There does not appear to be a relationship between morphological type and the slope of the inner rotation curve or the central gas mass. The early-types NGC 4501 and NGC 4569 are near the origin with the very late-type NGC 4654, while the remaining Sbc- and Sc-types are mixed farther along the line. The sample is probably too small, though, to permit a morphological pattern that might exist to emerge.

The current star formation efficiency, defined as the star formation rate per unit gas mass, may be calculated from values in Table 8–5 and Table 7–5. Star formation efficiencies for the program spirals in annuli 500 pc wide are listed in Table 8–14. Star formation efficiencies are generally higher by factors of three to five in the central kiloparsec than they are at 2–2.5 kpc radius. There are two possible explanations for this observation. One is that the physical conditions in the inner kiloparsec of spiral galaxies are such that many more stars are produced per cloud mass. As will be discussed below, this could be related to the increased rate of cloud-cloud collisions driven by epicyclic shaking near spiral galaxy nuclei. Note that the star formation efficiency in NGC 4254 is nearly constant with radius. The strong spiral arms that wind all the way to the center of this galaxy are like those in none of the other program spirals and probably drive an increased rate of cloud-cloud collisions. Epicyclic shaking near the nucleus is not likely to be as important in NGC 4254, which has a slowly rising inner rotation curve.

The other explanation for the enhanced central star formation efficiencies is that high-mass star formation is favored near spiral galaxy nuclei. Using the average masses in Table E–4, the lower mass cutoff of the initial mass function could be 0.7–1.5 $M_\odot$ in the central kiloparsec of those spiral galaxies that indicate an increased central star formation efficiency. These lower mass cutoffs would inflate the star formation efficiency estimates by factors of three to five because more high-mass stars would be made per stellar mass created.

No correlation is found between the central star formation efficiency and the central rotation curve slope. The implication of this result is that the central concentration of gas is as much responsible for the correlation as the star formation rate is. Since the program spirals follow the star formation law (equation 8–15) fairly well, the interdependence of the central star formation rate and gas surface density is not surprising. However, equation (8–26) relates the central star formation rate to an extrinsic property of the disk, the degree of central mass concentration, and so determines the scaling for the power law (8–15) relating the star formation rate to the gas surface density. By linking equation (8–15) with equation (8–26), it follows that spirals with steep inner rotation curves have greater concentrations of gas. A greater star formation rate would then follow merely from the larger amount of gas as already shown in Figure 8–15.

Is there a causal relation between the rotation curve slope and the central gas mass? Spirals could, for instance, naturally maintain a universally constant gas mass fraction through some sort of self-regulation. Then the larger amounts of gas at the center of spirals with steeper rotation curves would merely be the result of increasing the gas mass to scale with the increased dynamical mass producing the steep rotation curve. A physically more revealing explanation for the correlation between the central rotation curve and the star formation rate is that it is caused by the frequency of

TABLE 8–14. STAR FORMATION EFFICIENCY[a]

| NGC | Outer Radius (kpc) | | | | |
|---|---|---|---|---|---|
| | 0.5 | 1.0 | 1.5 | 2.0 | 2.5 |
| 4254 | 2.59 | 2.32 | 3.50 | 5.24 | 4.40 |
| 4303 | 6.08 | 0.259 | 0.333 | 0.745 | 0.894 |
| 4321 | 2.53 | 2.15 | 0.483 | 0.426 | 0.450 |
| 4501 | 4.21 | ··· | ··· | 0.035 | 0.377 |
| 4535 | 2.89 | 0.757 | 0.657 | 0.617 | 1.00 |
| 4536 | 3.01 | 2.47 | 1.37 | 0.783 | 0.568 |
| 4569 | 1.11 | 0.513 | 0.326 | 0.368 | 0.333 |

[a] Values are the current star formation rate in $M_\odot\,yr^{-1}$ per $10^9\,M_\odot$ of gas.

epicyclic shaking of molecular clouds. In the inner regions of spirals where the rotation curve is approximately linearly rising, the epicyclic frequency is proportional to the slope of the rotation curve. That is, if the rotation velocity $V_c(r)$ satisfies

$$V_c(r) \approx \alpha r, \tag{8-28}$$

where $\alpha$ is a constant, for small $r$, then the epicyclic frequency, $\kappa(r)$, behaves as

$$\kappa(r) = \left(\frac{2V_c}{r}\frac{dV_c}{dr} + \frac{2V_c^2}{r^2}\right)^{1/2} \approx 2\alpha. \tag{8-29}$$

Since molecular clouds behave as ballistic particles until they collide, their orbits resemble stellar orbits and may therefore be represented by the epicycle approximation. Viewed in a frame rotating with the disk at constant angular speed, a body in orbit executes small, circular librations about a point, the guiding center of the orbit. The frequency of the librations is the epicyclic frequency, $\kappa(r)$. If the amplitude of the epicyclic motion could be determined, then the velocities of clouds executing their

epicyclic orbits could be calculated. The inner part of a spiral disk rotates as a rigid body. Collisions between molecular clouds in the inner disk of a spiral could occur during epicyclic excursions of the clouds. In the outer disks of spirals, molecular clouds collide as a result of random motions, but the very large epicyclic frequencies near the center of spirals may cause larger relative velocities or shorten the time between collisions. The rate of collisions, which would be proportional to the epicyclic frequency, would increase with the increasing slope of the rotation curve, by equation (8–29). Since high-mass star formation is believed to result from cloud-cloud collisions, the increased cloud collision rate at the center of spirals with steep inner rotation curves would increase the rate of high-mass star formation as well. This could explain the correlation observed in Figure 8–15.

Where cloud-cloud collisions dominate over other physical mechanisms that lead to high-mass star formation, then the exponent in the star formation law (equation 8–15) should be around $N = 2$. This follows from a simple dimensional argument and some simplifying assumptions. Let all clouds have the same diameter, $a_{\rm cloud}$, and also assume that they are distributed randomly over a projected area so that their number surface density is easily defined as $\Sigma_{\rm clouds}$. Assume that the disk system in which the clouds reside is, on the size scale of the clouds, two-dimensional, so that when projected cloud areas overlap they have collided. The mean free path between collisions is

$$l_{\rm mfp} \approx 1/\Sigma_{\rm clouds} a_{\rm cloud}, \qquad (8-30)$$

by geometrical reasoning. The mean free path is also

$$l_{\rm mfp} = v\tau, \qquad (8-31)$$

where $v$ is the average velocity of a cloud, assumed to be randomly directed in the plane, and $\tau$ is the average time between collisions. Therefore, the average time

between collisions is

$$\tau \approx 1/\Sigma_{\rm clouds} v a_{\rm cloud}. \qquad (8-32)$$

The rate of collisions per unit area is

$$r_{\rm coll} \approx \Sigma_{\rm clouds}/\tau. \qquad (8-33)$$

If the number of stars made per collision (which can be translated into a mass of stars formed per collision through an IMF) is given by the efficiency $\epsilon_{\rm sfr}$, then the surface density of star formation is, from equation (8–32) and equation (8–33),

$$\Sigma_{\rm sfr} = \Sigma^2_{\rm clouds} v a_{\rm cloud}\, \epsilon_{\rm sfr}. \qquad (8-34)$$

The exponent $N = 2$ in equation (8–15) follows from equation (8–34) by converting cloud number density to mass density. The fact that real molecular clouds have a spectrum of masses and that the efficiency $\epsilon_{\rm sfr}$ may vary with the relative cloud masses and velocities will cause some variation from $N = 2$ in real observations. The clustering of values of $N$ around $N = 2$ in Table 8–13 suggests that the above dimensional analysis is basically correct and that cloud-cloud collisions may drive high-mass star formation in the inner regions of many spirals.

Equation (8–34) indicates that variations in the star formation rate surface density may be caused either by changing the surface density of clouds or else by varying the average relative velocity of clouds. The increasing epicycle frequency toward the centers of spirals may result in an increased relative velocity between clouds on slightly different orbits. Collisions could result as a result of the epicyclic excursions of clouds about their guiding centers. The fact that there is no correlation between the slope of the inner rotation curve and the star formation efficiency follows from the independence of $v$ and $\epsilon_{\rm sfr}$ in equation (8–34). Variations in $\epsilon_{\rm sfr}$ from galaxy to galaxy, and the relative importance of cloud-cloud collisions in causing high-mass star formation, may be the main causes of the scatter in Figure 8–14.

## 8.6. Accumulating Gas

Gas must be accumulated at the centers of spirals approximately at the rate needed to maintain the current star formation rate, if a steady state situation exists. The current star formation rate is listed in Table 8–5 for the program spirals, and is approximately a few $M_\odot\,yr^{-1}$ within annuli 500 pc wide. A process must be found that is capable of delivering this amount of gas to the central regions of spirals. The problem is that angular momentum must be removed from the clouds so that their orbital radius declines secularly. Angular momentum may be removed by several processes. Dynamical friction may remove angular momentum from a cloud moving through a sea of stars. It is also possible that a small mass may be ejected from a cloud to a large radius following a collision, the ejected mass carrying away substantial angular momentum. The processes in addition to dynamical friction which will be discussed below are transport of angular momentum by traveling spiral density waves and through the kinematic viscosity of the gas. All three processes operate efficiently enough to move on the order of $1\,M_\odot\,yr^{-1}$ of gas into the central regions of spirals.

### 8.6.1. Dynamical Friction

A massive molecular cloud moving through a large sea of stars perturbs the stars gravitationally in such a way that a higher than average mass density of stars accumulates in the wake of the cloud and the stars' combined gravitational effect slows the cloud in its orbit. This is the basis of dynamical friction. The dynamical friction force on a mass $M_s$ is

$$F_{\rm df} = -\phi \frac{4\pi G^2 M_s^2 \rho(r)}{v_s^2} \ln \Lambda, \qquad (8-35)$$

where $\phi$ is a function of order unity, $G$ is the gravitational constant, $M$ is the mass of the cloud, $\rho(r)$ is the volume density of the matter distribution, and $v_s$ is the speed of the mass $M_s$ with respect to the mean velocity of particles that make up the

background mass field (Binney and Tremaine 1987, p. 427). The quantity $\ln \Lambda$ is

$$\ln \Lambda = \ln \frac{b_{\max} v_c^2}{G(M_s + m)}, \qquad (8-36)$$

where the notation is the same as above, with the addition of $m$, the mass of an individual star, and $b_{\max}$, the distance of the farthest encounter that needs to be considered (Binney and Tremaine 1987, p. 423).

Considerable complications arise when analyzing the dynamical friction on a satellite mass in orbit within a rotating disk. The three phenomena discussed by Quinn and Goodman (1986) for masses in coplanar, prograde, circular orbits in a rotating galactic disk are: 1) dynamical friction as in equation (8–35) in which the asymmetric drift (Binney and Tremaine 1987, p. 198; Mihalas and Binney 1981, pp. 397*ff*) is the source of the relative velocity between the orbiting mass and the field (Keenan 1979); 2) perturbative torques at Lindbald resonances; and 3) dynamical friction due to passage of stars in "horseshoe" orbits. In the frame rotating with the satellite mass $M_s$ in a galactic disk, the orbits of some close-passing stars turn and loop back in a horseshoe shape due to the gravitational action of the satellite mass. If the satellite does not sink very fast, it encounters the same star many times on its horseshoe orbit. Using the criterion in equation (III.21) of Quinn and Goodman (1986), it can be determined that drag due to stars in horseshoe orbits is not as important as drag due to asymmetric drift for molecular clouds of mass $10^6$ $M_\odot$ in the disk of a typical spiral galaxy. Also, the criterion in equation (III.12) of Quinn and Goodman (1986) indicates that drag due to asymmetric drift also dominates the effect of torques at Lindblad resonances. Asymmetric drift is the term used to describe the fact that the radial velocity dispersion of stars allows them to lag or lead a particle orbiting at the mean speed at a given radius. Standard dynamical friction may then operate using the asymmetric drift speed as the encounter speed.

The torque $\Gamma$ per unit mass on the satellite due to asymmetric drift is

$$\frac{\Gamma}{M_s} = \frac{-\sqrt{32\pi}\, v_d R G^2 M_s \rho \ln \Lambda}{3\sigma^3} \qquad (8-37)$$

(Quinn and Goodman 1986), where $v_d$ is the asymmetric drift speed, $\rho$ is the mass volume density, and $\sigma$ is the velocity dispersion of the particles in the mass field. An empirical estimate of the drift speed in our Galaxy is

$$v_d \approx \sigma^2/120\,\mathrm{km\,sec^{-1}} \qquad (8-38)$$

(Mihalas and Binney 1981, p. 400). It is interesting to compare the magnitudes of dynamical friction on molecular clouds due to stars and due to other molecular clouds. Since the molecular gas disk has a small velocity dispersion (§7.2.3), it may be expected that the drag due to the gas disk is much greater than that due to the stellar disk because $\Gamma \propto \sigma^{-3}$. The decreased asymmetric drift speed $v_d$ and density $\rho$ for the gas disk, however, nearly compensate for the effect of the velocity dispersion $\sigma$, and as a result, locally in our Galaxy, the drag on molecular clouds due to stars is comparable to that due to gas. The effect of friction against stars in a nonrotating halo about our Galaxy is much smaller than that due to stars in the disk (see discussion below).

To take a concrete example to calculate the drag due to asymmetric drift, consider a galaxy whose mass distribution is described by a Mestel disk, for which the surface density is

$$\Sigma(r) = \Sigma_0\, R_0/r \qquad (8-39)$$

and the volume density is

$$\rho(r) \approx \Sigma_0\, R_0/2hr, \qquad (8-40)$$

where $h$ is the scale height of the disk. The Mestel disk allows easy analytical treatment, but its mass surface density declines with radius much slower than that of a realistic disk galaxy. For this reason, dynamical friction will act more efficiently in

the Mestel disk than it will in a galaxy with a more realistic mass distribution (say, an exponential disk). The rotation velocity of the Mestel disk is constant,

$$v_c^2 = 2\pi G\,\Sigma_0\,R_0 \qquad (8-41)$$

(Binney and Tremaine 1987, p. 76), so that its rotation curve approximates the rotation curve in the outer disks of real spirals. Let $v_c = 250\,\mathrm{km\,sec^{-1}}$, $b_{\max} = 2\,\mathrm{kpc}$ the luminosity scale length of a typical spiral, and $M_s = 5\times10^5\,\mathrm{M}_\odot$ an average molecular cloud mass in equation (8–36). Then

$$\ln\Lambda = 10.97, \qquad (8-42)$$

and even substantial changes in any of the parameters that define $\ln\Lambda$ do not alter its value very much because of the logarithm.

Dynamical friction applies a torque that causes a molecular cloud to lose angular momentum. Following Binney and Tremaine (1987), the infall time can be estimated from the torque. Let $L$ be the specific angular momentum, so that

$$\frac{dL}{dt} = \frac{d}{dt}(v_c\,r) = v_c\,\frac{dr}{dt} \qquad (8-43)$$

for the Mestel disk. Also,

$$\frac{dL}{dt} = \frac{\Gamma}{M_s}. \qquad (8-44)$$

Equating the time rate of change of the specific angular momentum in equation (8–43) and equation (8–44) with the circular velocity in equation (8–41) yields

$$dt = -\sqrt{2\pi G\Sigma_0 R_0}\cdot\frac{6h\sigma^3}{\sqrt{32\pi}\,v_d G^2 M_s \Sigma_0 R_0\,\ln\Lambda}\,dr, \qquad (8-45)$$

which can be integrated to yield

$$\tau \approx \frac{1}{4\sqrt{G^3\Sigma_0 R_0}}\cdot\frac{6h\sigma^3 r_i}{v_d M_s \ln\Lambda}, \qquad (8-46)$$

where $\tau$ is the time for a molecular cloud of mass $M_s$ to fall from radius $r = r_i$ to $r = 0$ in a Mestel disk.

To estimate the molecular cloud mass infall rate, take the molecular cloud population in our Galaxy as an example. The number density of clouds per unit mass interval is

$$\zeta(M)\,dM = 10^{3.2}\,M^{-1.5}\,dM, \qquad (8-47)$$

where $M$ is in solar masses and $\zeta$ is in clouds per square kiloparsec (Elmegreen 1985). The formula is normalized to the solar neighborhood. The radial dependence of the number density may be deduced from the radial distribution of $I_{\rm CO}$ in our Galaxy (Solomon and Sanders 1985), neglecting the lack of CO emission around $R = 2\,{\rm kpc}$:

$$\log\, I_{\rm CO}(R) = 1.5 - 0.175\,R_{\rm kpc}, \qquad (8-48)$$

where $I_{\rm CO}(R)$ is in $\rm K\,km\,sec^{-1}$. The integrated mass flux of all molecular clouds due to dynamical friction is then the integrated mass at each radius divided by the time for that mass to fall to the center, summed over the entire disk:

$$\dot{M} = \int\int 2\pi R\,M\zeta(M)10^{1.5-0.175R}\,\tau^{-1}\,dM\,dR. \qquad (8-49)$$

For a Mestel disk with scale height $h = 150\,{\rm pc}$, $\Sigma_0 = 475\,{\rm M_\odot\,pc^{-2}}$, and $R_0 = 2\,{\rm kpc}$ (so that $M(10\,{\rm kpc}) = 6\times10^{10}\,{\rm M_\odot}$), the mass infall rate to the center is

$$\dot{M}_{\rm M_\odot\,yr^{-1}} = (3.59\times10^{-9})\int dR\int dM\,M^{0.5}\,10^{-0.175R}, \qquad (8-50)$$

where $R$ is in kpc and $M$ is in $M_\odot$. For molecular cloud masses in the range $10^4$–$10^6\,M_\odot$ and a range in radius of 1–2 kpc, the integral (8–50) is

$$\dot{M} = 1.32\,{\rm M_\odot\,yr^{-1}}, \qquad (8-51)$$

while for a range in radius of 2–10 kpc, $\dot{M} = 2.54\,{\rm M_\odot\,yr^{-1}}$. Evidently, most of the mass flux is from gas that is already very near the center. The more massive clouds

sink fastest, and so make the greatest contribution to the mass flux into the central kiloparsec. Regarding the current star formation rates in Table 8–5, the mass infall rate in equation (8–51) is of the right order of magnitude to fuel the star formation in the inner kiloparsec of most of the program spirals. A calculation analogous to the one above, but for a galaxy with an isothermal sphere mass distribution and comparable mass (like a galactic halo), indicated mass infall rates about an order of magnitude less than those indicated by equation (8–51) Due to the concentration of mass in the disks of real spiral galaxies, dynamical friction will act more efficiently in spirals than in galaxies which have isothermal sphere mass distributions, but somewhat less efficiently than in the Mestel disk, which has a greater midplane density than realistic disk galaxies. Although the lifetime of molecular clouds has not been discussed in this calculation, it is assumed that they are destroyed and re-form at rates that preserve their azimuthally averaged density. In this way, even though no single cloud survives its trip from the outer disk to the center, the secular evolution of the cloud population is still described by equation (8–49).

### 8.6.2. Angular Momentum of Spiral Waves

Spiral density waves, as manifestations of a wave phenomenon, carry both energy and momentum. Trailing spiral waves are capable of transporting angular momentum from the inner parts of spirals to the outer disk, and in doing so enable a disk to lower its total energy, which is a natural tendency for physical systems. The time to remove a significant portion of the angular momentum of the gas in a region will be estimated below, following Lynden-Bell and Kalnajs (1972), and this time will be compared with the gas consumption times in Table 8–11.

The total angular momentum $H$ of an annular section of a disk is

$$H = MR^2\Omega, \qquad (8-52)$$

where the mass of the ring is $M$, its radius is $R$, and its angular speed is $\Omega$. The

torque $\Gamma$ of a spiral wave in a disk is

$$\Gamma = \frac{1}{4} m R S^2 / G, \qquad (8-53)$$

where $m$ is the mode number of the wave, $R$ is the radial distance from the center, $G$ is the gravitational constant, and $S$ is the amplitude of the wave potential per unit mass (Lynden-Bell and Kalnajs 1972). The angular momentum will be removed by the torque on a timescale of

$$\tau \approx H/\Gamma = 4GMR\Omega/mS^2. \qquad (8-54)$$

The maximum amplitude of the spiral wave can be determined by requiring that the phase velocity of the spiral wave, $v_{\rm phase} = m(\Omega + \Omega_p)/k$, be greater than the stellar velocities generated by the passage of the wave, which is

$$v_* = \frac{\kappa k S}{\kappa^2 - (\omega + m\Omega)^2}. \qquad (8-55)$$

Here, $kS$ is the force per unit mass, which leads to the radial displacement $kS/[\kappa^2 - (\omega + m\Omega)^2]$, from which a velocity is derived by multiplying by the epicyclic frequency (Binney and Tremaine 1987, p. 386). The condition on $S$ is

$$S \leq \frac{\omega + m\Omega}{\kappa k^2} [\kappa^2 - (\omega + m\Omega)^2], \qquad (8-56)$$

where $\omega = m\Omega_p$, $\Omega_p$ is the pattern speed, and $k$ is the wavenumber. Equation (8–54) is now

$$\tau = \frac{4GMR\Omega}{m} \frac{k^2}{\nu^2 \kappa^2} \frac{1}{(1-\nu^2)^2}, \qquad (8-57)$$

where

$$\nu = \frac{\omega + m\Omega}{\kappa}. \qquad (8-58)$$

Taking the wavenumber to be the wavelength of the most unstable long wave,

$$k \equiv k_{\rm crit} = \frac{\kappa^2}{2\pi G \Sigma}, \qquad (8-59)$$

equation (8–57) finally becomes

$$\tau = \frac{MR\Omega\kappa^4}{4\pi^4 mG\Sigma^4} \cdot \frac{1}{\nu^2(1-\nu^2)^2}$$
$$= (3.14 \times 10^6)\frac{MR\Omega\kappa^4}{m\Sigma^4\nu^2(1-\nu^2)^2} \text{ years,} \qquad (8-60)$$

where $M$ is in $10^8\,M_\odot$, $R$ is in kpc, $\Omega$ and $\kappa$ are in $\mathrm{km\,sec^{-1}\,kpc^{-1}}$, and $\Sigma$ is in $M_\odot\,\mathrm{pc^{-2}}$. The angular momentum of the gas in equation (8–52) enters equation (8–60) through $M$, and the torque exerted by the spiral wave from equation (8–53) enters through $\Sigma$. Using values of $M_{\rm gas}$ and $\Sigma_{\rm dyn}$ from Table 7–5 and Table 6–5, timescales for removing a significant fraction of the total angular momentum of the gas are listed in Table 8–15 for a thin disk mass distribution. Comparison of the values in Table 8–15 with the gas depletion times in Table 8–11 indicates that the rate of gas infall by removal of angular momentum by spiral waves is easily able to keep up with the current rate of star formation. The values in Table 8–15 are times to remove the angular momentum from the gas in an annulus 500 pc wide, given the local density of the disk through which the spiral wave travels. The lack of coherent, long spiral waves in a disk would decrease the efficiency of angular momentum transport, and so lengthen the gas infall time.

### 8.6.3. Kinematic Viscosity

In a galactic disk, wherever there is some differential rotation, the shear provides a means to transfer angular momentum. The shear rate, $A$, is

$$A = R\frac{d\Omega}{dR}, \qquad (8-61)$$

so that the part of a disk with a strictly linearly rising rotation curve ($\Omega$ = const.) has no shear. All of the program spirals have some curvature in their inner rotation curves (Figure 6–10), and hence have shear in their inner disks. Angular momentum of gas in the inner disk of a spiral may be transported to the outer disk through

TABLE 8–15.

TIMESCALE[a] TO REMOVE ANGULAR MOMENTUM

| NGC | Outer Radius (kpc) | | | | |
|---|---|---|---|---|---|
| | 0.5 | 1.0 | 1.5 | 2.0 | 2.5 |
| 4254 | 0.15 | 0.68 | 1.12 | 1.37 | 1.61 |
| 4303 | 50.0 | 12.1 | 10.7 | 10.4 | 10.3 |
| 4321 | 0.05 | 0.78 | 0.73 | 0.85 | 1.02 |
| 4501 | 0.02 | 0.07 | 0.10 | 0.13 | 0.18 |
| 4535 | 0.68 | 0.38 | 1.35 | 1.89 | 1.34 |
| 4536 | 0.44 | 0.36 | 1.80 | 6.79 | 11.8 |
| 4569 | 0.65 | 1.21 | 0.83 | 0.76 | 0.71 |
| 4654 | 0.53 | 0.15 | 0.12 | 0.29 | 0.54 |

[a]Units are $10^8$ years.

viscous forces. In time, more and more of the mass of the disk becomes concentrated at its center while a small fraction of the disk mass escapes to large radii and carries most of the angular momentum with it.

The efficiency of viscous transport depends on the physical magnitude of the coefficient of viscosity, $\eta$. In a dilute gas consisting of particles of mass $m$, mean speed $\bar{v}$, number density $n$, and mean free path $l$, the coefficient of viscosity is

$$\eta = \frac{1}{3} n\, m\, \bar{v}\, l \qquad (8-62)$$

(Reif 1965). Derivation of equation (8–62) assumes that the particles acquire a velocity after a collision that is typical of the velocities of other particles at the location at which the collision occurred. The formula (8–62) may be used to compute the coefficient of viscosity of the molecular gas in a spiral galaxy, in which the particles are molecular clouds, if molecular clouds move ballistically (until collision, when they

stick), and if their velocities after collision (or the velocities of the cloud pieces) are representative of velocities of other molecular clouds at the galactocentric radius at which the collision occurred. Both assumptions are reasonable and formula (8–62) will be adopted in analysis below.

In computing the rate of gas mass infall due to viscous transport of angular momentum, the *kinematic* coefficient of viscosity, $\nu$, will be more useful than $\eta$:

$$\nu = \eta/\rho = \frac{1}{3}\bar{v}l. \qquad (8-63)$$

The numerical value of $\nu$ can be estimated from observations. The mean free path of a molecular cloud is

$$l \approx 1/\sqrt{2}\, n\, a_{\rm cloud}, \qquad (8-64)$$

where $n$ is the number density of clouds and $a_{\rm cloud}$ is the area of the cloud; the factor of $\sqrt{2}$ accounts for the mean relative velocities of colliding clouds, which are $\sqrt{2}$ times the cloud mean velocity. The quantity $n\, a_{\rm cloud}$ may be estimated from the cloud area filling factor, $f_A$:

$$f_A \approx \frac{T_b \sigma_v}{T_k \Delta v_{\rm cloud}}, \qquad (8-65)$$

where $T_b$ is the observed mean brightness temperature in a single 5 MHz channel over an area containing many clouds, $\sigma_v$ is the velocity dispersion measured from the spectral line width (corrected for broadening due to rotation of the galaxy), $T_k$ is the areal average kinetic temperature of a single cloud, and $\Delta v_{\rm cloud}$ is the internal velocity dispersion of a single cloud. Values of mean $T_b$ are listed in Table 5–3, and $T_k \approx 10\,{\rm K}$ is assumed. The possible increase in $T_k$ by factors of two to four near the centers of spirals (§7.3.6) could decrease the estimate of $f_A$ by the same factors, as would an increase in the typical cloud internal velocity dispersion. The relative contribution of intercloud velocity dispersion and of cloud internal velocity dispersion to the increase in CO line widths near the centers of spiral galaxies (Table 7–9) is undetermined.

The area filling factor of clouds is also

$$f_A = 2n\, h\, a_{\rm cloud}, \qquad (8-66)$$

where $h$ is the scale height of the disk. Using equation (8–65) and equation (8–66) to estimate $n\, a_{\rm cloud}$ in equation (8–64), the kinematic viscosity coefficient in equation (8–63) is

$$\nu \approx \frac{\sqrt{2}}{3} \cdot \frac{\bar{v}\, h\, T_k \Delta v_{\rm cloud}}{T_b \sigma_v} = (3.64 \times 10^{22})/T_b \ {\rm m^2\,sec^{-1}}, \qquad (8-67)$$

where $T_b$ is in K. Equation (8–67) uses $T_k = 10\,{\rm K}$, $h = 50\,{\rm pc}$, $\Delta v_{\rm cloud} = 5\,{\rm km\,sec^{-1}}$, and assumes that $\bar{v} \approx \sigma_v$, which causes the dependence on $\sigma_v$ to drop out. If molecular cloud kinetic temperatures and internal velocity dispersions are greater in the central regions of spiral galaxies by factors of two to four, then the kinematic viscosity coefficient will be larger than indicated by equation (8–67) by factors of four to 16. Table 8–16 lists values of $\nu$ computed from equation (8–67) using $T_b$ from Table 5–3.

TABLE 8–16.

KINEMATIC VISCOSITY COEFFICIENT

| NGC | $\nu^a$ | NGC | $\nu$ |
|---|---|---|---|
| 4254 | 6.59 | 4535 | 8.60 |
| 4303 | 6.64 | 4536 | 6.37 |
| 4321 | 3.07 | 4569 | 6.89 |
| 4501 | 8.72 | 4654 | 12.0 |

[a]Units are $10^{22}\,{\rm m^2\,sec^{-1}}$.

By keeping account of the net mass flux through an annulus in a disk of gas and incorporating conservation of angular momentum, Pringle (1981) derived the equation describing secular evolution of an accretion disk:

$$\frac{d\Sigma}{dt} = \frac{1}{R}\frac{\partial}{\partial R}\left\{\frac{\partial}{\partial R}\left(-\nu\Sigma\, R^3 \frac{d\Omega}{dR}\right) \Big/ \frac{d}{dR}\left(R^2\Omega\right)\right\}, \qquad (8-68)$$

where $\Sigma$ is the mass surface density of the gas and $\Omega$ is the angular speed of the gas in orbit. Integration of equation (8–68) over an annular area leads to the net mass infall rate

$$\dot{M} = 2\pi \frac{d}{dR}\left(-\nu\Sigma R^3 \frac{d\Omega}{dR}\right) \Big/ \frac{d}{dR}(R^2\Omega)\Big|_{R_0}^{R_1}, \qquad (8-69)$$

where $R_0$ and $R_1$ are the inner and outer radii of the annulus. In deriving equation (8–69), it is assumed that $\Omega(R)$ is independent of time, which will not be true over long periods of time after much mass has flowed. Table 8–17 lists values of the mass flux across radii from 500 pc to 2 kpc computed using formula (8–69). Differential approximations of the derivative of $\nu\,\Sigma\,R^3\,\Omega'$ were used, but analytical derivatives of quantities involving $\Omega$ were computed using the rational function curves from Table 6–2. The mass fluxes in Table 8–17 are infall rates across each indicated radius. It is assumed for simplicity that $\nu$ is constant with radius, so that numerical derivatives involving $\nu$ in equation (8–69) would not have to be estimated. The gas masses from infall in Table 8–17 are of the right magnitude to fuel the current star formation rates listed in Table 8–5. Either viscous transport of angular momentum or transport of angular momentum by spiral waves could cause gas inflow to fuel star formation. Whatever gas is not consumed in star formation will enrich the gas reservoir at smaller radii, which could explain the large concentrations of molecular gas within 500 pc radius of the centers of many of the program spirals.

TABLE 8–17. MASS FLUX RATES[a]

| NGC | Radius (kpc) | | | |
|---|---|---|---|---|
| | 0.5 | 1.0 | 1.5 | 2.0 |
| 4254 | 1.05 | 0.75 | 0.31 | 0.31 |
| 4303 | 2.48 | 1.58 | 0.89 | 0.41 |
| 4321 | 0.77 | 0.58 | 0.16 | 0.13 |
| 4501 | 0.24 | 0.37 | 0.45 | 0.55 |
| 4535 | 0.44 | 0.42 | 0.40 | 0.14 |
| 4536 | 1.30 | 1.59 | 0.70 | 0.49 |
| 4569 | 0.64 | 0.31 | 0.26 | 0.21 |
| 4654 | 0.54 | 0.07 | 0.71 | 0.93 |

[a]Units are $M_\odot\,yr^{-1}$.

## References

Allen, C. W. 1973, *Astrophysical Quantities* (London: The Athlone Press).

Bertin, G., Lin, C. C., Lowe, S. A., and Thurstans, R. P. 1989, *Ap. J.*, **338**, 78.

Binney, J., and Tremaine, S. 1987, *Galactic Dynamics* (Princeton: Princeton University Press).

Elmegreen, B. G. 1985, in *Protostars and Planets II*, ed. D. C. Black and M. S. Matthews (Tucson: University of Arizona Press), p. 33.

Gallagher, J. S., III, Hunter, D. A., and Tutukov, A. V. 1984, *Ap. J.*, **284**, 544.

Keenan, D. W. 1979, *Astron. Ap.*, **71**, 245.

Kenney, J. D., 1987. Ph.D. thesis, University of Massachusetts.

Kennicutt, R. B., Jr. 1983, *Ap. J.*, **272**, 54.

Kennicutt, R. B., Jr. 1989, *Ap. J.*, **344**, 685.

Larson, R. B., and Timsley, B. M. 1978, *Ap. J.*, **219**, 46.

Longo, G., and de Vaucouleurs, A. 1983, *A General Catalogue of Photoelectric Magnitudes and Colors in the U, B, V System of 3,578 Galaxies Brighter than the 16th V-Magnitude* (Austin: University of Texas Press).

Lynden-Bell, D., and Kalnajs, A. J. 1972, *M.N.R.A.S.*, **157**, 1.

Mihalas, D., and Binney, J. 1981, *Galactic Astronomy* (San Francisco: W. H. Freeman).

Pringle, J. E. 1981, *Ann. Rev. Astron. Ap.*, **19**, 137.

Quinn, P. J., and Goodman, J. 1986, *Ap. J.*, **309**, 472.

Reif, F. 1965, *Fundamentals of Statistical and Thermal Physics* (New York: McGraw-Hill).

Rieke, G. W., Lebofsky, M. J., Thompson, R. I., Low, F. J., and Tokunaga, A. T. 1980, *Ap. J.*, **238**, 24.

Schmidt, M. 1959, *Ap. J.*, **129**, 243.

Solomon, P. M., and Sanders, D. B. 1985, in *Protostars and Planets II,* ed. D. C. Black and M. S. Matthews (Tucson: University of Arizona Press), p. 59.

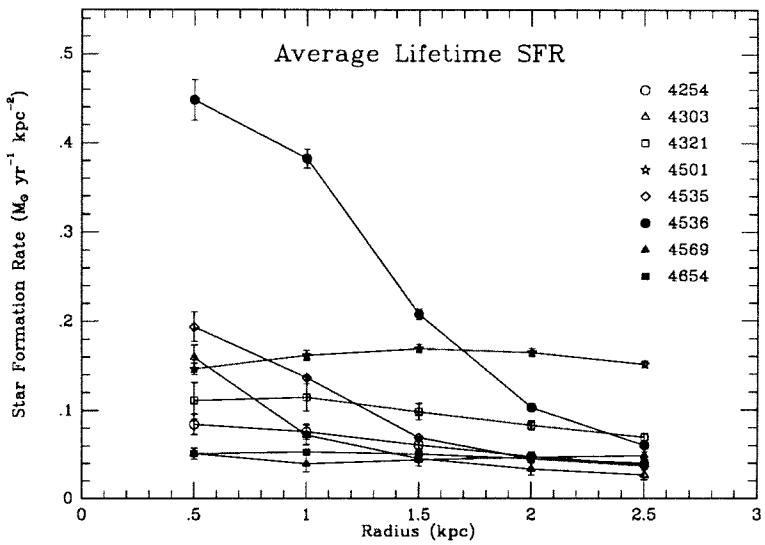


Figure 8–1. Average lifetime star formation rates in radial bins 500 pc wide computed from dynamical masses. Error bars denote the difference between subtracting or not subtracting gas mass; systematic errors due to choice of mass model are much larger.

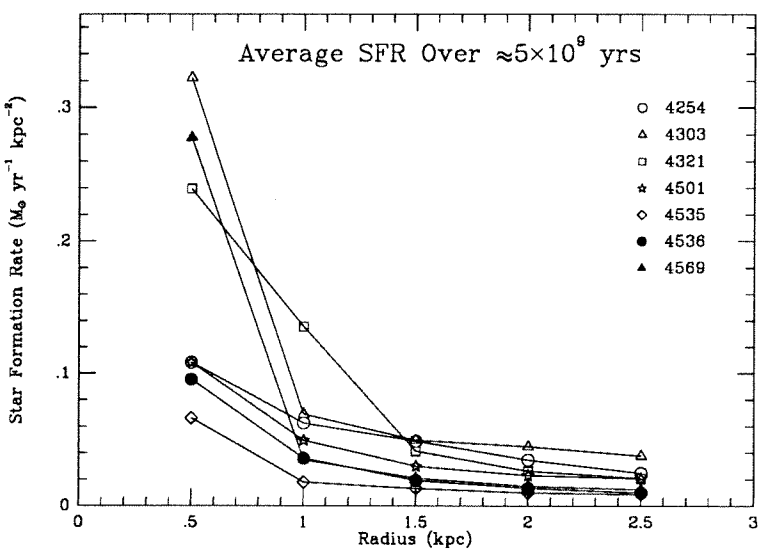


Figure 8–2. Average recent star formation rates over the last $\approx 5 \times 10^9$ years in radial bins 500 pc wide computed from $B$-band radiancies.

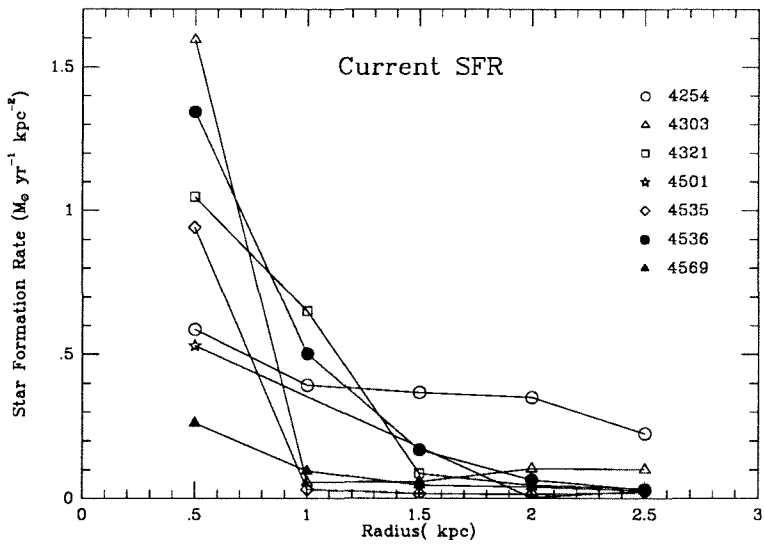


Figure 8–3. Average current star formation rates in radial bins 500 pc wide computed from H$\alpha$ radiancies.

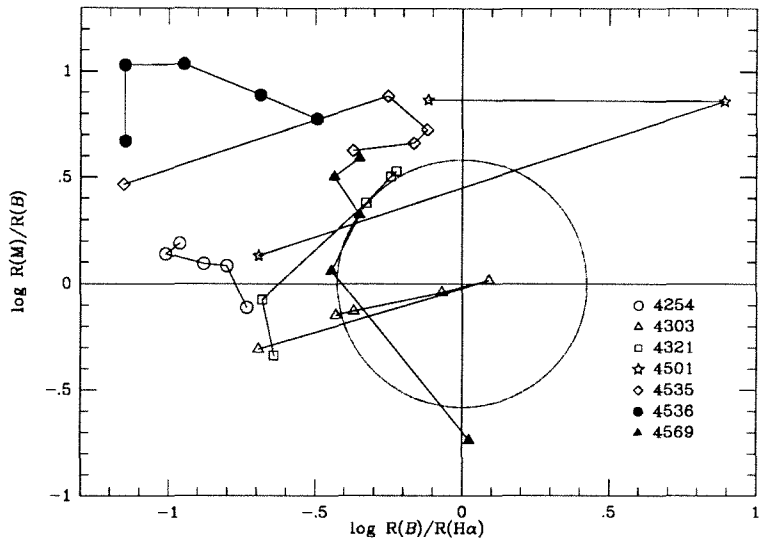


Figure 8–4. Comparative star formation histories. The logarithm of the ratio between average lifetime (from dynamical mass) and recent average (from $L_B$) star formation rates is graphed on the ordinate. The logarithm of the ratio between recent average (from $L_B$) and current (from H$\alpha$) star formation rates is graphed on the abscissa. The dotted circle denotes the size of probable errors in estimating rates; data within the circle are consistent with constant star formation rates.

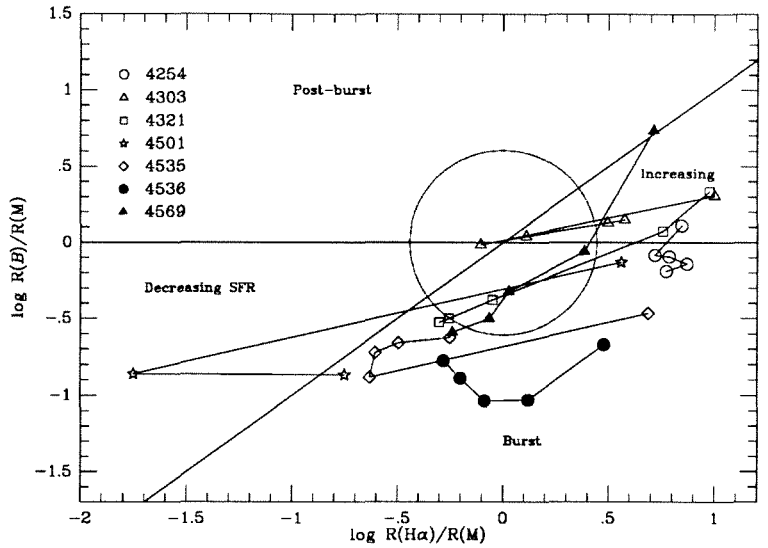


Figure 8–5. Comparative star formation histories. On each axis is graphed the logarithm of the ratio of recent (from $L_B$) or current (from H$\alpha$) star formation rates to the lifetime average rate (from dynamical mass). Labels in the sectors describe the gross star formation history. The dotted circle denotes the size of probable errors in estimating rates; data within the circle are consistent with constant star formation rates.

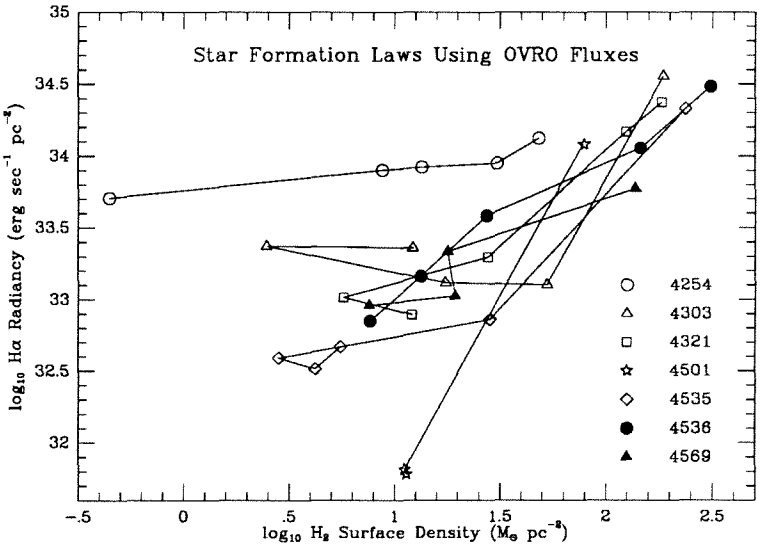


Figure 8–6. Star formation laws relating Hα radiancy to CO emission in interferometer maps.

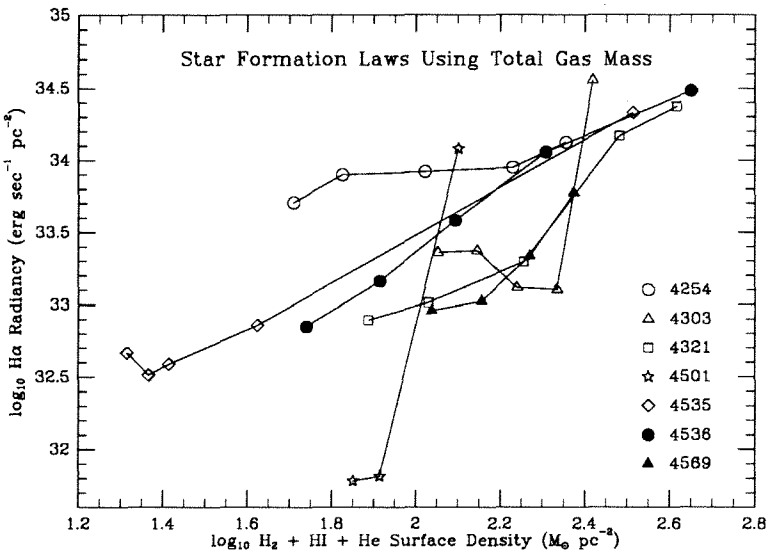


Figure 8–7. Star formation laws relating Hα radiancy to total gas mass.

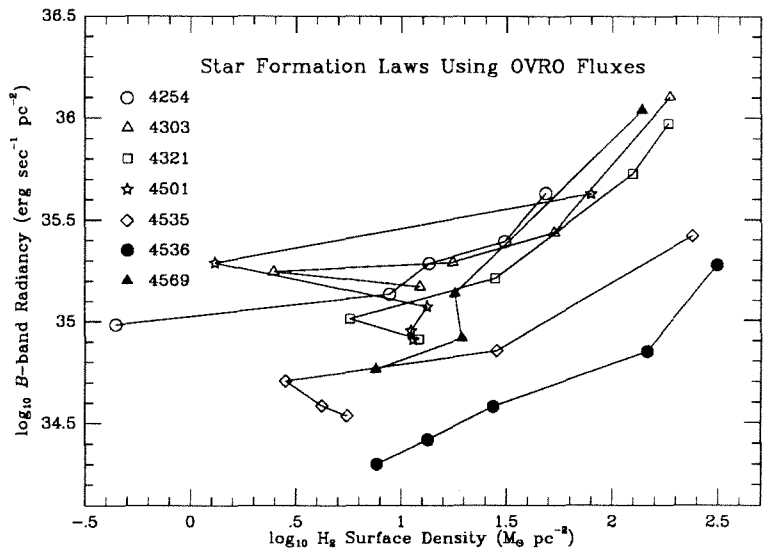


Figure 8–8. Star formation laws relating $B$-band radiancy to CO emission in interferometer maps.

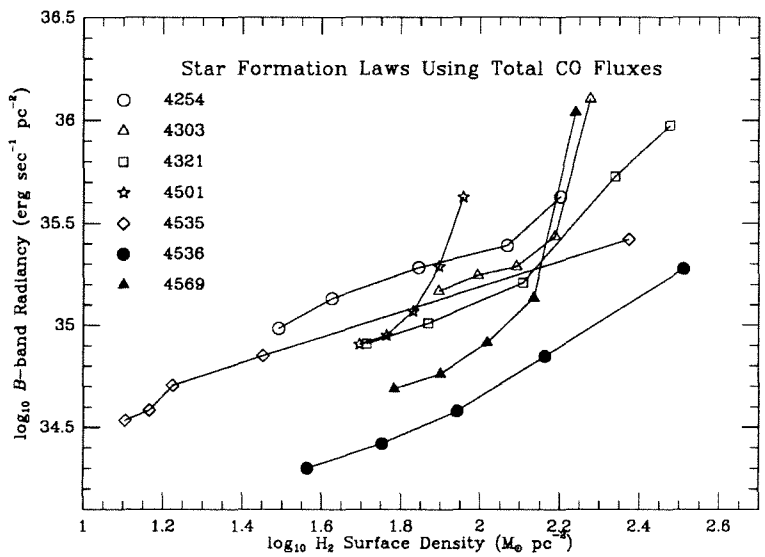


Figure 8–9. Star formation laws relating $B$-band radiancy to total gas mass.

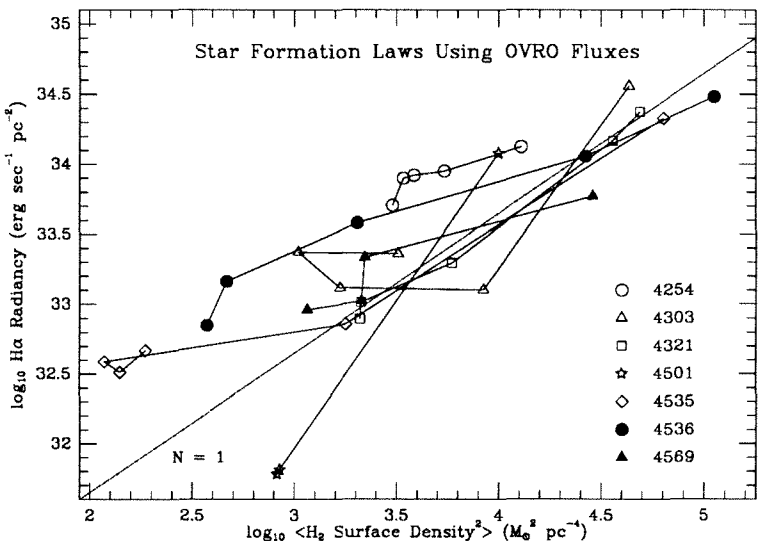


Figure 8–10. Star formation laws relating H$\alpha$ radiancy to mean square CO emission in interferometer maps.

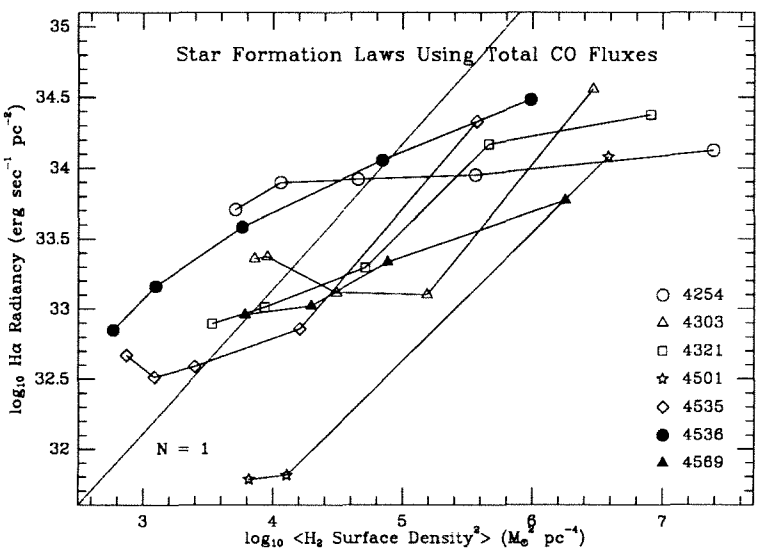


Figure 8–11. Star formation laws relating H$\alpha$ radiancy to mean square total CO emission.

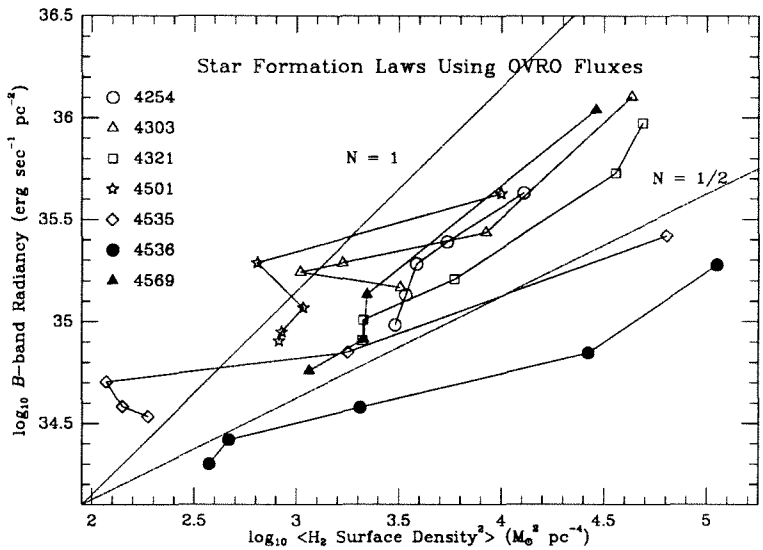


Figure 8–12. Star formation laws relating $B$-band radiancy to mean square CO emission in interferometer maps.

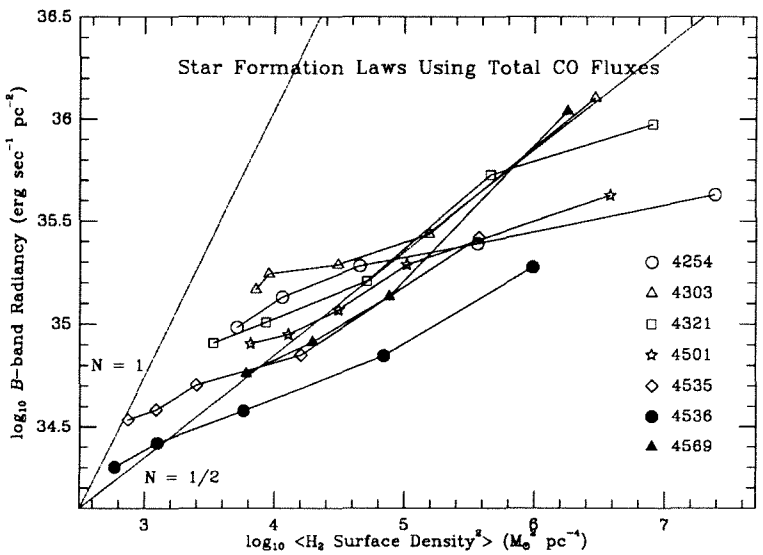


Figure 8–13. Star formation laws relating $B$-band radiancy to mean square total CO emission.

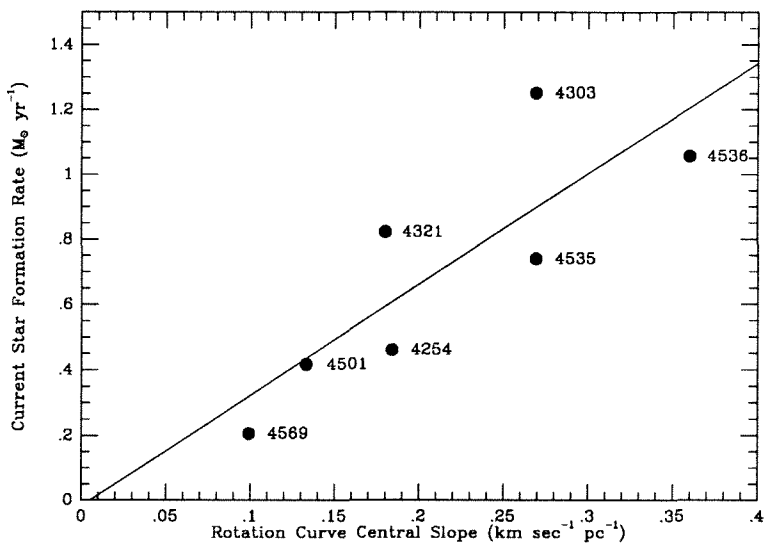


Figure 8–14. Relationship between the slopes of the inner rotation curves and the current central star formation rates (from H$\alpha$) in Virgo spirals.

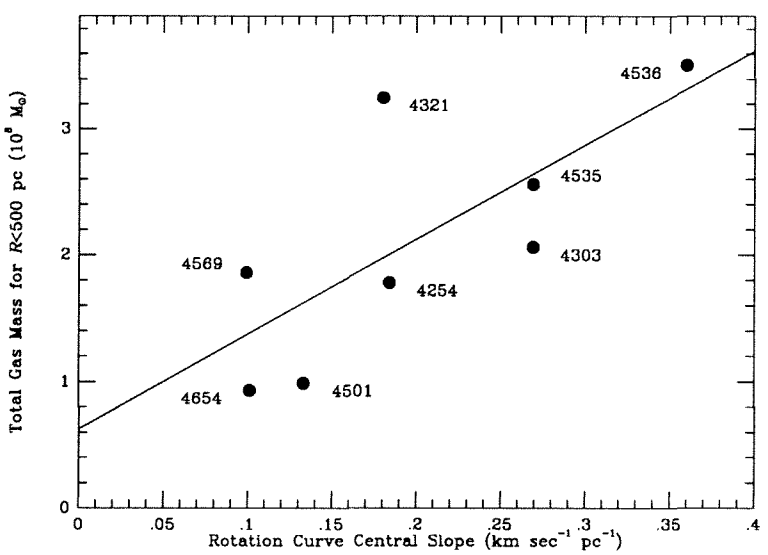


Figure 8–15. Relationship between the slopes of the inner rotation curves and the total gas mass in the central kiloparsec of Virgo spirals.

# Chapter 9
# Summary of Conclusions

Interferometric maps have been made of CO emission from the central regions of eight spiral galaxies of diverse morphological types in the Virgo Cluster. The CO maps show that the most common nuclear molecular gas morphology is a rather featureless, central concentration. There is no obvious connection between the morphological type of a spiral galaxy and the morphology of its nuclear molecular gas. When structure is evident in the nuclear molecular gas, it is generally associated with spiral arms and young stars.

Of considerable impact is the observation that molecular gas masses in the central regions of all of spirals are quite large. Within each annulus of width 500 pc centered on the nucleus, the typical molecular hydrogen mass is $1\text{–}3 \times 10^8$ $M_\odot$. Such masses are comparable with that in the inner kiloparsec of our Galaxy but exceed the amount of molecular gas in our Galaxy at radii from 1 kpc to 2.5 kpc. Molecular hydrogen is by far the dominant gaseous species in the central regions of the spiral galaxies studied. It typically outweighs atomic hydrogen within the same region by factors of 10–30. The area filling factors of molecular clouds in cloud complexes in the nuclear regions of the Virgo spiral galaxies are about 15–50%, which is significantly larger than the area filling factor molecular clouds in the disk of our Galaxy, which is a few percent. Although it may be expected that nuclear molecular clouds are more closely spaced than those in a typical spiral disk, the relatively large area filling factors suggest that some cloud heating is occurring in spiral galaxy nuclei and increasing their CO emissivities. The areal average molecular cloud densities in most of the Virgo spiral

galaxies are 1000–2000 $H_2$ $cm^{-3}$, which is similar to that of the Sgr B2 molecular cloud and other Galactic center molecular clouds.

Using the velocity field information from CO data, rotation curves for the inner disks of the program spirals were constructed. Agreement with optical and H I rotation curves is excellent where there is overlap with CO data. From the rotation curves, the dynamical mass within a given radius may be computed using a mass model, such as a thin disk or a spherically symmetric distribution. Comparison of the gas mass with the dynamical mass indicates that the local gas mass fraction is typically 5–15% at 2.5 kpc radius but generally increases to 15–30% at the centers of the program spirals. Values of the gas mass fraction are made uncertain by the dependence of the dynamical mass on the mass model used, but the total possible variation can be bracketed and indicates an increase of the gas mass fraction toward the center of the spirals. If the stellar mass is spherically distributed near the center of the spirals, then the local volume density of gas in the midplane of the disk could greatly exceed the stellar mass density.

The surprisingly massive gas disks found at the centers of the program spirals are stable against axisymmetric disturbances. Their stability is the result of the velocity dispersion of the gas; cold (dispersionless) disks are violently unstable to axisymmetric disturbances. The velocity dispersion of the gas, estimated from CO line widths corrected for rotational broadening, generally increases toward the centers of most spirals. An increase in the velocity dispersion as great as a factor of four from 2.5 kpc radius to the center is observed.

Despite the apparent stability of such massive gas disks, there is a suggestion that some of the central gas masses may be overestimated. The central gas mass fraction of NGC 4569, for instance, is in the range 30%–130%. The impossible upper estimate derives from the assumption of spherical symmetry for the overall mass distribution,

which is a natural assumption within the bulge of a spiral galaxy. To eliminate this and other alarmingly large central gas mass fractions, either the plausible assumption of a spherically symmetric mass distribution must be discarded, or else it must be admitted that some gas masses have been overestimated.

It is proposed that heating of molecular clouds through dissipation of turbulence increases cloud temperatures substantially in the central kiloparsec regions of some spirals. The increased temperatures would increase the CO emissivities of the molecular clouds and lead to overestimation of gas masses computed in the standard way. The increased velocity dispersions observed at the centers of some spirals supports the hypothesis of cloud heating by turbulence and could lead to gas mass overestimation by factors of two to four.

The molecular gas is frequently concentrated at the centers of spirals within compact structures of very small scale length, only 350–600 parsecs. The very small scale lengths are not artificially created by resolution effects of the interferometer, as demonstrated with analytic modeling. Collection of several $10^8$ $M_\odot$ of molecular gas at the centers of spirals could be due to dynamical friction of giant molecular clouds against disk stars, where the relative speed of the clouds and stars comes about from asymmetric drift. Drag on molecular clouds due to dynamical friction is able to move on the order of 1 $M_\odot$ $yr^{-1}$ of gas into the central region of a typical spiral galaxy. Two other processes which are able to deliver gas to the centers of spirals are gas infall through the transport of angular momentum by spiral density waves and through the kinematic viscosity of molecular clouds. Gas infall rates for these processes are 1–10 $M_\odot$ $yr^{-1}$, which are sufficient to fuel star formation at current rates with extra gas to deposit at the center.

H$\alpha$ emission is often centrally peaked in the program spirals and is usually much more centrally concentrated than the continuum light. Both CO and H$\alpha$ emission

profiles are often similarly peaked and, moreover, the similarity often extends to the detailed morphology as well. There are two reasons for the correspondence. First, simple assumptions about the star formation process imply that more stars are formed where there is more gas. Second, gas is often collected by dynamical processes that also strongly affect its motions. High-mass star formation is probably enhanced through cloud-cloud collisions caused by the dynamical process that organizes the gas structure.

Many galaxies have current rates of star formation that vary approximately as the mean gas surface density, that is, the star formation rate $R \propto \Sigma_{\rm gas}^{N}$, where $N \approx 1$. This relationship holds best when the gas mass is determined from the total CO emission and the star formation rate is determined from $B$-band emission. The exponent $N \approx 1$ is consistent with the notion that intermediate mass star formation occurs stochastically in molecular clouds that are average members of the general cloud population. Very simply, most stars form in proportion to the amount of gas available. Rather steady star formation in clouds could be mainly self-induced through the action of ejecta from young stellar objects (via outflows) or evolved stars (via sweeping by supernova shells). In contrast to the relation between total $H_2$ density and $B$-band emission, the relation between the average molecular hydrogen mass density and the high-mass star formation rate shows evidence for nonlinear behavior.

Although the above simple model of stochastic star formation within molecular clouds probably applies to the general cloud population as a whole, it neglects the important possibility that clouds may interact with each other and stimulate star formation. Such stimulation can come about through cloud-cloud collisions, whose rate could be enhanced through dynamical influences (clumping in spiral arms, for instance), through orbital shear or epicyclic motion, or through an increased velocity dispersion. Star formation in a molecular cloud could also be affected through the

influence of nearby supernovae, for example. Stimulated star formation is expected to dominate in regions of high gas density. The high-resolution data in this thesis are well-suited to study the influence of the *local* concentration of gas on the star formation rate.

It is found that the mean square molecular gas density from interferometer maps of CO emission correlates well with the current high-mass star formation rate in the central regions of Virgo spirals. This result supports a model of stimulated star formation based on the idea that the cloud environment affects the star formation rate within the cloud, since the influences between clouds will be greatest where the molecular gas is most concentrated. Both the hypothesis that high-mass stars are formed as a result of cloud-cloud collisions, and the hypothesis that the local star formation rate is enhanced (through cloud interactions) when the local density of clouds is high, predict for the high-mass star formation rate a quadratic dependence on the local gas density. The recent star formation rate computed from $B$-band emission depends sublinearly on the mean square of the total gas density. This observation may indicate that the stimulated star formation model is not a good description of the star formation process that leads to intermediate mass stars and that the steady, stochastic model of star formation in isolated clouds is more pertinent when comparing total molecular gas mass with the recent, intermediate mass star formation rate.

Based on current star formation rates, the gas at the centers of the Virgo spirals studied will be consumed in a few $10^8$ years. The gas consumption time is consistent with the gas replenishment rates provided by angular momentum transport by spiral waves or by kinematic viscosity of molecular clouds. Dynamical friction is not efficient enough to cause gas infall rates sufficient to fuel the current rates of star formation.

Current star formation rates at the centers of the program spirals are correlated very well with the slopes of the inner (linearly rising) rotation curves. The correlation

is best when only the central kiloparsec region is considered and disappears as larger and larger size regions are included. The central star formation efficiency, that is, the star formation rate per unit gas mass, is independent of the slope of the inner rotation curve. The central gas surface density is also correlated with the slope of the inner rotation curve, which explains the independence of star formation efficiency and rotation curve slope.

The correlation between gas mass surface density and the slope of the inner rotation curve arises because of the physical dependence of angular momentum transport processes (both viscous and spiral wave transport) on the angular speed $\Omega$ or the epicyclic frequency $\kappa$. Both $\Omega$ and $\kappa$ scale linearly with increasing rotation curve slope in the inner region of spirals where rotation curves are linear. In galaxies with steeper inner rotation curves, dynamical processes that lead to gas infall will operate on correspondingly shorter time scales and could lead to greater central concentration of gas. The high-mass star formation rate may be enhanced at the centers of spirals because of the increased frequency of cloud-cloud collisions. Collisions between molecular clouds, which move ballistically until they collide, occur in the disks of spirals because of the random velocities of the clouds. Near the centers of spirals, the epicyclic shaking of clouds in their orbits may become an important process for causing collisions between clouds. An increased rate of high-mass star formation induced by cloud collisions would then occur at the centers of spirals with steeper inner rotation curves.

Star formation efficiencies, defined as the current star formation rate (based on H$\alpha$ emission) per unit molecular gas mass, are generally higher by factors of three to five in the central kiloparsec regions of Virgo spiral galaxies than they are at radii to 2.5 kpc. A possible explanation for these higher star formation efficiencies is a higher rate of cloud-cloud collisions within the central kiloparsec. The collisions may be

driven by the rate of epicyclic shaking, which increases as the center is approached. An alternative explanation for the enhanced central star formation efficiency is that formation of high-mass stars is favored by the nuclear initial mass function. A lower mass cutoff of 0.7–1.5 $M_\odot$ could explain the apparent factor of three to five increase in the central star formation efficiencies based on H$\alpha$ emission.

Star formation rates in the inner 5 kpc of most of the program spirals are consistent, within the uncertainties, with being approximately constant over a Hubble time. Exponentially decreasing rates of star formation, which are commonly assumed to apply to spiral galaxy disks, are not indicated by the data. Star formation in the nuclear regions of Virgo spiral galaxies has apparently benefitted from a continuous influx of gas. Either of the two processes mentioned above for removing angular momentum from the gas, kinematic viscosity or spiral density waves, is efficient enough to induce gas infall rates that can keep pace with the current rate of star formation at the centers of Virgo spiral galaxies. These processes would have been operational as soon as molecular clouds, or spiral density waves, formed in spiral galaxy disks, which is probably shortly after the formation of the galactic disks.

Some of the galaxies show evidence for current or recently finished bursts of star formation in their central 5 kpc regions; moreover, many of them are currently undergoing bursts of star formation in their central kiloparsec regions. Star formation rates in the central regions appear to be influenced primarily by dynamical factors such as the presence of circum-nuclear spiral arms, the number of spiral arms, the strength of the density wave and possible wave modes, the presence of a bar, or (in one case) by the passage of the galaxy near the core of the Virgo cluster. Where strong spiral waves are present or where spiral arms are prominent even near the nucleus, high-mass star formation appears to be most active.

# Appendix A
# Calibration of Broadband Optical Photometry

Since the Landolt (1973, 1983) *RI* photometry is on the Cousins (1976) system, transformation to the Johnson system is necessary. These Cousins-Johnson transformations were already worked out with great precision by Taylor (1986). Then the massive literature of Johnson photometry can be used to derive accurate transformation equations between the Johnson and Thuan-Gunn systems. These Johnson–Thuan-Gunn transformation equations are new results.

The precision of Taylor's equations relating the Johnson and Cousins systems is due to the great literature Taylor drew from and the categorization of transformation equations by the specific color ranges and spectral classifications to which they should be applied. Many of the transformation equations require the interstellar reddening of the star, if it is known.

The extinction $A_\lambda$ at wavelength $\lambda$ can be related to the color excess $E_{B-V}$ using a model of the behavior of interstellar dust grains. van de Hulst's Curve No. 15 (Johnson 1968), shown in Figure A–1, is an excellent model of interstellar extinction as a function of wavelength. The value of the ratio

$$R_\lambda = A_\lambda / E_{B-V} \qquad (A-1)$$

between the extinction $A_\lambda$ at wavelength $\lambda$ and the color excess $E_{B-V}$ is computed from the curve by taking the limit

$$R_\lambda = \lim \frac{E_{\lambda-C}}{E_{B-V}}. \qquad (A-2)$$

Here, the limit is over filterbands $C$ such that $C$ becomes redder and redder. That is, $1/\lambda_{\rm eff}(C) \rightarrow 0$. In practice, a spline fit was made to the curve and the limit

was estimated numerically. Table A–1 shows values of $R_\lambda$ and $1/\lambda_{\rm eff}$ for various broadband filters.

TABLE A–1. EXTINCTION AND COLOR EXCESS

| Band | $\lambda_{\rm eff}$[a] Å | $1/\lambda_{\rm eff}$ $\rm nm^{-1}$ | $R_\lambda$ |
|---|---|---|---|
| $U$ | 3620 | 2.762 | 5.215 |
| $B$ | 4420 | 2.262 | 4.429 |
| $V$ | 5400 | 1.852 | 3.429 |
| $R$ | 6800 | 1.470 | 1.983 |
| $I$ | 8250 | 1.212 | 1.443 |
| $r$ | 6500 | 1.538 | 2.130 |
| $i$ | 8200 | 1.220 | 1.460 |

[a] From Sandage and Smith 1963, and Wade, Hoessel, and Elias 1979.

In order to use the extinction information, the reddening $E_{B-V}$ must be known or estimated. On the assumption that the gas and dust responsible for reddening are distributed like the H I in our Galaxy, Burstein and Heiles (1978) devised and calibrated a method for estimating $E_{B-V}$. The method relies on an H I map of calculated column density over nearly the entire sky (Heiles 1975) and reddening data for RR Lyrae and globular cluster stars. The photometric standard stars used in the work lie over a range $10° \leq |b_I| \leq 50°$ in Galactic latitude. Data used by Burstein and Heiles from this range of positions were used to calibrate the relationship between the atomic hydrogen column density $N_{\rm H\,I}$ and $E_{B-V}$. Linear least squares fits to the

data are adequate; they are

$$E_{B-V} = -0.02398 + (2.813 \times 10^{-4}) N_{\rm H\,I} \pm 0.033 \qquad (A-3)$$

and

$$E_{B-V} = (2.005 \times 10^{-4}) N_{\rm H\,I} \pm 0.034. \qquad (A-4)$$

The unit of column density is that used in Heiles's contour maps, which is $2.23 \times 10^{18}{\rm cm}^{-2}$. Note that equation (A–3) does not pass through zero for $N_{\rm H\,I} = 0$. There is some physical evidence that the curve should not, as expected, pass through zero at $N_{\rm H\,I} = 0$ (Heiles, Stark, and Kulkarni 1981) because of disk emission caught by the beam sidelobes. Equation (A–3) has been adopted for use here because, despite any physical objections, it is purely an interpolatory device. In making the linear fit, all points with $N_{\rm H\,I} > 450$ were omitted. The omission was necessary because of the dogleg and subsequent nonlinear behavior for $N_{\rm H\,I} > 500$. A graph of the subset of the data used, and the adopted linear fit, is shown in Figure A–2. A list of standard stars, values of $N_{\rm H\,I}$ at their positions, and values of $E_{B-V}$ calculated from the first equation above, are shown in Table A–2. Extinction in the various optical bands may be estimated using Table A–1.

When using Taylor's color transformation, the reddening correction is required occasionally. In the cases when the reddening correction is needed, the full correction implied by values in Tables A–1 and A–2 was applied. This approximation is probably not a bad one for the high-lattitude stars. Anyway, the reddening correction enters Taylor's equations with a small coefficient (see below), so the precision of Burstein and Heiles's method is probably wasted. Reddening information was required by Taylor's equations for only one of the two low-latitude stars, SA 98-193, for which such information is lacking.

With color-excess information and Taylor's color transformation equations in hand, Johnson colors and magnitudes may be deduced from Landolt's photometry.

TABLE A–2. REDDENING OF PHOTOMETRIC STANDARDS

| Star | $N_{\rm H\,I}^{a}$ | $E_{B-V}$ | $b_I$ | |
|---|---|---|---|---|
| | | | ° | ′ |
| SA 98-978[b] | ··· | ··· | +0 | 19 |
| SA 98-193[b] | ··· | ··· | 0 | 19 |
| SA 99-6 | 250 | 0.046 | 13 | 45 |
| SA 99-438 | 250 | 0.046 | 14 | 31 |
| HD 72055 | 225 | 0.039 | 18 | 34 |
| SA 100-241 | 125 | 0.011 | 26 | 39 |
| SA 100-280 | 175 | 0.025 | 26 | 53 |
| SA 101-333 | 175 | 0.025 | 40 | 02 |
| SA 101-282 | 175 | 0.025 | 40 | 06 |
| BD + 1°2447 | 225 | 0.039 | 47 | 08 |
| G162-66 | 275 | 0.053 | 38 | 55 |
| SA 107-970 | 350 | 0.074 | 41 | 34 |
| SA 107-1006 | 350 | 0.074 | 41 | 18 |
| SA 108-551 | 400 | 0.089 | 28 | 38 |

[a] Units are $2.23 \times 10^{18}\mathrm{cm}^{-2}$.

[b] Latitude out of range of maps by Heiles (1975).

The equations from Taylor (1986) used in this work are:

$$(R-I)_J = 1.109\,(R-I)_C + 0.096\,\delta_{BJ}(U-B) - 0.081 + C_1 \qquad (A-5)$$

$$(R-I)_J = 1.313\,(R-I)_C + 0.096\,\delta_{BJ}(U-B) - 0.097 + C_1 \qquad (A-6)$$

$$\delta_{BJ}(U-B) = \begin{cases} (U-B)_0 - 1.378(B-V)_0 + 0.709; \\ 0, \text{ G2 and later spectral type, or if } \delta_{BJ} < 0. \end{cases}$$

$$(R-I)_J = 1.070(R-I)_C + 0.032 + C_1 \qquad (A-7)$$

$$C_1 = \begin{cases} -0.009, & 5400 < \text{HR number} < 7200; \\ 0, & \text{otherwise.} \end{cases}$$

$$(R-I)_J = 1.023(R-I)_C + 0.012 \qquad (A-8)$$

$$(V-R)_J = 1.394(V-R)_C + \alpha + C_2 \qquad (A-9)$$

$$\alpha = \begin{cases} 0.030, & \text{for standard limits;} \\ 0.036, & -0.020 < (V-R)_C < -0.012 \text{ or} \\ & 0.414 < (V-R)_C < 0.463. \end{cases}$$

$$(V-R)_J = 1.394(V-R)_C + \beta + C_2 \qquad (A-10)$$

$$\beta = \begin{cases} 0.042, & \text{for standard limits;} \\ 0.036, & -0.020 < (V-R)_C < -0.012 \text{ or} \\ & 0.414 < (V-R)_C < 0.463. \end{cases}$$

$$(V-R)_J = 1.80(V-R)_C - 0.029 + C_2 \qquad (A-11)$$

$$C_2 = \begin{cases} -0.018, & \text{HR number} > 4700; \\ 0, & \text{otherwise.} \end{cases}$$

$$(V-R)_J = 1.59(V-R)_C - 0.11 \qquad (A-12)$$

The subscripts "J" and "C" refer to "Johnson" and "Cousins," respectively. $(U-B)_0$ and $(B-V)_0$ are colors corrected for reddening using the method of Burstein and Heiles. The range of color and the luminosity class to which each equation may be applied is quoted in Table A–3.

The general equations for all luminosity classes apply except where there is another equation for a specific luminosity class with the requisite color range. The range refers to limits on the independent variable in the indicated equation. Where a constant $C_1$ or $C_2$ is added, or where a reddening correction is made, the reddening correction should be made first or the constant subtracted first. Then the limits should be checked for applicability. Johnson colors can be deduced from equations A–5 through A–12, given information from the preceding tables. The Johnson colors

TABLE A–3. APPLICABILITY OF JOHNSON-COUSINS EQUATIONS

| Eq. No. | Lum. Class | Range |
|---|---|---|
| 5 | All | ..., 0.078 |
| 6 | All | 0.078, 0.531 |
| 7 | III | 0.531, 1.40 |
| 8 | V | 0.376, 2.00 |
| 9 | All | ..., −0.020 and 0.463, 0.788 |
| 10 | All | −0.012, 0.414 |
| 11 | III | 0.788, 1.10 |
| 12 | V | 0.70, 1.23 |

for photometric standard stars used in this work are listed in Table A–4, along with the equation number used to make the conversion.

Since observations were made using Thuan-Gunn $r$ and $i$ filters and not Johnson $R$ and $I$, transformation equations had to be worked out. For this purpose, the literature was culled for photometry of bright stars on both the Johnson system (Johnson *et al.* 1966) and the Thuan-Gunn system (Wade, Hoessel and Elias 1979). The data are listed in Table A–5.

The transformation equations relating Johnson $R$ and $I$ to Thuan-Gunn $r$ and $i$ worked out using least squares fitting to data from Table A–5 are:

$$\begin{aligned} R &= -0.474 + 0.994r - 0.298(r-i) \pm 0.027 \\ r &= \quad 0.403 + 1.006R + 0.231(R-I) \pm 0.028 \end{aligned} \qquad (A-13)$$

$$\begin{aligned} I &= -0.834 + 1.000i - 0.594(r-i) \pm 0.031 \\ i &= \quad 0.678 + 1.001I + 0.462(R-I) \pm 0.028 \end{aligned} \qquad (A-14)$$

TABLE A–4. JOHNSON COLORS[a]

| Star | Sp. | Eq. No. | $V$ | $B-V$ | $U-B$ | $V-R$ | $R-I$ |
|---|---|---|---|---|---|---|---|
| SA98-978 | G3 | 6,10 | 10.576 | 0.606 | 0.103 | 0.531 | 0.324 |
| SA98-193 | G8 | 8,9 | 10.027 | 1.175 | 1.163 | 0.889 | 0.561[b] |
| SA99-6 | G7 | 8,9 | 11.054 | 1.249 | 1.287 | 0.939 | 0.602[b] |
| SA99-438 | B7 | 5,9 | 9.399 | −0.155 | −0.719 | −0.054 | −0.155 |
| HD72055 | B8 | 5,9 | 8.113 | −0.137 | −0.460 | −0.013 | −0.103[c] |
| SA100-241 | A0 | 6,10 | 10.140 | 0.156 | 0.102 | 0.149 | 0.074 |
| SA100-280 | F5 | 6,10 | 11.802 | 0.496 | 0.009 | 0.453 | 0.294 |
| SA101-333 | K3 III | 7,11 | 7.835 | 1.485 | 1.787 | 1.141 | 0.811 |
| SA101-282 | F2 | 6,10 | 10.002 | 0.429 | 0.010 | 0.404 | 0.255 |
| BD + 1°2447 | M2.5V | 8,12 | 9.652 | 1.509 | 1.238 | 1.550 | 1.266 |
| G162-66 | | 5,9 | 13.015 | −0.174 | −0.982 | −0.146 | −0.232[c] |
| SA107-970 | K3 | 8,12 | 10.910 | 1.604 | 1.788 | 1.709 | 1.471 |
| SA107-1006 | G3 | 6,9 | 11.715 | 0.764 | 0.285 | 0.631 | 0.445 |
| SA108-551 | A0 | 6,10 | 10.705 | 0.175 | 0.180 | 0.159 | 0.094 |

[a] Based on Landolt (1983). The author has presented strong evidence that his system is on the original $UBV$ system.
[b] Assumes luminosity class V.
[c] Color exceeded limits of range of applicabiality of transformation equation.

$$\begin{aligned} R-I &= \quad 0.330 + 1.293(r-i) \pm 0.016 \\ r-i &= -0.255 + 0.770(R-I) \pm 0.013 \end{aligned} \qquad (A-15)$$

The data were far too few to attempt a categorization of transformation equations by color and luminosity class as Taylor did. The above equations suffice for the accuracy required of this work in deducing galaxy fluxes. With the above equations, the photometry from Landolt (1983), and information from Table A–4, magnitudes

TABLE A–5. RELATING JOHNSON AND THUAN-GUNN SYSTEMS

| Name (HR) | Sp. | $i$ | $r-i$ | $R$ | $R-I$ |
|---|---|---|---|---|---|
| 166 | K0 V | 5.66 | 0.07 | 5.21 | 0.39 |
| 493 | K1 V | 5.02 | 0.08 | 4.55 | 0.43 |
| 753 | K3 V | 5.39 | 0.15 | 4.99 | 0.53 |
| 801 | B3 V | 5.45 | −0.35 | 4.69 | −0.13 |
| 1380 | A7.5 V | 5.30 | −0.20 | 4.64 | 0.07 |
| 1748 | B1.5 V | 7.09 | −0.36 | 6.34 | −0.14 |
| 5105 | A2p | 5.56 | −0.29 | 4.86 | −0.03 |
| 5351 | A0p | 4.75 | −0.23 | 4.16 | 0.03 |
| 6070 | A0 V | 5.46 | −0.29 | 4.69 | −0.05 |
| 6161 | B9 IV | 5.66 | −0.30 | 4.96 | −0.02 |
| 6436 | A2 V | 5.25 | −0.26 | 4.57 | 0.00 |
| 6685 | F2 Ia | 5.67 | −0.10 | 5.13 | 0.21 |
| 6779 | B9.5 III | 4.51 | −0.27 | 3.80 | 0.00 |
| 6806 | K2 V | 6.08 | 0.12 | 5.63 | 0.49 |
| 7565 | B3 Ve | 5.78 | −0.37 | 4.98 | −0.14 |
| 7741 | G2 Ib | 4.84 | 0.13 | 4.41 | 0.48 |
| 7767 | O8 | 6.34 | −0.23 | 5.69 | 0.01 |
| 7847 | F5 Iab | 5.65 | 0.26 | 5.33 | 0.69 |
| 8585 | A2 V | 4.45 | −0.27 | 3.77 | −0.03 |
| 8808 | B3 V | 6.92 | −0.28 | 6.20 | −0.06 |
| 8832 | K3 V | 5.13 | 0.15 | 4.74 | 0.53 |

of the photometric standards may be calculated or quoted. These magnitudes are listed in Table A–6.

Calibration of the broadband optical frames was accomplished by constructing linear least squares fits of instrumental magnitudes and colors to the photometric standard stars' magnitudes. The instrumental magnitude in filter band $M$ is

$$M_{\rm inst} = -2.5 \log \left( \frac{\rm DN - sky}{\rm exposure} \right) - K_M \sec Z, \qquad (A-16)$$

where DN is the total counts in a pixel, "sky" is the estimate of the DN for the background, "exposure" is in seconds, $K_M$ is the K-correction in the $M$ band, and

$\sec Z$ is approximately the airmass for small $Z$. K-corrections for Palomar are 0.20, 0.14, 0.10, and 0.05 in $B$, $V$, $r$, and $i$ bands, respectively. Linear least square fits for magnitudes and colors were made separately for each night of observing. The coefficients of the fits and the associated errors are listed in Table A–7. The linear approximations have the following forms:

$$M = a + b\,M_{\rm inst} + c\,C_{\rm inst},$$
$$C = d + e\,C_{\rm inst}. \qquad (A-17)$$

$a, b, \ldots, e$ are numerical coefficients. $M$ refers to the magnitude in a particular filter-band, and $C$ refers to a color. For instance, in $B$ or $V$ band ($M \Rightarrow B$ or $M \Rightarrow V$), $C \Rightarrow B - V$ color; in $r$ or $i$ band, $C \Rightarrow r - i$. The "inst" subscript refers to the instrumental magnitude or color.

TABLE A–6. MAGNITUDES OF STANDARDS

| Star | $B$ | $V$ | $r$ | $i$ |
|---|---|---|---|---|
| SA98-978 | 11.182 | 10.576 | 10.578 | 10.562 |
| SA98-193 | 11.202 | 10.027 | 9.721 | 9.526 |
| SA99-6 | 12.303 | 11.054 | 10.712 | 10.482 |
| SA99-438 | 9.244 | 9.399 | 9.872 | 10.227 |
| HD72055 | 7.976 | 8.113 | 8.550 | 8.870 |
| SA100-241 | 10.296 | 10.140 | 10.466 | 10.642 |
| SA100-280 | 12.298 | 11.802 | 11.882 | 11.883 |
| SA101-333 | 9.320 | 7.835 | 7.321 | 6.943 |
| SA101-282 | 10.431 | 10.002 | 10.113 | 10.151 |
| BD + 1°2447 | 11.161 | 9.652 | 8.841 | 8.108 |
| G162-66 | 12.841 | 13.015 | 13.583 | 13.982 |
| SA107-970 | 12.514 | 10.910 | 9.994 | 9.098 |
| SA107-1006 | 12.479 | 11.715 | 11.651 | 11.537 |
| SA108-551 | 10.880 | 10.705 | 11.029 | 11.187 |

The errors quoted in the "$\sigma$" column are the $1\sigma$ formal errors of the fit. The last section of the table refers to "Night 3–5 hybrid." This unorthodox calibration was

TABLE A–7. PHOTOMETRIC CALIBRATION

| Filter/Color | $a$ | $b$ | $c$ | $d$ | $e$ | $\sigma$ |
|---|---|---|---|---|---|---|
| | | | **Night 1** | | | |
| $B$ | 21.767 | 0.958 | 0.257 | | | 0.029 |
| $V$ | 22.345 | 0.952 | 0.052 | | | 0.084 |
| $r$ | 22.440 | 0.968 | −0.183 | | | 0.060 |
| $i$ | 21.671 | 0.962 | −0.057 | | | 0.013 |
| $B-V$ | | | | −0.648 | 1.161 | 0.048 |
| $r-i$ | | | | 0.692 | 0.833 | 0.051 |
| | | | **Night 2** | | | |
| $B$ | 22.398 | 1.004 | 0.244 | | | 0.078 |
| $V$ | 22.940 | 0.994 | 0.055 | | | 0.034 |
| $r$ | 23.032 | 1.007 | −0.122 | | | 0.044 |
| $i$ | 22.363 | 1.010 | 0.034 | | | 0.051 |
| $B-V$ | | | | −0.673 | 1.193 | 0.049 |
| $r-i$ | | | | 0.710 | 0.856 | 0.061 |
| | | | **Night 3** | | | |
| $B$ | 22.351 | 1.011 | 0.252 | | | 0.093 |
| $V$ | 22.978 | 1.002 | 0.048 | | | 0.057 |
| $r$ | 23.164 | 1.022 | −0.106 | | | 0.048 |
| $i$ | 21.901 | 0.977 | −0.008 | | | 0.059 |
| $B-V$ | | | | −0.750 | 1.219 | 0.034 |
| $r-i$ | | | | 0.713 | 0.862 | 0.055 |
| | | | **Night 5** | | | |
| $B$ | 22.293 | 0.996 | 0.256 | | | 0.052 |
| $V$ | 23.038 | 1.008 | 0.080 | | | 0.034 |
| $r$ | 22.101 | 0.999 | −0.369 | | | 0.041 |
| $i$ | 23.342 | 1.012 | 0.090 | | | 0.051 |
| $B-V$ | | | | −0.606 | 1.190 | 0.027 |
| $r-i$ | | | | 0.666 | 0.810 | 0.040 |
| | | | **Night 3–5 Hybrid** | | | |
| $r_3$ | 22.608 | 0.976 | −0.154 | | | 0.031 |
| $i_5$ | 21.158 | 0.917 | −0.107 | | | 0.032 |
| $r_3-i_5$ | | | | 0.703 | 0.804 | 0.025 |

necessary for NGC 4569. None of the $i$ images from Night 3 was written to disk;

fortunately, $i$ images were made again on Night 5. Photometric standards observed both nights were used to make the calibration.

The calibration from Table A–7 was applied to sky-subtracted, cleaned, flattened, and registered frames using FIGARO modules ICMULT, IADD, ISUB, and ILOG in the obvious way. The constant $0.579716 = 5 \log 1.306$ was added to all frames to convert mag pixel$^{-1}$ to mag arcsec$^{-2}$. The pixel size, $1.306 \pm 0.004$ arcsec$^2$, is the mean of 18 measurements spanning four nights of observing.

## References

Burstein, D., and Heiles, C. 1978, *Ap. J.*, **225**, 40.

Cousins, A. W. J. 1976, *Mem. R. Astron. Soc.*, **81**, 25.

Heiles, C. 1975, *Astron. Astrophys. Suppl.*, **20**, 37.

Heiles, C., Stark, A. A., and Kulkarni, S. 1981, *Ap. J. (Letters)*, **247**, L73.

Johnson, H. L., Mitchell, R. I., Irarte, B., and Wisniewski, W. Z. 1966, *Comm. Lunar Planet. Lab.*, **4**, 99.

Johnson, H. L. 1968, *Nebulae and Interstellar Matter* (Chicago: University of Chicago Press), p. 167.

Landolt, A. U. 1973, *A. J.*, **78**, 959.

Landolt, A. U. 1983, *A. J.*, **88**, 439.

Sandage, A., and Smith, L. L. 1963, *Ap. J.*, **137**, 1057.

Taylor, B. J. 1986, *Ap. J. Suppl.*, **60**, 577.

Wade, R. A., Hoessel, J. G., and Elias, J. H. 1979, *P.A.S.P.*, **91**, 35.

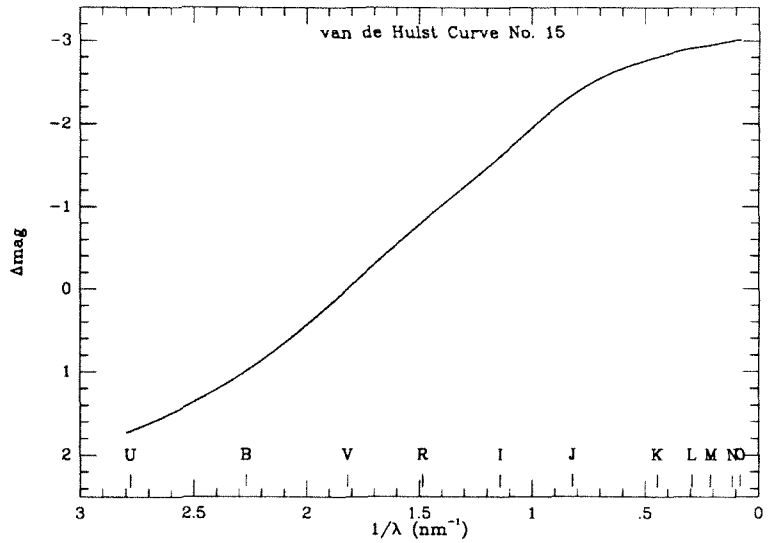


Figure A–1. van de Hulst's Curve No. 15, showing color excess as a function of reciprocal wavelength.

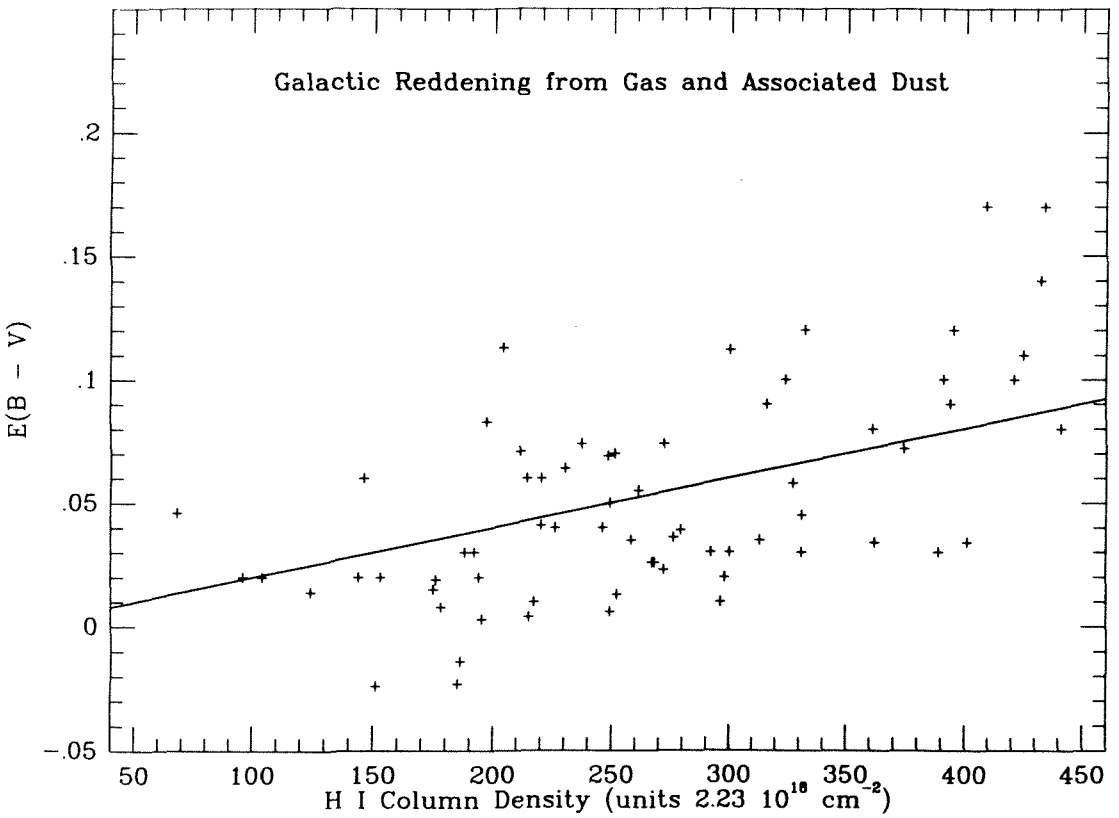


Figure A–2. Relation between extinction and H I column density (Burstein and Heiles 1978).

# Appendix B
# Calibration of Narrowband Hα Imagery

Hα CCD imaging of Virgo spirals was done using narrowband filters. Three filters were used in the imaging; their transmission curves are shown in Figure 3–2. Hα emission from a galaxy was typically strongest in the central filter, and imagery in the adjacent filters provided estimates of the nearby continuum emission.

The width of Hα λ6563 Å line emission from a typical bright spiral galaxy is only about 11 Å assuming that the width is due to rotation of the galaxy. Since the filters all have widths FWHM $\approx$ 80 Å, it is clear that a substantial portion of the flux passed by such a filter is continuum emission. The photometrist's problem is to isolate the Hα emission from the continuum. For example, say that the galaxy observed has a recession velocity which places the Hα λ6563 line at $\lambda_0$. Let the transmission profile of the filter centered on the Hα emission be denoted by the function $F_0(\lambda)$, and say the line profile is represented by the function $\mathcal{L}(\lambda)$. Denote by $C(\lambda)$ the value of the continuum, which is assumed to be slowly varying over the range of all three filter bandpasses. Then the spectrum of the galaxy in the neighborhood of the filter bandpasses is $C(\lambda) + \mathcal{L}(\lambda)$. The spectrum of radiation which is passed by filter $j$ is $[C(\lambda) + \mathcal{L}(\lambda)]\, F_j(\lambda)$. The other two filters will be denoted by $F_L(\lambda)$ and $F_U(\lambda)$, for the filter with bandpasses at wavelengths smaller and larger, respectively, than $\lambda_0$. The total power passed by filter $j$ is

$$I_j/\tau_j = \int [C(\lambda) + \mathcal{L}(\lambda)]\, F_j(\lambda)\, d\lambda, \qquad (B-1)$$

where $\tau_j$ is the integration time of the exposure through filter $j$. It is the object of the following calibration procedure to extract the quantity $\int \mathcal{L}(\lambda)\, d\lambda$ from the

photometry.

Since the $F_L$ and $F_U$ filters are nearby in wavelength, they do not necessarily completely exclude Hα emission from the galaxy from the radiation they pass. But $\mathcal{L}(\lambda)$ is a very peaked function with small support compared with the support of any of the filter functions. The effect of multiplying by $\mathcal{L}$ under the integral is like that of a delta function. Therefore, some approximations can be made which simplify the representation of the total energy passed through any of the filters. Let $\overline{F}_j$ be the mean value of $F_j(\lambda)$ in the neighborhood of $\lambda_0$. The total power $I_j$ passed by the $F_j$ filter can then be approximated

$$I_j/\tau_j \approx \overline{C}W_j + \overline{F}_j \int \mathcal{L}(\lambda)\, d\lambda, \qquad (B-2)$$

where $W_j$ is the equivalent width of the $F_j$ filter

$$W_j = \int F_j(\lambda)\, d\lambda \qquad (B-3)$$

and where $\overline{C}$ is the mean value of $C(\lambda)$ in the neighborhood of $\lambda_0$.

With the assumption that $\overline{C}_L \approx \overline{C}_U$, the total power equations for the two continuum filters can be solved for the value $\overline{C}$ of the continuum. The result is

$$\overline{C} \approx \frac{I_U/\tau_U\overline{F}_U - I_L/\tau_L\overline{F}_L}{W_U/\overline{F}_U - W_L/\overline{F}_L}. \qquad (B-4)$$

The Hα emission power is computed by subtracting the continuum power from the power passed by the central filter:

$$\int \mathcal{L}(\lambda)\, d\lambda \approx \frac{I_0}{\overline{F}_0\tau_0} - \frac{W_0}{\overline{F}_0\tau_0} \cdot \frac{I_U/\tau_U\overline{F}_U - I_L/\tau_L\overline{F}_L}{W_U/\overline{F}_U - W_L/\overline{F}_L}. \qquad (B-5)$$

In the case that an image was made through only one of the two continuum filters (or the specific case of NGC 4569, whose discrepant recession velocity places its Hα emission within the $F_L$ filter), a simpler expression applies. This time, the two

total power equations are solved for $\int \mathcal{L}(\lambda)\, d\lambda$ with the assumption that the continuum power is approximately equal within the two filter passbands. The following expression applies:

$$\int \mathcal{L}(\lambda)\, d\lambda \approx \frac{I_0/\tau_0 W_0 - I_1/\tau_1 W_1}{\overline{F}_0/W_0 - \overline{F}_1/W_1}. \qquad (B-6)$$

The profiles of the filters shown in Figure 3–2 were obtained using a Cary 17 spectrometer. The wavelengths of redshifted Hα corresponding to the recession velocities of the Virgo spirals are shown on the horizontal scale. Mean values of the filter transmission functions $F_j(\lambda)$ over 11 Å (corresponding to $500\,\mathrm{km\,sec^{-1}}$) were calculated from these curves for each of the galaxies. These numbers are shown in Table B–1, where the three filters are named "6563," "6600," and "6675" corresponding to their approximate centroids. The recessional velocities $V_{\mathrm{LSR}}$ are those at which the galaxies were observed at with the OVRO mm-wave interferometer. The systemic velocities determined by dynamical analysis of the OVRO data may be slightly different.

TABLE B–1. FILTER RESPONSES AT REDSHIFTED Hα

| Object NGC | $V_{\mathrm{LSR}}$ $\mathrm{km\,sec^{-1}}$ | $\overline{F}_{6563}$ | $\overline{F}_{6600}$ | $\overline{F}_{6675}$ |
|---|---|---|---|---|
| 4254 | +2419 | 0.1244 | 0.7166 | 0.4156 |
| 4303 | +1564 | 0.5018 | 0.7430 | 0.0649 |
| 4321 | +1571 | 0.4972 | 0.7425 | 0.0663 |
| 4501 | +2205 | 0.1866 | 0.7188 | 0.2838 |
| 4535 | +1966 | 0.2914 | 0.7240 | 0.1673 |
| 4536 | +1793 | 0.3799 | 0.7306 | 0.1126 |
| 4569 | −198 | 0.7338 | 0.3324 | 0.0000 |
| 4654 | +1075 | 0.6842 | 0.7605 | 0.0208 |

The standard stars which were observed as a part of the flux calibration are HD 42618 and HD 60298 at the suggestion of Greg Bothun. They are classed as G4V and G2V, respectively. No spectra of these stars were obtained. Instead, the well-known spectrum of the Sun was used to provide approximate spectral energy

distributions for these stars. The spectrum of the Sun from Kurucz *et al.* (1984) was numerically transcribed, taking into account all major absorption lines from λ6440.8Å to λ6750.5Å. The spectrum resulting from the transcription is shown in Figure B–1. The solar spectrum atlas consists of tabulated values of the continuum and graphs of the "residual," the line shape with the continuum baseline subtracted. The number of absorption lines excluded from the numerical transcription was estimated by counting all lines whose ("residual") absorption depth was between 1% and 5% (all lines with depth greater than 5% were transcribed). The number of lines excluded was 169. The mean ("residual") equivalent width of an excluded line was approximately 0.005Å. Over the entire range surveyed, these excluded lines would contribute approximately 0.845Å ("residual") equivalent width to the total absorption. The total integrated ("residual") absorption computed over the entire spectral range surveyed is 10.109Å, so the error introduced by missing lines is about 8%. The filter transmission functions were multiplied by the solar spectrum (continuum plus residual) to arrive at the total flux density expected to be passed by each filter. The values of the integrated flux density $I$ from the Sun through each filter are tabulated in Table B–2. The units are $\mu\mathrm{W\,cm^{-2}}$ at earth outside the atmosphere. Integrals of the filter functions yielded their equivalent widths $W_{eq}$. These equivalent widths, in Angstroms, are also reported in Table B–2.

TABLE B–2. TRANSMISSION PROPERTIES OF FILTERS

| | Filter (approximate center) | | |
|---|---|---|---|
| | λ6563 | λ6600 | λ6675 |
| $I$ ($\mu\mathrm{W\,cm^{-2}}$) | 997.70 | 931.96 | 913.858 |
| $W_{\mathrm{eq}}$ (Å) | 65.597 | 60.888 | 58.418 |

The stars used for calibration, HD42618 and HD60298, have properties which are found in the SAO catalogue or Hirshfeld and Sinnott (1982). These properties are

shown in Table B–3 along with various properties of the Sun for comparison. To complete the flux calibration scale, it is assumed that the luminosity of these stars in the spectral region around Hα scales by a factor Λ corresponding to the difference between their absolute magnitude and that of the Sun. Since $R$ photometry of HD42618 existed in the literature (Moffett and Barnes 1980), the scaling for HD42618 used the difference in $R$ magnitude with the Sun ($M_{R\odot} = +4.31$ from Allen 1973). No $R$ photometry for HD60298 could be found in the literature, so its scaling was determined from the difference in $V$ magnitude with the Sun ($M_{V\odot} = +4.83$, from Allen 1973). The magnitudes of these stars, along with the assumed luminosity scaling factor, Λ, and the distances to these stars, are quoted.

TABLE B–3. FLUX CALIBRATION STAR PROPERTIES

| | SAO | $\alpha_{1950}$ h m s | $\delta_{1950}$ ° ′ ″ | Sp | $D_{\rm pc}$ | $M_V$ | $M_R$ | Λ |
|---|---|---|---|---|---|---|---|---|
| HD42618 | 113580 | 06 09 18.2 | +06 47 58 | G4V | 26 | +5.0 | +4.234 | $1.073\,L_\odot$ |
| HD60298 | 79521 | 07 31 47.6 | +25 04 10 | G2V | 31 | +4.7 | | $1.127\,L_\odot$ |
| Sun | | | | G2V | | +4.83 | +4.31 | |

The absolute flux calibration of the image recorded by the CCD on earth is accomplished by equating the total energy from the Sun with the total number of counts which would be detected from the calibration star in the absence of atmospheric absorption if a sphere at the distance of the earth were surrounded with similar detectors. The total luminosity of the Sun in a spectral range determined by filter $j$ is $4\pi D_\oplus^2 I_j$, where $D_\oplus$ is the distance from the earth to the Sun. Multiply this expression by a factor Λ to obtain the total luminosity of a calibration star. The total count luminosity over $4\pi$ steradians from a calibration star is $(16\pi D_*^2/\pi a^2)\,\frac{\#\ \text{counts}}{\tau}$, where $D_*$ is the distance to the star, $a$ is the diameter of the aperture gathering photons,

and $\tau$ is the exposure time. The calibration factor is thus

$$\xi_j = \frac{4\pi D_\oplus^2 \; \Lambda I_j \; \pi a^2}{16\pi D_*^2 \; \frac{\#\text{counts}}{\tau}} = \frac{\pi}{4} a^2 \Lambda I_j \frac{\tau}{\#\text{ counts}} \frac{D_\oplus^2}{D_*^2}. \qquad (B-7)$$

To convert counts $\sec^{-1}$ pixel$^{-1}$ to erg $\sec^{-1}$ pixel$^{-1}$, multiply by

$$\xi_j = (1.846 \times 10^{-10}) \frac{\Lambda I_j a_{\rm cm}^2}{D_{\rm pc}^2} \frac{\tau}{\#\text{ counts}}, \qquad (B-8)$$

where $D_{\rm pc}$ is the distance to the star in parsecs, $a_{\rm cm}$ is the aperture diameter in centimeters, and $\Lambda$ is the luminosity of the calibration star in the $I_j$ passband in units of solar luminosities. To correct for atmospheric extinction, Beer's law is applied in the form of a simple $\sec Z$ dependence on $Z$, the zenith angle. The conversion factor $\xi_j'$ from erg $\sec^{-1}$ pixel$^{-1}$ on earth to erg $\sec^{-1}$ pixel$^{-1}$ *outside* the earth's atmosphere is

$$\xi_j' = \xi_j \cdot 10^{0.4 K_{\rm H\alpha} \sec Z}. \qquad (B-9)$$

$K_{\rm H\alpha}$ is the so-called $K$-correction near the wavelength of H$\alpha$. $K_{\rm H\alpha} = 0.08$ is the value used in this analysis for Palomar. Values of $\sec Z$ were recorded during the time of observation in a log book and were also (nearly always) written to the data headers. The number of sky-subtracted counts for each star on each night is shown with the $\sec Z$ values in Table B–4. The exposure times in seconds are also listed. Note that not all nights had viable observations of both standard stars.

The largest source of error in the determination of the conversion factor is the discrepancy between the two standards, about 10%. The internal dispersion among the three values for each star is much smaller than the difference between the mean values for each star. The source of this error is most likely due to the stars' energy output not being what is expected based on scaling by their absolute magnitudes and the unknown Galactic extinction. A smaller source of error concerns the fact that the stars' energy distribution among the three filters is not what is expected based

on integrating the product of the Sun's spectrum (as transcribed) with the filter functions. The size of this error is about 4%, and it is always in the same direction for each filter. Computed conversion factors based on the λ6600 filter frames are much higher than ones based on the λ6563 filter, and slightly larger than ones based on the λ6675 filter. Incidentally, Night 4 observation time was lost due to poor weather. The galaxies which were observed in Hα on each night are listed in Table B–5 along with the Hα conversion factor to flux *outside the earth's atmosphere* adopted for each night.

TABLE B–4. Hα FLUX CALIBRATION DATA

| | Star | Exp. (sec) | DN λ6563 | sec $Z$ | DN λ6600 | sec $Z$ | DN λ6675 | sec $Z$ |
|---|---|---|---|---|---|---|---|---|
| Night 1 | HD60298 | 1 | 108833 | 1.16 | 98919 | 1.16 | 97000 | 1.15 |
| Night 2 | HD42618 | 1 | 157667 | 1.20 | 141645 | 1.19 | 140822 | 1.18 |
| | HD60298 | 1 | 99727 | 1.02 | 89647 | 1.02 | 88363 | 1.03 |
| Night 3 | HD42618 | 2 | 342371 | 1.14 | 308406 | 1.15 | 303565 | 1.15 |
| | HD60298 | 2 | 217373 | 1.01 | 196660 | 1.01 | 193382 | 1.01 |
| Night 5 | HD60298 | 4 | 416120 | 1.03 | 375534 | 1.03 | 369942 | 1.03 |

TABLE B–5. GALAXY OBSERVATIONS IN Hα

| | Night 1 | Night 2 | Night 3 | Night 5 |
|---|---|---|---|---|
| NGC | 4303 | 4501 | 4254 | 4535 |
| | 4321 | 4536 | 4569 | |
| Factor[a] | $4.31 \pm 0.07$ | $4.41 \pm 0.41$ | $4.05 \pm 0.36$ | $4.57 \pm 0.09$ |

[a] Units are erg $\text{sec}^{-1}$ $\text{pixel}^{-1}$/(DN $\text{sec}^{-1}$ $\text{pixel}^{-1}$).

## References

Allen, C. W. 1973, *Astrophysical Quantities* (London: The Athlone Press).

Hirshfeld, A., and Sinnott, R. W. 1982, *Sky Catalogue 2000.0* (Cambridge: Cambridge University Press).

Kurucz, R. L., Furenlid, I., Brault, J., and Testerman, L. 1984, *Solar Flux Atlas from 296 to 1300nm* (Kitt Peak National Solar Observatory).

Moffett, T. J., and Barnes, T. G., III. 1980, *Ap. J. Suppl.*, **44**, 427.

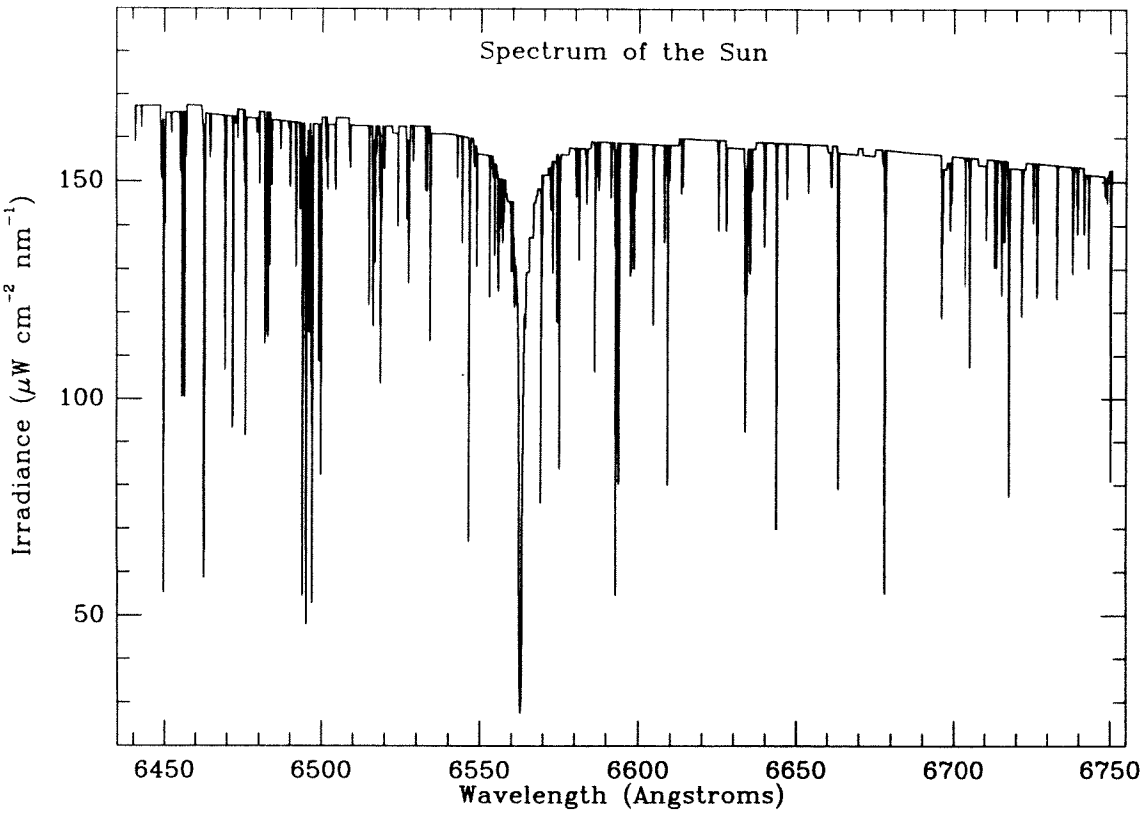


Figure B–1. Spectrum of the Sun in the vicinity of H$\alpha$.

# Appendix C
# Coordinate Transformations for Velocity Components

This appendix describes the coordinate transformations used frequently in the study of extragalactic velocity fields and dimensions. Here is the realm of inclined, rotating objects whose deprojected dimensions and velocity components can be found by transforming the observed, projected components.

Imagine a galaxy viewed face-on by an observer looking down the $z$-axis (in the $(-z)$-direction), so the disk appears circular. Name the coordinate axes $x$, $y$, and $z$ (Figure C–1). Now tip the galaxy by rotating it about the $x$-axis so that the "top" edge (the side extended in the $y$-direction) is farthest fom the observer and the "bottom" edge is near (Figure C–2). Let the angle through which such a rotation is accomplished be called $i$, for inclination. The value of $i$ lies in the range $[0°, 90°]$, where $i = 90°$ corresponds to an edge-on view. Orientations with the "top" edge far away, for example, are accomplished with a suitable rotation about the $z$-axis (see the $\mathbf{R}$ matrix below), thus preserving the range $i \in [0°, 90°]$. Let the observer be looking now in the $(-z')$-direction, and let the coordinates in the plane of the sky be $x'$ and $y'$. The matrix $\mathbf{T}$ which transforms the vector $\mathbf{x} = (x, y, z)$ to $\mathbf{x}' = (x', y', z')$ is

$$\mathbf{T} = \begin{pmatrix} 1 & 0 & 0 \\ 0 & \cos i & -\sin i \\ 0 & \sin i & \cos i \end{pmatrix} . \qquad (C-1)$$

Now rotate the galaxy counterclockwise through an angle $pa$. The angle $pa$ here is not the usual definition of position angle, but instead follows the mathematical convention of measuring angles counterclockwise from the positive branch of the horizontal axis.

$$\text{"conventional meaning of position angle PA"} = pa - 90°. \qquad (C-2)$$

Let the sky coordinates now be $u$ and $v$ while maintaining the $z'$-axis as the line of sight (Figure C–3). The matrix $\mathbf{R}$ which gives this rotation is

$$\mathbf{R} = \begin{pmatrix} \cos pa & \sin pa & 0 \\ -\sin pa & \cos pa & 0 \\ 0 & 0 & 1 \end{pmatrix}. \qquad (C-3)$$

The product $\mathbf{G} = \mathbf{TR}$ is

$$\mathbf{G} = \begin{pmatrix} \cos pa & \sin pa & 0 \\ -\sin pa \cos i & \cos pa \cos i & -\sin i \\ -\sin pa \sin i & \cos pa \sin i & \cos i \end{pmatrix}, \qquad (C-4)$$

so $\mathbf{xTR} = \mathbf{xG} = \mathbf{s}$, where $\mathbf{s} = (u, v, z')$. That is, coordinates $\mathbf{x} = (x, y, z)$ in the plane of the galaxy with the $x$-axis along the projected major axis are transformed to sky coordinates $\mathbf{s} = (u, v, z')$ through $\mathbf{G}$.

It is useful to know how to transform from the vector $\mathbf{s}$ in sky coordinates $(u, v, z')$ to the same vector in galaxy coordinates $\mathbf{x} = (x, y, z)$, since sky coordinates are what can actually be measured. This is given by the inverse matrix $\mathbf{G^{-1}} = \mathbf{R^{-1}T^{-1}}$, so $\mathbf{sG^{-1}} = \mathbf{x}$.

$$\mathbf{G^{-1}} = \begin{pmatrix} \cos pa & -\sin pa \cos i & -\sin pa \sin i \\ \sin pa & \cos pa \cos i & \cos pa \sin i \\ 0 & -\sin i & \cos i \end{pmatrix}. \qquad (C-5)$$

Velocity information in the $(x, y, z)$ coordinate system transforms to the $(u, v, z')$ system in the same way as do spatial coordinates. Since the interesting components of a velocity $\mathbf{v} = (v_x, v_y, v_z)$ in galactic coordinates are not $v_y$ and $v_z$ but rather the circular and radial components $v_c$ and $v_r$ of $\mathbf{v}$, yet another transformation must be made. Define a cylindrical coordinate system $(c, r, z)$ in which to describe velocity components. $c$ is the tangential component of a vector and $r$ is the radial component, leaving $z$ to be, as before, the component in the direction toward the observer (Figure C–4). $(c, r, z)$ is a left-handed coordinate system. Use the matrix $\mathbf{Q}$ to transform

from $\mathbf{x} = (x, y, z)$ to $\mathbf{o} = (c, r, z)$, where

$$\mathbf{Q} = \begin{pmatrix} -\sin\theta & \cos\theta & 0 \\ \cos\theta & \sin\theta & 0 \\ 0 & 0 & 1 \end{pmatrix}. \qquad (C-6)$$

$\theta$ is the azimuth of the vector referred to the galactic coordinate system, as shown in Figure C–4. So $\mathbf{xQ} = \mathbf{o}$. $\mathbf{Q}$ has the interesting property $\mathbf{Q^{-1}} = \mathbf{Q}$.

Since velocities are measured in sky coordinates, whereas the interesting components are the polar quantities, it is useful to know the transformation matrix $\mathbf{\Lambda} = \mathbf{G^{-1}Q}$. Let $\mathbf{v_{sky}} = (v_u, v_v, v_{z'})$ and $\mathbf{v_{polar}} = (v_c, v_r, v_z)$. Then $\mathbf{v_{polar}} = \mathbf{v_{sky}\Lambda}$.

$$\mathbf{\Lambda} = \begin{pmatrix} -\cos pa\sin\theta - \sin pa\cos\theta\cos i & \cos pa\cos\theta - \sin pa\sin\theta\cos i & -\sin pa\sin i \\ -\sin pa\sin\theta + \cos pa\cos\theta\cos i & \sin pa\cos\theta + \cos pa\sin\theta\cos i & \cos pa\sin i \\ -\cos\theta\sin i & -\sin\theta\sin i & \cos i \end{pmatrix}. \qquad (C-7)$$

The inverse matrix $\mathbf{\Lambda^{-1}}$ is

$$\mathbf{\Lambda^{-1}} = \begin{pmatrix} -\cos pa\sin\theta - \sin pa\cos\theta\cos i & -\sin pa\sin\theta + \cos pa\cos\theta\cos i & -\cos\theta\sin i \\ \cos pa\cos\theta - \sin pa\sin\theta\cos i & \sin pa\cos\theta + \cos pa\sin\theta\cos i & \sin\theta\sin i \\ -\sin pa\sin i & \cos pa\sin i & \cos i \end{pmatrix}. \qquad (C-8)$$

Some other useful collected relationships are

$$x' = x, \qquad (C-9)$$

$$y' = y\cos i, \qquad (C-10)$$

$$\theta = \arctan\frac{y}{x} = \arctan\frac{y'}{x'\cos i}, \qquad (C-11)$$

$$r = \sqrt{x^2 + y^2} = \sqrt{(x')^2 + (y'/\cos i)^2}. \qquad (C-12)$$

If work is done in two dimensions only, so the data is the projection of the galaxy onto the $(u, v)$ plane (the sky plane), then the full three-dimensional analysis is not necessary. In the two-dimensional case, use instead the submatrices which are formed from the first two rows and first two columns of the $3 \times 3$ matrices for $\mathbf{G}$ and $\mathbf{\Lambda^{-1}}$.

That is, the appropriate submatrix occupies the upper left-hand corner of the larger matrix. The corresponding two-dimensional matrices $\mathbf{G^{-1}}$ and $\Lambda$ are

$$\mathbf{G^{-1}} = \begin{pmatrix} \cos pa & -\sin pa \sec i \\ \sin pa & \cos pa \sec i \end{pmatrix}, \qquad (C-13)$$

$$\mathbf{\Lambda} = \begin{pmatrix} -\cos pa \sin\theta - \sin pa \cos\theta \sec i & \cos pa \cos\theta - \sin pa \cos\theta \sec i \\ -\sin pa \sin\theta + \cos pa \cos\theta \sec i & \sin pa \cos\theta + \cos pa \sin\theta \sec i \end{pmatrix}. \qquad (C-14)$$

It often happens that velocity data presented in the literature in the form of rotation curves are at variance with more current data. The old values assumed for the position angle of the major axis and for the inclination may be different from those now accepted. In that case, a correction can be made to those old data to make them agree with the new convention.

Let the old quoted values of the position angle and inclination be $\mathrm{PA_0}$ and $i_0$, and let the measured velocity be $\mathrm{V_{obs}}$ at position $(x'_0, y'_0)$ in the plane of the sky relative to the center of rotation of the galaxy, where the positive $x'$-axis coincides with the receding side of the (old value) major axis (Figure C–2). The velocity corrected for the old orientation, $\mathrm{V_0}$, is

$$\mathrm{V_0} = \frac{\mathrm{V_{obs}}}{\sin \mathrm{i_0} \cos\phi_0}, \qquad (C-15)$$

where $\phi_0$ is the angle subtended by the point $(x_0, y_0)$ and the (old) major axis, as measured in the plane of the galaxy. That is,

$$\phi_0 = \arctan \frac{y_0/\cos i_0}{x_0} - \mathrm{PA_0} - 90°. \qquad (C-16)$$

PA has its conventional meaning and is measured counter-clockwise from the positive ray of the $y'_0$-axis.

To correct the old quoted velocity, the old deprojections must be undone and new ones inserted based on the new orientation parameters. Let $\mathrm{V_{true}}$ be the true value of the rotation velocity, based on corrections using the new orientation parameters

$\mathrm{PA_{true}}$ and $i_{\mathrm{true}}$.

$$\mathrm{V_{true}} = \mathrm{V_0} \frac{\sin i_0 \cos \phi_0}{\sin i_{\mathrm{true}} \cos \phi_{\mathrm{true}}}. \qquad (C-17)$$

Less obvious, but equally important, is the fact that coordinates which were based on the old orientation parameters also need to be corrected. Measurements of the galactocentric radius fall into this category. The old coordinates $(x_0, y_0)$ in the plane of the galaxy must be reprojected onto the sky through the old-valued transformation matrix $\mathbf{T_{i_0}}$ to give old coordinates in the plane of the sky. $\mathbf{x_0 T_{i_0}} = \mathbf{x'_0}$, where

$$\mathbf{T_{i_0}} = \begin{pmatrix} 1 & 0 \\ 0 & \cos i_0 \end{pmatrix} \qquad (C-18)$$

is the matrix $\mathbf{T}$ with arguments $i_0$ instead of $i$. The resulting reprojection is then rotated through the difference between $\mathrm{PA_0}$ and $\mathrm{PA_{true}}$ with the matrix $\mathbf{R_{\Delta PA}}$. $\mathbf{R_{\Delta PA}}$ is the matrix $\mathbf{R}$ with arguments $\Delta\mathrm{PA} = \mathrm{PA_0} - \mathrm{PA_{true}}$ instead of $pa$:

$$\mathbf{R_{\Delta PA}} = \begin{pmatrix} \cos \Delta\mathrm{PA} & \sin \Delta\mathrm{PA} \\ -\sin \Delta\mathrm{PA} & \cos \Delta\mathrm{PA} \end{pmatrix}. \qquad (C-19)$$

$\mathbf{x_0 T_{i_0} R_{\Delta PA}} = \mathbf{x'_{true}}$. Finally, the coordinates are deprojected onto the galactic plane using the new value for the inclination through $\mathbf{T^{-1}_{i_{true}}}$, where

$$\mathbf{T^{-1}_{i_{true}}} = \begin{pmatrix} 1 & 0 \\ 0 & \sec i_{\mathrm{true}} \end{pmatrix}. \qquad (C-20)$$

Thus, $\mathbf{x_{true}} = \mathbf{x_0 T_{i_0} R_{\Delta PA} T^{-1}_{i_{true}}}$. If the sky coordinates $(u, v)$ are used (instead of coordinates $(x, y)$ referred to the major axis), then surround the matrix multiplication with $\mathbf{G_0^{-1}}$ on the left and $\mathbf{G_{true}}$ on the right.

If the old velocity data are taken *along the presumed major axis only,* then the corrected velocities depend only on the old and new position angle values:

$$\mathrm{V_{true}} = \mathrm{V_0} \frac{\sin i_0}{\sin i_{\mathrm{true}} \cos\left\{\arctan\left[(\tan \Delta PA)/\cos i_{\mathrm{true}}\right]\right\}}. \qquad (C-21)$$

The corrected radius for an off-major axis datum is $r_{\mathrm{true}} = \sqrt{x^2_{\mathrm{true}} + y^2_{\mathrm{true}}}$, where

$$\begin{aligned} (x, y)_{\mathrm{true}} &= (r_0, 0)\mathbf{R_{\Delta PA} T^{-1}_{i_{true}}} \\ &= \left(r_0 \cos \Delta\mathrm{PA},\ (r_0 \sin \Delta\mathrm{PA})/\cos i_{\mathrm{true}}\right). \end{aligned} \qquad (C-22)$$

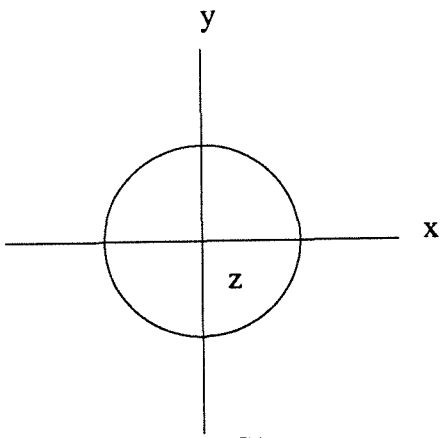


Figure C1

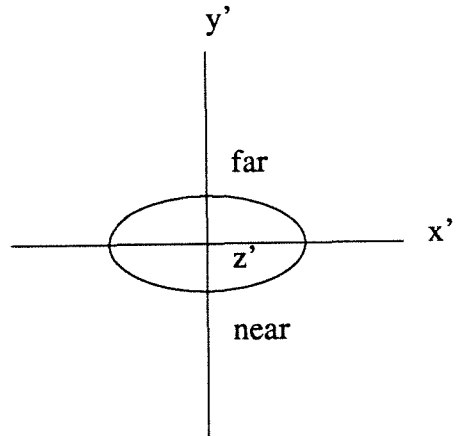


Figure C2

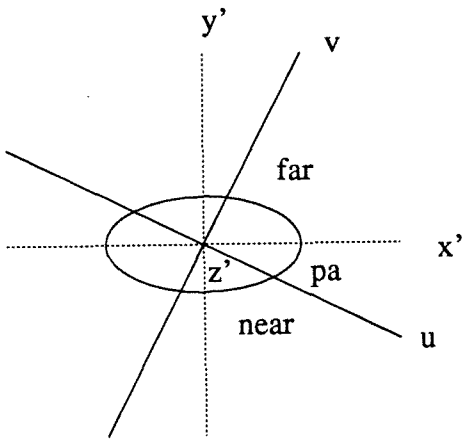


Figure C3

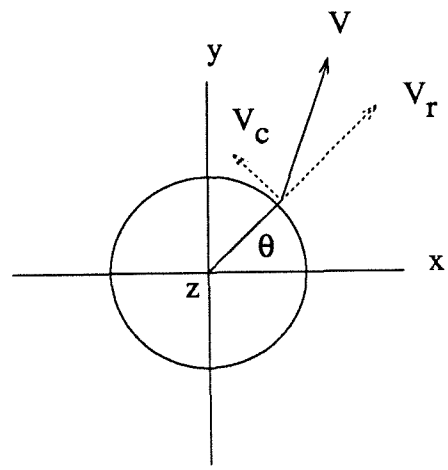


Figure C4

Figure C-1. Coordinate axes for a face-on disk galaxy.
Figure C-2. Coordinate axes for an inclined disk galaxy.
Figure C-3. Coordinate axes for an inclined disk galaxy in the plane of the sky.
Figure C-4. Coordinate system for motions in the plane of a disk galaxy.

# Appendix D
# Flux Recovery in Interferometric Observations of Exponential Disks

Interferometric observations typically are able to recover only a fraction of the flux that a single dish detects from an extended source. The problem of flux recovery given incomplete coverage in the $uv$ plane is expected to be particularly troublesome in the case that the source emission distribution falls off exponentially, as in a galactic exponential disk. This is because the Fourier transform of an exponential has considerable power at lower spatial frequencies. Comparison of interferometer flux with single-dish measurements (Table 5–6) shows that about 10% to 60% of the single-dish flux was recovered in the images made with OVRO data. The observed CO surface brightness profiles are modeled here as reconstructions based on incomplete $uv$ coverage of a decaying exponential source function. Both the shapes of the observed profiles and the amount of flux recovered are well fit by the models.

Let the surface brightness of a distant galaxy be represented by a suitable normalized exponential function, $\mathbf{f}(r) = \exp(-r/a)$, where $r$ is the radial distance from the center of the galaxy and $a$ is a scale length. Let the galaxy be viewed face-on. An interferometer observing the model galaxy will gather data which are values of the two-dimensional Fourier transform of $\mathbf{f}(r)$ sampled along ellipses in the $uv$ plane.

The presence of circular symmetry in the model surface brightness allows the two-dimensional Fourier transform to be interpreted as a one-dimensional Hankel transform (Bracewell 1986). Let $f(x,y)$ and $F(s,t)$ be a Fourier transform pair. Whenever $f(x,y) = \mathbf{f}(r)$, where $r^2 = x^2 + y^2$ so that $\mathbf{f}$ is circularly symmetric, then

the transform, $\mathbf{F}$, also has circular symmetry: $F(s,t) = \mathbf{F}(q)$, where $q^2 = s^2 + t^2$. The Hankel transform is the one-dimensional relationship between $\mathbf{f}$ and $\mathbf{F}$ and is defined

$$\begin{aligned} \mathbf{F}(q) &= 2\pi \int_0^\infty \mathbf{f}(r)\, J_0(2\pi q r)\, r\, dr, \\ \mathbf{f}(r) &= 2\pi \int_0^\infty \mathbf{F}(q)\, J_0(2\pi q r)\, q\, dq. \end{aligned} \qquad (D-1)$$

Here, $J_0(z)$ is the Bessel function of order zero. In particular, the Hankel transform of $\mathbf{f}(r) = \exp(-r/a)$ is

$$\mathbf{F}(q) = \frac{2\pi a^2}{(4\pi^2 a^2 q^2 + 1)^{3/2}}. \qquad (D-2)$$

Let the interferometer sample $\mathbf{F}$ uniformly for all values of $q$ corresponding to the range of baselines achieved. That is, the $uv$ sampling function is being modelled as a filled annulus. For OVRO, the minimum baseline length is $b_{\rm min} = 10.4$ m, and the typical maximum baseline is $b_{\rm max} = 60$ m. These lengths correspond to values of the Fourier conjugate coordinate $q$ of

$$\begin{aligned} q_{\rm min} &= \frac{1}{\lambda / b_{\rm min}} = 4000\,{\rm rad}^{-1} = 0.0194\,{\rm arcsec}^{-1}, \\ q_{\rm max} &= 0.112\,{\rm arcsec}^{-1}, \end{aligned} \qquad (D-3)$$

where $\lambda = 2.6 \times 10^{-3}$ m is the wavelength of the observations. An interferometer is able to recover only a fraction of the flux from an extended source because it is sensitive only to those Fourier components between $q_{\rm min}$ and $q_{\rm max}$. Consequently, the shape of the surface brightness profile recovered by interferometric observations is obtained by evaluating the inverse Hankel transform of $\mathbf{F}(q)$ with the limits $q_{\rm min}$ and $q_{\rm max}$ on the integral, instead of zero and infinity. Call this function $R(q_{\rm min}, q_{\rm max}, r)$, which models the variation of surface brightness with radius, $r$, in the image reconstructed from interferometric observations of an exponentially decaying source function:

$$R(q_0, q_1, r) = 2\pi \int_{q_0}^{q_1} \frac{2\pi a^2}{(4\pi^2 a^2 q^2 + 1)^{3/2}}\, J_0(2\pi q r)\, q\, dq. \qquad (D-4)$$

A Taylor series expansion of $R(q_0, q_1, r)$ useful for small $r$ may be derived by substituting the Taylor series for $J_0(z)$ into the inverse Hankel transform integral and integrating term-by-term. For simplicity of notation, change variables to $z = 2\pi aq$. Then

$$R(z_0, z_1, r) = \int_{z_0}^{z_1} \frac{z}{(z^2+1)^{3/2}} J_0\left(\frac{rz}{a}\right) dz. \qquad (D-5)$$

The Taylor series expansion of $J_0(z)$, valid for all $z$, is (Watson 1958)

$$J_0(z) = \sum_{k=0}^{\infty} \frac{(-1)^k}{(k!)^2} \left(\frac{z}{2}\right)^{2k} = 1 - \frac{z^2}{2^2} + \frac{z^4}{2^2 \cdot 4^2} - + \cdots. \qquad (D-6)$$

Substituting this sum into the integral (D–5) yields

$$R(z_0, z_1, r) = \int_{z_0}^{z_1} \left[ \sum_{k=0}^{\infty} \frac{(-1)^k}{(k!)^2} \left(\frac{zr}{2a}\right)^{2k} \right] \frac{z}{(z^2+1)^{3/2}} dz. \qquad (D-7)$$

The sum under the integral is uniformly convergent on the interval $[0, 1]$ by the Weierstrass M-test (cf. Whittaker and Watson 1927): each term, $u_k(z)$, of the sum satisfies

$$|u_k(z)| = \left| \frac{(-1)^k}{(k!)^2} \left(\frac{zr}{2a}\right)^{2k} \frac{z}{(z^2+1)^{3/2}} \right| \leq M_k = \frac{1}{(k!)^2} \left(\frac{r}{2a}\right)^{2k}, \qquad (D-8)$$

and the sum

$$\sum_{k=0}^{\infty} \frac{1}{(k!)^2} \left(\frac{r}{2a}\right)^{2k} \qquad (D-9)$$

converges for any $r$ and $a$. Since the sum in equation (D–7) is uniformly convergent, it may be integrated term-by-term to yield

$$R(z_0, z_1, r) = \sum_{k=0}^{\infty} \frac{(-1)^k}{(k!)^2} \left(\frac{r}{2a}\right)^{2k} \int_{z_0}^{z_1} \frac{z^{2k+1}}{(z^2+1)^{3/2}} dz. \qquad (D-10)$$

The integral is a standard one (Gradshteyn and Ryzhik 1980), tabulated for small values of $k$ from which the general formula may be deduced:

$$\int \frac{x^{2m+1}}{(cx^2+1)^{3/2}} dx = \sum_{k=0}^{m} \frac{(-1)^{m+k}}{(2k-1)c^{m+1}} \binom{m}{k} (cx^2+1)^{(2k-1)/2}, \qquad (D-11)$$

where $m \geq 0$ and is integral and $c$ is a constant. $\binom{m}{k} = m!/k!(m-k)!$ is the binomial coefficient. Setting $c = 1$ and substituting into equation (D–10) leads to the double sum

$$R(z_0, z_1, r) = \sum_{k=0}^{\infty} \frac{1}{(k!)^2} \left(\frac{r}{2a}\right)^{2k} \sum_{n=0}^{k} \frac{(-1)^n}{2n-1} \binom{k}{n} (z^2+1)^{(2n-1)/2} \Big|_{z_0}^{z_1}. \qquad (D-12)$$

Figure D–1 shows the graph of $R$ for $z_0$ and $z_1$ corresponding to the typical values of $q_{\min}$ and $q_{\max}$ for the OVRO interferometer. Also shown are successive approximations to $R$ calculated using the first few terms in equation (D–12).

The behavior of $R(z_0, z_1, r)$ for large $r$ may be found by substituting the asymptotic series for $J_0(z)$ in the integral (D–5) and integrating by parts. The leading-order term in the asymptotic expansion of $J_0(z)$ is (Watson 1958)

$$J_0(z) \sim \sqrt{\frac{2}{\pi z}} \cos\left(z - \frac{\pi}{4}\right), \qquad z \to \infty. \qquad (D-13)$$

So

$$R(z_0, z_1, r) \sim \int_{z_0}^{z_1} \frac{z}{(z^2+1)^{3/2}} \left(\frac{2z}{\pi r z}\right)^{1/2} \cos\left(\frac{rz}{a} - \frac{\pi}{4}\right) dz, \qquad r \to \infty. \qquad (D-14)$$

Integrating by parts once yields

$$R(z_0, z_1, r) \sim \left(\frac{2a^3}{\pi r^3}\right)^{1/2} \frac{z^{1/2}}{(z^2+1)^{3/2}} \sin\left(\frac{rz}{a} - \frac{\pi}{4}\right) \Big|_{z_0}^{z_1} -$$
$$- \left(\frac{2a^3}{\pi r^3}\right)^{1/2} \int_{z_0}^{z_1} \frac{\frac{1}{2} z^{1/2}(z^2+1) - 3z^{3/2}}{(z^2+1)^{5/2}} \sin\left(\frac{rz}{a} - \frac{\pi}{4}\right) dz, \qquad r \to \infty. \qquad (D-15)$$

The integral on the right is $O(r^{-5/2})$, which is higher order than the leading term, $O(r^{-3/2})$, establishing

$$R(z_0, z_1, r) \sim \left(\frac{2a^3}{\pi r^3}\right)^{1/2} \frac{z^{1/2}}{(z^2+1)^{3/2}} \sin\left(\frac{rz}{a} - \frac{\pi}{4}\right) \Big|_{z_0}^{z_1}, \qquad r \to \infty \qquad (D-16)$$

as an asymptotic approximation to $R$. Further terms may be calculated with much labor and little reward using more terms in the asymptotic expansion of $J_0(z)$ and successive integrations by parts. Equation (D–16) shows explicitly the oscillatory nature of $R$ for large $r$, which is due to the sharp cutoffs of the sampling function at radii $q_0$ and $q_1$. The minimum of the first negative sidelobe of $R$ for one particular choice of $q_0$ and $q_1$ may be seen near $r = 19''$ in Figure D–1. The "negative bowl" upon which source structure often appears superimposed in images processed using a CLEAN-type algorithm may be due, in part, to accurate reconstruction of the first negative sidelobe of $R$ outside its central peak.

Knowledge of the relative sizes of the central surface brightness as determined from interferometer data and single-dish measurements can yield an estimate for the amount of flux recovered by the interferometer. The value of the fraction of central surface brightness recovered, $\mu_0$, is a function of the scale length of the model exponential, $a$, and the limits of the $uv$ coverage, $q_0$ and $q_1$. This fact can be seen by setting $r = 0$ in equation (D–12) and noting that all terms are zero except the first:

$$\mu_0 = R(z_0, z_1, 0) = \frac{-1}{(z^2+1)^{1/2}}\bigg|_{z_0}^{z_1} = \frac{-1}{(4\pi^2 a^2 q^2 + 1)^{1/2}}\bigg|_{q_0}^{q_1}. \qquad (D-17)$$

Recall that the central surface brightness of the model function is unity. Thus, an estimate for the scale length, $a$, may be arrived at using equation (D–17) with a measurement of the fraction of central surface brightness recovered for a particular $uv$ coverage. The total flux from an exponential source surface brightness distribution is

$$2\pi \int_0^\infty r e^{-r/a}\, dr = 2\pi a^2. \qquad (D-18)$$

The term "total recovered flux" as used in this appendix is the sum of *positive* contributions to the flux, so regions where $R < 0$ do not diminish the sum. This convention mimics the procedure used in determining total emission in images made using a CLEAN-type algorithm (see §3.1.4).

Figures D–2 and D–3 are graphs which sketch the relationships among $q_0$, $q_1$, $a$, $\mu_0$, and $\phi$, the fraction of the total flux recovered. Figure D–2 aids the prediction of $\phi$ given knowledge of $\mu_0$, $q_0$, and $q_1$. Figure D–3 displays the same information in a manner which aids the selection of a model source scale length $a$ given knowledge of $q_0$ and $\phi$. From extensive computations of a grid of models, it was found that $\phi$ is completely insensitive to $q_1$ when $q_0$ and $q_1$ have reasonable values for an astronomical interferometer; that is, when $q_1$ is not too small nor too near to $q_0$. This is because the vast majority of the power is at small $q$, while power at large $q$ serves to make $R$ tend to be positive, especially at large radii where the oscillatory nature of $R$ is evident. In Figure D–2, changing $q_1$ amounts to shifting the curves horizontally to the left (toward smaller $\mu_0$) with near-constant $\phi$.

## References

Bracewell, R. N. 1986, *The Fourier Transform and Its Applications* (New York: McGraw Hill, Inc.).

Gradshteyn, I. S., and Ryzhik, I. M. 1980, *Table of Integrals, Series, and Products* (New York: Academic Press).

Watson, G. N. 1958, *A Treatise on the Theory of Bessel Functions* (London: Cambridge University Press).

Whittaker, E. T., and Watson, G. N. 1927, *A Course of Modern Analysis* (London: Cambridge University Press).

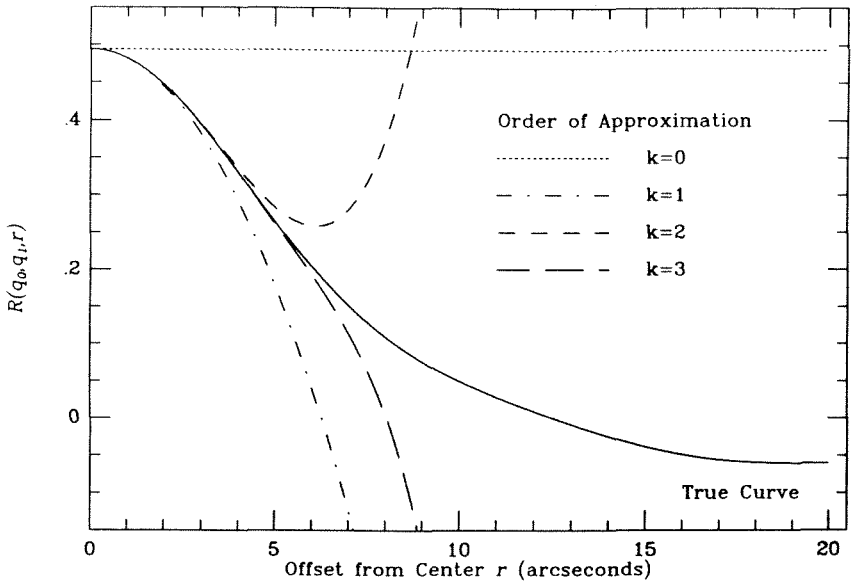


Figure D–1. Series approximations to $R$, the surface brightness of an exponential disk partially resolved by interferometric observations.

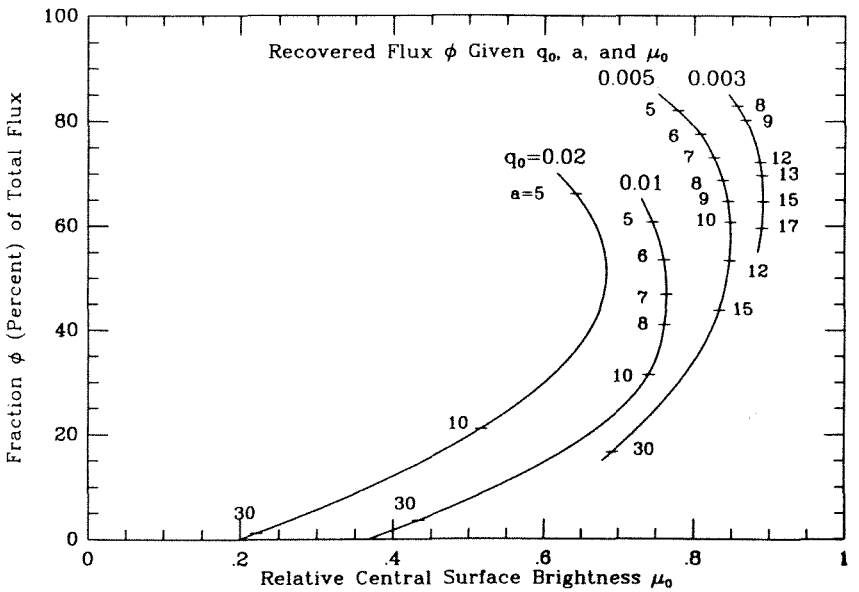


Figure D–2. Recovered fraction of flux $\phi$ versus the ratio of recovered to true central surface brightness $\mu$, the scale length $a$, and the minimum spacing $q_0$.

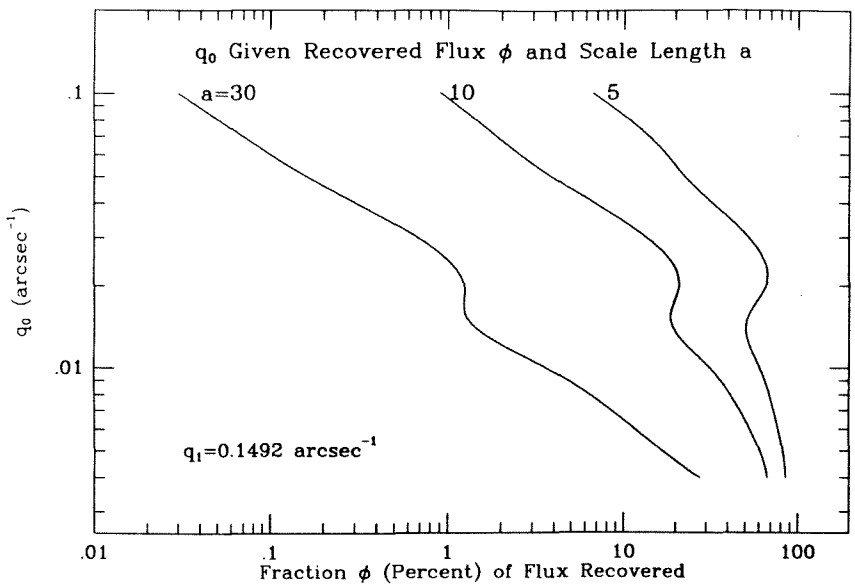


Figure D–3. Minimum spacing $q_0$ versus the fraction $\phi$ of flux recovered and scale length $a$ for a single value of the maximum spacing $q_1$.

# Appendix E
# Quantities Related to Two IMFs

The normalization constant, $\chi$, for an initial mass function $\xi(m)$ is

$$\chi(m_{\rm lo}, m_{\rm up}) = \int_{m_{\rm lo}}^{m_{\rm up}} \xi(m)\, dm. \qquad (E-1)$$

Values of $\chi$ for various mass cutoffs are tabulated in Table E–1 for the Salpeter IMF, $\xi(m) = m^{-2.35}$, and in Table E–2 for the extended Miller-Scalo IMF (equation 3–16).

TABLE E–1

NORMALIZATION OF THE SALPETER IMF

| $m_{\rm lo}$ ($M_\odot$) | $m_{\rm up}$ ($M_\odot$) | | | | | |
|---|---|---|---|---|---|---|
| | 30 | 40 | 50 | 60 | 80 | 100 |
| 8.0 | 0.0372 | 0.0396 | 0.0410 | 0.0418 | 0.0427 | 0.0432 |
| 5.0 | 0.0768 | 0.0793 | 0.0806 | 0.0814 | 0.0823 | 0.0829 |
| 2.0 | 0.283 | 0.285 | 0.287 | 0.288 | 0.289 | 0.289 |
| 1.0 | 0.733 | 0.736 | 0.737 | 0.738 | 0.739 | 0.739 |
| 0.8 | 0.994 | 0.996 | 0.997 | 0.998 | 0.999 | 1.000 |
| 0.6 | 1.469 | 1.471 | 1.472 | 1.473 | 1.474 | 1.475 |
| 0.5 | 1.881 | 1.883 | 1.884 | 1.885 | 1.886 | 1.887 |
| 0.4 | 2.544 | 2.547 | 2.548 | 2.549 | 2.550 | 2.550 |
| 0.3 | 3.756 | 3.758 | 3.759 | 3.760 | 3.761 | 3.762 |
| 0.2 | 6.498 | 6.500 | 6.502 | 6.502 | 6.503 | 6.504 |
| 0.1 | 16.578 | 16.578 | 16.579 | 16.580 | 16.581 | 16.582 |

The average mass per star in a stellar population that follows a given IMF is

$$\langle m \rangle = \frac{1}{\chi} \int_{m_{\rm lo}}^{m_{\rm up}} m\, \xi(m)\, dm \qquad (E-2).$$

TABLE E–2

NORMALIZATION OF THE MILLER-SCALO IMF

| $m_{lo}$ ($M_\odot$) | $m_{up}$ ($M_\odot$) | | | | | |
|---|---|---|---|---|---|---|
| | 30 | 40 | 50 | 60 | 80 | 100 |
| 8.0 | 0.0254 | 0.0268 | 0.0276 | 0.0280 | 0.0285 | 0.0288 |
| 5.0 | 0.0556 | 0.0570 | 0.0577 | 0.0582 | 0.0587 | 0.0590 |
| 2.0 | 0.2316 | 0.2331 | 0.2338 | 0.2343 | 0.2348 | 0.2350 |
| 1.0 | 0.6626 | 0.6640 | 0.6648 | 0.6652 | 0.6657 | 0.6660 |
| 0.8 | 0.8960 | 0.8974 | 0.8982 | 0.8986 | 0.8991 | 0.8994 |
| 0.6 | 1.2294 | 1.2308 | 1.2315 | 1.2320 | 1.2325 | 1.2328 |
| 0.5 | 1.4614 | 1.4628 | 1.4636 | 1.4640 | 1.4645 | 1.4648 |
| 0.4 | 1.7694 | 1.7708 | 1.7715 | 1.7720 | 1.7725 | 1.7727 |
| 0.3 | 2.2092 | 2.2106 | 2.2114 | 2.2118 | 2.2123 | 2.2126 |
| 0.2 | 2.9217 | 2.9232 | 2.9239 | 2.9244 | 2.9249 | 2.9251 |
| 0.1 | 4.4423 | 4.4437 | 4.4445 | 4.4449 | 4.4455 | 4.4457 |

TABLE E–3

AVERAGE MASS PER STAR – SALPETER IMF

| $m_{lo}$ ($M_\odot$) | $m_{up}$ ($M_\odot$) | | | | | |
|---|---|---|---|---|---|---|
| | 30 | 40 | 50 | 60 | 80 | 100 |
| 8.0 | 13.734 | 14.997 | 15.953 | 16.714 | 17.872 | 18.728 |
| 5.0 | 9.863 | 10.612 | 11.170 | 11.609 | 12.269 | 12.751 |
| 2.0 | 4.850 | 5.100 | 5.282 | 5.423 | 5.632 | 5.782 |
| 1.0 | 2.712 | 2.816 | 2.891 | 2.949 | 3.033 | 3.094 |
| 0.8 | 2.235 | 2.313 | 2.369 | 2.412 | 2.475 | 2.520 |
| 0.6 | 1.735 | 1.788 | 1.827 | 1.856 | 1.899 | 1.930 |
| 0.5 | 1.474 | 1.517 | 1.547 | 1.570 | 1.604 | 1.628 |
| 0.4 | 1.206 | 1.237 | 1.260 | 1.277 | 1.302 | 1.320 |
| 0.3 | 0.928 | 0.950 | 0.965 | 0.977 | 0.994 | 1.006 |
| 0.2 | 0.639 | 0.651 | 0.660 | 0.667 | 0.677 | 0.684 |
| 0.1 | 0.333 | 0.338 | 0.342 | 0.345 | 0.349 | 0.351 |

Values of the average mass per star for the Salpeter and the extended Miller-Scalo IMF are listed in Table E–3 and Table E–4.

TABLE E–4

AVERAGE MASS PER STAR – MILLER-SCALO IMF

| $m_{lo}$ ($M_\odot$) | $m_{up}$ ($M_\odot$) | | | | | |
|---|---|---|---|---|---|---|
| | 30 | 40 | 50 | 60 | 80 | 100 |
| 8.0 | 13.460 | 14.570 | 15.385 | 16.016 | 16.946 | 17.610 |
| 5.0 | 9.524 | 10.145 | 10.591 | 10.933 | 11.428 | 11.778 |
| 2.0 | 4.529 | 4.711 | 4.839 | 4.934 | 5.071 | 5.166 |
| 1.0 | 2.467 | 2.536 | 2.583 | 2.618 | 2.668 | 2.703 |
| 0.8 | 2.058 | 2.109 | 2.144 | 2.171 | 2.208 | 2.234 |
| 0.6 | 1.688 | 1.725 | 1.752 | 1.771 | 1.798 | 1.817 |
| 0.5 | 1.507 | 1.539 | 1.561 | 1.577 | 1.600 | 1.616 |
| 0.4 | 1.322 | 1.349 | 1.367 | 1.381 | 1.400 | 1.413 |
| 0.3 | 1.128 | 1.150 | 1.164 | 1.175 | 1.190 | 1.201 |
| 0.2 | 0.913 | 0.929 | 0.940 | 0.949 | 0.960 | 0.968 |
| 0.1 | 0.649 | 0.660 | 0.667 | 0.673 | 0.680 | 0.686 |